

CLOSED-FORM DYADIC GREEN'S FUNCTIONS FOR ELECTRIC DIPOLE
OVER PLANAR PERIODIC STRUCTURES PRINTED ON MULTILAYERED
MEDIA

A THESIS SUBMITTED TO
THE GRADUATE SCHOOL OF NATURAL AND APPLIED SCIENCES
OF
MIDDLE EAST TECHNICAL UNIVERSITY

BY

SÜLEYMAN ADANIR

IN PARTIAL FULFILLMENT OF THE REQUIREMENTS
FOR
THE DEGREE OF DOCTOR OF PHILOSOPHY
IN
ELECTRICAL AND ELECTRONICS ENGINEERING

SEPTEMBER 2022

Approval of the thesis:

**CLOSED-FORM DYADIC GREEN'S FUNCTIONS FOR ELECTRIC
DIPOLE OVER PLANAR PERIODIC STRUCTURES PRINTED ON
MULTILAYERED MEDIA**

submitted by **SÜLEYMAN ADANIR** in partial fulfillment of the requirements for
the degree of **Doctor of Philosophy in Electrical and Electronics Engineering De-
partment, Middle East Technical University** by,

Prof. Dr. Halil KALIPÇILAR
Dean, Graduate School of Natural and Applied Sciences _____

Prof. Dr. İlkey Ulusoy
Head of Department, **Electrical and Electronics Engineering** _____

Assoc. Prof. Dr. Lale Alatan
Supervisor, **Electrical and Electronics Engineering, METU** _____

Examining Committee Members:

Prof. Dr. Gülbin Dural
Electrical and Electronics Engineering, METU _____

Assoc. Prof. Dr. Lale Alatan
Electrical and Electronics Engineering, METU _____

Prof. Dr. Özlem Aydın Çivi
Electrical and Electronics Engineering, METU _____

Prof. Dr. Vakur B. Ertürk
Electrical and Electronics Engineering, Bilkent Univ. _____

Prof. Dr. Asım Egemen Yılmaz
Electrical and Electronics Engineering, Ankara Univ. _____

Date: 16.09.2022

I hereby declare that all information in this document has been obtained and presented in accordance with academic rules and ethical conduct. I also declare that, as required by these rules and conduct, I have fully cited and referenced all material and results that are not original to this work.

Name, Surname: Süleyman Adanır

Signature :

ABSTRACT

CLOSED-FORM DYADIC GREEN'S FUNCTIONS FOR ELECTRIC DIPOLE OVER PLANAR PERIODIC STRUCTURES PRINTED ON MULTILAYERED MEDIA

Adanır, Süleyman

Ph.D., Department of Electrical and Electronics Engineering

Supervisor: Assoc. Prof. Dr. Lale Alatan

September 2022, 144 pages

Aperiodic sources placed over periodic structures have attracted great interest from researchers of electromagnetics area. The analysis of such structures is a very challenging task since such an analysis must handle the infinite periodicity of the structure while also dealing with the aperiodic source over it which forbids a direct application of a periodic analysis to the problem. Full wave methods addressing these problems involve infinite summations and double integrations which make the analysis cumbersome. Homogenization based methods reduce the complexity of the analysis but at the expense of a loss of flexibility in handling different kinds of structures while the resulting Green's functions still need integrations as opposed to being in closed-form. The aim of this thesis is to propose a novel full-wave approach in obtaining closed-form expressions for the Green's functions of such structures which makes the analysis of these problems efficient while offering more flexibility compared to existing homogenization methods in the literature.

Keywords: closed-form Green's functions, planar periodic structures, multilayered

media, electric dipole excitation, Method of Moments

ÖZ

ÇOK KATMANLI ORTAMLAR ÜSTÜNE BASILI DÜZLEMSEL PERİYODİK YAPILARIN ÜZERİNDEKİ ELEKTRİK DİPOLÜN KAPALI FORM DİYADİK GREEN FONKSİYONLARI

Adanır, Süleyman

Doktora, Elektrik ve Elektronik Mühendisliği Bölümü

Tez Yöneticisi: Doç. Dr. Lale Alatan

Eylül 2022 , 144 sayfa

Periyodik yapıların üzerine yerleştirilen aperiodyik kaynaklar elektromanyetik alanındaki arařtırmacıların yıllardır büyük ilgisini çekmektedir. Bu tarz yapıların analizi, yapının sonsuz periyodikliđini hesaba katarken aynı zamanda dođrudan bir periyodik analize izin vermeyecek řekilde bir aperiodyik kaynađı ele almak zorunda olduđu için çok zorlu bir problemdir. Bu problemi ele alan tam dalga çözümleri analizin karmařıklıđını artıran sonsuz toplamlar ve çift integraller içermektedir. Homojenleřtirmeye dayanan metodlar bu karmařıklıđı azaltsa da incelenebilecek yapıların çeřitliliđi bakımından dezavantaj yaratmakta ve Green fonksiyonlarına ulařmak için integral alma gerekliliđini tamamen ortadan kaldırmamaktadırlar. Bu tezin amacı, bu tarz yapıların kapalı form Green fonksiyonlarını elde etmeye yönelik yenilikçi bir tam dalga çözümleri önererek, söz konusu problemlerin analizini verimli bir hale getirirken, incelenebilecek yapılar konusunda mevcut homojenleřtirme yöntemlerine kıyasla daha fazla esneklik sunmaktır.

Anahtar Kelimeler: kapalı form Green fonksiyonları, düzlemsel periyodik yapılar, çok katmanlı ortamlar, elektrik dipol kaynağı, moment yöntemi

to Doruk and Gülgün

ACKNOWLEDGMENTS

I would like to express my gratitude to my supervisor Assoc. Prof. Dr. Lale Alatan for her guidance, support and valuable recommendations throughout my thesis work. Every conversation with her helped me refresh my motivation towards this thesis work.

I am also grateful to the members of my Thesis Monitoring Committee, Prof. Dr. Gülbin Dural and Prof. Dr. Vakur B. Ertürk for their valuable time, comments, suggestions and criticism.

I want to express my appreciation to my wife Gülgün for her patience during my thesis work and also to my son Doruk for his understanding towards my PhD studies despite his young age.

Finally I would like to thank my father, mother, brother and sister for their continuous support throughout my life.

TABLE OF CONTENTS

ABSTRACT	v
ÖZ	vii
ACKNOWLEDGMENTS	x
TABLE OF CONTENTS	xi
LIST OF TABLES	xiv
LIST OF FIGURES	xvi
CHAPTERS	
1 INTRODUCTION	1
1.1 Motivation and Problem Definition	1
1.2 The Outline of the Thesis	3
2 BACKGROUND ON ANALYSIS OF PLANAR PERIODIC STRUCTURES	5
2.1 Homogenization of Metasurfaces	5
2.1.1 Surface Susceptibility Method	6
2.1.2 Surface Impedance Method	7
2.2 Dipole Excitation of Periodic Surfaces	8
2.2.1 Full-wave Approaches	8
2.2.2 Homogenization Based Approaches	11
2.3 Remarks on the Available Approaches in the Literature	18

3	MOM ANALYSIS OF PERIODIC PLANAR STRUCTURES - REFLECTION COEFFICIENTS	19
3.1	Introduction	19
3.2	Formulation for MoM Analysis	23
3.3	Periodic Surfaces in Free Space	27
3.4	Periodic Surfaces Printed on Multilayered Media	29
3.5	Concluding Remarks	42
4	SINGULARITY CANCELLATION FOR MOM ANALYSIS OF PERIODIC PLANAR STRUCTURES	45
4.1	Introduction	45
4.2	Formulation	48
4.3	Integral Tests	49
4.4	S-Parameter Analysis	56
4.5	Concluding Remarks	60
5	CLOSED-FORM DYADIC GREEN'S FUNCTIONS FOR DIPOLE EXCITATION OF PLANAR PERIODIC STRUCTURES	61
5.1	Introduction	61
5.2	Formulation	64
5.3	Numerical Results	85
5.3.1	Periodic Surface in Free Space	86
5.3.2	Periodic Surface Printed on Dielectric Slab	96
5.3.3	Reducing Patch Size	108
5.3.4	Increasing Periodicity	109
5.3.5	Increasing Periodicity and Patch Size	112

5.4	Proposals for Extending the Approach to Structures With ϕ Dependence	119
5.4.1	Fourier Series Approach	119
5.4.2	Averaging Approach	121
5.4.3	2-D Complex Image Approximation Approach	121
6	CONCLUSION	125
	REFERENCES	127
	APPENDICES	
A	HANKEL TRANSFORM AND BESSEL IDENTITIES	137
B	2-D ESPRIT METHOD	139
	CURRICULUM VITAE	143

LIST OF TABLES

TABLES

Table 3.1 Mode/port definitions and indices	22
Table 3.2 Parameters of the reflection coefficient analysis problem for free space case	28
Table 3.3 Parameters of the reflection coefficient analysis problem for multi- layered case	37
Table 3.4 Test of symmetric gaussian quadrature w.r.t reference results in [73]	44
Table 4.1 Comparison of Integration Results for equation (3.46) with $p = q =$ $i = 0$	50
Table 4.2 Comparison of Integration Results for equation (3.46) with $p = q =$ 0 and $i = 6$	52
Table 4.3 Comparison of Integration Results for equation (3.50) with $p = q = 0$	53
Table 5.1 Parameters of the problem for free space case	87
Table 5.2 Parameters of the problem for multilayered case	97
Table 5.3 Parameters of the problem for multilayered case with reduced patch size	109
Table 5.4 Parameters of the problem for multilayered case with increased pe- riodicity	111

Table 5.5 Parameters of the problem for multilayered case with increased pe- riodicity and patch size	113
--------------------------------------------------------------------------------------------------------------------	-----

LIST OF FIGURES

FIGURES

Figure 1.1	Classification according to the analysis approaches of periodic composite materials [1]	1
Figure 1.2	Examples of metascreen and metafilm [1]	3
Figure 2.1	Excitation of the periodic structure, in ASM approach, by an infinite set of phased dipole sources at locations \vec{r}_{mn}	10
Figure 2.2	Original problem and its equivalent homogenized problem in [52]	12
Figure 2.3	One of the sample geometries in [52]	14
Figure 2.4	Fig. 3 of [52]	15
Figure 2.5	Magnitude of y component of the total and incident electric field due to the dipole oriented in y direction	16
Figure 2.6	Magnitude of z component of the total and incident electric field due to the dipole oriented in z direction	16
Figure 2.7	Ratio of reflected to total field for $ E_{yy} $ and $ E_{zz} $	17
Figure 3.1	A sample geometry for the general periodic structure and TE-TM decomposition of incident and reflected electromagnetic fields . . .	19
Figure 3.2	Geometry of RWG basis functions	24
Figure 3.3	Magnitude of S_{11} versus θ for various ϕ values	29
Figure 3.4	Real part of S_{41} versus θ for various ϕ values	30

Figure 3.5	Imaginary part of S_{41} versus θ for various ϕ values	30
Figure 3.6	Real part of S_{32} versus θ for various ϕ values	31
Figure 3.7	Imaginary part of S_{32} versus θ for various ϕ values	31
Figure 3.8	Magnitude of $S_{12}, S_{22}, S_{32}, S_{42}$ versus θ for $\phi = 50$	32
Figure 3.9	Magnitude of S_{11} versus θ for various ϕ values, obtained by using the DCIM technique in [67]	38
Figure 3.10	Magnitude of S_{11} versus θ for various ϕ values	39
Figure 3.11	Real part of S_{21} versus θ for various ϕ values	39
Figure 3.12	Imaginary part of S_{21} versus θ for various ϕ values	40
Figure 3.13	Real part of S_{22} versus θ for various ϕ values	40
Figure 3.14	Imaginary part of S_{22} versus θ for various ϕ values	41
Figure 3.15	Real part of S_{42} versus θ for various ϕ values	41
Figure 3.16	Imaginary part of S_{42} versus θ for various ϕ values	42
Figure 3.17	Magnitude of $S_{11}, S_{21}, S_{31}, S_{41}$ versus θ for $\phi = 50$	43
Figure 4.1	Local coordinate system in each subtriangle	47
Figure 4.2	Location of quadrature points after arcsinh transformation when the observation point is at the center of the source triangle	54
Figure 4.3	Location of quadrature points after arcsinh transformation when the observation point is outside of but close to the source triangle	55
Figure 4.4	Location of quadrature points after arcsinh transformation when the observation point is very far from the source triangle	55
Figure 4.5	Magnitude of S_{32} versus θ for various ϕ values; free space case with singularity cancellation	56

Figure 4.6	Magnitude of S_{11} , S_{21} , S_{31} , S_{41} versus θ for $\phi = 50$, including the results obtained without singularity cancellation (w/o sc); free space case	57
Figure 4.7	Magnitude of S_{21} versus θ for various ϕ values; multilayered case with singularity cancellation	58
Figure 4.8	Real part of S_{22} versus θ for various ϕ values, including the results obtained without singularity cancellation (w/o sc); multilayered case	58
Figure 4.9	Imaginary part of S_{22} versus θ for various ϕ values, including the results obtained without singularity cancellation (w/o sc); multilayered case	59
Figure 4.10	Magnitude of S_{11} , S_{21} , S_{31} , S_{41} versus θ for $\phi = 50$, including the results obtained without singularity cancellation (w/o sc); multilayered case	59
Figure 5.1	Periodic structure with a rectangular lattice of PEC scatterers with spacings D_x and D_y , excited by a dipole source at point r_d	62
Figure 5.2	Sampling path described in [67] (C_0) and modified sampling path used in the proposed method in this thesis (C_1)	64
Figure 5.3	Periodic surface in free space	86
Figure 5.4	Magnitude of S_{11} for the structure described in Fig. 5.3 and Table 5.1	87
Figure 5.5	Magnitude of E_{yz} with respect to y_o ($x_o = 0$ and $z_o = 5$ mm), scattered from the 2-D periodic structure in free space	88
Figure 5.6	Magnitude of E_{yz} with respect to y_o ($x_o = 0$ and $z_o = 2$ mm), scattered from the 2-D periodic structure in free space	89
Figure 5.7	Phase of E_{yz} with respect to y_o ($x_o = 0$ and $z_o = 2$ mm), scattered from the 2-D periodic structure in free space	89

Figure 5.8	Magnitude of E_{zz} with respect to x_o ($y_o = 0$ and $z_o = 2$ mm), scattered from the 2-D periodic structure in free space	90
Figure 5.9	Phase of E_{zz} with respect to x_o ($y_o = 0$ and $z_o = 2$ mm), scat- tered from the 2-D periodic structure in free space	90
Figure 5.10	Magnitude of E_{zy} with respect to y_o ($x_o = 0$ and $z_o = 5$ mm), scattered from the 2-D periodic structure in free space	91
Figure 5.11	Magnitude of E_{zy} with respect to y_o ($x_o = 0$ and $z_o = 2$ mm), scattered from the 2-D periodic structure in free space	91
Figure 5.12	Phase of E_{zy} with respect to y_o ($x_o = 0$ and $z_o = 2$ mm), scat- tered from the 2-D periodic structure in free space	92
Figure 5.13	Magnitude of E_{yy} with respect to y_o ($x_o = 0$ and $z_o = 5$ mm), scattered from the 2-D periodic structure in free space	93
Figure 5.14	Magnitude of E_{yy} with respect to y_o ($x_o = 0$ and $z_o = 2$ mm), scattered from the 2-D periodic structure in free space	93
Figure 5.15	Phase of E_{yy} with respect to y_o ($x_o = 0$ and $z_o = 2$ mm), scattered from the 2-D periodic structure in free space	94
Figure 5.16	Magnitude of E_{yy} with respect to x_o ($y_o = 0$ and $z_o = 5$ mm), scattered from the 2-D periodic structure in free space	94
Figure 5.17	Magnitude of E_{yy} with respect to x_o ($y_o = 0$ and $z_o = 2$ mm), scattered from the 2-D periodic structure in free space	95
Figure 5.18	Phase of E_{yy} with respect to x_o ($y_o = 0$ and $z_o = 2$ mm), scattered from the 2-D periodic structure in free space	95
Figure 5.19	Periodic surface printed on dielectric slab	96
Figure 5.20	Magnitude of E_{yz} with respect to y_o ($x_o = 0$ and $z_o = 5$ mm), scattered from the 2-D periodic structure printed on dielectric slab . . .	97

Figure 5.21	Magnitude of E_{yz} with respect to y_o ($x_o = 0$ and $z_o = 2$ mm), scattered from the 2-D periodic structure printed on dielectric slab . . .	98
Figure 5.22	Phase of E_{yz} with respect to y_o ($x_o = 0$ and $z_o = 2$ mm), scat- tered from the 2-D periodic structure printed on dielectric slab	98
Figure 5.23	Magnitude of E_{zz} with respect to x_o ($y_o = 0$ and $z_o = 2$ mm), scattered from the 2-D periodic structure printed on dielectric slab . . .	99
Figure 5.24	Phase of E_{zz} with respect to x_o ($y_o = 0$ and $z_o = 2$ mm), scat- tered from the 2-D periodic structure printed on dielectric slab	100
Figure 5.25	Magnitude of E_{zy} with respect to y_o ($x_o = 0$ and $z_o = 5$ mm), scattered from the 2-D periodic structure printed on dielectric slab . . .	100
Figure 5.26	Magnitude of E_{zy} with respect to y_o ($x_o = 0$ and $z_o = 2$ mm), scattered from the 2-D periodic structure printed on dielectric slab . . .	101
Figure 5.27	Phase of E_{zy} with respect to y_o ($x_o = 0$ and $z_o = 2$ mm), scat- tered from the 2-D periodic structure printed on dielectric slab	101
Figure 5.28	Magnitude of E_{yy} with respect to y_o ($x_o = 0$ and $z_o = 5$ mm), scattered from the 2-D periodic structure printed on dielectric slab . . .	102
Figure 5.29	Magnitude of E_{yy} with respect to y_o ($x_o = 0$ and $z_o = 2$ mm), scattered from the 2-D periodic structure printed on dielectric slab . . .	103
Figure 5.30	Phase of E_{yy} with respect to y_o ($x_o = 0$ and $z_o = 2$ mm), scattered from the 2-D periodic structure printed on dielectric slab . . .	103
Figure 5.31	Magnitude of E_{yy} with respect to x_o ($y_o = 0$ and $z_o = 5$ mm), scattered from the 2-D periodic structure printed on dielectric slab . . .	104
Figure 5.32	Magnitude of E_{yy} with respect to x_o ($y_o = 0$ and $z_o = 2$ mm), scattered from the 2-D periodic structure printed on dielectric slab . . .	104
Figure 5.33	Phase of E_{yy} with respect to x_o ($y_o = 0$ and $z_o = 2$ mm), scattered from the 2-D periodic structure printed on dielectric slab . . .	105

Figure 5.34	Comparison of magnitudes of E_{zz} with respect to x_o ($y_o = 0$ and $z_o = 2$ mm), obtained with various scatterers	106
Figure 5.35	Comparison of magnitudes of E_{zy} with respect to y_o ($x_o = 0$ and $z_o = 2$ mm), obtained with various scatterers	106
Figure 5.36	Comparison of magnitudes of E_{yy} with respect to x_o ($y_o = 0$ and $z_o = 2$ mm), obtained with various scatterers	107
Figure 5.37	Comparison of magnitudes of E_{yy} with respect to y_o ($x_o = 0$ and $z_o = 2$ mm), obtained with various scatterers	107
Figure 5.38	Magnitude of E_{yy} with respect to y_o ($x_o = 0$ and $z_o = 2$ mm), scattered from the 2-D periodic structure with parameters given in Table 5.3	110
Figure 5.39	Magnitude of E_{yy} with respect to x_o ($y_o = 0$ and $z_o = 2$ mm), scattered from the 2-D periodic structure with parameters given in Table 5.3	110
Figure 5.40	Magnitude of E_{yy} with respect to y_o ($x_o = 0$ and $z_o = 2$ mm), scattered from the 2-D periodic structure with parameters given in Table 5.4	111
Figure 5.41	Magnitude of E_{yy} with respect to x_o ($y_o = 0$ and $z_o = 2$ mm), scattered from the 2-D periodic structure with parameters given in Table 5.4	112
Figure 5.42	Magnitude of E_{yy} with respect to y_o ($x_o = 0$ and $z_o = 2$ mm), scattered from the 2-D periodic structure with parameters given in Table 5.5	113
Figure 5.43	Magnitude of E_{yy} with respect to x_o ($y_o = 0$ and $z_o = 2$ mm), scattered from the 2-D periodic structure with parameters given in Table 5.5	114
Figure 5.44	Sampled data (result of numerical calculation) and the complex image approximation (by DCIM) of SP1 for Problem-2	115

Figure 5.45 Sampled data (result of numerical calculation) and the complex image approximation (by DCIM) of SP1 for Problem-5 116

Figure 5.46 Sampled data (result of numerical calculation) and the complex image approximation (by DCIM) of SP3 for Problem-2 117

Figure 5.47 Sampled data (result of numerical calculation) and the complex image approximation (by DCIM) of SP3 for Problem-5 117

Figure 5.48 Sampled data (result of numerical calculation) and the complex image approximation (by DCIM) of SP5 for Problem-2 118

Figure 5.49 Sampled data (result of numerical calculation) and the complex image approximation (by DCIM) of SP5 for Problem-5 118

CHAPTER 1

INTRODUCTION

1.1 Motivation and Problem Definition

Interaction of electromagnetic field with periodic structures can be investigated by classifying them into three regions as explained in [1] and shown in Fig. 1.1.

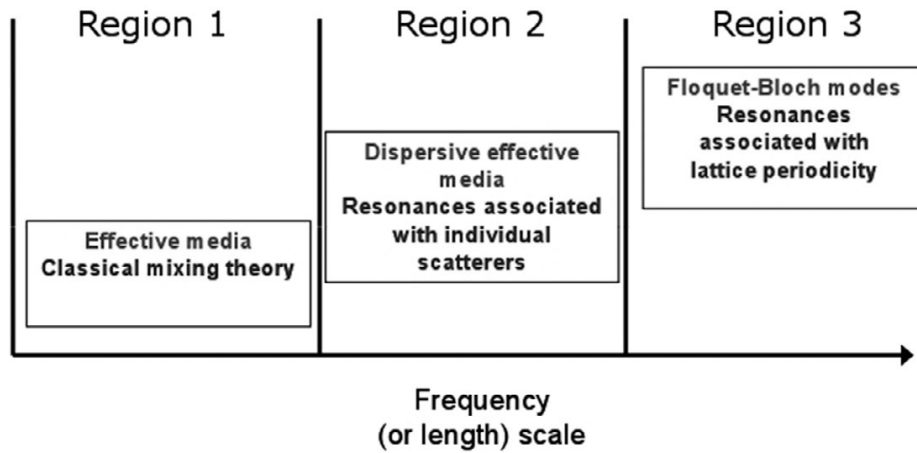


Figure 1.1: Classification according to the analysis approaches of periodic composite materials [1]

Region 1 is known as quasistatic region where the frequency is low or equivalently the periodicity of the structure is much smaller than the wavelength. Electromagnetic field behavior mimics the situation in a homogeneous material. Classical mixing formulas are utilized in this region to obtain equivalent homogenized material properties. This approach is called as effective medium theory and it has a long history in electromagnetics community, a survey of which can be found in [2] - [4].

At the other end of the spectrum, we have Region 3 where the wavelength is compa-

rable to or smaller than the periodicity of the structure. Electromagnetic field interaction is more complicated in this region and the fields no longer behave as if they are in an effective medium which means that homogenization approach does not work here. The complicated field behavior in this region requires more elaborate methods to be utilized like Floquet-Bloch mode approach [5], [6]. Resonances associated with lattice periodicity occur in this region making the implementation of structures like photonic bandgap (PBG) materials [7] possible. 2-D counterparts of these structures are frequency selective surfaces (FSS) [8].

Between the two regions described above, lies the Region 2 with its very interesting properties. Wavelength is still large compared to the periodicities of the structure. Thus, no resonances related to the lattice periodicity occur. However, the individual scatterers can be designed (by adjusting scatterer geometry and/or constitutive parameters) such that the scatterers themselves resonate. This phenomenon takes us to the world of metamaterials [9], [10]. The electromagnetic behaviour of the medium can be characterized by effective parameters which are frequency dependent (dispersive media) in contrast to the frequency independent effective parameters of Region 1.

Two dimensional version of metamaterials are called metasurfaces. Works on metasurface designs, properties, applications and analysis have dominated much of the metamaterial literature in the last years [11]. This is very understandable due to the compatibility of metasurfaces with planar fabrication technologies and ease of integration into the on-chip devices. They take up less space and often have lower losses compared to their 3-D relatives while still being able to offer most of the functionalities that metamaterials can. Diverse range of applications can be found in [12].

It has been found useful by some researchers to introduce two subclasses of metasurfaces based on their shape: metafilms and metascreens [1]. Metasurfaces consisting of an array of isolated scatterers are called metafilms while metasurfaces formed by an array of isolated apertures are called metascreens (Fig. 1.2).

A very important classification of metasurfaces is based on the uniformity of the periodic structure. If the constitutive elements in different unit cells are identical, the metasurface is said to be uniform. Non-uniform or modulated metasurfaces are obtained when the geometrical parameters of the elements are varied throughout the

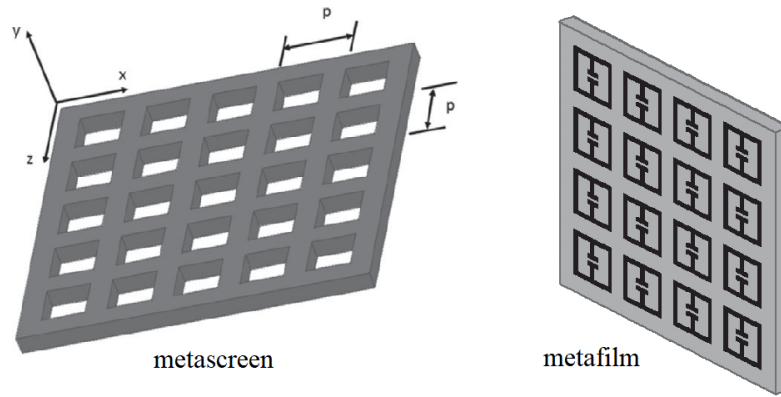


Figure 1.2: Examples of metascreen and metafilm [1]

surface. This class of metasurfaces are utilized for manipulation of radiated waves, guided waves and also conversion between these two types [13]. The interested reader can find many areas of applications and design procedures for modulated metasurfaces in [13] and the references therein.

The subclass of metasurfaces which is the subject of this thesis is the class of uniform metasurfaces. High-impedance surfaces (HIS), which are also referred to as reactive impedance surfaces (RIS) or artificial magnetic conductors (AMC), are special types of metasurfaces originally proposed in [14]. It is generally utilized in antenna applications enabling further improvements that cannot be achieved by conventional materials, such as reduced size [15], [16], increased side-lobe suppression [17], enhanced bandwidth [18], reduced mutual coupling [19] and wider scanning angles [20]. They have also found use in design of endfire antennas [21], [22], low profile multi-beam omnidirectional antennas [23] and null-steering antennas with deep nulls in wide bandwidths [24]. All these important applications utilize HIS in the vicinity of aperiodic conductors which provides the motivation behind this thesis work to analyze electric dipole sources over planar periodic structures printed on multilayered media.

1.2 The Outline of the Thesis

A literature review has been conducted on the analysis of planar periodic structures with a focus on uniform metasurfaces and aperiodic excitations of them. A summary

of the findings of this research is presented in Chapter 2 including a discussion on the strengths and weaknesses of the available methods.

At the core of this thesis work lies the reflection coefficient analysis of planar periodic structures since the proposed method is raised on the foundations of accurate S-Parameter representation of these structures. Method of Moments (MoM) is utilized for this reflection coefficient analysis whose formulation is presented in Chapter 3 which includes the details on formation of the impedance matrix, associated Green's functions of the structure, acceleration of the infinite summations and approximation technique used for the multilayered media. S-Parameter results demonstrating the accuracy and efficiency of the developed code are presented in this chapter for both free space and multilayered media problems.

Due to the considerations mentioned in the last section of Chapter 3, singularity cancellation is also studied in this thesis work and an adaptation of a well-known technique from the literature to MoM analysis of planar periodic structures is formulated. Chapter 4 is devoted to this adaptation. The accuracy of the formulation is verified by performing detailed tests on the integrals arising in the impedance matrix computation. The outcomes of these integral tests are presented in this chapter which are followed by the calculated S-Parameters of the periodic structures in free space and multilayered media by utilizing singularity cancellation.

Chapter 5 presents the proposed method of this thesis work for the analysis of dipole sources above periodic planar structures. After a brief introduction, comes the formulation section in which the derivation of the closed-form dyadic Green's function for the problem is given in detail. The approach is tested on a numerical example taken from the literature and also on a modified version of it. Results of the proposed technique are presented in this chapter which includes also the results obtained by a commercial 3D EM software, demonstrating the accuracy and efficiency of the technique. This chapter also includes a section on proposals to extend the method for rotationally asymmetric structures that have ϕ dependent S-Parameters.

This thesis ends with Chapter 6 in which conclusions drawn from this work are presented. Final remarks on the proposed method and the challenges it helps to overcome are also discussed together with the possible future studies.

CHAPTER 2

BACKGROUND ON ANALYSIS OF PLANAR PERIODIC STRUCTURES

A summary of the findings of the literature review conducted on the analysis of planar periodic structures with a focus on aperiodic dipole excitation of uniform metasurfaces is presented in this chapter.

Analysis of metasurfaces with dipole excitation can be made by a full wave approach or a homogenization based approach. Before giving details on these approaches, it would be appropriate to summarize the characterization of metasurfaces by homogenized models. The first section of the chapter is devoted to this summary.

2.1 Homogenization of Metasurfaces

Early works on characterization of electrically thin surfaces were based on approaches similar to the ones applied for 3-D metamaterials. These methods utilized measurement of the reflection and transmission coefficients from the surface. The periodic surface is considered as a homogeneous slab, the effective parameters of which can be retrieved by using the reflection and transmission data [25], [26], [27]. Using this bulk parameter analysis for metasurfaces has some issues related to non-uniqueness of the obtained effective parameter as detailed in [28]. Since a metasurface acts like an infinitesimal sheet, it is best characterized by generalized sheet transition conditions (GSTCs) [12] in contrast to effective medium parameters used for a 3-D metamaterial. GSTCs are boundary conditions relating the electromagnetic fields and surface parameters. Homogenization of metasurfaces can be classified according to the type of parameters used in these boundary conditions. If the GSTCs are expressed in terms of polarizabilities of the scatterers or effective polarizability dyadics, we have

a polarizability based model [29]. GSTCs can also be expressed in terms of surface susceptibilities [30] and surface impedance matrices [31]. The latter two approaches are more pronounced in the works for dipole excitation of periodic structures as will be detailed later. Thus, these two methods will be explained further in the following subsections.

2.1.1 Surface Susceptibility Method

Generalized sheet transition conditions based on surface susceptibilities were derived for a metafilm in [30] as:

$$\begin{aligned}\hat{a}_z \times \vec{H}|_{z=0^-}^{0+} &= j\omega \bar{\chi}_{ES} \cdot \vec{E}_{t,av}|_{z=0} - \hat{a}_z \times \nabla_t [\chi_{MS}^{zz} H_{z,av}]_{z=0} \\ \vec{E}|_{z=0^-}^{0+} \times \hat{a}_z &= j\omega \bar{\chi}_{MS} \cdot \vec{H}_{t,av}|_{z=0} + \hat{a}_z \times \nabla_t [\chi_{ES}^{zz} E_{z,av}]_{z=0}\end{aligned}\quad (2.1)$$

Here, "av" means the average of the fields on either side of the metafilm. $\bar{\chi}_{ES}$ and $\bar{\chi}_{MS}$ are the dyadic surface electric and magnetic susceptibilities, which have units of meters and are related to the electric and magnetic polarizability densities of the scatterers per unit area.

There are some assumptions and limitations of the GSTC derivation in [30]:

- The formulations are for metafilms only and are not for metascreens.
- The scatterers are in free space.
- The scatterers do not occupy too large a fraction of the surface (sparse approximation).
- Only the case, where the scatterers and lattice have sufficient symmetry such that the surface susceptibility dyadics are diagonal, is considered, i.e.

$$\begin{aligned}\bar{\chi}_{ES} &= \hat{a}_x \hat{a}_x \chi_{ES}^{xx} + \hat{a}_y \hat{a}_y \chi_{ES}^{yy} + \hat{a}_z \hat{a}_z \chi_{ES}^{zz} \\ \bar{\chi}_{MS} &= \hat{a}_x \hat{a}_x \chi_{MS}^{xx} + \hat{a}_y \hat{a}_y \chi_{MS}^{yy} + \hat{a}_z \hat{a}_z \chi_{MS}^{zz}\end{aligned}\quad (2.2)$$

- Periodicity of the scatterer lattice is small compared to the wavelength (like 0.1λ) (basic assumption of homogenization).

Having derived the GSTCs, same authors analyzed the plane wave incidence on metafilms by using GSTCs and derived expressions for reflection (R) and transmission (T) coefficients in terms of surface susceptibilities in [32].

A retrieval approach is presented in [28] based on these reflection and transmission coefficients. Once the reflection and transmission coefficients are obtained (either from measurements or from numerical calculations), the surface susceptibilities can be determined. Two different sets of R and T (for example, one at normal incidence and one at oblique incidence) are required for each polarization.

Reflection and transmission coefficient expressions in [32] and the retrieval approach in [28] are based on the GSTC derivation in [30]. Thus, they all have the same assumptions mentioned above. Works on more general problems have been presented by similar group of authors in [33] - [36].

2.1.2 Surface Impedance Method

As an alternative to the surface susceptibility model, a planar metasurface can be characterized in terms of a one sided or two-sided surface impedance condition. In general, the two-sided surface-impedance method and the susceptibility method can be made equivalent to each other if the impedances are defined in terms of the susceptibilities as shown in [1] and repeated here as:

$$\begin{aligned}\hat{a}_z \times \vec{H}|_{z=0^-}^{0+} &= \bar{\bar{Y}}_{ES} \cdot \vec{E}_{t,av}|_{z=0} \\ \vec{E}|_{z=0^-}^{0+} \times \hat{a}_z &= \bar{\bar{Z}}_{MS} \cdot \vec{H}_{t,av}|_{z=0}\end{aligned}\quad (2.3)$$

in which the surface transfer admittance $\bar{\bar{Y}}_{ES}$ and the surface transfer impedance $\bar{\bar{Z}}_{MS}$ are given by

$$\begin{aligned}\bar{\bar{Y}}_{ES} &= j\omega\bar{\bar{\chi}}_{ES} + \frac{j\bar{\bar{\chi}}_{MS}^{zz}}{\omega\mu}(\hat{a}_z \times \vec{k})(\hat{a}_z \times \vec{k}) \\ \bar{\bar{Z}}_{MS} &= j\omega\bar{\bar{\chi}}_{MS} + \frac{j\bar{\bar{\chi}}_{ES}^{zz}}{\omega\epsilon}(\hat{a}_z \times \vec{k})(\hat{a}_z \times \vec{k})\end{aligned}\quad (2.4)$$

The surface impedance model is studied mainly by a group of researchers other than

the group working on susceptibility model. The work of this surface impedance model group is mainly analytical [31], [37], [38]. This modeling is also limited to dense arrays whose periodicity are small compared to wavelength.

2.2 Dipole Excitation of Periodic Surfaces

The full wave techniques will be summarized first and the homogenization based approaches will follow this in the second subsection.

2.2.1 Full-wave Approaches

Two methods are generally mentioned in the literature as full wave approaches for solving the problem of dipole excitation of periodic structures. These are direct plane-wave expansion method (PWM) and array scanning method (ASM).

PWM and ASM techniques are presented and compared in [39]. A very brief summary will be given here by using figures and expressions of this reference.

A unit electric dipole current source is assumed to be over the periodic structure, described by $\vec{J}^i(\vec{r}') = \hat{J}\delta(\vec{r}' - \vec{r}_0)$. The field in free space at \vec{r} radiated by this dipole source is denoted by $\vec{E}_{inc}(\vec{r}, \vec{r}_0)$. Plane wave expansion method relies on the fact that a spherical wave can be written as an integral summation of plane waves. This integration is actually an inverse Fourier transformation and also known as Weyl Identity [40]. Thus, the incident field due to the dipole is expressed in terms of plane wave spectrum as:

$$\vec{E}_{inc}(\vec{r}, \vec{r}_0) = \frac{-j}{8\pi^2} \iint_{-\infty}^{+\infty} \frac{1}{k_z} \bar{\bar{G}}(\vec{k}_t) \cdot \hat{J} e^{-j[k_x(x-x_0)+k_y(y-y_0)+k_z|z-z_0|]} dk_x dk_y \quad (2.5)$$

$\bar{\bar{G}}(\vec{k}_t)$ is a dyad defined in (2.6).

$$\bar{\bar{G}}(\vec{k}_t) = [-j\omega\mu\bar{\bar{I}} - \frac{1}{j\omega\epsilon}\vec{k}\vec{k}] \quad (2.6)$$

where \vec{k} is the wavenumber vector and \vec{k}_t is the transverse (with respect to z) part of it. The incident field below the dipole source can be seen as a continuum of plane waves of the form:

$$\vec{E}_{inc}^{PW}(\vec{r}, \vec{r}_0, \vec{k}_t) = \hat{p}(\vec{k}_t) W_{inc}(\vec{k}_t, \vec{r}_0) e^{-j[k_x x + k_y y - k_z z]} \quad (2.7)$$

with

$$W_{inc}(\vec{k}_t, \vec{r}_0) = \frac{-j}{8\pi^2} \frac{1}{k_z} \hat{p}(\vec{k}_t) \cdot \vec{G}(\vec{k}_t) \cdot \hat{J} e^{j[k_x x_0 + k_y y_0 - k_z z_0]} \quad (2.8)$$

where $\hat{p}(\vec{k}_t)$ is the unit direction vector corresponding to the plane wave with transverse wavenumber \vec{k}_t . The unit amplitude incident plane wave is

$$\vec{E}_{inc}^{upw}(\vec{r}, \vec{k}_t) = \hat{p}(\vec{k}_t) e^{-j[k_x x + k_y y - k_z z]} \quad (2.9)$$

and the scattered field due to this wave is denoted as $\vec{E}_{sca}^{upw}(\vec{r}, \vec{k}_t)$. Therefore, by using the superposition principle, the scattered field due to the dipole source is expressed by

$$\vec{E}_{sca}(\vec{r}, \vec{r}_0) = \iint_{-\infty}^{+\infty} W_{inc}(\vec{k}_t, \vec{r}_0) \vec{E}_{sca}^{upw}(\vec{r}, \vec{k}_t) dk_x dk_y \quad (2.10)$$

In order to find the scattered electric field due to a unit amplitude incident plane wave, electric field integral equation (EFIE) is used. This formulation involves the periodic Green's function (PGF) of the structure which is expressed as a double infinite spectral summation. Thus, calculation of the scattered field due to the dipole source involves a double infinite integral and a double infinite summation when the direct plane wave expansion method is employed.

Array scanning method [41] - [43] can be utilized to reduce the limits of the double integration to finite values. It was applied for the problem of calculating the fields of a line source above a 1-D periodic structure in [44] and for the problem with a line source above a 2-D periodic structure in [45]. The problem with a dipole

source over 2-D periodic structure is investigated in [39]. This method is based on synthesizing the single dipole source, $\vec{J}^i(\vec{r}^i)$, from an infinite phased array of dipole sources, $\vec{J}^{i,\infty}(\vec{r}^i, \vec{k}_t)$, which can be expressed mathematically as:

$$\vec{J}^{i,\infty}(\vec{r}^i, \vec{k}_t) = \hat{J} \sum_{m=-\infty}^{+\infty} \sum_{n=-\infty}^{+\infty} \delta(\vec{r}^i - \vec{r}_{mn}) e^{-j(k_x ma + k_y nb)} \quad (2.11)$$

where a and b are the periodicities of the structure and $\vec{r}_{mn} = \vec{r}_0 + ma\hat{x} + nb\hat{y}$ specifies the locations of the infinite set of phased dipole sources as shown in Fig. 2.1.

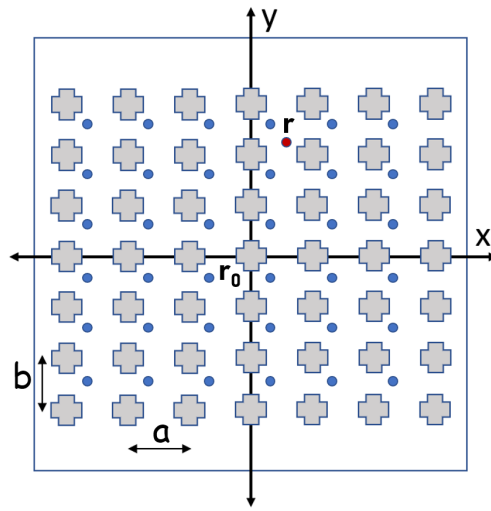


Figure 2.1: Excitation of the periodic structure, in ASM approach, by an infinite set of phased dipole sources at locations \vec{r}_{mn}

According to the ASM identity, the current of the single dipole can be obtained by integrating (2.11) over the Brillouin zone [42] as:

$$\vec{J}^i(\vec{r}^i) = \frac{ab}{4\pi^2} \int_{-\pi/a}^{\pi/a} \int_{-\pi/b}^{\pi/b} \vec{J}^{i,\infty}(\vec{r}^i, \vec{k}_t) dk_x dk_y \quad (2.12)$$

This equality forms the basis of ASM. The procedure starts by assuming that the periodic structure is excited by the infinite source in (2.11) instead of a single dipole. The scattered field due to this infinitely periodic source can be found by utilizing EFIE

and a periodic moment method. If we denote this scattered field by $\vec{E}_{sca}^\infty(\vec{r}, \vec{r}_0, \vec{k}_t)$, then the scattered field due to the dipole source is found by an integration over the Brillouin zone as follows:

$$\vec{E}_{sca}(\vec{r}, \vec{r}_0) = \frac{ab}{4\pi^2} \int_{-\pi/a}^{\pi/a} \int_{-\pi/b}^{\pi/b} \vec{E}_{sca}^\infty(\vec{r}, \vec{r}_0, \vec{k}_t) dk_x dk_y \quad (2.13)$$

Compared to PWM, the reduction of the integration limits makes ASM more efficient. This comparison is studied in [39] and the ratio of the computational effort needed for two methods is obtained numerically for various vertical separations between the dipole source and the periodic structure. Efficiency increase achieved by ASM is very high especially when the distance between the dipole and the periodic structure becomes smaller.

Array scanning method is utilized to analyze shielding effectiveness of 2-D periodic screens with high-pass behaviors against dipole sources in [46] and [47]. Resonant periodic screens in the presence of dipole sources are investigated in [48]. In all these three works, the periodicity of the structure studied is kept below $\lambda/2$. When this limit is exceeded, care must be taken in order for the integrations over complex plane to yield correct results. This issue is studied in [49] with a proposal to extend the periodicity beyond $\lambda/2$.

Due to the successful applications of the array scanning method mentioned above, this technique is considered as the source of reference results when homogenization based approaches are studied.

2.2.2 Homogenization Based Approaches

Homogenization based approaches were applied for the problem of calculating the fields of a line source above a 1-D periodic structure in [50] and for the problem with a line source above a 2-D periodic structure in [51]. To the best of our knowledge, first study on homogenized Green's functions for the problem with a dipole source over 2-D periodic structure is [52].

The geometry of the problem studied in [52] is shown in Fig. 2.2.

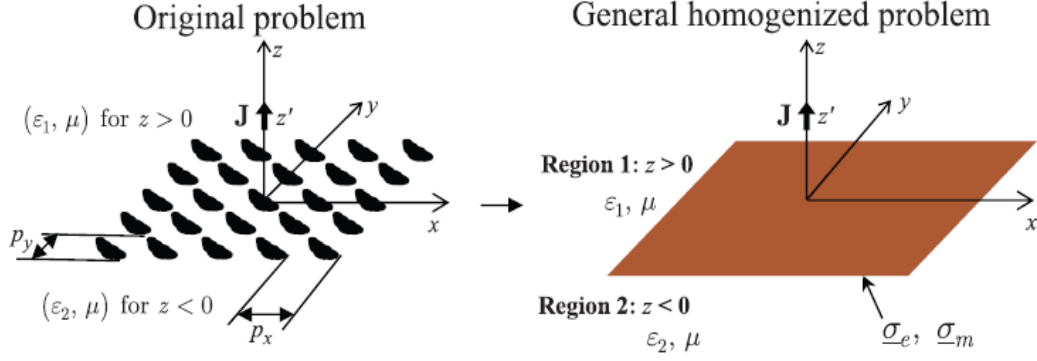


Figure 2.2: Original problem and its equivalent homogenized problem in [52]

In [52], the Green's functions for the reflected, $\bar{\bar{G}}_r^{(1)}$, and transmitted fields, $\bar{\bar{G}}_t^{(2)}$, are expressed as integrations in the spectral domain which are shown below:

$$\bar{\bar{G}}_r^{(1)} = \frac{-j}{8\pi^2} \iint \frac{1}{k_{1z}} (r_{tt}\hat{t}_1^+\hat{t}_1^- + r_{tp}\hat{t}_1^+\hat{p}_1^- + r_{pt}\hat{p}_1^+\hat{t}_1^- + r_{pp}\hat{p}_1^+\hat{p}_1^-) \times e^{-j\vec{k}_1^+\cdot\vec{r}} e^{j\vec{k}_1^-\cdot\vec{r}'} dk_x dk_y \quad (2.14)$$

$$\bar{\bar{G}}_t^{(2)} = \frac{-j}{8\pi^2} \iint \frac{1}{k_{1z}} (t_{tt}\hat{t}_2^-\hat{t}_1^- + t_{tp}\hat{t}_2^-\hat{p}_1^- + t_{pt}\hat{p}_2^-\hat{t}_1^- + t_{pp}\hat{p}_2^-\hat{p}_1^-) \times e^{-j\vec{k}_2^-\cdot\vec{r}} e^{j\vec{k}_1^-\cdot\vec{r}'} dk_x dk_y \quad (2.15)$$

with the definitions given as:

$$\begin{aligned} \vec{k}_n^\pm &= \hat{a}_x k_x + \hat{a}_y k_y \pm \hat{a}_z k_{nz} \quad ; \quad k_{nz} = \sqrt{k_n^2 - k_x^2 - k_y^2} \\ \hat{k}_n^\pm &= \frac{1}{k_n} (\hat{a}_x k_x + \hat{a}_y k_y \pm \hat{a}_z k_{nz}) \quad ; \quad k_n = |\vec{k}_n^\pm| \\ \hat{t}_n^\pm &= \frac{\hat{a}_z \times \hat{k}_n^\pm}{|\hat{a}_z \times \hat{k}_n^\pm|} \quad ; \quad \hat{p}_n^\pm = \hat{k}_n^\pm \times \hat{t}_n^\pm \end{aligned} \quad (2.16)$$

In equations (2.14) and (2.15), $r_{\alpha\beta}$ and $t_{\alpha\beta}$, where α and β is t or p , are reflection and transmission coefficients, respectively, whose calculation procedure will be mentioned below.

The boundary conditions which are actually generalized sheet transition conditions

(GSTCs) mentioned in the previous sections are given in the tangential transform domain as:

$$\begin{aligned}\hat{a}_z \times (\vec{H}^{(1)} - \vec{H}^{(2)}) &= \frac{1}{2} \bar{\bar{\sigma}}_e \cdot (\vec{E}_T^{(1)} + \vec{E}_T^{(2)}) \\ -\hat{a}_z \times (\vec{E}^{(1)} - \vec{E}^{(2)}) &= \frac{1}{2} \bar{\bar{\sigma}}_m \cdot (\vec{H}_T^{(1)} + \vec{H}_T^{(2)})\end{aligned}\quad (2.17)$$

Subscript T denotes the tangential components. The dyads $\bar{\bar{\sigma}}_e$ and $\bar{\bar{\sigma}}_m$ are electric and magnetic conductivity tensors. By using the expressions of these tensors together with the boundary conditions and the Green's function expressions, a system of linear equations is obtained whose solution gives the parameters $r_{\alpha\beta}$ and $t_{\alpha\beta}$ where α and β are t or p . These parameters are then put in the expressions (2.14) and (2.15) and spatial domain Green's functions are found by calculating these inverse Fourier integrals numerically.

The electric and magnetic conductivity tensors can be expressed in terms of susceptibilities or surface impedances. For simple objects, closed form expressions may be obtained whereas for more complicated scatterer geometries, surface susceptibilities may be retrieved from reflection and transmission data obtained by measurements or full wave simulations as mentioned in the previous section.

The authors of [52] presented expressions for $r_{\alpha\beta}$ and $t_{\alpha\beta}$ obtained by surface susceptibility approach and also surface impedance approach. However, this formulation is given for the special case of a homogeneous background (i.e., Region 1 and Region 2 is identical) and isotropic structures.

In [52], numerical results for dipole excitation of periodic square PEC patches (Figure 2.3) in free space are presented. They obtained the susceptibilities and surface impedances from analytical closed form expressions in the literature.

They compared their results to the results from ASM which is considered to be exact up to the numerical accuracy. It is reported that their results are in agreement with the full-wave ASM results when periodicity is smaller than 0.1λ and distances of the source and observation points to the surface are larger than the periodicity. However, there seems to be a problem in the way they present their results which raises suspicion about an inaccuracy in their calculations which is explained below.

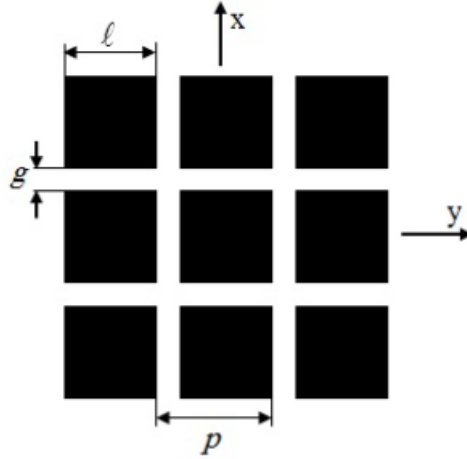


Figure 2.3: One of the sample geometries in [52]

The parameters of the studied geometry are given as $l = 1.8$ mm, $p = 2$ mm (Figure 2.3). The dipole source is placed at $(x', y', z') = (0, 0, 3)$ mm. The frequency of analysis is specified as 15 GHz. In Fig. 3 of [52] they presented the y component of the field due to a y oriented dipole and z component of the field due to a z oriented dipole with respect to x at two different observation heights (z) together with the results obtained by ASM (see Figure 2.4). The fields they presented are the total fields instead of the scattered ones alone. This is not a good choice to demonstrate the accuracy of the homogenization approach since the total field with these parameters is heavily dominated by the incident field which is independent of the homogenized periodic structure. This can easily be verified by simulating the structure in a commercial EM full-wave simulation software like HFSS [53] or running a simple code for incident field in MATLAB [54] which is the simulation environment used for all coding work in this thesis. The incident and total field plots obtained by HFSS are presented in Figures 2.5 and 2.6. One can easily observe the dominance of the total fields by the incident fields.

The same geometry is studied in this thesis work and the scattered fields are chosen for analysis and comparison. As can be seen in Chapter 5, results of our proposed method is highly accurate.

A very interesting point about the results presented in [52] manifests itself when the ratio of the reflected field to the total field is plotted by using the results of our method.

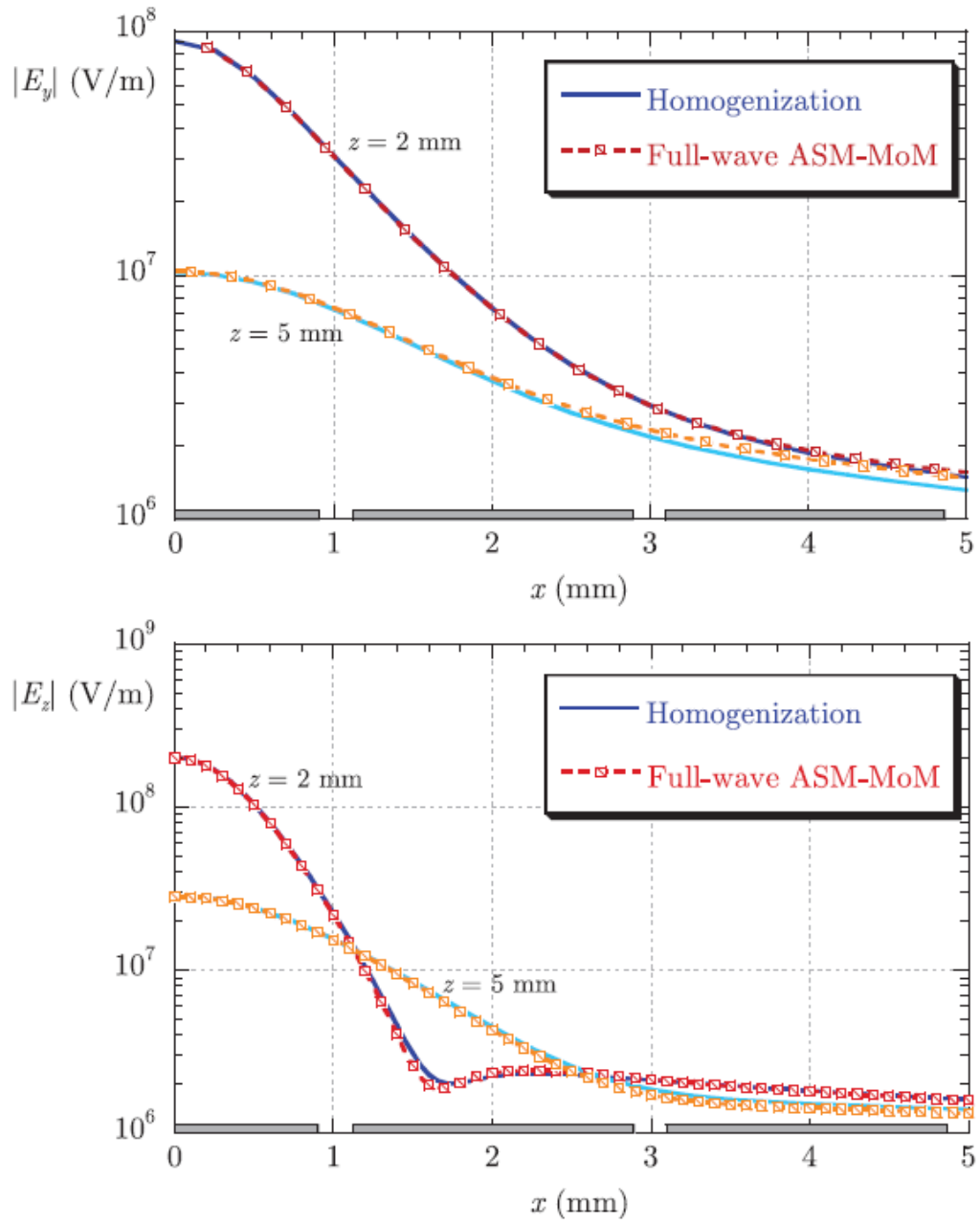


Figure 2.4: Fig. 3 of [52]

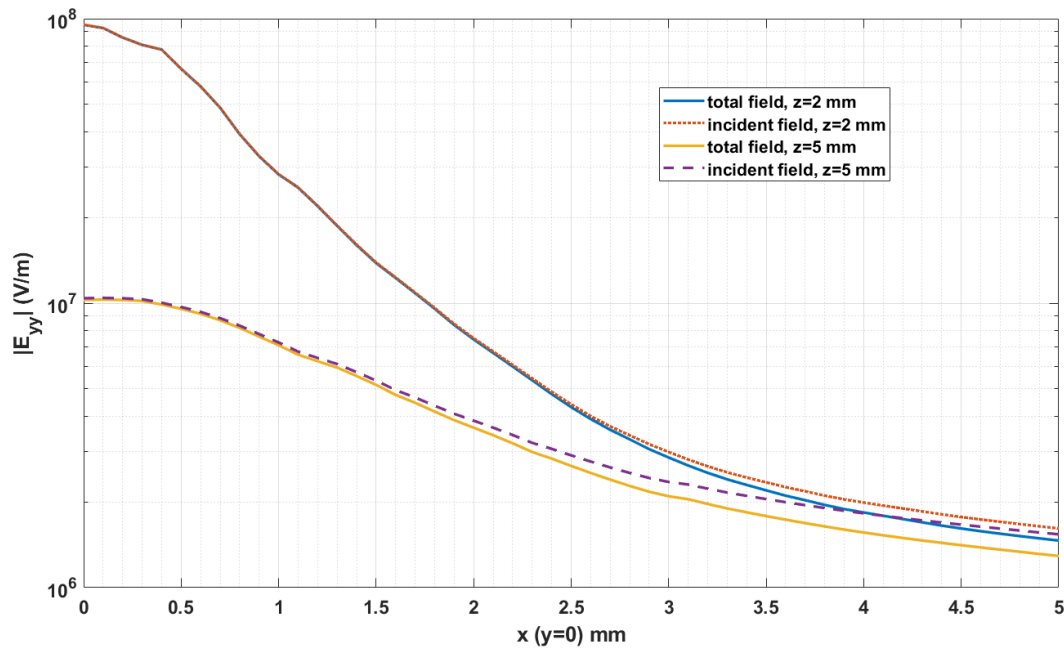


Figure 2.5: Magnitude of y component of the total and incident electric field due to the dipole oriented in y direction

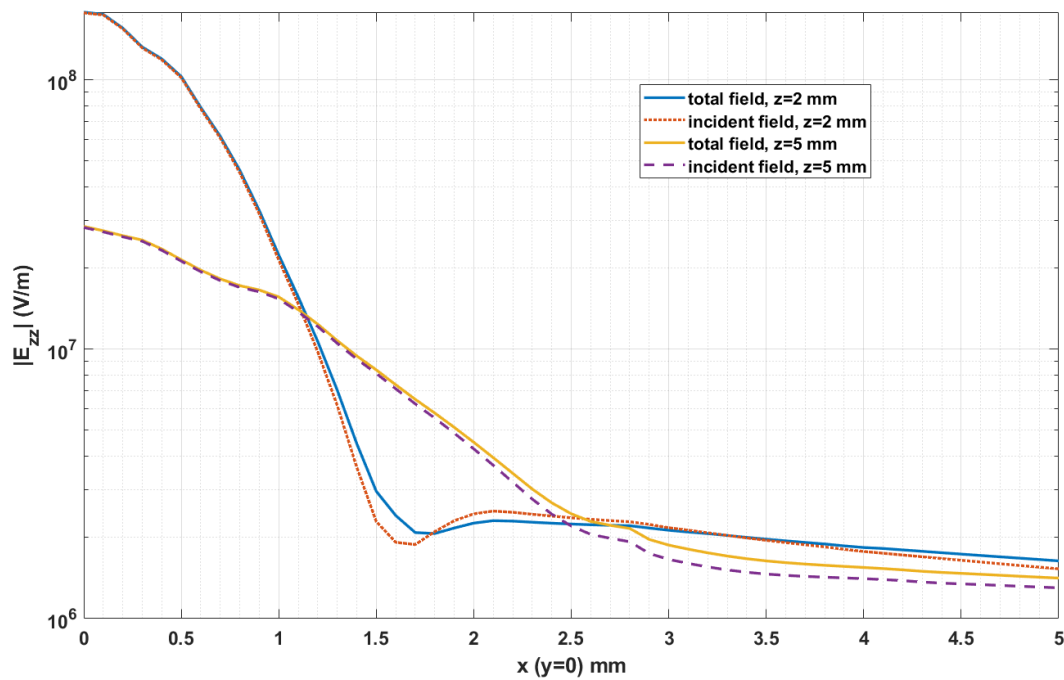


Figure 2.6: Magnitude of z component of the total and incident electric field due to the dipole oriented in z direction

The ratio of the y component of the reflected field to the total field in y direction due to the y oriented dipole for $z = 5$ mm is plotted in Figure 2.7 together with the ratio of the z component of the reflected field to the total field in z direction due to the z oriented dipole for $z = 2$ mm. By investigating these plots and Fig. 3 of [52], it is seen that there are slight discrepancies in the results of homogenization method with respect to the results of ASM at the observation points where the ratio of reflected field increases. Note that these 'slight' discrepancies are in logarithmic scale which means that the results obtained by homogenization of [52] has an accuracy problem which is not negligible but is hindered by the chosen form of presentation.

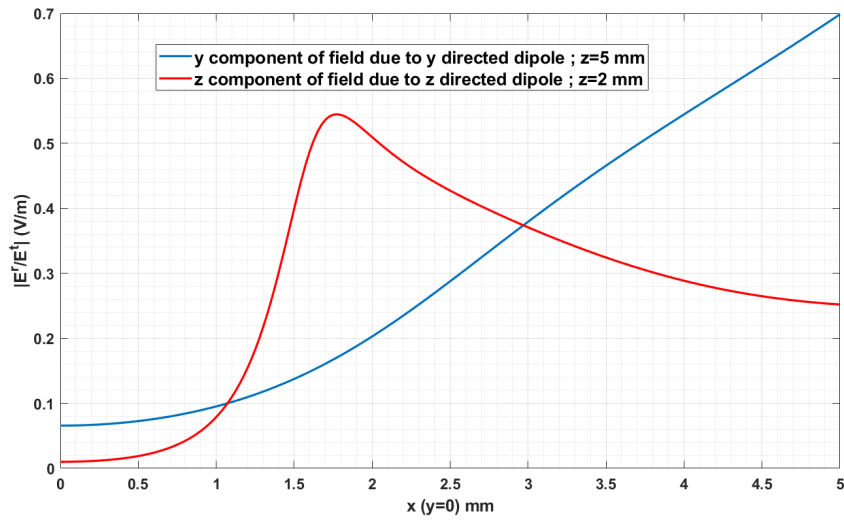


Figure 2.7: Ratio of reflected to total field for $|E_{yy}|$ and $|E_{zz}|$

In [55], authors studied on the potential Green's functions instead of Green's functions for electric field. They have presented the results for the same field components, due to the same geometry and parameters as of [52]. The results are identical to the ones of [52], thus the aforementioned comments apply also to [55]. The approach is extended for metafilms at the interface of two half spaces in [56]. They again studied the same scatterer geometry, which is placed on the dielectric half space while the medium above the structure is free space. They presented the results for two different dielectric constants. Even though the relative permittivities are very different (5 and 16) they have obtained nearly the same field plots and reported these as accurate results. The problem in these results are again plotting the total fields while incident fields heavily dominate them. Same authors studied a more general geometry in [57]

where the metasurface is placed on a dielectric slab. Since they modeled the finite thickness slab by an effective half space, the rest of the problem is dealt in a way similar to [56]. As a numerical example they studied two slabs of same permittivity but with different heights (2 mm and 10 mm). Despite the high ratio of the heights of the two slabs, the field plots for the two geometries are almost perfectly the same, again due to the dominance of the incident field.

2.3 Remarks on the Available Approaches in the Literature

Homogenization based approaches offer efficient solutions to the problem of aperiodic excitation of periodic structures. They can be used as effective design tools. However, the accuracy of the scattered fields due to a dipole source near 2-D periodic structures obtained by homogenized Green's function approach is not properly verified as explained in the previous section. Moreover in [32], in which the reflection and transmission properties of a metasurface homogenized by surface susceptibilities are studied, the authors state the following:

"The fields appearing in the GSTCs are "macroscopic" fields, in the sense that they do not exhibit variations on a length scale comparable to scatterer dimensions or spacing, but only on larger scales such as the wavelength in the surrounding medium."

This statement means that the scattered fields obtained by homogenized Green's function approaches based on GSTCs will fail to accurately represent the actual field variations, which limits its usage to the applications where approximate field values on the scales of a wavelength are sufficient. On the other end, the fields obtained by using full wave approaches such as PWM or ASM will be highly accurate but at the expense of exhaustive computation power and time.

The aim of this thesis work is to calculate the scattered fields due to the electric dipole source near planar periodic structures in a more efficient way than the available full wave methods in the literature while keeping the accuracy at high levels even for the field variations at small scales as opposed to the currently available homogenization based approaches.

CHAPTER 3

MOM ANALYSIS OF PERIODIC PLANAR STRUCTURES - REFLECTION COEFFICIENTS

3.1 Introduction

Method of moments (MoM) is the numerical technique that is employed in this thesis work for the analysis of periodic planar structures. Definitions, concepts and notations used in this work are introduced in this section whereas a more detailed formulation and numerical results obtained for free space and multilayered cases are presented in the next sections of this chapter.

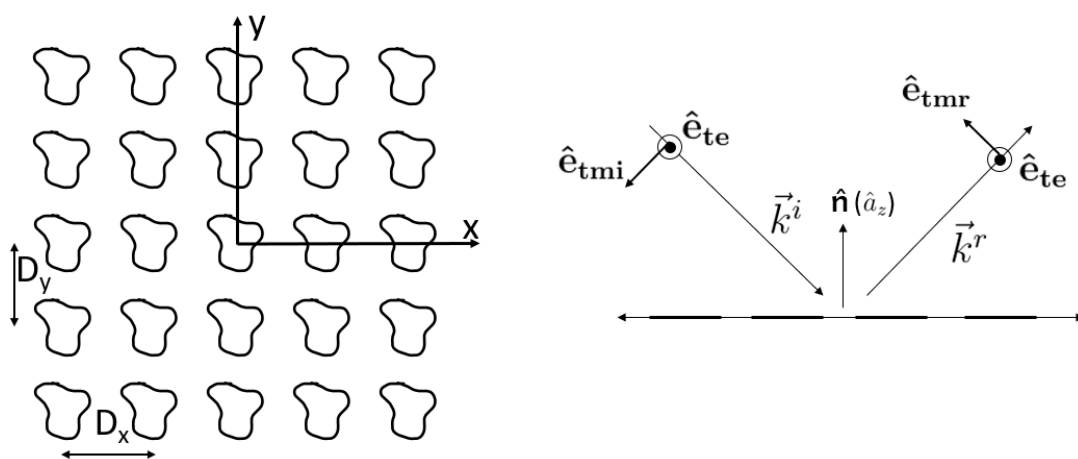


Figure 3.1: A sample geometry for the general periodic structure and TE-TM decomposition of incident and reflected electromagnetic fields

Electric fields scattered by infinitely periodic structures, lying on a plane transverse to z as shown in Fig. 3.1 and excited by a plane wave, can be expressed in the form

of an infinite spectral summation as [58], [59]:

$$\vec{E}^s(\vec{r}, \vec{r}') = \sum_{p=-\infty}^{+\infty} \sum_{q=-\infty}^{+\infty} \vec{E}_{pq}(k_{xp}, k_{yq}, \vec{r}') e^{-j(k_{xp}x + k_{yq}y + k_{zpq}z)} \quad (3.1)$$

where transverse and longitudinal wavenumbers are defined below as:

$$k_{xp} = k_x + \frac{2\pi p}{D_x}, \quad k_{yq} = k_y + \frac{2\pi q}{D_y} \quad (3.2)$$

$$k_{zpq} = \begin{cases} \sqrt{k_s^2 - (k_{xp}^2 + k_{yq}^2)} & k_s^2 \geq k_{xp}^2 + k_{yq}^2 \\ -j\sqrt{(k_{xp}^2 + k_{yq}^2) - k_s^2} & k_s^2 \leq k_{xp}^2 + k_{yq}^2 \end{cases} \quad (3.3)$$

k_s is the wavenumber in the medium whereas k_x and k_y are the incident transverse wavenumbers. D_x and D_y are the periodicities (spacing between elements) in x and y directions, respectively.

Equation (3.1) is a general expression covering both free space and multilayered media even though Fig. 3.1 does not reflect this detail for the sake of simplicity.

The exponential term inside the summation in (3.1) is known as a Floquet mode or a Floquet modal function [58]. Electromagnetic fields can be decomposed into Transverse Electric (TE) and Transverse Magnetic (TM) parts with respect to the plane of incidence based on a definition of unit electric field vectors for these two orthogonal modes as seen in Fig. 3.1.

\hat{e}_{tmi} is the unit electric field vector for incident (down-going) TM plane waves and \hat{e}_{tmr} is the unit electric field vector for reflected (up-going) TM plane waves. Unit electric field vector for TE waves, \hat{e}_{te} , is the same for both down-going and up-going waves. Their definitions are based on the following fundamental facts:

- Plane of incidence is the plane containing both the normal vector of the surface (\hat{n} , which is \hat{a}_z in our case) and propagation vector ($\vec{k}^i = \hat{a}_x k_{xp} + \hat{a}_y k_{yq} - \hat{a}_z k_{zpq}$ for incident, $\vec{k}^r = \hat{a}_x k_{xp} + \hat{a}_y k_{yq} + \hat{a}_z k_{zpq}$ for reflected wave).
- \hat{e}_{te} is orthogonal to the plane of incidence.

- \hat{e}_{tm} is orthogonal to \hat{e}_{te} and the propagation vector.

From the first two items, we can define \hat{e}_{te} as:

$$\hat{e}_{te}(\vec{k}_{ppq}) = \frac{\vec{k}^i \times \hat{a}_z}{|\vec{k}^i \times \hat{a}_z|} = \frac{\vec{k}^r \times \hat{a}_z}{|\vec{k}^r \times \hat{a}_z|} = \hat{a}_x \frac{k_{yq}}{k_{ppq}} + \hat{a}_y \frac{-k_{xp}}{k_{ppq}} \quad (3.4)$$

Definitions of \hat{e}_{tmi} and \hat{e}_{tmr} follow from third and first items as:

$$\hat{e}_{tmi}(\vec{k}_{ppq}) = \frac{\vec{k}^i \times \hat{e}_{te}}{|\vec{k}^i \times \hat{e}_{te}|} = \hat{a}_x \frac{-k_{xp}k_{zppq}}{k_{ppq}k_s} + \hat{a}_y \frac{-k_{yq}k_{zppq}}{k_{ppq}k_s} + \hat{a}_z \frac{-k_{ppq}}{k_s} \quad (3.5)$$

$$\hat{e}_{tmr}(\vec{k}_{ppq}) = \frac{\vec{k}^r \times \hat{e}_{te}}{|\vec{k}^r \times \hat{e}_{te}|} = \hat{a}_x \frac{-k_{xp}k_{zppq}}{k_{ppq}k_s} + \hat{a}_y \frac{-k_{yq}k_{zppq}}{k_{ppq}k_s} + \hat{a}_z \frac{k_{ppq}}{k_s} \quad (3.6)$$

where k_{ppq} is the magnitude of \vec{k}_{ppq} which is given as:

$$\vec{k}_{ppq} = \hat{a}_x k_{xp} + \hat{a}_y k_{yq} \quad (3.7)$$

Note that for an incident plane wave $p = q = 0$. The decomposition of the field into TE and TM parts are expressed mathematically as:

$$\vec{E}_{pq} = E_{te,pq} \hat{e}_{te} + E_{tmr,pq} \hat{e}_{tmr} \quad (3.8)$$

Reflection coefficient analysis of periodic structures is associated with calculating these complex $E_{te,pq}$ and $E_{tmr,pq}$ parameters when the structure is excited with a unit amplitude TE or TM plane wave, namely $\hat{e}_{te}(\vec{k}_{p00})$ or $\hat{e}_{tmi}(\vec{k}_{p00})$. This analysis is generally performed by using the concept of S-Parameter which is the ratio of the outgoing power wave from a port to the incoming power wave to the same or any other port. Each TE and TM mode is considered as a port in the context of this analysis and S_{ij} refers to the S-Parameter where j is the mode of the incident wave and i is the mode of the reflected wave. The indexing of the ports/modes are shown in Table 3.1. First two modes are always reserved for the TE and TM polarized fundamental Floquet modes. After that, propagating higher order Floquet modes are considered and they

are sorted in descending order with respect to their propagation constant. After all of the propagating higher order modes are listed, evanescent modes are considered and they are sorted in ascending order with respect to their attenuation constant. One high order Floquet mode is taken into account in the numerical examples considered in this chapter which is evanescent for some incidence angles while being a propagating wave for some other angles.

Table 3.1: Mode/port definitions and indices

Index	Definition
1	TE polarized fundamental ($p = q = 0$) Floquet mode
2	TM polarized fundamental ($p = q = 0$) Floquet mode
3	TE polarized higher order Floquet mode
4	TM polarized higher order Floquet mode

S-Parameters are associated with the ratio of the power waves flowing in z direction. Total power carried by each plane wave mode is simply equal to $|E|^2/2\eta$, where E is the electric field amplitude corresponding to the mode and η is the wave impedance of the medium. The portion of this power that is flowing in z direction can be found by multiplying by k_{zpq}/k_s . From the definition of power waves and generalized S-Parameters [60], taking the square of the magnitude of the power wave and dividing by two should give us the power flowing in z direction. Thus, the power wave associated for any mode is found by $|E|\sqrt{k_{zpq}/(\eta k_s)}$. This means that the power wave of a mode can be found from the electric field of the corresponding mode by multiplying the field by a factor, F_{pq} , which is given as:

$$F_{pq} = \sqrt{\frac{k_{zpq}}{\eta k_s}} \quad (3.9)$$

3.2 Formulation for MoM Analysis

The MoM analysis in this work is based on Mixed Potential Integral Equation (MPIE). Scattered electric field can be expressed in terms of potentials as follows:

$$\vec{E}^s = -j\omega\vec{A} - \vec{\nabla}\Phi \quad (3.10)$$

Enforcing the boundary condition that the tangential electric field on the surface is zero yields:

$$-\vec{E}_{tan}^i = (-j\omega\vec{A} - \vec{\nabla}\Phi)_{tan} \quad \vec{r} \text{ on } S \quad (3.11)$$

where \vec{E}^i is the incident wave and S is the surface of the scatterer. Potentials in (3.11) are created by surface currents, which are represented by finite sum of basis functions with associated coefficients as follows:

$$\vec{J}_s(\vec{r}) \approx \sum_{n=1}^N I_n \vec{f}_n(\vec{r}) \quad (3.12)$$

RWG basis function introduced in [61] is utilized in this work for its flexibility in handling arbitrary geometries. This basis function is expressed mathematically as:

$$\vec{f}_n(\vec{r}) = \begin{cases} \frac{l_n}{2A_n^{\Delta+}} \vec{\rho}_n^+(\vec{r}), & \vec{r} \text{ in } T_n^+ \\ \frac{l_n}{2A_n^{\Delta-}} \vec{\rho}_n^-(\vec{r}), & \vec{r} \text{ in } T_n^- \\ 0, & \text{otherwise} \end{cases} \quad (3.13)$$

with l_n being the length of the n^{th} edge. $A_n^{\Delta+}$ and $A_n^{\Delta-}$ are the areas of the positive (T_n^+) and negative triangles (T_n^-) associated with the edge respectively. \vec{r} is the position vector where the basis function is to be evaluated and the $\vec{\rho}_n^{\pm}(\vec{r})$ vectors are defined from \vec{r} to the nodes at the opposite of edge n as shown in Fig. 3.2.

A necessary part of the MoM analysis is the testing procedure. An inner product

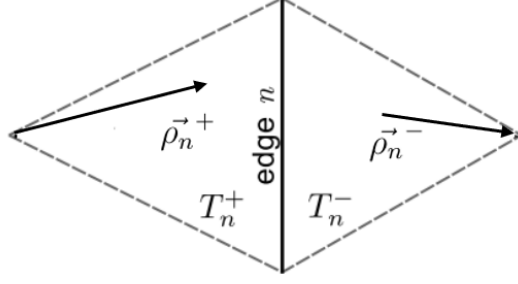


Figure 3.2: Geometry of RWG basis functions

definition is needed which is given as:

$$\langle \vec{g}, \vec{h} \rangle \equiv \int_S \vec{g} \cdot \vec{h} dS \quad (3.14)$$

Galerkin method is utilized in this work where the testing function is the same as the basis function. Testing (3.11) with \vec{f}_m yields the following equation:

$$\langle \vec{E}^i, \vec{f}_m \rangle = j\omega \langle \vec{A}, \vec{f}_m \rangle + \langle \vec{\nabla} \Phi, \vec{f}_m \rangle \quad (3.15)$$

By using vector calculus and properties of the basis function, [61], the inner product involving Φ takes the form below:

$$\langle \vec{\nabla} \Phi, \vec{f}_m \rangle = - \int_S \Phi \vec{\nabla}_S \cdot \vec{f}_m dS \quad (3.16)$$

$$\int_S \Phi \vec{\nabla}_S \cdot \vec{f}_m dS = l_m \left(\frac{1}{A_m^{\Delta+}} \int_{T_n^+} \Phi dS - \frac{1}{A_m^{\Delta-}} \int_{T_n^-} \Phi dS \right) \quad (3.17)$$

where $\vec{\nabla}_S \cdot$ denotes the surface divergence operator. Other inner products involving \vec{A} and \vec{E}^i are expressed as integrals shown below:

$$\langle \vec{A}, \vec{f}_m \rangle = l_m \left(\frac{1}{2A_m^{\Delta+}} \int_{T_n^+} \vec{A} \cdot \rho_m^+ dS + \frac{1}{2A_m^{\Delta-}} \int_{T_n^-} \vec{A} \cdot \rho_m^- dS \right) \quad (3.18)$$

$$\langle \vec{E}^i, \vec{f}_m \rangle = V_m = l_m \left(\frac{1}{2A_m^{\Delta+}} \int_{T_m^+} \vec{E}^i \cdot \rho_m^+ dS + \frac{1}{2A_m^{\Delta-}} \int_{T_m^-} \vec{E}^i \cdot \rho_m^- dS \right) \quad (3.19)$$

$$\begin{aligned} V_m = j\omega l_m \left(\frac{1}{2A_m^{\Delta+}} \int_{T_m^+} \vec{A} \cdot \rho_m^+ dS + \frac{1}{2A_m^{\Delta-}} \int_{T_m^-} \vec{A} \cdot \rho_m^- dS \right) \\ + l_m \left(-\frac{1}{A_m^{\Delta+}} \int_{T_m^+} \Phi dS + \frac{1}{A_m^{\Delta-}} \int_{T_m^-} \Phi dS \right) \end{aligned} \quad (3.20)$$

The potentials \vec{A} and Φ appearing in the testing (weighting) integrals above are results of the convolution of the surface currents with the corresponding Green's functions. They are expressed mathematically as:

$$\vec{A}(\vec{r}) = \mu \int_{S'} \vec{G}^A(\vec{r}, \vec{r}') \cdot \vec{J}_s(\vec{r}') d\vec{r}' \quad (3.21)$$

$$\vec{A}(\vec{r}) = \mu \sum_{n=1}^N I_n \left(\int_{T_n^+} \vec{G}^A(\vec{r}, \vec{r}') \cdot \vec{f}_n(\vec{r}') d\vec{r}' + \int_{T_n^-} \vec{G}^A(\vec{r}, \vec{r}') \cdot \vec{f}_n(\vec{r}') d\vec{r}' \right) \quad (3.22)$$

$$\vec{A}(\vec{r}) = \mu \sum_{n=1}^N I_n \frac{l_n}{2} \left(\frac{1}{A_n^{\Delta+}} \int_{T_n^+} \vec{G}^A(\vec{r}, \vec{r}') \cdot \rho_n^+ d\vec{r}' + \frac{1}{A_n^{\Delta-}} \int_{T_n^-} \vec{G}^A(\vec{r}, \vec{r}') \cdot \rho_n^- d\vec{r}' \right) \quad (3.23)$$

$$\Phi(\vec{r}) = -\frac{1}{j\omega\epsilon} \int_{S'} G^\Phi(\vec{r}, \vec{r}') \vec{\nabla}_S \cdot \vec{J}_s(\vec{r}') d\vec{r}' \quad (3.24)$$

$$\vec{\nabla}_S \cdot \vec{J}_s(\vec{r}') = \begin{cases} \sum_{n=1}^N I_n \frac{l_n}{A_n^{\Delta+}}, & \vec{r}' \text{ in } T_n^+ \\ -\sum_{n=1}^N I_n \frac{l_n}{A_n^{\Delta-}}, & \vec{r}' \text{ in } T_n^- \end{cases} \quad (3.25)$$

$$\Phi(\vec{r}) = -\frac{1}{j\omega\epsilon} \sum_{n=1}^N I_n l_n \left(\frac{1}{A_n^{\Delta+}} \int_{T_n^+} G^\Phi(\vec{r}, \vec{r}') d\vec{r}' - \frac{1}{A_n^{\Delta-}} \int_{T_n^-} G^\Phi(\vec{r}, \vec{r}') d\vec{r}' \right) \quad (3.26)$$

Using these integrals in (3.15), MoM equation can be expressed in terms of entries of excitation or voltage vector (V_m), current vector (I_n) and impedance matrix (Z_{mn}) as follows:

$$V_m = \sum_{n=1}^N I_n Z_{mn} \quad (3.27)$$

An impedance matrix entry can be decomposed into four components as:

$$Z_{mn} = Z_{mn}^{A+} + Z_{mn}^{A-} + Z_{mn}^{\Phi+} + Z_{mn}^{\Phi-} \quad (3.28)$$

These components are found by taking the following integrals:

$$Z_{mn}^{A+} = j\omega\mu \frac{l_m l_n}{4A_m^{\Delta+}} \int_{T_m^+} \left(\frac{1}{A_n^{\Delta+}} \int_{T_n^+} \bar{G}^A(\vec{r}, \vec{r}') \cdot \vec{\rho}_n^+ d\vec{r}' + \frac{1}{A_n^{\Delta-}} \int_{T_n^-} \bar{G}^A(\vec{r}, \vec{r}') \cdot \vec{\rho}_n^- d\vec{r}' \right) \cdot \vec{\rho}_m^+ d\vec{r} \quad (3.29)$$

$$Z_{mn}^{A-} = j\omega\mu \frac{l_m l_n}{4A_m^{\Delta-}} \int_{T_m^-} \left(\frac{1}{A_n^{\Delta+}} \int_{T_n^+} \bar{G}^A(\vec{r}, \vec{r}') \cdot \vec{\rho}_n^+ d\vec{r}' + \frac{1}{A_n^{\Delta-}} \int_{T_n^-} \bar{G}^A(\vec{r}, \vec{r}') \cdot \vec{\rho}_n^- d\vec{r}' \right) \cdot \vec{\rho}_m^- d\vec{r} \quad (3.30)$$

$$Z_{mn}^{\Phi+} = \frac{1}{j\omega\epsilon} \frac{l_m l_n}{A_m^{\Delta+}} \int_{T_m^+} \left(\frac{1}{A_n^{\Delta+}} \int_{T_n^+} G^{\Phi}(\vec{r}, \vec{r}') d\vec{r}' - \frac{1}{A_n^{\Delta-}} \int_{T_n^-} G^{\Phi}(\vec{r}, \vec{r}') d\vec{r}' \right) d\vec{r} \quad (3.31)$$

$$Z_{mn}^{\Phi-} = -\frac{1}{j\omega\epsilon} \frac{l_m l_n}{A_m^{\Delta-}} \int_{T_m^-} \left(\frac{1}{A_n^{\Delta+}} \int_{T_n^+} G^{\Phi}(\vec{r}, \vec{r}') d\vec{r}' - \frac{1}{A_n^{\Delta-}} \int_{T_n^-} G^{\Phi}(\vec{r}, \vec{r}') d\vec{r}' \right) d\vec{r} \quad (3.32)$$

This section would be incomplete without mentioning the techniques used for calculating the integrals (3.29) to (3.32) which yield the impedance matrix components. Symmetric Gaussian product [62] is utilized for both source integrals and testing integrals which is able to calculate the integral over a triangular region in terms of a finite 1-D summation. The number of terms in the summation depends on the order chosen for the quadrature. The resolution of the quadrature points can be adjusted as needed while avoiding the overlaps of source and test points by carefully choosing the orders.

3.3 Periodic Surfaces in Free Space

Application of the MoM analysis formulated in previous sections starts with a simpler case in which the periodic planar structure is in free space. Free space periodic Green's function is used in equations (3.29) through (3.32). In free space, $\bar{G}^A(\vec{r}, \vec{r}')$ becomes a scalar and takes the same value as $G^{\Phi}(\vec{r}, \vec{r}')$ which is given below:

$$G_{fs,per}^{\Phi,A}(\vec{r}, \vec{r}') = \frac{1}{D_x D_y} \sum_{p=-\infty}^{+\infty} \sum_{q=-\infty}^{+\infty} \frac{e^{-jk_{zpq}(z-z')}}{j2k_{zpq}} e^{-jk_{xp}(x-x')} e^{-jk_{yq}(y-y')} \quad (3.33)$$

This double infinite summation is not suitable for directly using in the computation of impedance matrix elements due to its slowly converging nature. Ewald's transformation [63], [64] is utilized in this work to accelerate the infinite summations arising from periodic Green's functions (PGF). This transformation converts the spectral summation in (3.33) into the superposition of a spatial and a spectral series given below:

$$G_{fs,spec}^{\Phi,A}(\vec{r}, \vec{r}') = \frac{1}{4D_x D_y} \sum_{p=-\infty}^{\infty} \sum_{q=-\infty}^{\infty} \frac{e^{-j[k_{xp}(x-x') + k_{yq}(y-y')]}{jk_{zpq}} \times \sum_{\pm} e^{\pm jk_{zpq}(z-z')} \operatorname{erfc}\left(\frac{jk_{zpq}}{2E} \pm (z-z')E\right) \quad (3.34)$$

$$G_{fs,spat}^{\Phi,A}(\vec{r}, \vec{r}') = \frac{1}{8\pi} \sum_{p=-\infty}^{\infty} \sum_{q=-\infty}^{\infty} \frac{e^{-j(k_x p D_x + k_y q D_y)}}{R_0} \times \sum_{\pm} e^{\pm j k_s R_0} \operatorname{erfc}\left(R_0 E \pm \frac{j k_0}{2E}\right) \quad (3.35)$$

where erfc is the complementary error function [65]. Expression for R_0 is shown in (3.36). E is the Ewald splitting parameter which affects the convergence rates of the spectral and spatial domain series and also the accuracy of the result to which the Ewald method converges. For PGF of free space, the optimum E value proposed in [64] is used which is given in (3.37).

$$R_0 = \sqrt{(x - x' - p D_x)^2 + (y - y' - q D_y)^2 + (z - z')^2} \quad (3.36)$$

$$E_{opt} = \sqrt{\frac{\pi}{D_x D_y}} \quad (3.37)$$

Formulation for calculating the S-Parameters of a periodic structure in free space is now complete and it is time to test this in a sample problem. The geometry of the numerical example in [59] is used and the results are compared to the ones obtained from a commercial 3-D EM simulation software, CST [66]. The structure is 2-D periodic with a rectangular lattice and each unit cell consists of a rectangular PEC sheet as a scatterer. The parameters are given in Table 3.2

Table 3.2: Parameters of the reflection coefficient analysis problem for free space case

Parameter	Description	Value
f	frequency	13 GHz
D_x	periodicity in x direction	0.76 cm
D_y	periodicity in y direction	1.52 cm
w	width of the PEC scatterer	0.127 cm
l	length of the PEC scatterer	1.35 cm

Magnitude of S_{11} (recall Table 3.1 for S-Parameters definitions) is plotted for various ϕ values together with the results obtained by CST in Figure 3.3. A very good agreement can be observed in this plot.

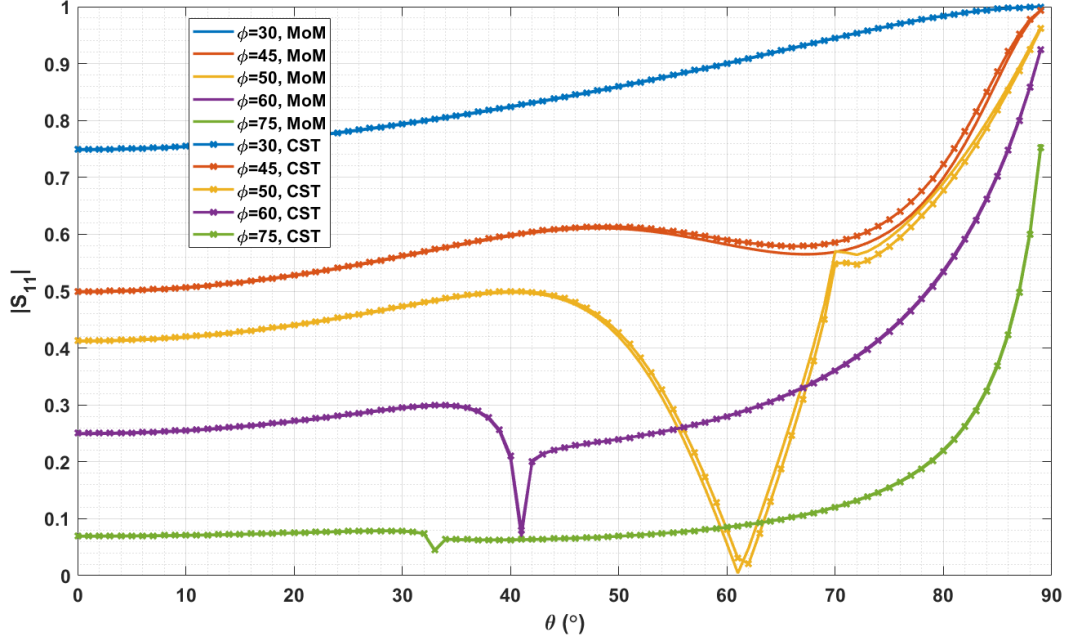


Figure 3.3: Magnitude of S_{11} versus θ for various ϕ values

In order to verify the accuracy further instead of only magnitude, real and imaginary parts of S_{41} and S_{32} are presented separately in Figures 3.4 to 3.7.

In order to evaluate the accuracy of different S-Parameters in one plot, magnitude of S_{12} , S_{22} , S_{32} and S_{42} are presented in Figure 3.8. ϕ is chosen as 50° for this plot.

This section will end after briefly mentioning the computing times needed. CST needed 26 seconds to solve for each incidence angle while MoM formulation used in this work needed 2.2 seconds for the first incidence angle and 1.4 seconds for each of the other angles.

3.4 Periodic Surfaces Printed on Multilayered Media

In this section, the formulation and numerical results for reflection analysis of planar periodic structures printed on multilayered media are presented. This is a more

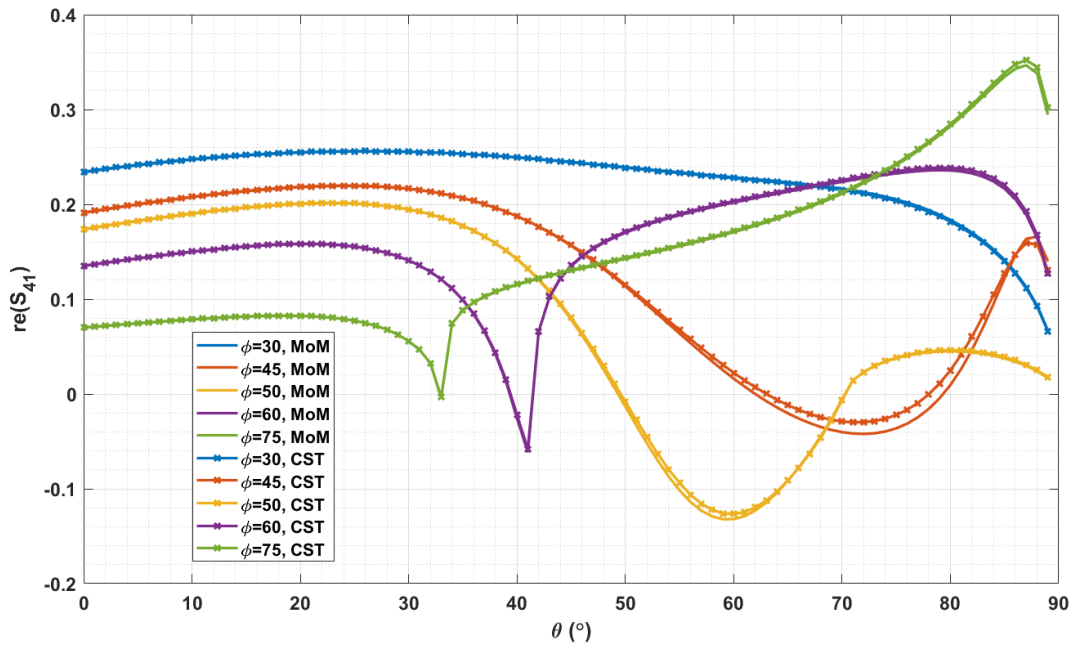


Figure 3.4: Real part of S_{41} versus θ for various ϕ values

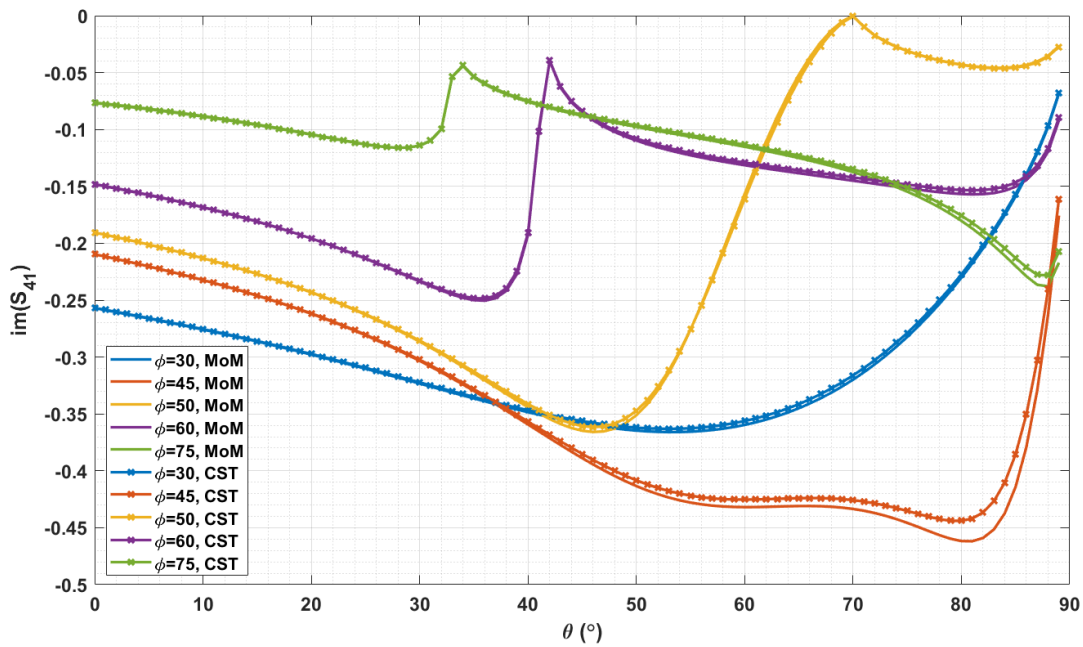


Figure 3.5: Imaginary part of S_{41} versus θ for various ϕ values

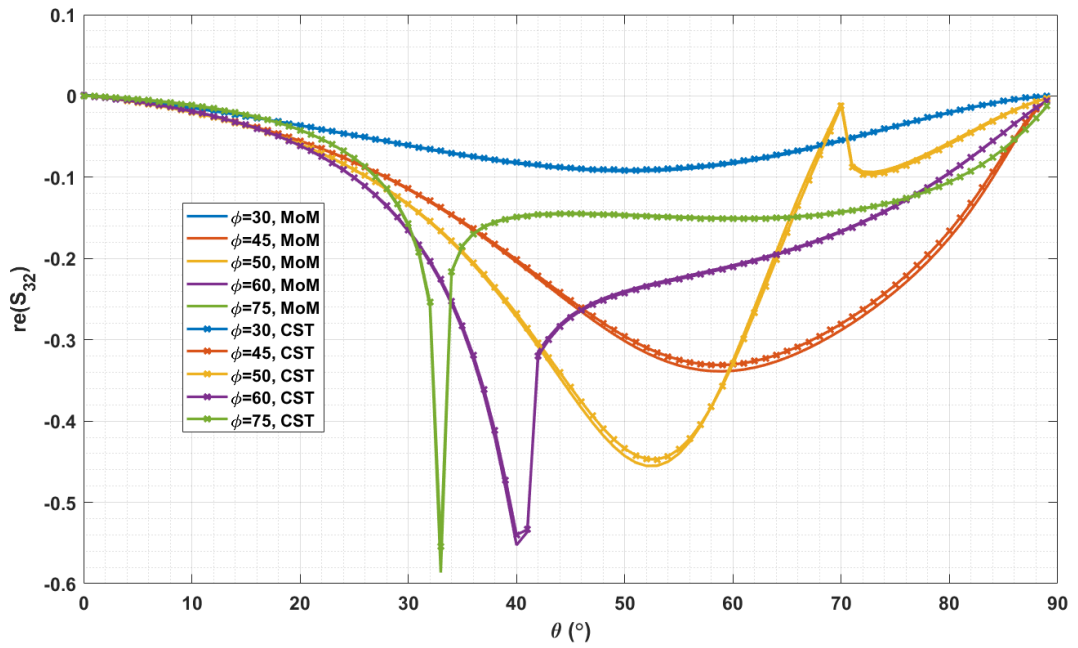


Figure 3.6: Real part of S_{32} versus θ for various ϕ values

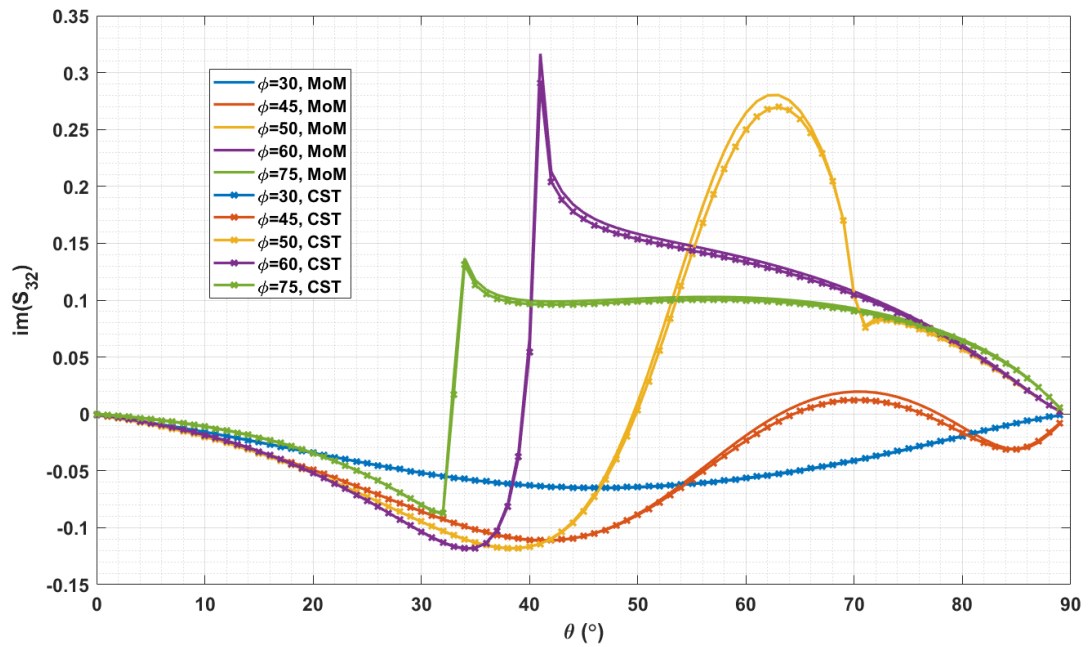


Figure 3.7: Imaginary part of S_{32} versus θ for various ϕ values

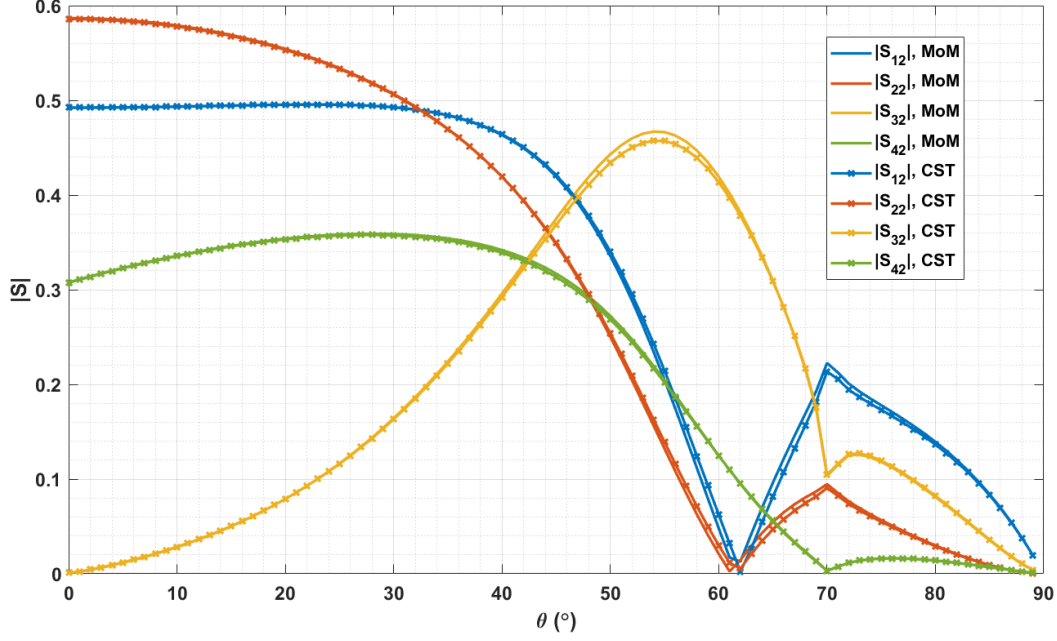


Figure 3.8: Magnitude of S_{12} , S_{22} , S_{32} , S_{42} versus θ for $\phi = 50$

realistic and complex problem compared to the free space case.

For a planar multilayered structure with stratification in z direction, the dyadic Green's function for vector potential \vec{A} takes the form in (3.38) where $G_{xx}^A = G_{yy}^A$.

$$\bar{\bar{G}}^A = \begin{bmatrix} G_{xx}^A & 0 & 0 \\ 0 & G_{yy}^A & 0 \\ G_{zx}^A & G_{zy}^A & G_{zz}^A \end{bmatrix} \quad (3.38)$$

This representation of vector potential is not unique, but the form given in (3.38), which is called the traditional form, is the one commonly preferred for analyzing printed structures in multilayered media [40].

Since the periodic structure printed on the layered medium is 2-D, there will be no surface currents in z direction. Therefore, G_{zz}^A has no importance and can be ignored for the purpose of this analysis. For the same reason, \vec{f}_m has no longitudinal part and z component of \vec{A} is canceled in the process of testing as can be seen in (3.15). As a result, G_{zx}^A and G_{zy}^A have no use in the computation of the impedance matrix entries.

They must, however, be taken into account while calculating the scattered fields from the surface currents which takes place after the computation of the impedance matrix. This last part of the analysis is straightforward and constitutes a very small part of the total computation time. Thus, there is no need for an approximation scheme or an acceleration technique for these components. No further detail will be given about these components in this section since the focus will be on the computation of the impedance matrix. Two of the five entries in $\bar{\bar{G}}^A$ dyadic are involved in forming of the impedance matrix and since these two components are equal, we have $G^A = G_{xx}^A = G_{yy}^A$.

Periodic Green's function, for any component, can be expressed in terms of its spectral components as follows:

$$G_{per}^{\Phi,A}(\vec{r}, \vec{r}') = \frac{1}{D_x D_y} \sum_{p=-\infty}^{+\infty} \sum_{q=-\infty}^{+\infty} \tilde{G}_{pq}^{\Phi,A}(k_{xp}, k_{yq}) e^{-jk_{xp}(x-x')} e^{-jk_{yq}(y-y')} \quad (3.39)$$

The spectral domain Green's functions for a planar multilayered media have the general form for \vec{A} and ϕ as follows:

$$\tilde{G}_{pq}^{\Phi,A}(k_{xp}, k_{yq}) = \frac{1}{j2k_{zpq}} [e^{-jk_{zpq}(z-z')} + R^{\Phi,A} e^{-jk_{zpq}(z+z')}] \quad (3.40)$$

The first term in these expressions is for the direct wave whereas the second term is for the wave reflected from the layered media (source is assumed to be above the stratified media which is the case in this thesis work). R^Φ and R^A are the generalized reflection coefficients for the multilayered media below the source for scalar and vector potentials, respectively. The derivation of these reflection coefficients for a general planar multilayered media can be found in [40].

The spectral domain summation of periodic Green's function is slowly convergent and requires an acceleration technique like Ewald's method as mentioned in Section 3.3. However, the expression (3.40) for the spectral domain Green's functions is not suitable for the utilization of Ewald's transform directly. If the reflection coefficients in these expressions can be expressed as summations of complex images, this transform is possible. Discrete Complex Image Method (DCIM) [67] can be utilized to obtain

complex image representations of the reflection coefficients which are expressed as follows:

$$R^{\Phi,A} \approx \sum_{i=1}^{N_{ci}^{\Phi,A}} \alpha_i^{\Phi,A} e^{-jk_{zpq}\beta_i^{\Phi,A}} \quad (3.41)$$

with N_{ci} being the total number of complex images in the model. β_i represents the complex distance of the image point and α_i specifies the complex amplitude of the corresponding image in DCIM.

The sampling path used for the approximation in [67] is a deformed version of the Sommerfeld integration path on which k_ρ has positive real and imaginary values. For an aperiodic source on the layered media, the spatial domain Green's function is obtained by the inverse Hankel transform (or Sommerfeld integral). A change of path in the complex plane does not alter the integration result as long as it does not cross over any pole or branch point. However, for periodic structures, spatial domain Green's function is obtained by double infinite spectral summations where k_x and k_y , thus k_ρ takes real values. Therefore, the sampling path proposed in [67] has a reduced accuracy for periodic structures. As a solution to this issue, the sampling scheme proposed in [68] is utilized in this work where the sampling path is simply the real k_ρ axis. This method is successfully applied to periodic structures printed on multilayered media in [69] where numerical results demonstrating the high accuracy and efficiency are presented together with the formulation.

Surface wave poles are unavoidable for lossless or low-loss dielectrics while sampling in real k_ρ axis. In order to prevent complex image approximation from failing, contribution from surface wave poles are extracted in spectral domain prior to sampling and they are added later in spatial domain. The spectral domain Green's functions in (3.40) can be decomposed into 3 components which are associated with direct wave, complex images and surface waves. Direct wave contribution is exactly the same as the spectral domain Green's function for the free space case. The formulation for this part will not be pursued further in this section. The complex image contribution is found by putting the expressions of (3.41) in (3.40). Surface wave contribution in

spectral domain is expressed as:

$$\tilde{G}_{sw,pq}^{\Phi,A} = \sum_{i=1}^{N_{sw}^{\Phi,A}} \frac{2k_{\rho\rho i}^{\Phi,A} \text{Res}(k_{\rho\rho i}^{\Phi,A})}{k_{\rho\rho q}^2 - (k_{\rho\rho i}^{\Phi,A})^2} \quad (3.42)$$

where N_{sw} is the total number of surface wave poles of the layered structure, $k_{\rho\rho i}$ are the surface wave poles and $\text{Res}(k_{\rho\rho i})$ are the residues associated with those poles. The superscripts " Φ, A " is used in the surface wave and complex image representations above to imply that there are separate sets of complex images and surface wave poles for the Green's function components of the scalar and vector potentials. For brevity and clearness, they will be omitted in the following expressions, keeping in mind that these expressions are valid for both the scalar and vector potentials as long as the corresponding sets of complex images and surface wave poles are used.

Periodic Green's function components are expressed in the form of spectral summations as:

$$G_{ci,per}(\vec{r}, \vec{r}') = \frac{1}{D_x D_y} \sum_{i=1}^{N_{ci}} \alpha_i \sum_{p=-\infty}^{+\infty} \sum_{q=-\infty}^{+\infty} \frac{e^{-jk_{zpq}(z+z'+\beta_i)} e^{-jk_{xp}(x-x')} e^{-jk_{yq}(y-y')}}{j2k_{zpq}} \quad (3.43)$$

$$G_{sw,per}(\vec{r}, \vec{r}') = \frac{1}{D_x D_y} \sum_{i=1}^{N_{sw}} \sum_{p=-\infty}^{+\infty} \sum_{q=-\infty}^{+\infty} \frac{2k_{\rho\rho i} \text{Res}(k_{\rho\rho i})}{k_{\rho\rho q}^2 - k_{\rho\rho i}^2} e^{-jk_{xp}(x-x')} e^{-jk_{yq}(y-y')} \quad (3.44)$$

Ewald's method is applied for the contribution of complex images as in [70] and [69] and following series are obtained:

$$G_{ci,spec}(\vec{r}, \vec{r}') = \frac{1}{4D_x D_y} \sum_{p=-\infty}^{\infty} \sum_{q=-\infty}^{\infty} \sum_{i=1}^{N_{ci}} \alpha_i \frac{e^{-j[k_{xp}(x-x') + k_{yq}(y-y')]} }{jk_{zpq}} \times \sum_{\pm} e^{\pm jk_{zpq}(z+z'+\beta_i)} \text{erfc} \left(\frac{jk_{zpq}}{2E_{ci}} \pm (z+z'+\beta_i)E_{ci} \right) \quad (3.45)$$

$$G_{ci,spat}(\vec{r}, \vec{r}') = \frac{1}{8\pi} \sum_{p=-\infty}^{\infty} \sum_{q=-\infty}^{\infty} \sum_{i=1}^{N_{ci}} \alpha_i \frac{e^{-j(k_x p D_x + k_y q D_y)}}{R_i} \times \sum_{\pm} e^{\pm j k_s R_i} \operatorname{erfc}\left(R_i E_{ci} \pm \frac{j k_s}{2 E_{ci}}\right) \quad (3.46)$$

where R_i is given as:

$$R_i = \sqrt{(x - x' - p D_x)^2 + (y - y' - q D_y)^2 + (z + z' + \beta_i)^2} \quad (3.47)$$

E_{ci} is the Ewald splitting parameter for complex image contribution similar to the one for the free space case mentioned in the previous section. Optimum value defined in (3.37) causes the Ewald technique to collapse for some geometries when complex images are involved. A modification to optimum splitting parameter is needed when dealing with complex images. This issue is studied in [71] and a phase modification is suggested in the optimum splitting parameter. However, it is seen during this work that the suggested phase modification is not enough for complex images with large magnitudes. Without a rigorous mathematical analysis, only by making some simple deductions from the expressions in Ewald series and by some trials with the code, a correction factor for the optimum Ewald splitting parameter, cf , that works well for all complex images has been obtained as follows:

$$cf(\beta_i) = \left(\frac{D_x^2 + D_y^2}{D_x^2 + D_y^2 + \beta_i^2} \right)^{0.25} \quad (3.48)$$

By making suitable modifications, Ewald method proposed in [72] is applied to surface wave contributions successfully in [69] and the resulting series are given below:

$$G_{sw,spec}(\vec{r}, \vec{r}') = \frac{1}{D_x D_y} \sum_{p=-\infty}^{\infty} \sum_{q=-\infty}^{\infty} \sum_{i=1}^{N_{sw}} \frac{2k_{\rho p i} \operatorname{Res}(k_{\rho p i})}{k_{\rho p q}^2 - k_{\rho p i}^2} \times e^{-\frac{k_{\rho p q}^2 - k_{\rho p i}^2}{4E_{sw}}} e^{-j[k_{x p}(x-x') + k_{y q}(y-y')]} \quad (3.49)$$

$$G_{sw,spat}(\vec{r}, \vec{r}') = \sum_{p=-\infty}^{+\infty} \sum_{q=-\infty}^{+\infty} \sum_{i=1}^{N_{sw}} \frac{k_{\rho p_i} \text{Res}(k_{\rho p_i})}{2\pi} e^{-j(k_x p D_x + k_y q D_y)} \times \sum_{s=0}^{+\infty} \left(\frac{k_{\rho p_i}^2}{4E_{sw}} \right)^s \frac{1}{s!} E_{s+1}^i(\rho^2 E_{sw}) \quad (3.50)$$

with ρ defined as:

$$\rho = \sqrt{(x - x' - p D_x)^2 + (y - y' - q D_y)^2} \quad (3.51)$$

$E_s^i(z)$ is the s^{th} order exponential integral [65]. E_{sw} is the Ewald splitting parameter for surface wave contribution. Its optimum value is found in [72] as:

$$E_{sw} = E_{sw,opt} = \frac{\pi}{D_x D_y} \quad (3.52)$$

In order to verify the formulation presented in this section, a numerical example is studied. The structure of this sample problem is formed by printing the periodic conductors in free space problem on a grounded dielectric substrate. All parameters related to this analysis are given in Table 3.3.

Table 3.3: Parameters of the reflection coefficient analysis problem for multilayered case

Parameter	Description	Value
f	frequency	13 GHz
D_x	periodicity in x direction	0.76 cm
D_y	periodicity in y direction	1.52 cm
w	width of the PEC scatterer	0.127 cm
l	length of the PEC scatterer	1.35 cm
h	height of the substrate	2.3061 mm ($0.1\lambda_s$)
ϵ_r	relative dielectric permittivity of substrate	3.38

Before moving to the results of the formulation presented in this section, one sample plot is presented which shows the S-Parameter curves obtained when the sampling

path in [67] is used for DCIM. Figure 3.9 shows the magnitude of S_{11} obtained this way together with the results of CST. One can see that while the results are accurate for small θ values, the accuracy decreases severely as θ increases. This makes very much sense since the distance between the sampling path in [67] and the actual summation path which is the real k_ρ axis increases as k_ρ , which is equal to $k_s \sin \theta$, approaches k_s .

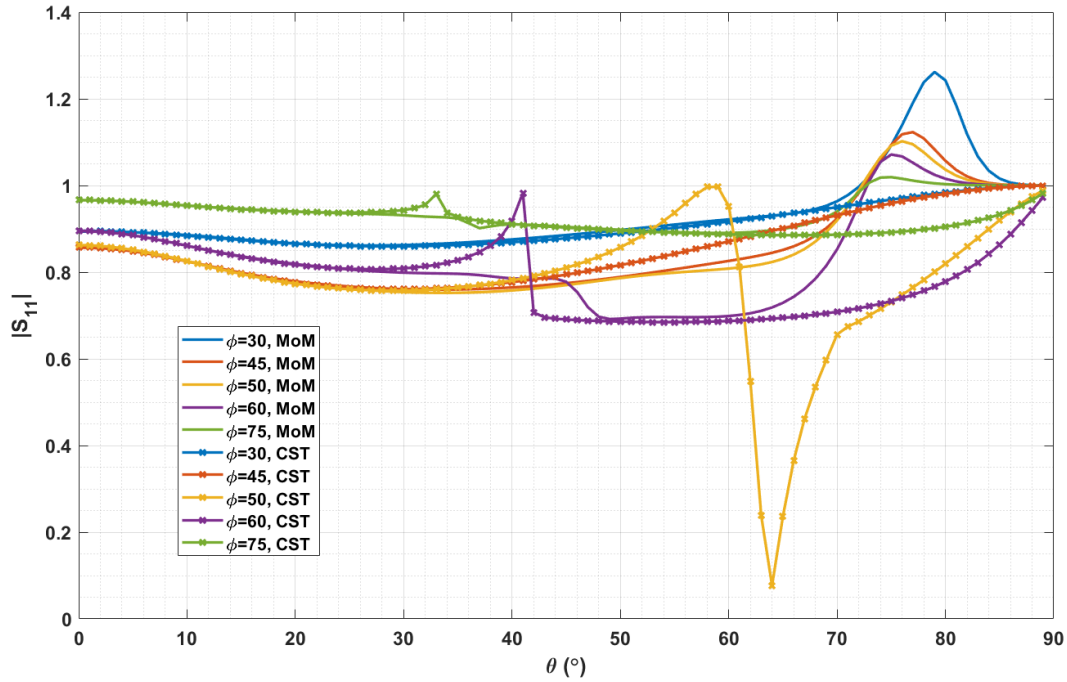


Figure 3.9: Magnitude of S_{11} versus θ for various ϕ values, obtained by using the DCIM technique in [67]

In Figure 3.10, S_{11} obtained by the main formulation given above (with the sampling scheme in [68] and [69]) is presented. The accuracy is very high for every ϕ and θ values.

Real and imaginary parts of S_{21} , S_{22} and S_{42} are presented in Figures 3.11 to 3.16. One can observe the success of the formulation at calculating S-Parameters for high order Floquet modes as well as fundamental modes. This accuracy is achieved for both polarizations of incident wave, TE and TM.

Figure 3.17 shows the magnitude of S_{11} , S_{21} , S_{31} and S_{41} in one plot. For clarity,

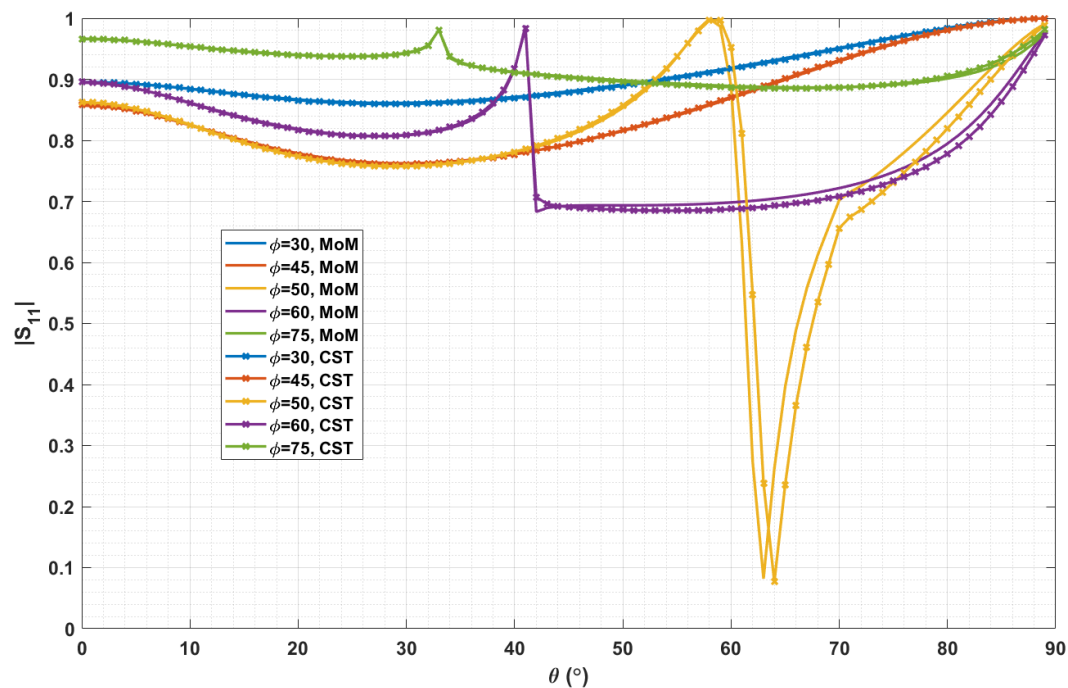


Figure 3.10: Magnitude of S_{11} versus θ for various ϕ values

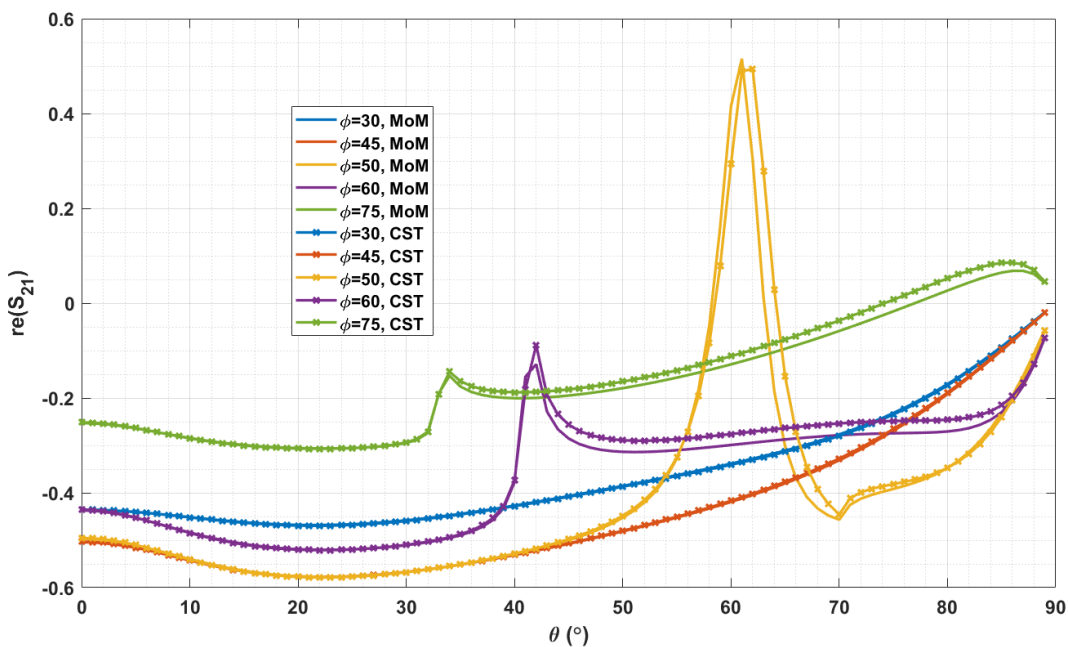


Figure 3.11: Real part of S_{21} versus θ for various ϕ values

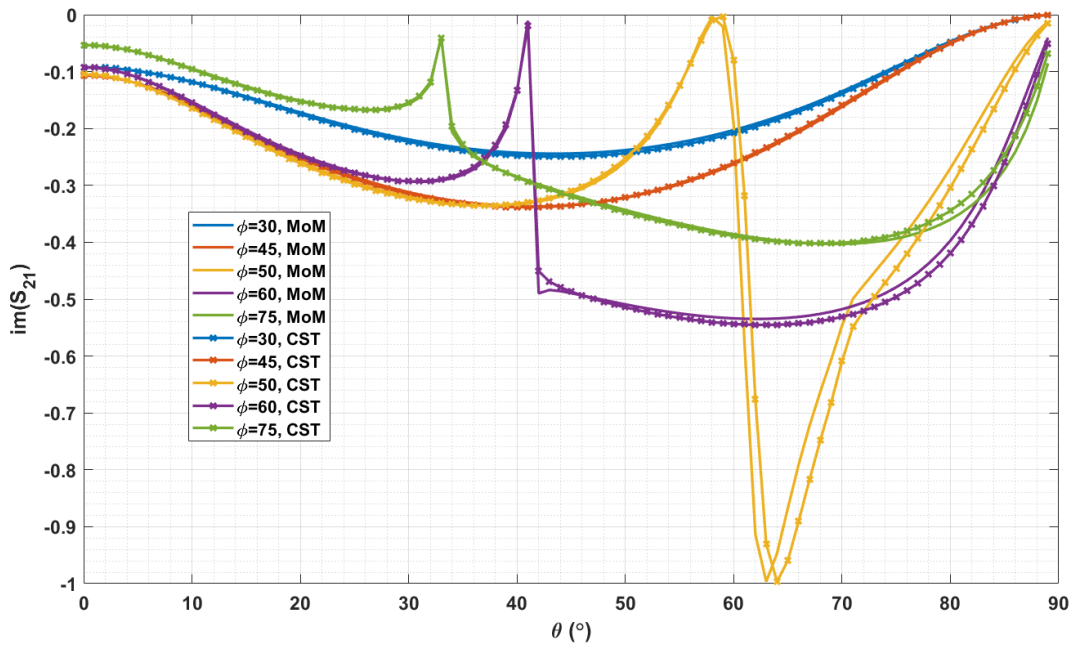


Figure 3.12: Imaginary part of S_{21} versus θ for various ϕ values

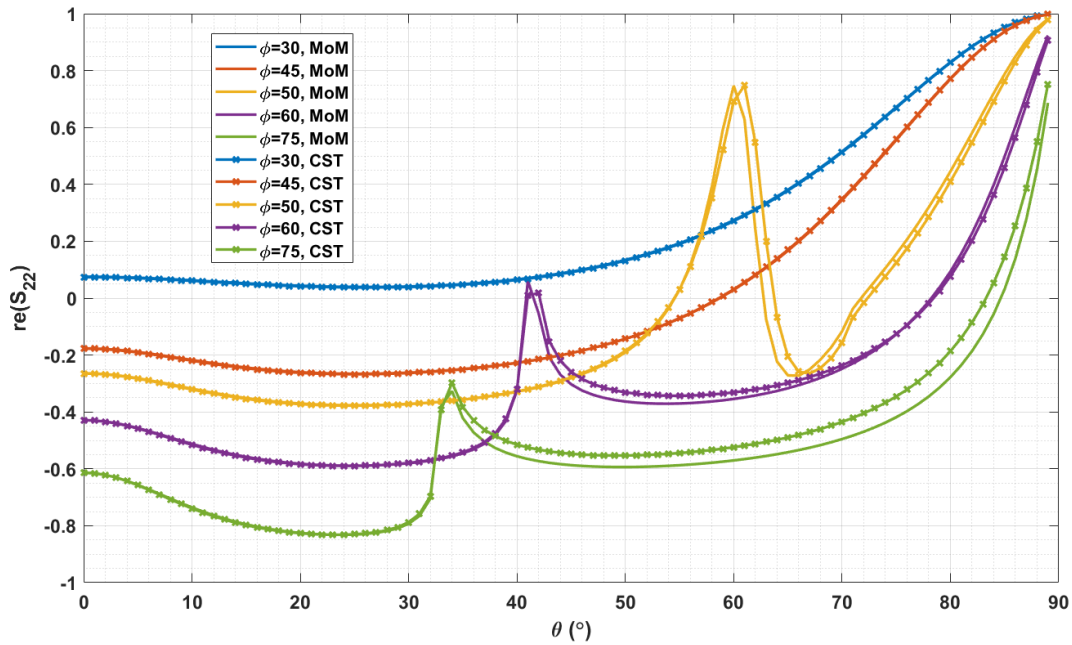


Figure 3.13: Real part of S_{22} versus θ for various ϕ values

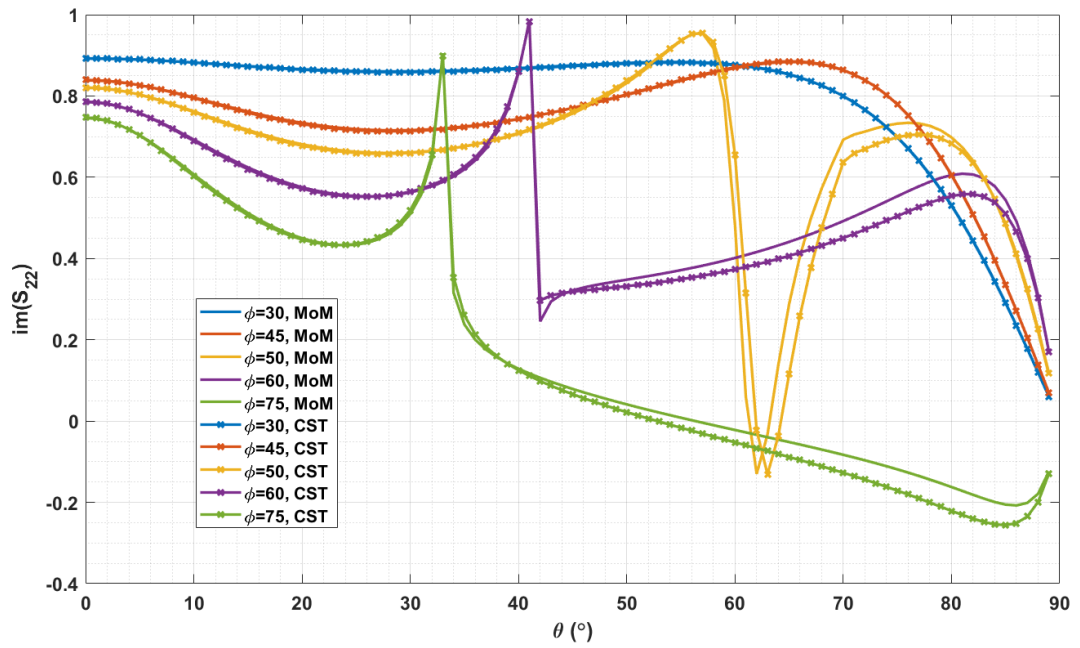


Figure 3.14: Imaginary part of S_{22} versus θ for various ϕ values

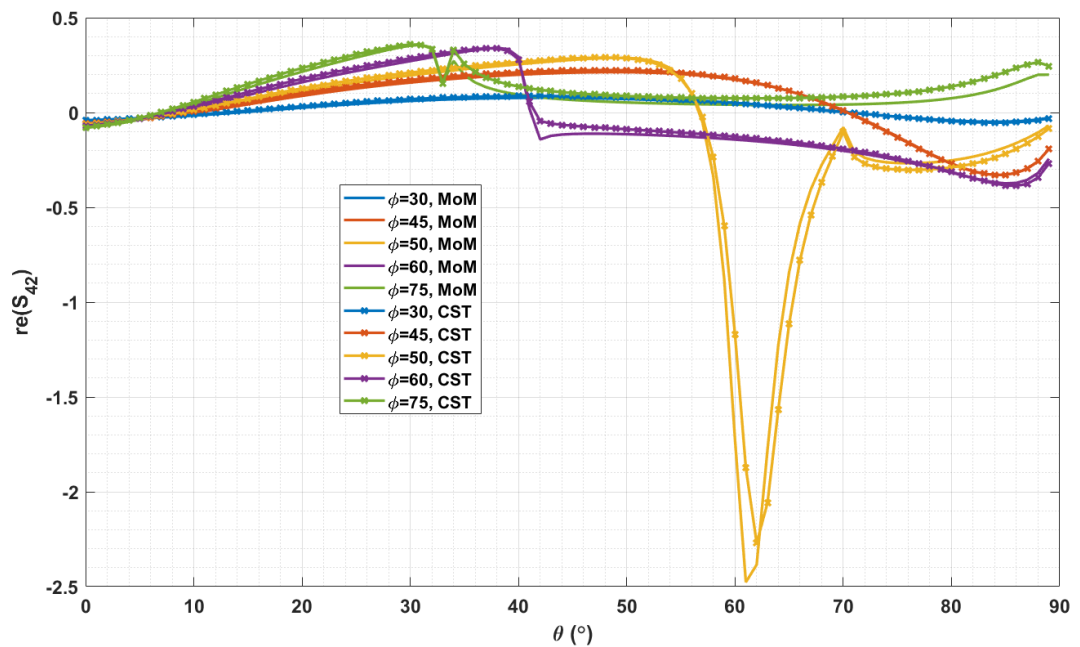


Figure 3.15: Real part of S_{42} versus θ for various ϕ values

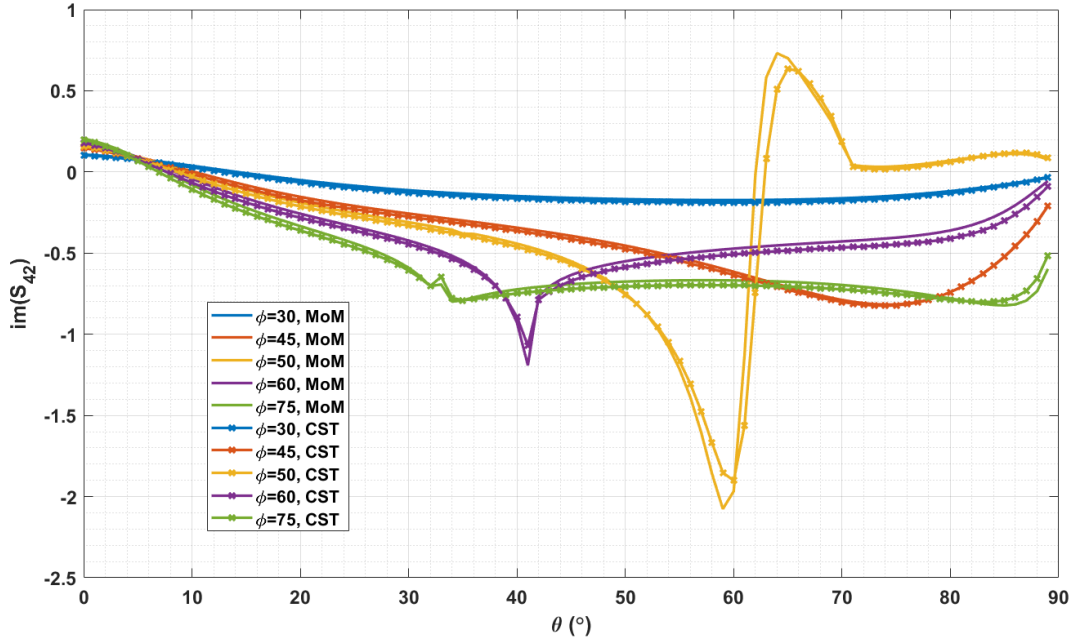


Figure 3.16: Imaginary part of S_{42} versus θ for various ϕ values

results for only one ϕ value are given. It is chosen as 50° as the most abrupt changes occur at this ϕ angle.

Last thing to mention in this section is about the efficiency of the code. CST solves the S-Parameter problem for each incidence angle in 42 seconds. Our MoM code solves the initial angle in 37 seconds and only 2.7 seconds is needed for the other angles which makes MoM very efficient for calculations including incidence angle sweeps.

3.5 Concluding Remarks

Observing the results, one can conclude that the formulation presented in this chapter for MoM analysis of planar periodic structures is very successful at calculating the S-Parameters of the structure. The accuracy of the results is sufficient for many applications.

If the height of the observation point above the surface is large, there are only propagating modes reaching this point. As the distance becomes smaller, the effect of other

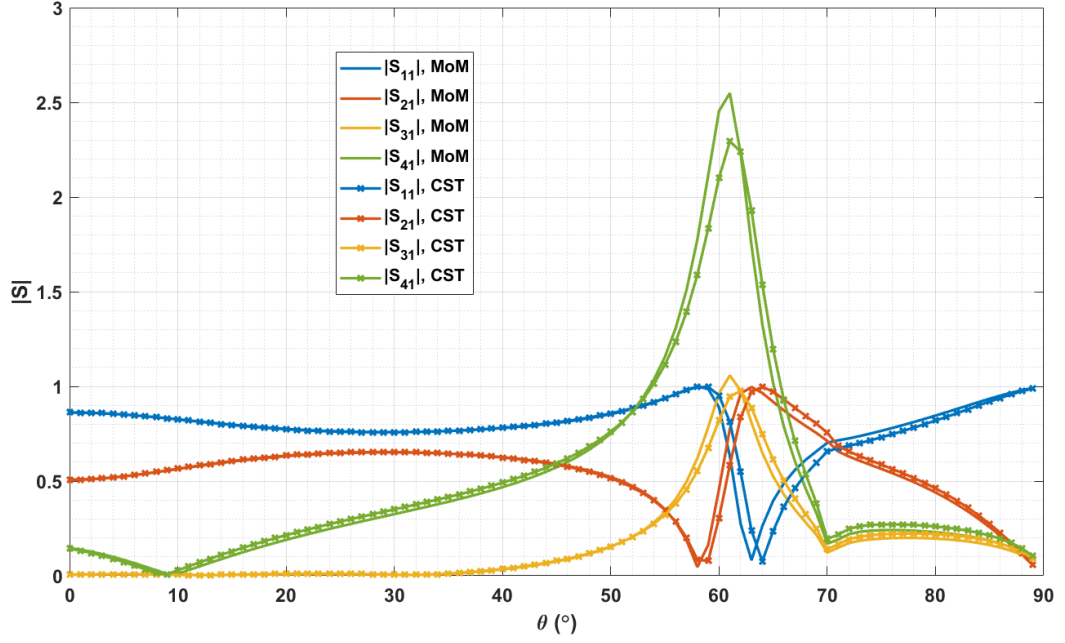


Figure 3.17: Magnitude of S_{11} , S_{21} , S_{31} , S_{41} versus θ for $\phi = 50$

modes which are evanescent increases. Eventually, when the height is very small compared to wavelength many evanescent modes should be taken into account to calculate the near field at these points accurately. With this in mind, the little differences in the results of the formulation presented compared to the results of CST at some θ angles have been taken a closer look.

It is questioned whether the results would improve further if the order of the symmetric gaussian quadrature is increased. However, the results did not improve and in fact they got worse for some orders of quadrature. This observation has been associated with the convergence of the integrals and a test regarding the accuracy of the symmetric gaussian quadrature has been performed. The sample integral problem is taken from [73] where the integration of e^{-jkR}/R is carried out on a right triangle with vertices at $(0, 0, 0)$, $(0.1\lambda, 0, 0)$, $(0, 0.1\lambda, 0)$ and $\lambda=10$ m. Quadrature results are tested at four different observation points seen in the columns of Table 3.4 whereas the integral results for different orders and the associated relative error with respect to the reference result are presented at the rows of the table.

One can conclude that to make the integrals in the MoM analysis convergent and

accurate, a singularity handling scheme should be adapted which is the topic of the next chapter.

Table 3.4: Test of symmetric gaussian quadrature w.r.t reference results in [73]

Obs.Point (x,y,z) [m]	(0.1,0.1,0)	(0.2,0.2,0)	(0.3,0.3,0)	(0.4,0.4,0)
Reference	1.8985699 - 0.3096430i	2.2462800 - 0.3111440i	2.3809900 - 0.3118260i	2.2838600 - 0.3116880i
1 st order Sym. Gau.	1.4827772 - 0.3119133i	2.6330619 - 0.3134248i	10.6019497 -0.3141133i	5.2939982 - 0.3139755i
Rel. Error (1. order)	0.2161505	0.1705623	3.4235137	1.3059000
2 nd order Sym. Gau.	2.3117304 - 0.3096404i	4.2158909 - 0.3111405i	1.7065020 - 0.3118230i	1.4117616 - 0.3116847i
Rel. Error (2. order)	0.2147789	0.8685399	0.2808819	0.3783457
3 rd order Sym. Gau.	1.9695597 - 0.3096377i	Inf - 0.1475135i	-2.5148220 -0.3118209i	-0.2592415 -0.3116828i
Rel. Error (3. order)	0.0369036	∞	2.0387983	1.1032832
4 th order Sym. Gau.	5.6006341 - 0.3096431i	1.6717311 - 0.3111435i	1.8211663 - 0.3118263i	2.7825863 - 0.3116882i
Rel. Error (4. order)	1.9244953	0.2533589	0.2331314	0.2163643
5 th order Sym. Gau.	35.5728569 -0.3096431i	1.8301966 - 0.3111435i	3.5419278 - 0.3118263i	2.6140983 - 0.3116882i
Rel. Error (5. order)	17.5053711	0.1834804	0.4834578	0.1432685
6 th order Sym. Gau.	1.7422847 - 0.3096431i	2.2069256 - 0.3111435i	2.2844298 - 0.3118263i	1.7822686 - 0.3116882i
Rel. Error (6. order)	0.0812440	0.0173541	0.0402113	0.2176073

CHAPTER 4

SINGULARITY CANCELLATION FOR MOM ANALYSIS OF PERIODIC PLANAR STRUCTURES

4.1 Introduction

The accuracy of the results presented in Chapter 3 is high and sufficient for many applications. However, these results do not converge as the order of quadrature is increased since the integrals involved in the MoM analysis do not converge with the increasing number of points because of the singularity they possess.

The singularity is an unavoidable fact in spatial domain MoM formulations, arising due to overlapping of source and observation regions. One of the approaches to solve this issue is the extraction of the part involving singularity, taking the integral of that portion analytically and adding this result to the numerical integration result of the remaining part. This singularity extraction approach is used in [74] - [76]. The other approach is the singularity cancellation where a transformation is applied to integration variables to cancel the singularity in the integrand with the Jacobian of the transformation. Duffy's [77], arcsinh [73] and polar [78] are some of the successful examples of the transformations applied to cancel the singularities associated with the MoM analysis of aperiodic structures. In [79], the performance of these three transformations are compared for the evaluation of near singular integrals where the observation point is slightly out of the source plane, i.e., $z \neq 0$. It is demonstrated that arcsinh transformation gives the most accurate results for singular cases ($z = 0$), but it is sensitive to variations in z for near-singular cases. To eliminate this problem, radial-angular transformation is proposed. But in [79], it is also reported that if Gauss-Legendre quadrature is applied after the transformation, the accuracy of

the radial-angular transformation is similar to the arcsinh transformation. Therefore, a new quadrature method is proposed to improve the accuracy of the radial-angular transformation. For the sake of simple implementation with acceptable accuracy, arcsinh transformation is chosen for singularity cancellation in this work.

It was demonstrated in [80] that arcsinh transformation can successfully handle the singularity arising in the analysis of periodic structures in free space. The approach was extended in [81] to the analysis of periodic structures in layered media, where we have demonstrated the accuracy achieved by arcsinh transformation for layered media problems in which both singular ($z = 0$) and near-singular ($z \neq 0$) situations arise for self-term integrals due to the complex images used in DCIM.

Free space problem can be seen as a special case of the multilayered problem. Actually, the direct wave contribution in multilayered media formulation is exactly the same as the field in free space. Thus, free space formulation is not studied as a separate topic in this chapter. Formulation will be given for the general case of periodic structure in multilayered media in Section 4.2. Before that, arcsinh technique is briefly summarized in this section as presented in its original paper [73].

In the MoM analysis of aperiodic structures, the source integrals of the following form are considered:

$$I = \frac{1}{4\pi} \int_D \Lambda(\vec{r}') \frac{e^{-jkR_i}}{R_i} dD \quad (4.1)$$

where $\Lambda(\vec{r}')$ is a quantity related to the basis function with triangular domain, D . The triangle D is subdivided into three sub-triangles by using the projection of the observation point onto the plane of source triangle. Each sub-triangle has its first vertex as the observation point or the projection point of it. The other two vertices of sub-triangles are the pairs of vertices of the main triangle.

In each sub-triangle, the following arcsinh transformation is applied by defining a local coordinate system as seen in Fig. 4.1 with the origin at the observation (or projection) point and with two orthogonal axes one of which is radial (y') and the other is transverse (x') while Δz_i is the height of the observation point from the source

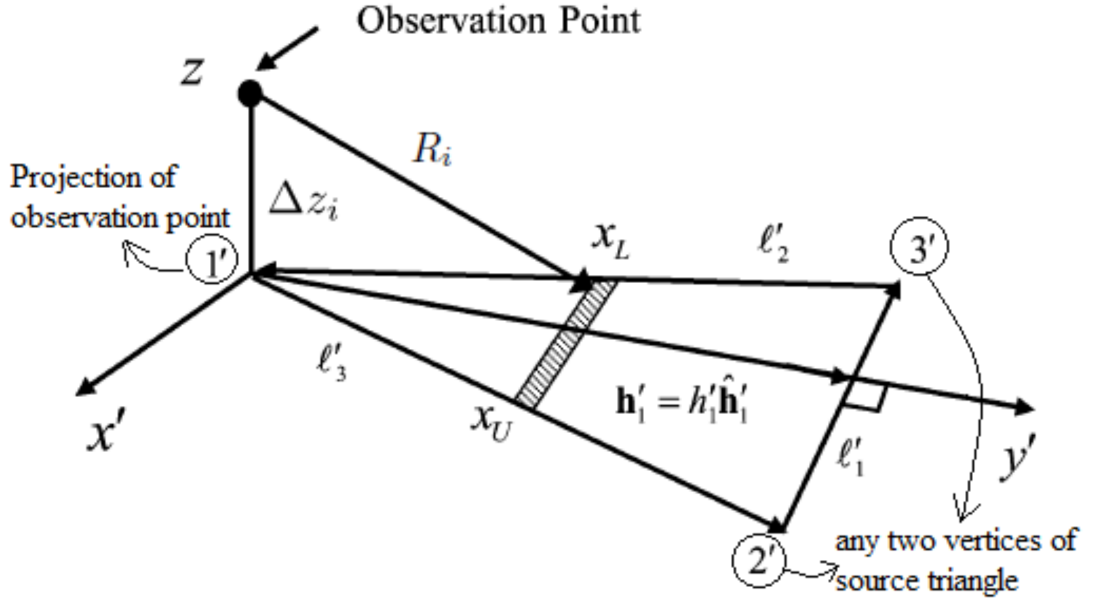


Figure 4.1: Local coordinate system in each subtriangle

triangle plane:

$$u(x') = \sinh^{-1} \frac{x'}{\sqrt{y'^2 + \Delta z_i^2}} \quad (4.2)$$

The change of variable in (4.2) transforms (4.1) into the form:

$$I = \frac{1}{4\pi} \int_0^{h'_1} \int_{u_L}^{u_U} \vec{\Lambda}(\vec{r}') e^{-jkR_i} du dy' \quad (4.3)$$

For definitions of the integral limits, u_L , u_U and h'_1 , please refer to [73]. Since the integrand in (4.3) is free of any singularity, it can be computed accurately by using numerical quadrature methods. Gauss-Legendre quadrature technique is utilized in this work.

Arcsinh method was implemented for aperiodic source in free space and the results were compared to the ones in [73] and results obtained from Mathematica. Perfect agreement has been observed. Much more detailed integration results will be presented in Section 4.3.

4.2 Formulation

Formulation for the direct wave contribution (which is also equal to field in free space case) can be handled together with the complex image contribution by redefining R_i in (3.47) as follows:

$$R_i = \sqrt{(x - x' - pD_x)^2 + (y - y' - qD_y)^2 + (\Delta z_i)^2} \quad (4.4)$$

where Δz_i is given as:

$$\Delta z_i = \begin{cases} z - z', & i = 0 \text{ (direct wave term)} \\ z + z' + \beta_i, & i > 0 \end{cases} \quad (4.5)$$

Index $i = 0$ is reserved for the direct wave contribution. For this term, we have a singularity when the observation point is in the source plane. For the contribution of reflected waves Δz_i is nonzero even if the observation point is in the source plane, due to the complex exponential β_i 's. Arcsinh transformation is also applied to handle near-singularity problem associated with small complex exponentials (i.e., $|\beta_i| < 10^{-4}\lambda_s$)

For the application of arcsinh transformation to the generalized complex exponential contribution defined above, the Green's function in (4.1) is replaced by the corresponding Green's function expression. For $(p, q) = (0, 0)$ term of $G_{ci,spat}(\vec{r}, \vec{r}')$ in (3.46), the source integral in one of the sub-triangles, will take the following form after applying the arcsinh transformation:

$$I_{ci} = \frac{\alpha_i}{8\pi} \int_0^{h'_1} \int_{u_L}^{u_U} \vec{\Lambda}(\vec{r}') \sum_{\pm} e^{\pm jk_s R_i} \operatorname{erfc}\left(R_i E_{ci} \pm \frac{jk_s}{2E_{ci}}\right) du dy' \quad (4.6)$$

When (4.3) and (4.6) are compared, it can be observed that integral, which will be computed numerically, is modified and complementary error function with complex argument is introduced due to the periodicity in layered media.

Numerical computation of integrals involving the fundamental term $((p, q) = (0, 0))$

of the spatial series of Green's functions corresponding to surface waves have also a convergence problem because of the singularity which needs a closer look to be identified. The only term with position dependence in (3.50) is the exponential integral function. The series expansion of this function is given in [65] and its small argument behavior is deduced from this expansion as follows:

$$E_s(z \approx 0) = -\frac{(-z)^{s-1}}{(s-1)!} \ln(z) \quad (4.7)$$

It can be observed from (4.7) that when $z \rightarrow 0$ there isn't any singularity problem for $s > 1$. But, for $s = 1$, there is a logarithmic singularity.

$$\begin{aligned} G_{spat}^{sw}(\rho \rightarrow 0) &\approx -\ln(\rho^2 E_{sw}) \sum_{i=1}^{N_{sw}} \frac{k_{\rho p_i} \text{Res}(k_{\rho p_i})}{2\pi} \\ &\approx -(2 \ln \rho + \ln E_{sw}) \sum_{i=1}^{N_{sw}} \frac{k_{\rho p_i} \text{Res}(k_{\rho p_i})}{2\pi} \\ &\approx -\ln \rho \sum_{i=1}^{N_{sw}} \frac{k_{\rho p_i} \text{Res}(k_{\rho p_i})}{\pi} \end{aligned} \quad (4.8)$$

If arcsinh transformation is applied to (3.50), one has $\rho \ln(\rho)$ instead of $\ln(\rho)$ alone in the final expression due to the Jacobian of the change of variables associated with the transformation. While $\ln(\rho)$ has a logarithmic singularity at $\rho = 0$, $\rho \ln(\rho)$ goes to zero as ρ goes to zero. The transformed integral is thus free of singularity and can be computed by quadrature methods which is Gauss-Legendre in this work.

4.3 Integral Tests

The formulation for adapting arcsinh transformation to the complex image and surface wave contribution arising in multilayered media has been presented briefly in section 4.2. Now it is time to test the accuracy of this formulation. First test is directly on calculating the integrals with singularity. The verification is done by comparing our integration results to the ones obtained from a commercial symbolic math software, Mathematica [82].

The sample source triangle chosen in this test, over which the integration is carried out, is a right angle triangle with orthogonal sides of lengths 4.233×10^{-4} and 4.219×10^{-4} meters. This is a typical triangle element that can be encountered in our code during the meshing of the scatterers considered in the numerical examples of Chapter 3.

The observation point is swept on the line between the centroid of the source triangle and a point which is at a distance of about one diagonal length of the PEC plate in the aforementioned numerical example.

In the tables of integral results, the column named *in/out* states whether the corresponding observation point is inside or outside of the source triangle. Column *R* gives the distance of the observation point from the centroid of the source triangle.

Table 4.1: Comparison of Integration Results for equation (3.46) with $p = q = i = 0$

in/out	<i>R</i>	Mathematica	Sym. Gau. w/o Arcsinh	Gau. Leg. w/ Arcsinh
in	0	8.06199e-5	Inf	8.06203e-5
in	9.275e-6	8.07311e-5	7.65823e-4	8.07313e-5
in	2.715e-5	8.05285e-5	2.61389e-4	8.05288e-5
in	6.161e-5	7.84245e-5	1.15013e-4	7.84247e-5
in	1.280e-4	6.43336e-5	5.51644e-5	6.43340e-5
out	2.561e-4	2.81724e-5	2.73829e-5	2.81724e-5
out	5.029e-4	1.38747e-5	1.37043e-5	1.38747e-5
out	9.786e-4	6.75934e-6	6.72982e-6	6.75934e-6
out	1.895e-3	3.05812e-6	3.05353e-6	3.05812e-6
out	3.663e-3	1.07007e-6	1.06922e-6	1.07004e-6
out	7.069e-3	1.61078e-7	1.60891e-7	1.60441e-7
out	1.364e-2	1.38923e-9	1.38486e-9	4.23348e-9

Table 4.1 shows the integration results when the integrand is the one given in equation (3.46) with $p = q = i = 0$ (fundamental Floquet mode of direct wave contribution). It

is observed that symmetric Gaussian quadrature without arcsinh transformation yields correct results as observation point moves away from the source triangle. Inside the triangle it yields very inaccurate results as expected. Gauss Legendre quadrature with arcsinh transformation gives highly accurate results inside and outside the triangle. However, as the distance of the observation point gets larger, the accuracy of this quadrature diminishes severely after a point.

Table 4.2 shows the integration results when the integrand is equation (3.46) with $p = q = 0$ and $i = 6$. $i = 6$ refers to the complex image with the smallest distance in the numerical example of Chapter 3. Same observations as of Table 4.1 applies also to these results.

Table 4.3 shows the integration results when the integrand is as in equation (3.50) with $p = q = 0$. This is the fundamental Floquet mode of the spatial summation part of the surface wave contribution (there is only one surface wave pole for the aforementioned numerical problem). Table 4.3 verifies that there is a singularity problem also in the integrals corresponding to the spatial domain surface wave contribution and that arcsinh transformation can successfully cancel out this singularity yielding a convergent and accurate quadrature result.

The inaccuracy of the arcsinh method at far observation points has been analyzed and it has been found that the reason lies in the distribution of the quadrature points after arcsinh transformation. Without any transformation, all of the quadrature points lie inside the source triangle independent of the observation point. However, once arcsinh transformation is applied, position of quadrature points change according to the observation point since the coordinate system of the sub-triangles depends on the point of observation [73]. This fact is visualized in Figures 4.2 to 4.4. Figure 4.2 shows the sub-triangles and quadrature points when the observation point (or projection of it) is in the source triangle. Figure 4.3 shows the situation when the observation point is outside the triangle. Two of the sub-triangles have parts that is out of the main triangle and the third one is completely outside. The formulation of arcsinh [73] is such that the weight of the contribution of this third sub-triangle to the total integral is negative while the weights of the contributions of other two sub-

Table 4.2: Comparison of Integration Results for equation (3.46) with $p = q = 0$ and $i = 6$

in/out	R	Mathematica	Sym. Gau. w/o Arcsinh	Gau. Leg. w/ Arcsinh
in	0	-4.36248e-5 - j1.03429e-13	-1.55883e-1 - j8.77137e-8	-4.36316e-5 - j9.97053e-14
in	9.275e-6	-4.36867e-5 - j1.03758e-13	-4.14461e-4 - j9.49e-13	-4.36917e-5 - j9.98427e-14
in	2.715e-5	-4.35753e-5 - j1.03316e-13	-1.41464e-4 - j3.23e-13	-4.35821e-5 - j9.95922e-14
in	6.161e-5	-4.24366e-5 - j1.00711e-13	-6.22450e-5 - j1.42e-13	-4.24434e-5 - j9.69900e-14
in	1.280e-4	-3.48106e-5 - j8.32853e-14	-2.98549e-5 - j6.8e-14	-3.48175e-5 - j7.95636e-14
out	2.561e-4	-1.52469e-5 - j3.48410e-14	-1.48196e-5 - j3.4e-14	-1.52469e-5 - j3.48416e-14
out	5.029e-4	-7.50900e-6 - j1.71589e-14	-7.41675e-6 - j1.7e-14	-7.50900e-6 - j1.71593e-14
out	9.786e-4	-3.65815e-6 - j8.35928e-15	-3.64217e-6 - j8e-15	-3.65815e-6 - j8.3595e-15
out	1.895e-3	-1.65505e-6 - j3.78197e-15	-1.65257e-6 - j4e-15	-1.65505e-6 - j3.7821e-15
out	3.663e-3	-5.79121e-7 - j1.32336e-15	-5.78661e-7 - j1e-15	-5.79106e-7 - j1.3234e-15
out	7.069e-3	-8.71753e-8 - j1.99205e-16	-8.70742e-8 - j0	-8.68304e-8 - j1.984e-16
out	1.364e-2	-7.51848e-10 - j1.71806e-18	-7.49486e-10 - j0	-2.29116e-9 - j5.2e-18

Table 4.3: Comparison of Integration Results for equation (3.50) with $p = q = 0$

in/out	R	Mathematica	Sym. Gau. w/o Arcsinh	Gau. Leg. w/ Arcsinh
in	0	-2.93656e-6 + j1.69552e-12	NaN	-2.93896e-6 + j1.69691e-12
in	9.275e-6	-2.93739e-6 + j1.696e-12	-4.64372e-6 + j2.68121e-12	-2.93980e-6 + j1.69739e-12
in	2.715e-5	-2.93295e-6 + j1.69344e-12	-3.90555e-6 + j2.25501e-12	-2.93538e-6 + j1.69485e-12
in	6.161e-5	-2.90099e-6 + j1.67499e-12	-3.34229e-6 + j1.92979e-12	-2.90345e-6 + j1.67641e-12
in	1.280e-4	-2.74417e-6 + j1.58444e-12	-2.83894e-6 + j1.63916e-12	-2.74637e-6 + j1.58571e-12
out	2.561e-4	-2.34133e-6 + j1.35185e-12	-2.36034e-6 + j1.36283e-12	-2.34390e-6 + j1.35333e-12
out	5.029e-4	-1.88676e-6 + j1.08939e-12	-1.88993e-6 + j1.09121e-12	-1.88930e-6 + j1.09085e-12
out	9.786e-4	-1.41452e-6 + j8.16722e-13	-1.41511e-6 + j8.17062e-13	-1.41705e-6 + j8.18184e-13
out	1.895e-3	-9.24581e-7 + j5.33839e-13	-9.24659e-7 + j5.33884e-13	-9.27099e-7 + j5.35293e-13
out	3.663e-3	-4.35318e-7 + j2.51346e-13	-4.35220e-7 + j2.51289e-13	-4.37775e-7 + j2.52764e-13
out	7.069e-3	-8.14017e-8 + j4.70001e-14	-8.13260e-8 + j4.69564e-14	-8.32254e-8 + j4.80531e-14
out	1.364e-2	-8.02709e-10 + j4.63472e-16	-8.00261e-10 + j4.6206e-16	-3.30545e-9 + j1.90851e-15

triangles are positive. This way, the contributions from the regions outside the main triangle cancel each other.

As the observation point gets further away from the triangle, the shape of the sub-triangles become far from being ideal and after some point the distribution of the quadrature points becomes severely deteriorated as can be seen in Figure 4.4 which makes the quadrature fail. This problem may be solved by increasing the number of points (order) used in the Gauss-Legendre quadrature after arcsinh transformation but this approach causes an unnecessarily large computational cost. As can be seen in Tables 4.1 to 4.3, integrals for the distant observation points can be accurately and simply carried out by symmetric Gaussian quadrature without any transformation. The reasonable solution is to choose the technique for calculating the integrals according to the distance between source and weighting (testing) triangles which is the implemented solution in this work.

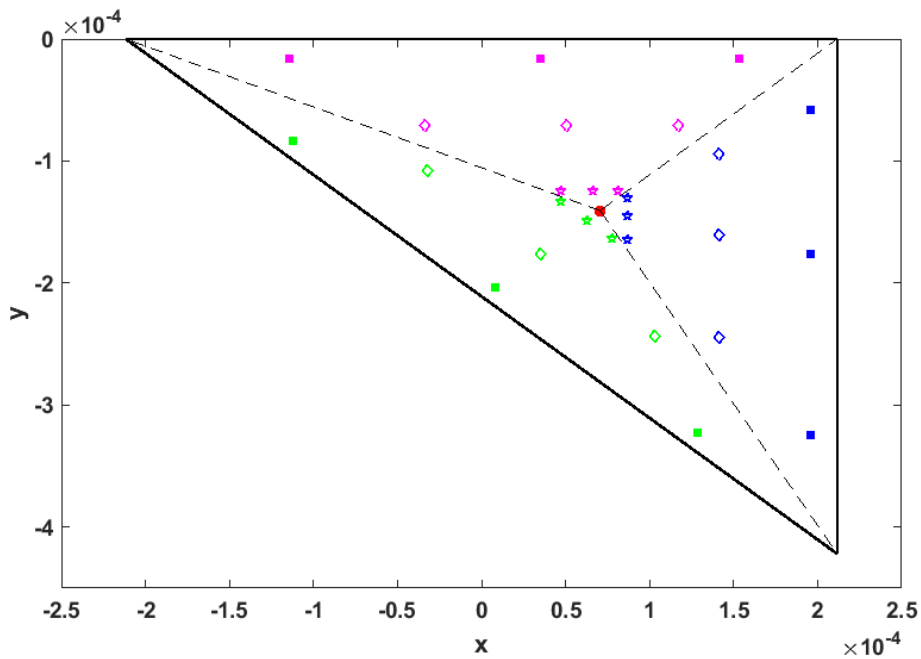


Figure 4.2: Location of quadrature points after arcsinh transformation when the observation point is at the center of the source triangle

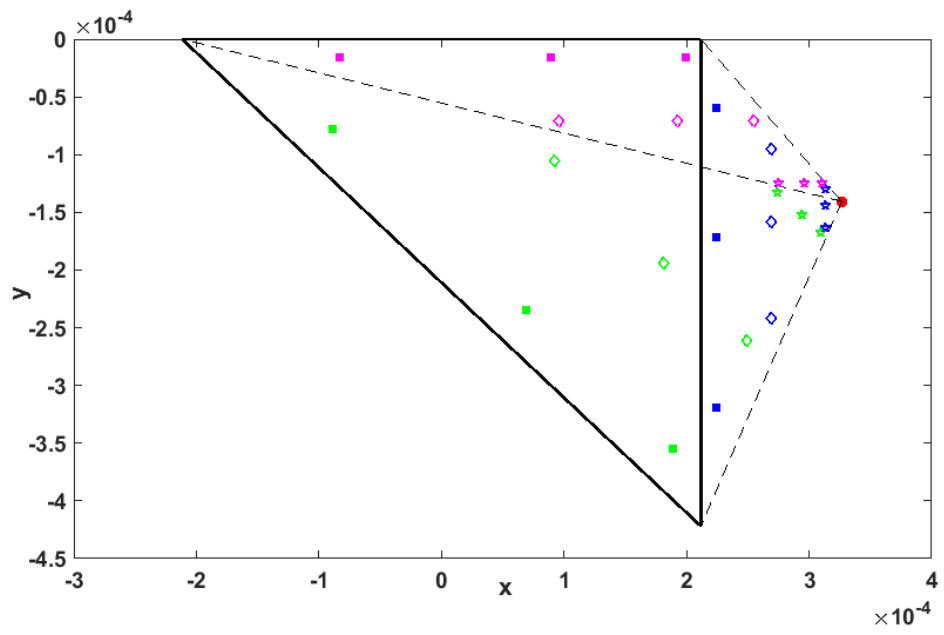


Figure 4.3: Location of quadrature points after arcsinh transformation when the observation point is outside of but close to the source triangle

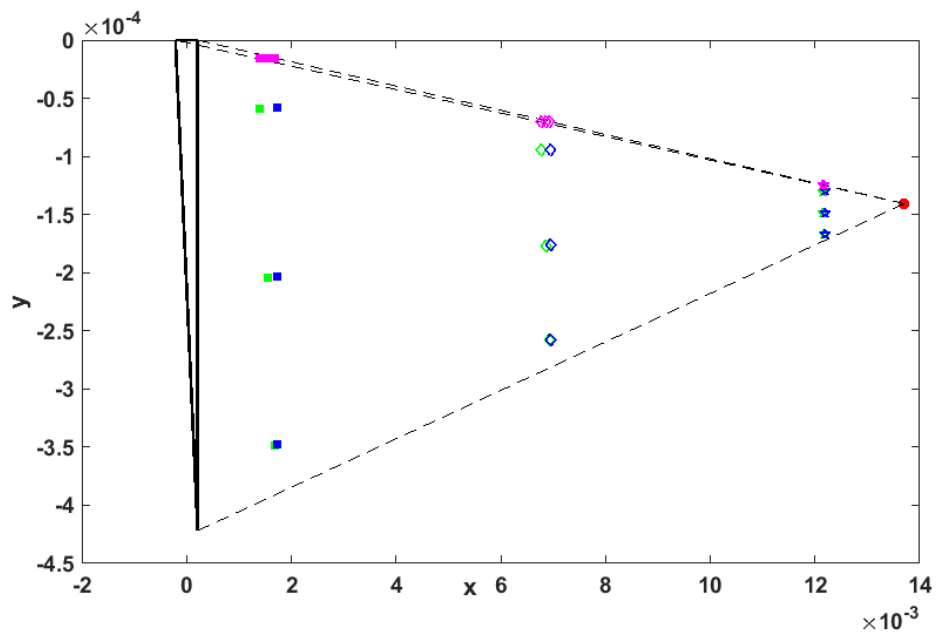


Figure 4.4: Location of quadrature points after arcsinh transformation when the observation point is very far from the source triangle

4.4 S-Parameter Analysis

In order to be able to make comparisons, S-Parameter analysis has been performed on the exact same numerical problems of Chapter 3. First, S-Parameters obtained by using arcsinh transformation for the free space problem defined in Table 3.2 are presented in Figures 4.5 and 4.6. Figure 4.5 shows the magnitude of S_{32} for various ϕ values together with the CST results. Figure 4.6 presents the magnitude of S_{11} , S_{21} , S_{31} and S_{41} for $\phi = 50$. The results obtained by MoM without a singularity cancellation are also included in this plot. Good agreement is observed between the results of MoM with singularity cancellation, CST and also MoM without singularity cancellation.

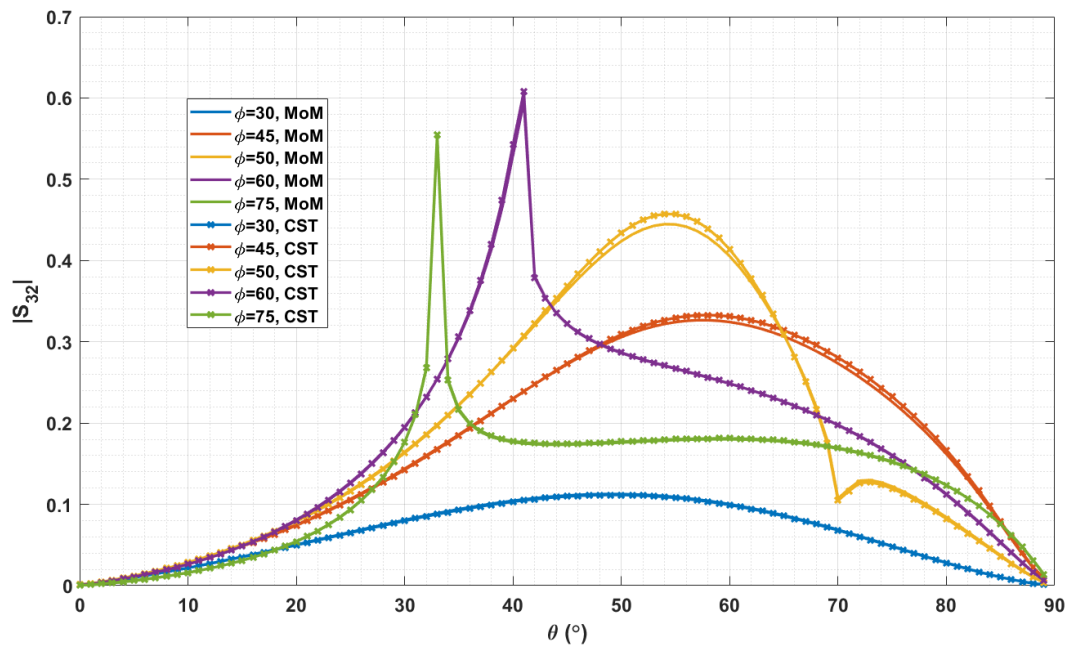


Figure 4.5: Magnitude of S_{32} versus θ for various ϕ values; free space case with singularity cancellation

For the free space results presented, MoM formulation with arcsinh adaptation needed 2.7 seconds to solve the initial angle while other angles were solved in 1.4 seconds. Without arcsinh transformation, these numbers were 2.2 and 1.4 seconds respectively. CST solved each angle in 26 seconds as mentioned in Chapter 3.

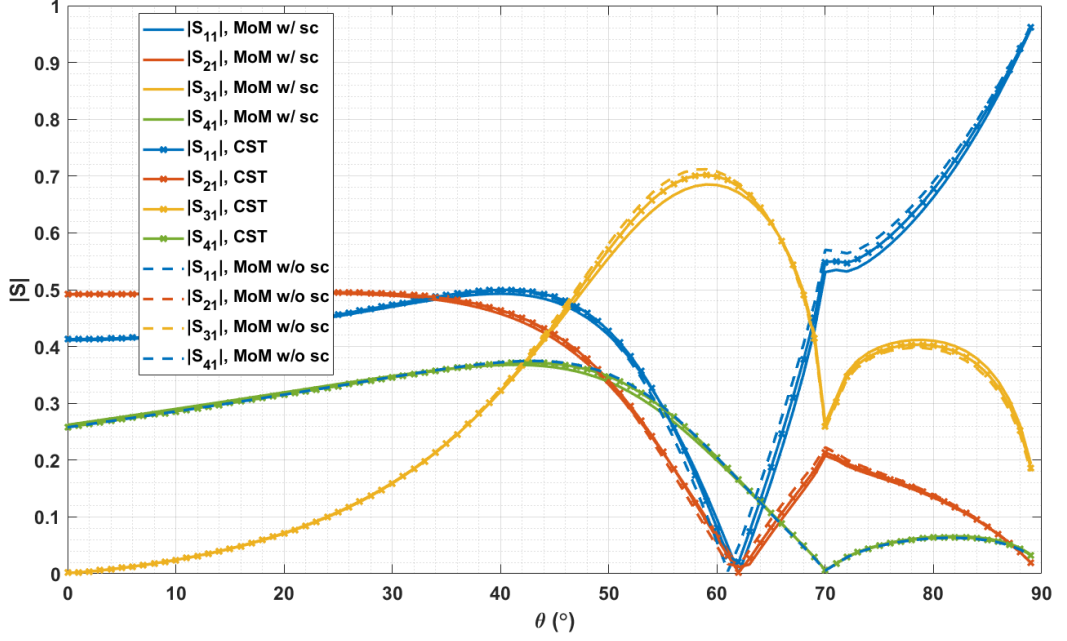


Figure 4.6: Magnitude of S_{11} , S_{21} , S_{31} , S_{41} versus θ for $\phi = 50$, including the results obtained without singularity cancellation (w/o sc); free space case

Results for the multilayered case are presented in Figures 4.7 to 4.10. Figure 4.7 shows the magnitude of S_{21} for various ϕ values together with the CST results. In order to see the effect of singularity cancellation on S-Parameters, the results obtained by MoM without a singularity cancellation are also included in Figures 4.8 to 4.10. Figures 4.8 and 4.9 present the real and imaginary parts of S_{22} and Figure 4.10 shows the magnitude of S_{11} , S_{21} , S_{31} and S_{41} for $\phi = 50$. Again, a very good agreement is observed between the results of MoM with and without singularity cancellation and CST. However, one can also observe a slight improvement of the results when arcsinh transformation is implemented.

Efficiency of the MoM formulation with singularity cancellation will be mentioned briefly before ending this section. Our MoM code solved the problem for the first incidence angle in 39 seconds while solving the following angles in 2.8 seconds. CST, as mentioned in Chapter 3, needs 42 seconds to solve for each incidence angle.

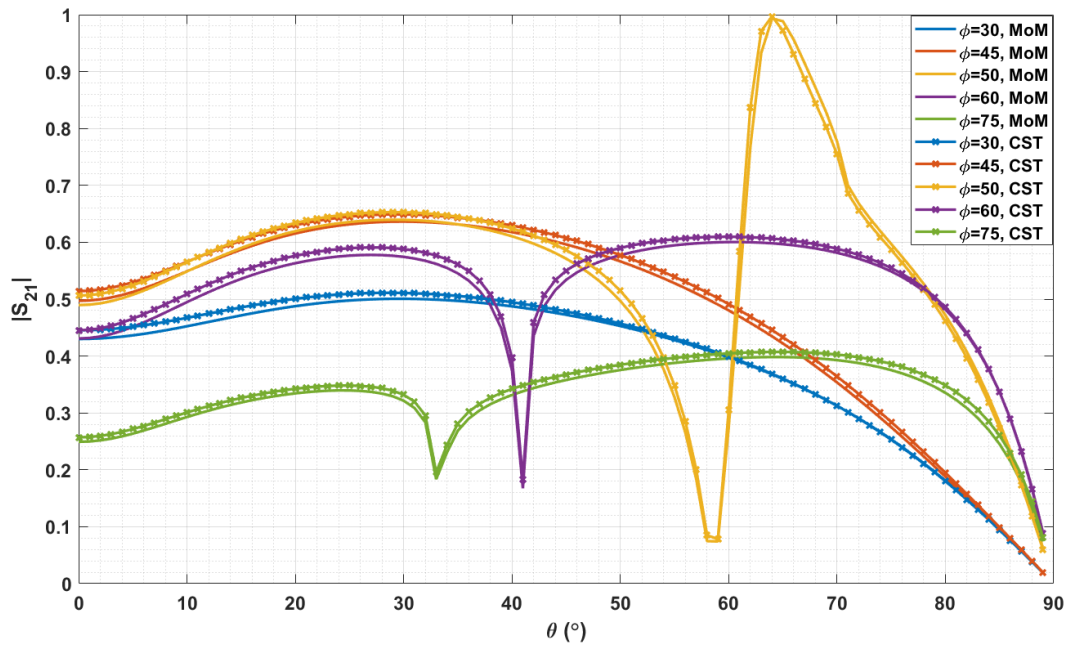


Figure 4.7: Magnitude of S_{21} versus θ for various ϕ values; multilayered case with singularity cancellation

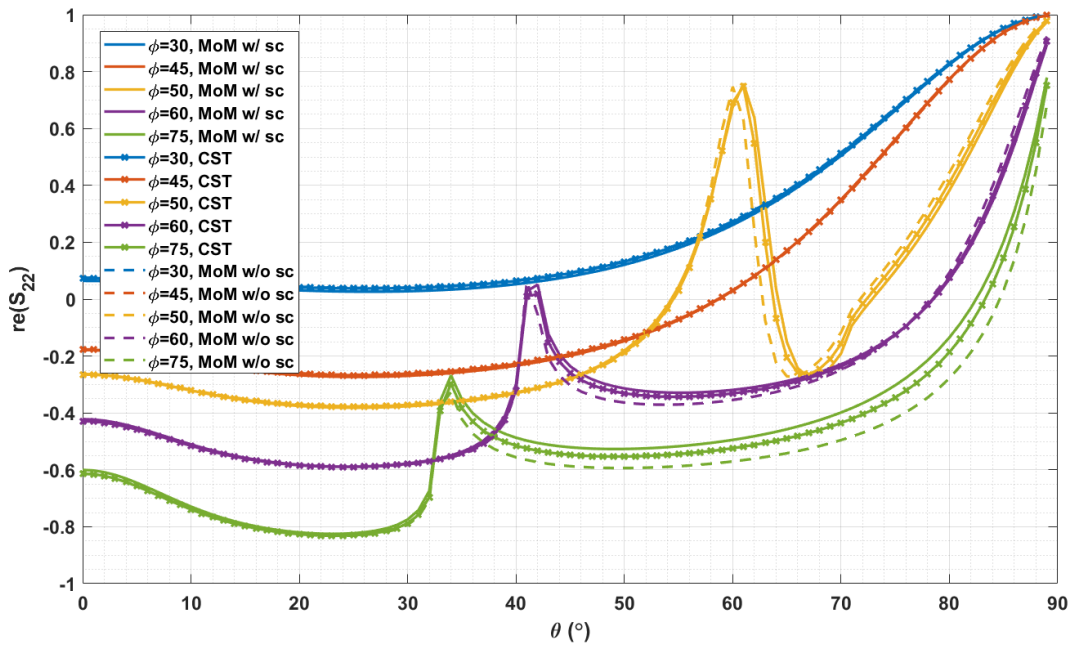


Figure 4.8: Real part of S_{22} versus θ for various ϕ values, including the results obtained without singularity cancellation (w/o sc); multilayered case

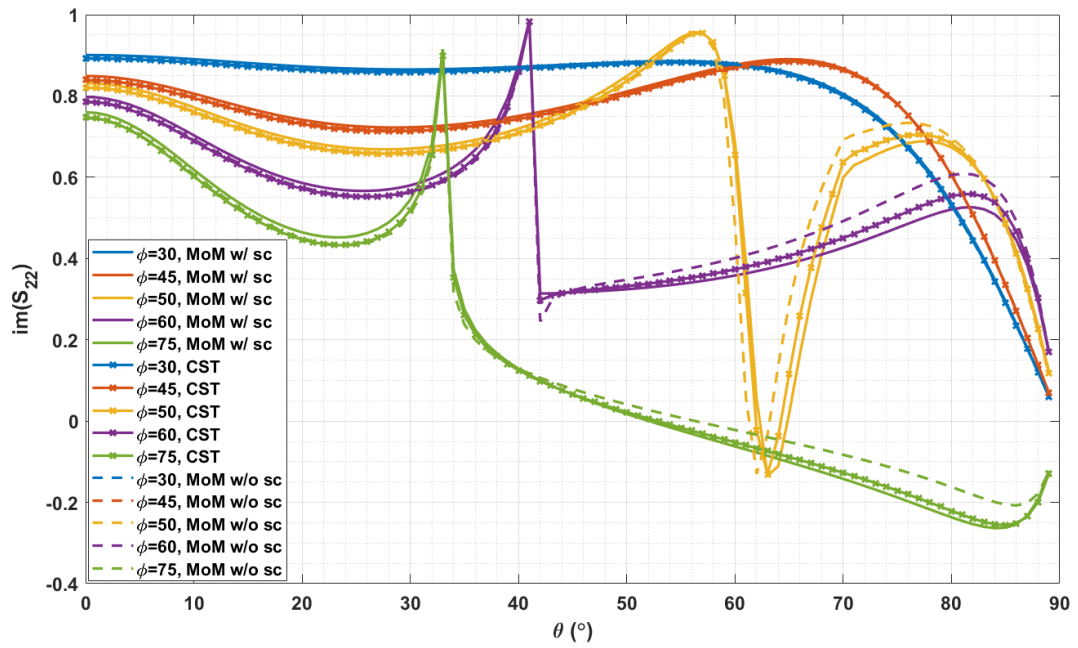


Figure 4.9: Imaginary part of S_{22} versus θ for various ϕ values, including the results obtained without singularity cancellation (w/o sc); multilayered case

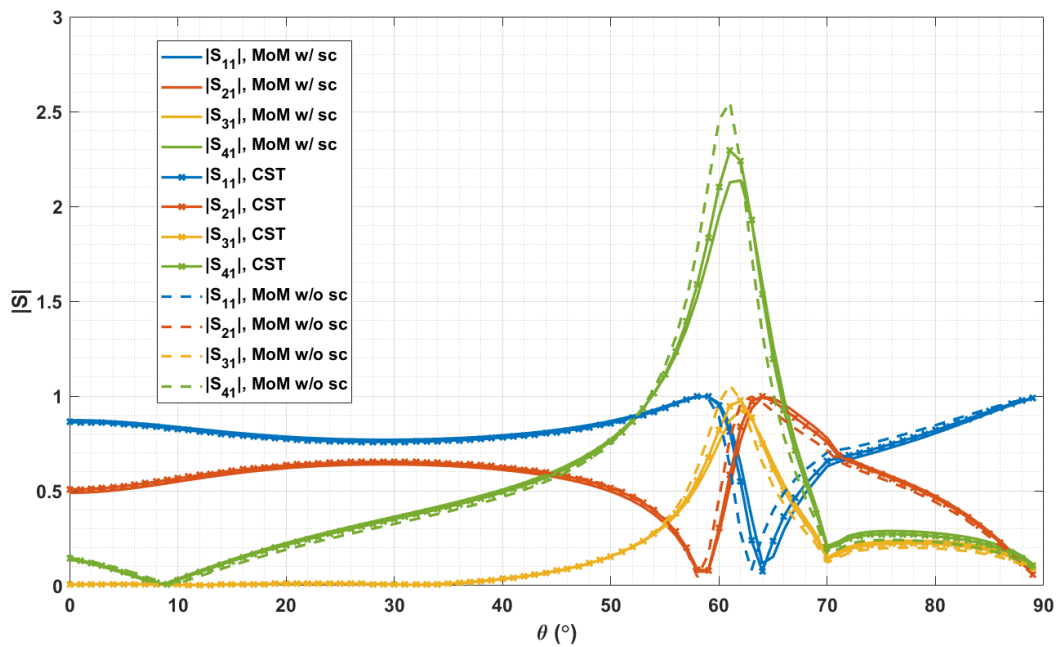


Figure 4.10: Magnitude of S_{11} , S_{21} , S_{31} , S_{41} versus θ for $\phi = 50$, including the results obtained without singularity cancellation (w/o sc); multilayered case

4.5 Concluding Remarks

As stated in the last section of Chapter 3, accuracy of the S-Parameters obtained without any singularity cancellation is very high and sufficient for many applications. However, the integrations involved in this formulation are not convergent and accurate as shown in Chapter 3 and previous sections of this chapter. Based on this fact, it is reasonable to predict that the field calculations at points very close to the surface where many Floquet modes should be taken into account, would involve increased level of inaccuracy compared to the S-Parameter calculations for fundamental and propagating high order Floquet modes only.

Considering our goal in this thesis work, the accuracy of the S-Parameters without any singularity cancellation is sufficient for us. This is because we focus our attention to the problems in which the periodicity is very small and the aperiodic source above the surface is placed at a distance of at least a tenth of a wavelength so that only fundamental mode is propagating and all evanescent modes are negligible at the point of field calculation. Thus, the rest of the formulation and numerical examples in this thesis do not involve singularity cancellation scheme. Considering the results presented, however, the singularity cancellation adaptation described in this chapter would form a reliable basis for future works if fields at much closer points are of interest.

CHAPTER 5

CLOSED-FORM DYADIC GREEN'S FUNCTIONS FOR DIPOLE EXCITATION OF PLANAR PERIODIC STRUCTURES

5.1 Introduction

MoM analysis of planar periodic structures with a focus on reflection coefficients is presented in Chapter 3 and the work on singularity cancellation is presented in Chapter 4. Now, it is time to introduce the proposed method for obtaining closed-form dyadic Green's functions for dipole excitation of planar periodic structures.

The method is intended for structures with periodicities very small compared to wavelength for which the higher order Floquet modes are evanescent and attenuated to negligible levels at the point of observation which is also the basic assumption in the homogenization based approaches in the literature. However, the method proposed here has the potential to be extended to cover higher order Floquet modes and thus larger periodicities since reflection coefficients of the structure can readily be obtained accurately even for high order Floquet modes.

The proposed method can take into account TE-TM couplings since the formulation involves the contribution from S_{21} and S_{12} as will be seen in Section 5.2.

The approach proposed in this thesis is limited for structures with S-Parameters independent of ϕ , for now. However, it is very promising to cover the asymmetric structures as well. Three approaches are proposed in Section 5.4 for extending the presented method to handle the ϕ dependence.

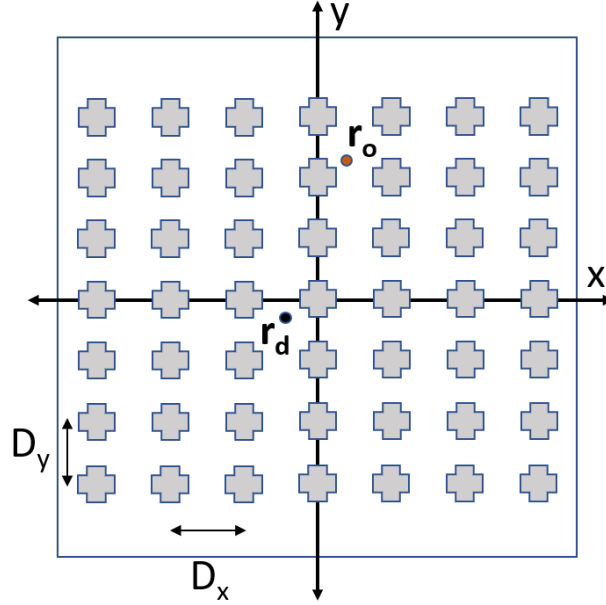


Figure 5.1: Periodic structure with a rectangular lattice of PEC scatterers with spacings D_x and D_y , excited by a dipole source at point r_d .

The outline of the proposed method is presented briefly in this section. A simple illustration of the problem is given in Fig. 5.1. The point of observation is shown as r_o and the location of the electric dipole source is r_d .

The incident field of the dipole is spherical in nature. On the other hand, the boundaries of the structure under the dipole is planar and we can calculate the response (reflection coefficients) of the structure for plane wave incidence which was the topic of Chapter 3. Thus, the formulation starts with expressing the dipole field as a plane wave spectrum. The incident field for each plane wave is the sum of its TE and TM components. These components are found analytically as a function of transverse wavenumbers. Numerically calculated S-Parameters of the structure are utilized to find the TE and TM components at the output. Then, electric field contributions from TE and TM plane waves are summed together to find the total field at the output for each plane wave. The scattered field due to dipole is the integration of these field values over 2-D infinite $k_x - k_y$ domain. This integration is actually an inverse Fourier transformation.

In order to be able to obtain closed-form expressions, we need ways to take the integral analytically. Using identities like Weyl or Sommerfeld helps to achieve this goal. There are branch point singularities in the integration domain at $k_z = 0$ or $k_\rho = k_s$. Since these points form a circle in the Cartesian $k_x - k_y$ plane, they pose a bigger challenge in this domain compared to the cylindrical coordinates. Thus, by a change of variables, electric field expressions are transformed into polar coordinates. When the structure has ϕ -independent S-Parameters, the integration with respect to ϕ can be found analytically by using Bessel integral identities (proposals for structures with ϕ -dependent S-Parameters are presented in section 5.4). The remaining 1-D integral is with respect to k_ρ and one can obtain analytical results for this integration by using Sommerfeld Identity or the derivative of it. In order to make the integrand compatible with these identities, a complex image approximation is made for the S-Parameters or modified versions of them by utilizing DCIM [67]. The path used for the sampling in this approximation is nearly the same as described in [67]. In Fig. 5.2, C_0 denotes the sampling path defined in [67] and C_1 denotes the path used in this work. The difference is that one end of the sampling path is not exactly at $k_z = k_s$ as is the case in [67] but instead it is at a slightly shifted point on the real k_z axis. The other end of the path is shifted slightly upwards on the imaginary k_z axis. This modification is made to prevent errors occurring in the approximation process due to the pole at $k_\rho = 0$ for the functions to be approximated. All of the complex image approximations utilizing 1-D DCIM mentioned in this chapter are performed on this modified sampling path.

Extraction of the complex images from the sampled data is performed by the Generalized Pencil of Function (GPOF) technique [83]. In an intermediate step of this technique, a singular value decomposition (SVD) is applied on the sampled data matrix. Only significant singular values which are larger than a preset threshold value are taken into account in the procedure. This truncation of the singular values determines the number of complex exponentials used in the approximation. The threshold value used in the approximations in this chapter is 1×10^{-8} , unless stated otherwise.

All of the derived field expressions are for the scattered fields. The notation used in naming the field components is such that the second index in subscript specifies the direction of the electric dipole whereas the first index specifies the direction of the scattered field. As an example E_{zy} is the z component of the electric field scattered

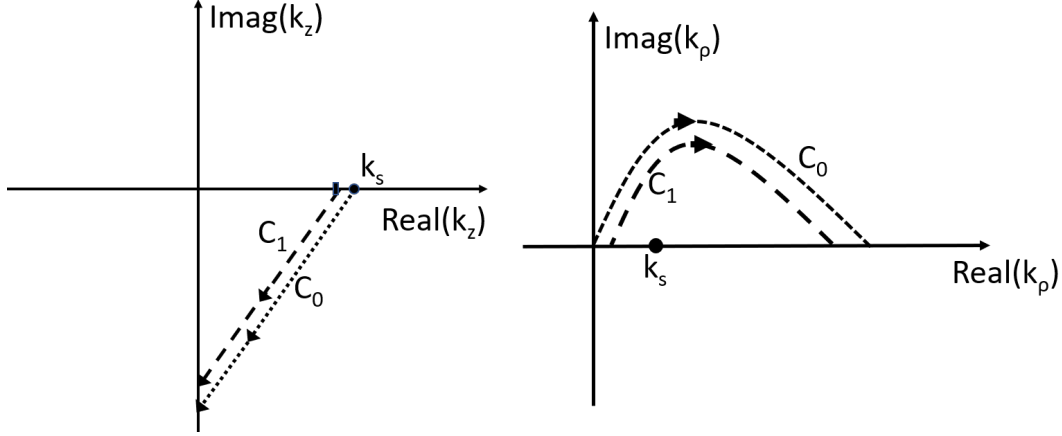


Figure 5.2: Sampling path described in [67] (C_0) and modified sampling path used in the proposed method in this thesis (C_1)

from the periodic structure excited by a y oriented dipole source.

5.2 Formulation

The electric dipole current source oriented along the direction \hat{a}_j can be expressed as follows:

$$\vec{J}_d(\vec{r}') = \hat{a}_j \delta(\vec{r}' - \vec{r}_d) \quad (5.1)$$

The incident electric field due to this current source may be expressed in terms of plane wave spectrum as in (5.2) [39].

$$\vec{E}_{inc}(\vec{r}, \vec{r}_d) = \frac{-j}{8\pi^2} \iint_{-\infty}^{+\infty} \frac{1}{k_z} \vec{G}(\vec{k}_\rho) \cdot \hat{a}_j e^{-j[k_x(x-x_d) + k_y(y-y_d) + k_z|z-z_d|]} dk_x dk_y \quad (5.2)$$

Since the formulation starts with this expansion, similar to the plane wave expansion method summarized in section 2.2.1, some of the parameters which have already been defined in that section will be repeated here for the sake of completeness. $\vec{G}(\vec{k}_\rho)$ is a

dyad defined in (5.3) and the wavenumber expressions are given in (5.4).

$$\bar{\bar{G}}(\vec{k}_\rho) = [-j\omega\mu\bar{\bar{I}} - \frac{1}{j\omega\epsilon}\vec{k}\vec{k}] \quad (5.3)$$

$$\vec{k} = \hat{a}_x k_x + \hat{a}_y k_y \mp \hat{a}_z k_z \quad ; \quad \vec{k}_\rho = \hat{a}_x k_x + \hat{a}_y k_y \quad (5.4)$$

The "minus (plus)" sign is used when the observation point is below (above) the source point. For the problem we focus on, the aperiodic source is above the periodic structure and we are interested in the plane waves incident on the periodic structure. Thus, for the incident plane waves, observation point is below the source point and hence the "minus" sign is used in the wavenumber definition. When dealing with the reflected plane waves from the periodic structure, the observation point is above the source (surface currents on the periodic scatterers) point and thus a "plus" sign is used in the wavenumber definition.

Incident electric field is a continuum of plane waves of the form given by equations (5.5) to (5.7).

$$\vec{E}_{inc}^{PW}(\vec{r}, \vec{r}_d, \vec{k}_\rho) = \vec{E}_{pwi}(\vec{r}, \vec{r}_d, \vec{k}_\rho) e^{-j[k_x x + k_y y - k_z z]} \quad (5.5)$$

$$\vec{E}_{pwi}(\vec{k}_\rho, \vec{r}_d) = \bar{\bar{G}}(\vec{k}_\rho) \cdot \hat{a}_j W_{inc}(\vec{k}_\rho, \vec{r}_d) \quad (5.6)$$

$$W_{inc}(\vec{k}_\rho, \vec{r}_d) = \frac{-j}{8\pi^2} \frac{1}{k_z} e^{j[k_x x_d + k_y y_d - k_z z_d]} \quad (5.7)$$

In this approach, S-Parameters of the periodic structure will be utilized. Thus, the incident plane waves should be decomposed into TE and TM modes. In order to do this, it is meaningful to remind the unit electric field vectors for TE and TM polarizations which were defined in (3.4) to (3.6) for any Floquet mode. Since we limit our

attention to fundamental modes, they are simplified to the following expressions:

$$\hat{e}_{te}(\vec{k}_\rho) = \hat{a}_x \frac{k_y}{k_\rho} + \hat{a}_y \frac{-k_x}{k_\rho} \quad (5.8)$$

$$\hat{e}_{tmi}(\vec{k}_\rho) = \hat{a}_x \frac{-k_x k_z}{k_\rho k_s} + \hat{a}_y \frac{-k_y k_z}{k_\rho k_s} + \hat{a}_z \frac{-k_\rho}{k_s} \quad (5.9)$$

$$\hat{e}_{tmr}(\vec{k}_\rho) = \hat{a}_x \frac{-k_x k_z}{k_\rho k_s} + \hat{a}_y \frac{-k_y k_z}{k_\rho k_s} + \hat{a}_z \frac{k_\rho}{k_s} \quad (5.10)$$

All incident plane waves can be decomposed into TE and TM components as:

$$\vec{E}_{pwi}(\vec{k}_\rho, \vec{r}_d) = E_{te}(\vec{k}_\rho, \vec{r}_d) \hat{e}_{te}(\vec{k}_\rho) + E_{tm}(\vec{k}_\rho, \vec{r}_d) \hat{e}_{tmi}(\vec{k}_\rho) \quad (5.11)$$

E_{te} and E_{tmi} can be obtained simply by scalar multiplication of \vec{E}_{pwi} with \hat{e}_{te} and \hat{e}_{tmi} , respectively, following the fact that $\hat{e}_{te} \cdot \hat{e}_{te} = \hat{e}_{tmi} \cdot \hat{e}_{tmi} = 1$ and $\hat{e}_{te} \cdot \hat{e}_{tmi} = 0$.

$$E_{te,tmi}(\vec{k}_\rho, \vec{r}_d) = \vec{E}_{pwi}(\vec{k}_\rho, \vec{r}_d) \cdot \hat{e}_{te,tmi}(\vec{k}_\rho) \quad (5.12)$$

$$E_{te,tmi}(\vec{k}_\rho, \vec{r}_d) = (\vec{G}(\vec{k}_t) \cdot \hat{a}_j) \cdot \hat{e}_{te,tmi}(\vec{k}_\rho) W_{inc}(\vec{k}_\rho, \vec{r}_d) \quad (5.13)$$

$$E_{te,tmi}(\vec{k}_\rho, \vec{r}_d) = [-j\omega\mu\vec{I} - \frac{1}{j\omega\epsilon} \vec{k}\vec{k}] \cdot \hat{a}_j \cdot \hat{e}_{te,tmi}(\vec{k}_\rho) W_{inc}(\vec{k}_\rho, \vec{r}_d) \quad (5.14)$$

Since field vectors are orthogonal to propagation direction, $\vec{k} \cdot \hat{e}_{te,tmi} = 0$ which yields:

$$E_{te,tmi}(\vec{k}_\rho, \vec{r}_d) = -j\omega\mu \hat{a}_j \cdot \hat{e}_{te,tmi}(\vec{k}_\rho) W_{inc}(\vec{k}_\rho, \vec{r}_d) \quad (5.15)$$

If the dipole source is x oriented, $\hat{a}_j = \hat{a}_x$ and

$$E_{te}^x(\vec{k}_\rho, \vec{r}_d) = -j\omega\mu \frac{k_y}{k_\rho} W_{inc}(\vec{k}_\rho, \vec{r}_d) \quad (5.16)$$

$$E_{te}^x(\vec{k}_\rho, \vec{r}_d) = -\frac{\omega\mu}{8\pi^2} \frac{k_y}{k_z k_\rho} e^{j[k_x x_d + k_y y_d - k_z z_d]} \quad (5.17)$$

$$E_{tmi}^x(\vec{k}_\rho, \vec{r}_d) = E_{tmr}^x(\vec{k}_\rho, \vec{r}_d) = j\omega\mu \frac{k_x k_z}{k_\rho k_s} W_{inc}(\vec{k}_\rho, \vec{r}_d) \quad (5.18)$$

$$E_{tmi}^x(\vec{k}_\rho, \vec{r}_d) = E_{tmr}^x(\vec{k}_\rho, \vec{r}_d) = \frac{\omega\mu}{8\pi^2} \frac{k_x}{k_\rho k_s} e^{j[k_x x_d + k_y y_d - k_z z_d]} \quad (5.19)$$

If the dipole source is y oriented, $\hat{a}_j = \hat{a}_y$ and

$$E_{te}^y(\vec{k}_\rho, \vec{r}_d) = j\omega\mu \frac{k_x}{k_\rho} W_{inc}(\vec{k}_\rho, \vec{r}_d) \quad (5.20)$$

$$E_{te}^y(\vec{k}_\rho, \vec{r}_d) = \frac{\omega\mu}{8\pi^2} \frac{k_x}{k_z k_\rho} e^{j[k_x x_d + k_y y_d - k_z z_d]} \quad (5.21)$$

$$E_{tmi}^y(\vec{k}_\rho, \vec{r}_d) = E_{tmr}^y(\vec{k}_\rho, \vec{r}_d) = j\omega\mu \frac{k_y k_z}{k_\rho k_s} W_{inc}(\vec{k}_\rho, \vec{r}_d) \quad (5.22)$$

$$E_{tmi}^y(\vec{k}_\rho, \vec{r}_d) = E_{tmr}^y(\vec{k}_\rho, \vec{r}_d) = \frac{\omega\mu}{8\pi^2} \frac{k_y}{k_\rho k_s} e^{j[k_x x_d + k_y y_d - k_z z_d]} \quad (5.23)$$

If the dipole source is z oriented, $\hat{a}_j = \hat{a}_z$ and

$$E_{te}^z(\vec{k}_\rho, \vec{r}_d) = 0 \quad (5.24)$$

$$E_{tmi}^z(\vec{k}_\rho, \vec{r}_d) = -E_{tmr}^z(\vec{k}_\rho, \vec{r}_d) = j\omega\mu \frac{k_\rho}{k_s} W_{inc}(\vec{k}_\rho, \vec{r}_d) \quad (5.25)$$

$$E_{tmi}^z(\vec{k}_\rho, \vec{r}_d) = -E_{tmr}^z(\vec{k}_\rho, \vec{r}_d) = \frac{\omega\mu}{8\pi^2} \frac{k_\rho}{k_z k_s} e^{j[k_x x_d + k_y y_d - k_z z_d]} \quad (5.26)$$

By using the unit TE and TM vectors as incident plane waves, S-Parameters of the periodic structure are calculated by solving the MPIE with MoM as described in Chapter 3.

E_{te} , E_{tmi} and E_{tmr} values in (5.16) - (5.26) are utilized together with the calculated S-parameters of the periodic structure to compute TE and TM polarized reflected waves. TE and TM unit vector definitions are used to obtain the electric field components due to a dipole source above the periodic structure.

For an x directed unit electric dipole, electric field components (for the fundamental mode) at an arbitrary point above the surface can be found by the expressions:

$$E_{xx}(\vec{r}_o, \vec{r}_d) = \int_{-\infty}^{+\infty} \left[E_{te}^x(\vec{k}_\rho, \vec{r}_d) S_{11}(\vec{k}_\rho) \frac{k_y}{k_\rho} + E_{te}^x(\vec{k}_\rho, \vec{r}_d) S_{21}(\vec{k}_\rho) \frac{-k_x k_z}{k_\rho k_s} \right. \\ \left. + E_{tmi}^x(\vec{k}_\rho, \vec{r}_d) S_{12}(\vec{k}_\rho) \frac{k_y}{k_\rho} + E_{tmi}^x(\vec{k}_\rho, \vec{r}_d) S_{22}(\vec{k}_\rho) \frac{-k_x k_z}{k_\rho k_s} \right] \\ \times e^{-jk_x x_o} e^{-jk_y y_o} e^{-jk_z z_o} dk_x dk_y \quad (5.27)$$

$$E_{xx}(\vec{r}_o, \vec{r}_d) = \frac{\omega\mu}{8\pi^2} \int_{-\infty}^{+\infty} \int_{-\infty}^{+\infty} \left\{ dk_x dk_y e^{-jk_x(x_o-x_d)} e^{-jk_y(y_o-y_d)} \frac{e^{-jk_z(z_o+z_d)}}{k_z} \right. \\ \left. \times \left[-\frac{k_y^2}{k_\rho^2} S_{11}(\vec{k}_\rho) + \frac{k_x k_y k_z}{k_s k_\rho^2} S_{21}(\vec{k}_\rho) + \frac{k_x k_y k_z}{k_s k_\rho^2} S_{12}(\vec{k}_\rho) - \frac{k_x^2 k_z^2}{k_s^2 k_\rho^2} S_{22}(\vec{k}_\rho) \right] \right\} \quad (5.28)$$

$$E_{yx}(\vec{r}_o, \vec{r}_d) = \int_{-\infty}^{+\infty} \left[E_{te}^x(\vec{k}_\rho, \vec{r}_d) S_{11}(\vec{k}_\rho) \frac{-k_x}{k_\rho} + E_{te}^x(\vec{k}_\rho, \vec{r}_d) S_{21}(\vec{k}_\rho) \frac{-k_y k_z}{k_\rho k_s} \right. \\ \left. + E_{tmi}^x(\vec{k}_\rho, \vec{r}_d) S_{12}(\vec{k}_\rho) \frac{-k_x}{k_\rho} + E_{tmi}^x(\vec{k}_\rho, \vec{r}_d) S_{22}(\vec{k}_\rho) \frac{-k_y k_z}{k_\rho k_s} \right] \\ \times e^{-jk_x x_o} e^{-jk_y y_o} e^{-jk_z z_o} dk_x dk_y \quad (5.29)$$

$$E_{yx}(\vec{r}_o, \vec{r}_d) = \frac{\omega\mu}{8\pi^2} \int_{-\infty}^{+\infty} \int_{-\infty}^{+\infty} \left\{ dk_x dk_y e^{-jk_x(x_o-x_d)} e^{-jk_y(y_o-y_d)} \frac{e^{-jk_z(z_o+z_d)}}{k_z} \right. \\ \left. \times \left[\frac{k_x k_y}{k_\rho^2} S_{11}(\vec{k}_\rho) + \frac{k_y^2 k_z}{k_s k_\rho^2} S_{21}(\vec{k}_\rho) - \frac{k_x^2 k_z}{k_s k_\rho^2} S_{12}(\vec{k}_\rho) - \frac{k_x k_y k_z^2}{k_s^2 k_\rho^2} S_{22}(\vec{k}_\rho) \right] \right\} \quad (5.30)$$

$$E_{zx}(\vec{r}_o, \vec{r}_d) = \int_{-\infty}^{+\infty} \left[E_{te}^x(\vec{k}_\rho, \vec{r}_d) S_{21}(\vec{k}_\rho) \frac{k_\rho}{k_s} + E_{tmi}^x(\vec{k}_\rho, \vec{r}_d) S_{22}(\vec{k}_\rho) \frac{k_\rho}{k_s} \right] \times e^{-jk_x x_o} e^{-jk_y y_o} e^{-jk_z z_o} dk_x dk_y \quad (5.31)$$

$$E_{zx}(\vec{r}_o, \vec{r}_d) = \frac{\omega\mu}{8\pi^2} \int_{-\infty}^{+\infty} \left\{ dk_x dk_y e^{-jk_x(x_o-x_d)} e^{-jk_y(y_o-y_d)} \frac{e^{-jk_z(z_o+z_d)}}{k_z} \times \left[-\frac{k_y}{k_s} S_{21}(\vec{k}_\rho) + \frac{k_x k_z}{k_s^2} S_{22}(\vec{k}_\rho) \right] \right\} \quad (5.32)$$

For a y directed unit electric dipole, electric field components at an arbitrary point above the surface can be found by the expressions:

$$E_{xy}(\vec{r}_o, \vec{r}_d) = \int_{-\infty}^{+\infty} \left[E_{te}^y(\vec{k}_\rho, \vec{r}_d) S_{11}(\vec{k}_\rho) \frac{k_y}{k_\rho} + E_{te}^y(\vec{k}_\rho, \vec{r}_d) S_{21}(\vec{k}_\rho) \frac{-k_x k_z}{k_\rho k_s} + E_{tmi}^y(\vec{k}_\rho, \vec{r}_d) S_{12}(\vec{k}_\rho) \frac{k_y}{k_\rho} + E_{tmi}^y(\vec{k}_\rho, \vec{r}_d) S_{22}(\vec{k}_\rho) \frac{-k_x k_z}{k_\rho k_s} \right] \times e^{-jk_x x_o} e^{-jk_y y_o} e^{-jk_z z_o} dk_x dk_y \quad (5.33)$$

$$E_{xy}(\vec{r}_o, \vec{r}_d) = \frac{\omega\mu}{8\pi^2} \int_{-\infty}^{+\infty} \left\{ dk_x dk_y e^{-jk_x(x_o-x_d)} e^{-jk_y(y_o-y_d)} \frac{e^{-jk_z(z_o+z_d)}}{k_z} \times \left[\frac{k_x k_y}{k_\rho^2} S_{11}(\vec{k}_\rho) - \frac{k_x^2 k_z}{k_s k_\rho^2} S_{21}(\vec{k}_\rho) + \frac{k_y^2 k_z}{k_s k_\rho^2} S_{12}(\vec{k}_\rho) - \frac{k_x k_y k_z^2}{k_s^2 k_\rho^2} S_{22}(\vec{k}_\rho) \right] \right\} \quad (5.34)$$

$$E_{yy}(\vec{r}_o, \vec{r}_d) = \int_{-\infty}^{+\infty} \left[E_{te}^y(\vec{k}_\rho, \vec{r}_d) S_{11}(\vec{k}_\rho) \frac{-k_x}{k_\rho} + E_{te}^y(\vec{k}_\rho, \vec{r}_d) S_{21}(\vec{k}_\rho) \frac{-k_y k_z}{k_\rho k_s} + E_{tmi}^y(\vec{k}_\rho, \vec{r}_d) S_{12}(\vec{k}_\rho) \frac{-k_x}{k_\rho} + E_{tmi}^y(\vec{k}_\rho, \vec{r}_d) S_{22}(\vec{k}_\rho) \frac{-k_y k_z}{k_\rho k_s} \right] \times e^{-jk_x x_o} e^{-jk_y y_o} e^{-jk_z z_o} dk_x dk_y \quad (5.35)$$

$$\begin{aligned}
E_{yy}(\vec{r}_o, \vec{r}_d) &= \frac{\omega\mu}{8\pi^2} \iint_{-\infty}^{+\infty} \left\{ dk_x dk_y e^{-jk_x(x_o-x_d)} e^{-jk_y(y_o-y_d)} \frac{e^{-jk_z(z_o+z_d)}}{k_z} \right. \\
&\times \left. \left[-\frac{k_x^2}{k_\rho^2} S_{11}(\vec{k}_\rho) - \frac{k_x k_y k_z}{k_s k_\rho^2} S_{21}(\vec{k}_\rho) - \frac{k_x k_y k_z}{k_s k_\rho^2} S_{12}(\vec{k}_\rho) - \frac{k_y^2 k_z^2}{k_s^2 k_\rho^2} S_{22}(\vec{k}_\rho) \right] \right\}
\end{aligned} \tag{5.36}$$

$$\begin{aligned}
E_{zy}(\vec{r}_o, \vec{r}_d) &= \iint_{-\infty}^{+\infty} \left[E_{te}^y(\vec{k}_\rho, \vec{r}_d) S_{21}(\vec{k}_\rho) \frac{k_\rho}{k_s} + E_{tmi}^y(\vec{k}_\rho, \vec{r}_d) S_{22}(\vec{k}_\rho) \frac{k_\rho}{k_s} \right] \\
&\times e^{-jk_x x_o} e^{-jk_y y_o} e^{-jk_z z_o} dk_x dk_y
\end{aligned} \tag{5.37}$$

$$\begin{aligned}
E_{zy}(\vec{r}_o, \vec{r}_d) &= \frac{\omega\mu}{8\pi^2} \iint_{-\infty}^{+\infty} \left\{ dk_x dk_y e^{-jk_x(x_o-x_d)} e^{-jk_y(y_o-y_d)} \frac{e^{-jk_z(z_o+z_d)}}{k_z} \right. \\
&\times \left. \left[\frac{k_x}{k_s} S_{21}(\vec{k}_\rho) + \frac{k_y k_z}{k_s^2} S_{22}(\vec{k}_\rho) \right] \right\}
\end{aligned} \tag{5.38}$$

For a z directed unit electric dipole, electric field components at an arbitrary point above the surface can be found by the expressions:

$$\begin{aligned}
E_{xz}(\vec{r}_o, \vec{r}_d) &= \iint_{-\infty}^{+\infty} \left[E_{te}^z(\vec{k}_\rho, \vec{r}_d) S_{11}(\vec{k}_\rho) \frac{k_y}{k_\rho} + E_{te}^z(\vec{k}_\rho, \vec{r}_d) S_{21}(\vec{k}_\rho) \frac{-k_x k_z}{k_\rho k_s} \right. \\
&+ E_{tmi}^z(\vec{k}_\rho, \vec{r}_d) S_{12}(\vec{k}_\rho) \frac{k_y}{k_\rho} + E_{tmi}^z(\vec{k}_\rho, \vec{r}_d) S_{22}(\vec{k}_\rho) \frac{-k_x k_z}{k_\rho k_s} \left. \right] \\
&\times e^{-jk_x x_o} e^{-jk_y y_o} e^{-jk_z z_o} dk_x dk_y
\end{aligned} \tag{5.39}$$

$$\begin{aligned}
E_{xz}(\vec{r}_o, \vec{r}_d) &= \frac{\omega\mu}{8\pi^2} \iint_{-\infty}^{+\infty} \left\{ dk_x dk_y e^{-jk_x(x_o-x_d)} e^{-jk_y(y_o-y_d)} \frac{e^{-jk_z(z_o+z_d)}}{k_z} \right. \\
&\times \left. \left[\frac{k_y}{k_s} S_{12}(\vec{k}_\rho) - \frac{k_x k_z}{k_s^2} S_{22}(\vec{k}_\rho) \right] \right\}
\end{aligned} \tag{5.40}$$

$$\begin{aligned}
E_{yz}(\vec{r}_o, \vec{r}_d) = & \int_{-\infty}^{+\infty} \int_{-\infty}^{+\infty} \left[E_{te}^z(\vec{k}_\rho, \vec{r}_d) S_{11}(\vec{k}_\rho) \frac{-k_x}{k_\rho} + E_{te}^z(\vec{k}_\rho, \vec{r}_d) S_{21}(\vec{k}_\rho) \frac{-k_y k_z}{k_\rho k_s} \right. \\
& \left. + E_{tmi}^z(\vec{k}_\rho, \vec{r}_d) S_{12}(\vec{k}_\rho) \frac{-k_x}{k_\rho} + E_{tmi}^z(\vec{k}_\rho, \vec{r}_d) S_{22}(\vec{k}_\rho) \frac{-k_y k_z}{k_\rho k_s} \right] \\
& \times e^{-jk_x x_o} e^{-jk_y y_o} e^{-jk_z z_o} dk_x dk_y
\end{aligned} \tag{5.41}$$

$$\begin{aligned}
E_{yz}(\vec{r}_o, \vec{r}_d) = & \frac{\omega\mu}{8\pi^2} \int_{-\infty}^{+\infty} \int_{-\infty}^{+\infty} \left\{ dk_x dk_y e^{-jk_x(x_o-x_d)} e^{-jk_y(y_o-y_d)} \frac{e^{-jk_z(z_o+z_d)}}{k_z} \right. \\
& \left. \times \left[-\frac{k_x}{k_s} S_{12}(\vec{k}_\rho) - \frac{k_y k_z}{k_s^2} S_{22}(\vec{k}_\rho) \right] \right\}
\end{aligned} \tag{5.42}$$

$$\begin{aligned}
E_{zz}(\vec{r}_o, \vec{r}_d) = & \int_{-\infty}^{+\infty} \int_{-\infty}^{+\infty} \left[E_{te}^z(\vec{k}_\rho, \vec{r}_d) S_{21}(\vec{k}_\rho) \frac{k_\rho}{k_s} + E_{tmi}^z(\vec{k}_\rho, \vec{r}_d) S_{22}(\vec{k}_\rho) \frac{k_\rho}{k_s} \right] \\
& \times e^{-jk_x x_o} e^{-jk_y y_o} e^{-jk_z z_o} dk_x dk_y
\end{aligned} \tag{5.43}$$

$$\begin{aligned}
E_{zz}(\vec{r}_o, \vec{r}_d) = & \frac{\omega\mu}{8\pi^2} \int_{-\infty}^{+\infty} \int_{-\infty}^{+\infty} \left\{ dk_x dk_y e^{-jk_x(x_o-x_d)} e^{-jk_y(y_o-y_d)} \frac{e^{-jk_z(z_o+z_d)}}{k_z} \right. \\
& \left. \times \left[\frac{k_\rho^2}{k_s^2} S_{22}(\vec{k}_\rho) \right] \right\}
\end{aligned} \tag{5.44}$$

The electric field components will be analyzed further to obtain closed-form expressions for the contributions from each S-Parameters. Some of these expressions will be derived in detail and others will be written directly by observing the similarities between the expressions of different electric field components. This analysis can best be performed in cylindrical coordinates. Thus we need a change of variables defined as follows:

$$\begin{aligned}
k_x &= k_\rho \cos(\phi) \quad ; \quad k_y = k_\rho \sin(\phi) \\
x_o - x_d &= \rho \cos(\Psi) \quad ; \quad y_o - y_d = \rho \sin(\Psi) \\
dk_x dk_y &= k_\rho dk_\rho d\phi
\end{aligned} \tag{5.45}$$

At this point, we limit our attention to the case of circularly symmetric structures whose S-Parameters depend only on k_ρ and are independent of ϕ . For the derivation of the closed-form expressions, we assume a y oriented dipole and start with the y component of the scattered electric field. By using (5.36) and (5.45), the contribution to $E_{yy}(\vec{r}_o, \vec{r}_d)$ from $S_{11}(k_\rho)$ can be written in cylindrical coordinates as in (5.47), but before that, the form in Cartesian coordinates is repeated in (5.46) as a reminder :

$$E_{yy}^{S_{11}}(\vec{r}_o, \vec{r}_d) = -\frac{\omega\mu}{8\pi^2} \iint_{-\infty}^{+\infty} \left\{ dk_x dk_y e^{-jk_x(x_o-x_d)} e^{-jk_y(y_o-y_d)} \frac{e^{-jk_z(z_o+z_d)}}{k_z} \right. \\ \left. \times \frac{k_x^2}{k_\rho^2} S_{11}(k_\rho) \right\} \quad (5.46)$$

$$E_{yy}^{S_{11}}(\vec{r}_o, \vec{r}_d) = -\frac{j\omega\mu}{8\pi} \int_0^{+\infty} k_\rho dk_\rho \frac{e^{-jk_z(z_o+z_d)}}{jk_z} S_{11}(k_\rho) \\ \times \frac{1}{\pi} \int_0^{2\pi} d\phi \cos^2(\phi) e^{-jk_\rho \rho \cos(\phi-\Psi)} \quad (5.47)$$

The integral w.r.t ϕ (let's name it as I) can be divided into two parts ($I = I_1 + I_2$) as follows, by using the trigonometric identity for square of cosine function:

$$I_1 = \frac{1}{2\pi} \int_0^{2\pi} d\phi e^{-jk_\rho \rho \cos(\phi-\Psi)} = J_0(k_\rho \rho) \quad (5.48)$$

$$I_2 = \frac{1}{2\pi} \int_0^{2\pi} d\phi \cos(2\phi) e^{-jk_\rho \rho \cos(\phi-\Psi)} \quad (5.49)$$

I_2 can be decomposed further into two parts ($I_2 = I_{21} + I_{22}$) to make it more suitable for Bessel identities:

$$I_{21} = \frac{1}{4\pi} \int_0^{2\pi} d\phi e^{j2\phi} e^{-jk_\rho \rho \cos(\phi-\Psi)} \quad ; \quad I_{22} = \frac{1}{4\pi} \int_0^{2\pi} d\phi e^{-j2\phi} e^{-jk_\rho \rho \cos(\phi-\Psi)} \quad (5.50)$$

We make a change of variable as $\phi - \Psi = \psi$ to write I_{21} and I_{22} as follows:

$$I_{21} = \frac{e^{j2\Psi}}{4\pi} \int_0^{2\pi} d\psi e^{j2\psi} e^{-jk_\rho\rho \cos(\psi)} \quad ; \quad I_{22} = \frac{e^{-j2\Psi}}{4\pi} \int_0^{2\pi} d\psi e^{-j2\psi} e^{-jk_\rho\rho \cos(\psi)} \quad (5.51)$$

Both integrals (excluding the factors outside the integration) above are actually $-2\pi J_2(k_\rho\rho)$ which can be verified by Bessel identities (A.6). Thus:

$$I_2 = I_{21} + I_{22} = -\cos(2\Psi) J_2(k_\rho\rho) \quad (5.52)$$

From the recurrence relation of Bessel functions (A.7) we know that:

$$J_2(k_\rho\rho) = \frac{2}{k_\rho\rho} J_1(k_\rho\rho) - J_0(k_\rho\rho) \quad (5.53)$$

$$I_2 = I_{2a} + I_{2b}$$

$$I_{2a} = \cos(2\Psi) J_0(k_\rho\rho) \quad (5.54)$$

$$I_{2b} = -\frac{2\cos(2\Psi)}{\rho} \frac{1}{k_\rho} J_1(k_\rho\rho)$$

Now, we focus on the contributions from I_1 , I_{2a} and I_{2b} separately.

$$E_{yy}^{S_{11}:I_1}(\vec{r}_o, \vec{r}_d) = -\frac{j\omega\mu}{8\pi} \int_0^{+\infty} k_\rho dk_\rho \frac{e^{-jk_z(z_o+z_d)}}{jk_z} S_{11}(k_\rho) J_0(k_\rho\rho) \quad (5.55)$$

In order to be able to use the Sommerfeld Identity (A.3) and obtain the result of integration in a closed form, we approximate $S_{11}(k_\rho)$ in terms of complex exponentials by utilizing Discrete Complex Image Method (DCIM) as:

$$S_{11}(k_\rho) = \sum_{k=1}^{N_1} B_{1k} e^{-jk_z\gamma_{1k}} \quad (5.56)$$

Applying the Sommerfeld Identity gives us the contribution in a finite summation form as:

$$E_{yy}^{S_{11}:I_1}(\vec{r}_o, \vec{r}_d) = -\frac{j\omega\mu}{8\pi} \sum_{k=1}^{N_1} B_{1k} \frac{e^{-jk_s r_{1k}}}{r_{1k}} \quad (5.57)$$

where r_{1k} is defined as:

$$r_{1k} = \sqrt{(x_o - x_d)^2 + (y_o - y_d)^2 + (z_o + z_d + \gamma_{1k})^2} \quad (5.58)$$

Since I_{2a} is just the scaled version of I_1 by $\cos(2\Psi)$, the contribution from I_{2a} can be directly written as:

$$E_{yy}^{S_{11}:I_{2a}}(\vec{r}_o, \vec{r}_d) = -\frac{j\omega\mu}{8\pi} \cos(2\Psi) \sum_{k=1}^{N_1} B_{1k} \frac{e^{-jk_s r_{1k}}}{r_{1k}} \quad (5.59)$$

Considering I_{2b} , we use (5.54) and (5.47) to obtain the integral as:

$$E_{yy}^{S_{11}:I_{2b}}(\vec{r}_o, \vec{r}_d) = \frac{j\omega\mu}{8\pi} \frac{2 \cos(2\Psi)}{\rho} \int_0^{+\infty} \frac{e^{-jk_z(z_o+z_d)}}{jk_z} \frac{S_{11}(k_\rho)}{k_\rho^2} J_1(k_\rho \rho) k_\rho^2 dk_\rho \quad (5.60)$$

This integral resembles the derivative form of Sommerfeld Identity (A.4) and in order to use this identity, we should again use DCIM to make a complex image approximation as:

$$\frac{S_{11}(k_\rho)}{k_\rho^2} = \sum_{k=1}^{N_{a1}} B_{a1k} e^{-jk_z \gamma_{a1k}} \quad (5.61)$$

By using this approximation in (5.60) and utilizing the derivative form of Sommerfeld Identity gives us the contribution from I_{2b} in a finite summation form as:

$$E_{yy}^{S_{11}:I_{2b}}(\vec{r}_o, \vec{r}_d) = \frac{j\omega\mu}{4\pi} \cos(2\Psi) \sum_{k=1}^{N_{a1}} B_{a1k} (1 + jk_s r_{a1k}) \frac{e^{-jk_s r_{a1k}}}{r_{a1k}^3} \quad (5.62)$$

where r_{a1k} is defined as:

$$r_{a1k} = \sqrt{(x_o - x_d)^2 + (y_o - y_d)^2 + (z_o + z_d + \gamma_{a1k})^2} \quad (5.63)$$

Now, let's analyze the contribution of $S_{21}(k_\rho)$ to $E_{yy}(\vec{r}_o, \vec{r}_d)$. By using (5.36) and (5.45), this contribution can be written in Cartesian coordinates as in (5.64) and in polar coordinates as shown in (5.65):

$$E_{yy}^{S_{21}}(\vec{r}_o, \vec{r}_d) = -\frac{\omega\mu}{8\pi^2} \int_{-\infty}^{+\infty} \int_{-\infty}^{+\infty} \left\{ dk_x dk_y e^{-jk_x(x_o-x_d)} e^{-jk_y(y_o-y_d)} \frac{e^{-jk_z(z_o+z_d)}}{k_z} \right. \\ \left. \times \frac{k_x k_y k_z}{k_s k_\rho^2} S_{21}(\vec{k}_\rho) \right\} \quad (5.64)$$

$$E_{yy}^{S_{21}}(\vec{r}_o, \vec{r}_d) = -\frac{j\omega\mu}{8\pi} \int_0^{+\infty} k_\rho dk_\rho \frac{e^{-jk_z(z_o+z_d)}}{jk_z} \frac{S_{21}(k_\rho) k_z}{k_s} \\ \times \frac{1}{\pi} \int_0^{2\pi} d\phi \cos(\phi) \sin(\phi) e^{-jk_\rho \rho \cos(\phi-\Psi)} \quad (5.65)$$

We take a closer look at the integral with $d\phi$ (named as I):

$$I = \frac{1}{2\pi} \int_0^{2\pi} d\phi \sin(2\phi) e^{-jk_\rho \rho \cos(\phi-\Psi)} \\ I = \frac{1}{j4\pi} \int_0^{2\pi} d\phi e^{j2\phi} e^{-jk_\rho \rho \cos(\phi-\Psi)} - \frac{1}{j4\pi} \int_0^{2\pi} d\phi e^{-j2\phi} e^{-jk_\rho \rho \cos(\phi-\Psi)} \quad (5.66)$$

We make a change of variable as $\phi - \Psi = \psi$ to write I as follows:

$$I = \frac{e^{j2\Psi}}{j4\pi} \int_0^{2\pi} d\psi e^{j2\psi} e^{-jk_\rho \rho \cos(\psi)} - \frac{e^{-j2\Psi}}{j4\pi} \int_0^{2\pi} d\psi e^{-j2\psi} e^{-jk_\rho \rho \cos(\psi)} \quad (5.67)$$

Applying the Bessel integral identity (A.6) and the relations in (A.8), I is obtained as:

$$I = -\frac{e^{j2\Psi}}{j2} J_2(k_\rho \rho) + \frac{e^{-j2\Psi}}{j2} J_2(k_\rho \rho) = -\sin(2\Psi) J_2(k_\rho \rho) \quad (5.68)$$

It is decomposed into lower order Bessel functions by using the recurrence relations of Bessel functions (A.7) which yields:

$$I = I_a + I_b \quad (5.69)$$

$$I_a = \sin(2\Psi) J_0(k_\rho \rho) \quad ; \quad I_b = -\frac{2 \sin(2\Psi)}{\rho} \frac{1}{k_\rho} J_1(k_\rho \rho)$$

Using these expressions in (5.65), the contribution of I_a to $E_{yy}^{S_{21}}(\vec{r}_o, \vec{r}_d)$ is written as:

$$E_{yy}^{S_{21}:I_a}(\vec{r}_o, \vec{r}_d) = -\frac{j\omega\mu \sin(2\Psi)}{8\pi} \int_0^{+\infty} k_\rho dk_\rho \frac{e^{-jk_z(z_o+z_d)}}{jk_z} \frac{S_{21}(k_\rho)k_z}{k_s} J_0(k_\rho \rho) \quad (5.70)$$

Sommerfeld Identity can directly be used for this integration if we make the following modelling:

$$\frac{S_{21}(k_\rho)k_z}{k_s} = \sum_{k=1}^{N_2} B_{2k} e^{-jk_z \gamma_{2k}} \quad (5.71)$$

The final form of this contribution can now be written as a finite sum as follows:

$$E_{yy}^{S_{21}:I_a}(\vec{r}_o, \vec{r}_d) = -\frac{j\omega\mu}{8\pi} \sin(2\Psi) \sum_{k=1}^{N_2} B_{2k} \frac{e^{-jk_s r_{2k}}}{r_{2k}} \quad (5.72)$$

$$r_{2k} = \sqrt{(x_o - x_d)^2 + (y_o - y_d)^2 + (z_o + z_d + \gamma_{2k})^2} \quad (5.73)$$

The contribution of I_b is found by using (5.69) in (5.65):

$$E_{yy}^{S_{21}:I_b}(\vec{r}_o, \vec{r}_d) = \frac{j\omega\mu \sin(2\Psi)}{4\pi\rho} \int_0^{+\infty} \frac{e^{-jk_z(z_o+z_d)} S_{21}(k_\rho) k_z}{jk_z k_s k_\rho^2} J_1(k_\rho \rho) k_\rho^2 dk_\rho \quad (5.74)$$

Because of the Bessel function of order 1 in the integration, it would be suitable to make use of the derivative form of Sommerfeld Identity. In order for this to be possible, one should make the following approximation in terms of complex exponentials:

$$\frac{S_{21}(k_\rho) k_z}{k_s k_\rho^2} = \sum_{k=1}^{N_{a2}} B_{a2k} e^{-jk_z \gamma_{a2k}} \quad (5.75)$$

Using this approximation in (5.74) together with the derivative of Sommerfeld Identity yields the following finite summation in spatial domain:

$$E_{yy}^{S_{21}:I_b}(\vec{r}_o, \vec{r}_d) = \frac{j\omega\mu}{4\pi} \sin(2\Psi) \sum_{k=1}^{N_{a2}} B_{a2k} (1 + jk_s r_{a2k}) \frac{e^{-jk_s r_{a2k}}}{r_{a2k}^3} \quad (5.76)$$

$$r_{a2k} = \sqrt{(x_o - x_d)^2 + (y_o - y_d)^2 + (z_o + z_d + \gamma_{a2k})^2} \quad (5.77)$$

By observing (5.36) and noting that $S_{21} = S_{12}$ due to reciprocity, the contribution from S_{12} is exactly the same as the one from S_{21} . Thus,

$$E_{yy}^{S_{12}}(\vec{r}_o, \vec{r}_d) = E_{yy}^{S_{21}}(\vec{r}_o, \vec{r}_d) \quad (5.78)$$

The analysis of the contribution of $S_{22}(k_\rho)$ to $E_{yy}(\vec{r}_o, \vec{r}_d)$ starts by observing (5.36) and applying (5.45) to obtain the related contribution integral in polar coordinates as in (5.80). The contribution in Cartesian coordinates is recalled first in (5.79).

$$E_{yy}^{S_{22}}(\vec{r}_o, \vec{r}_d) = -\frac{\omega\mu}{8\pi^2} \iint_{-\infty}^{+\infty} \left\{ dk_x dk_y e^{-jk_x(x_o-x_d)} e^{-jk_y(y_o-y_d)} \frac{e^{-jk_z(z_o+z_d)}}{k_z} \right. \\ \left. \times \frac{k_y^2 k_z^2}{k_s^2 k_\rho^2} S_{22}(\vec{k}_\rho) \right\} \quad (5.79)$$

$$\begin{aligned}
E_{yy}^{S_{22}}(\vec{r}_o, \vec{r}_d) &= -\frac{j\omega\mu}{8\pi} \int_0^{+\infty} k_\rho dk_\rho \frac{e^{-jk_z(z_o+z_d)} S_{22}(k_\rho) k_z^2}{jk_z k_s^2} \\
&\times \frac{1}{\pi} \int_0^{2\pi} d\phi \sin^2(\phi) e^{-jk_\rho \rho \cos(\phi-\Psi)}
\end{aligned} \tag{5.80}$$

The integral w.r.t ϕ (lets name it as I) can be divided into two parts ($I = I_1 + I_2$) as follows, by using the trigonometric identity for square of sine function:

$$I_1 = \frac{1}{2\pi} \int_0^{2\pi} d\phi e^{-jk_\rho \rho \cos(\phi-\Psi)} = J_0(k_\rho \rho) \tag{5.81}$$

$$I_2 = -\frac{1}{2\pi} \int_0^{2\pi} d\phi \cos(2\phi) e^{-jk_\rho \rho \cos(\phi-\Psi)} \tag{5.82}$$

Note that I_2 in (5.82) is just the oppositely signed version of I_2 in (5.49). Thus,

$$\begin{aligned}
I_{2a} &= -\cos(2\Psi) J_0(k_\rho \rho) \\
I_{2b} &= \frac{2\cos(2\Psi)}{\rho} \frac{1}{k_\rho} J_1(k_\rho \rho)
\end{aligned} \tag{5.83}$$

Now, these expressions are used in (5.80) to obtain the contribution integrals. For I_1 , we have:

$$E_{yy}^{S_{22}:I_1}(\vec{r}_o, \vec{r}_d) = -\frac{j\omega\mu}{8\pi} \int_0^{+\infty} k_\rho dk_\rho \frac{e^{-jk_z(z_o+z_d)} S_{22}(k_\rho) k_z^2}{jk_z k_s^2} J_0(k_\rho \rho) \tag{5.84}$$

Utilizing DCIM, we make the following approximation:

$$\frac{S_{22}(k_\rho) k_z^2}{k_s^2} = \sum_{k=1}^{N_3} B_{3k} e^{-jk_z \gamma_{3k}} \tag{5.85}$$

Sommerfeld Identity is applied to obtain the final form as a finite summation:

$$E_{yy}^{S_{22}:I_1}(\vec{r}_o, \vec{r}_d) = -\frac{j\omega\mu}{8\pi} \sum_{k=1}^{N_3} B_{3k} \frac{e^{-jk_s r_{3k}}}{r_{3k}} \quad (5.86)$$

$$r_{3k} = \sqrt{(x_o - x_d)^2 + (y_o - y_d)^2 + (z_o + z_d + \gamma_{3k})^2} \quad (5.87)$$

Contribution of I_{2a} can be obtained simply by scaling (5.86) by $-\cos(2\Psi)$:

$$E_{yy}^{S_{22}:I_{2a}}(\vec{r}_o, \vec{r}_d) = \frac{j\omega\mu}{8\pi} \cos(2\Psi) \sum_{k=1}^{N_3} B_{3k} \frac{e^{-jk_s r_{3k}}}{r_{3k}} \quad (5.88)$$

For I_{2b} , we have the following integral:

$$E_{yy}^{S_{22}:I_{2b}}(\vec{r}_o, \vec{r}_d) = \frac{-j\omega\mu \cos(2\Psi)}{4\pi\rho} \int_0^{+\infty} \frac{e^{-jk_z(z_o+z_d)}}{jk_z} \frac{S_{22}(k_\rho)k_z^2}{k_\rho^2 k_s^2} J_1(k_\rho\rho) k_\rho^2 dk_\rho \quad (5.89)$$

We need a complex exponential approximation which is given as follows:

$$\frac{S_{22}(k_\rho)k_z^2}{k_s^2 k_\rho^2} = \sum_{k=1}^{N_{a3}} B_{a3k} e^{-jk_z \gamma_{a3k}} \quad (5.90)$$

Applying the derivative of Sommerfeld Identity yields a finite summation given as:

$$E_{yy}^{S_{22}:I_{2b}}(\vec{r}_o, \vec{r}_d) = -\frac{j\omega\mu}{4\pi} \cos(2\Psi) \sum_{k=1}^{N_{a3}} B_{a3k} (1 + jk_s r_{a3k}) \frac{e^{-jk_s r_{a3k}}}{r_{a3k}^3} \quad (5.91)$$

$$r_{a3k} = \sqrt{(x_o - x_d)^2 + (y_o - y_d)^2 + (z_o + z_d + \gamma_{a3k})^2} \quad (5.92)$$

We have completed the derivation of closed-form expressions for the y component of scattered electric field due to a y oriented electric dipole over the periodic structure. Derivation for the other transverse components (E_{xy} , E_{xx} and E_{yx}) are similar in form. Therefore, there is no need to write down each step in detail. By observing

the similarities and differences in the expressions for contributions of S-Parameters to the electric field components in equations (5.27) through (5.38), one can quickly determine the closed-form expressions for other transverse components. For E_{xy} , the resulting expressions are given below:

$$E_{xy}^{S_{11}}(\vec{r}_o, \vec{r}_d) = E_{xy}^{S_{11}:I_a}(\vec{r}_o, \vec{r}_d) + E_{xy}^{S_{11}:I_b}(\vec{r}_o, \vec{r}_d) \quad (5.93)$$

$$E_{xy}^{S_{11}:I_a}(\vec{r}_o, \vec{r}_d) = \frac{j\omega\mu}{8\pi} \sin(2\Psi) \sum_{k=1}^{N_1} B_{1k} \frac{e^{-jk_s r_{1k}}}{r_{1k}} \quad (5.94)$$

$$E_{xy}^{S_{11}:I_b}(\vec{r}_o, \vec{r}_d) = -\frac{j\omega\mu}{4\pi} \sin(2\Psi) \sum_{k=1}^{N_{a1}} B_{a1k} (1 + jk_s r_{a1k}) \frac{e^{-jk_s r_{a1k}}}{r_{a1k}^3} \quad (5.95)$$

$$E_{xy}^{S_{21}}(\vec{r}_o, \vec{r}_d) = E_{xy}^{S_{21}:I_1}(\vec{r}_o, \vec{r}_d) + E_{xy}^{S_{21}:I_{2a}}(\vec{r}_o, \vec{r}_d) + E_{xy}^{S_{21}:I_{2b}}(\vec{r}_o, \vec{r}_d) \quad (5.96)$$

$$E_{xy}^{S_{21}:I_1}(\vec{r}_o, \vec{r}_d) = -\frac{j\omega\mu}{8\pi} \sum_{k=1}^{N_2} B_{2k} \frac{e^{-jk_s r_{2k}}}{r_{2k}} \quad (5.97)$$

$$E_{xy}^{S_{21}:I_{2a}}(\vec{r}_o, \vec{r}_d) = -\frac{j\omega\mu}{8\pi} \cos(2\Psi) \sum_{k=1}^{N_2} B_{2k} \frac{e^{-jk_s r_{2k}}}{r_{2k}} \quad (5.98)$$

$$E_{xy}^{S_{21}:I_{2b}}(\vec{r}_o, \vec{r}_d) = \frac{j\omega\mu}{4\pi} \cos(2\Psi) \sum_{k=1}^{N_{a2}} B_{a2k} (1 + jk_s r_{a2k}) \frac{e^{-jk_s r_{a2k}}}{r_{a2k}^3} \quad (5.99)$$

$$E_{xy}^{S_{12}}(\vec{r}_o, \vec{r}_d) = E_{xy}^{S_{12}:I_1}(\vec{r}_o, \vec{r}_d) + E_{xy}^{S_{12}:I_{2a}}(\vec{r}_o, \vec{r}_d) + E_{xy}^{S_{12}:I_{2b}}(\vec{r}_o, \vec{r}_d) \quad (5.100)$$

$$\begin{aligned} E_{xy}^{S_{12}:I_1}(\vec{r}_o, \vec{r}_d) &= -E_{xy}^{S_{21}:I_1}(\vec{r}_o, \vec{r}_d) \\ E_{xy}^{S_{12}:I_{2a}}(\vec{r}_o, \vec{r}_d) &= E_{xy}^{S_{21}:I_{2a}}(\vec{r}_o, \vec{r}_d) \\ E_{xy}^{S_{12}:I_{2b}}(\vec{r}_o, \vec{r}_d) &= E_{xy}^{S_{21}:I_{2b}}(\vec{r}_o, \vec{r}_d) \end{aligned} \quad (5.101)$$

$$E_{xy}^{S_{22}}(\vec{r}_o, \vec{r}_d) = E_{xy}^{S_{22}:I_a}(\vec{r}_o, \vec{r}_d) + E_{xy}^{S_{22}:I_b}(\vec{r}_o, \vec{r}_d) \quad (5.102)$$

$$E_{xy}^{S22:Ia}(\vec{r}_o, \vec{r}_d) = -\frac{j\omega\mu}{8\pi} \sin(2\Psi) \sum_{k=1}^{N_3} B_{3k} \frac{e^{-jk_s r_{3k}}}{r_{3k}} \quad (5.103)$$

$$E_{xy}^{S22:Ib}(\vec{r}_o, \vec{r}_d) = \frac{j\omega\mu}{4\pi} \sin(2\Psi) \sum_{k=1}^{N_{a3}} B_{a3k} (1 + jk_s r_{a3k}) \frac{e^{-jk_s r_{a3k}}}{r_{a3k}^3} \quad (5.104)$$

For an x oriented dipole, expressions for the x component of the scattered field are given as:

$$E_{xx}^{S11}(\vec{r}_o, \vec{r}_d) = E_{xx}^{S11:I1}(\vec{r}_o, \vec{r}_d) + E_{xx}^{S11:I2a}(\vec{r}_o, \vec{r}_d) + E_{xx}^{S11:I2b}(\vec{r}_o, \vec{r}_d) \quad (5.105)$$

$$E_{xx}^{S11:I1}(\vec{r}_o, \vec{r}_d) = E_{yy}^{S11:I1}(\vec{r}_o, \vec{r}_d)$$

$$E_{xx}^{S11:I2a}(\vec{r}_o, \vec{r}_d) = -E_{yy}^{S11:I2a}(\vec{r}_o, \vec{r}_d) \quad (5.106)$$

$$E_{xx}^{S11:I2b}(\vec{r}_o, \vec{r}_d) = -E_{yy}^{S11:I2b}(\vec{r}_o, \vec{r}_d)$$

$$E_{xx}^{S21}(\vec{r}_o, \vec{r}_d) = E_{xx}^{S12}(\vec{r}_o, \vec{r}_d) = -E_{yy}^{S21}(\vec{r}_o, \vec{r}_d) \quad (5.107)$$

$$E_{xx}^{S22}(\vec{r}_o, \vec{r}_d) = E_{xx}^{S22:I1}(\vec{r}_o, \vec{r}_d) + E_{xx}^{S22:I2a}(\vec{r}_o, \vec{r}_d) + E_{xx}^{S22:I2b}(\vec{r}_o, \vec{r}_d) \quad (5.108)$$

$$E_{xx}^{S22:I1}(\vec{r}_o, \vec{r}_d) = E_{yy}^{S22:I1}(\vec{r}_o, \vec{r}_d)$$

$$E_{xx}^{S22:I2a}(\vec{r}_o, \vec{r}_d) = -E_{yy}^{S22:I2a}(\vec{r}_o, \vec{r}_d) \quad (5.109)$$

$$E_{xx}^{S22:I2b}(\vec{r}_o, \vec{r}_d) = -E_{yy}^{S22:I2b}(\vec{r}_o, \vec{r}_d)$$

For y component of the scattered electric field due to an x oriented dipole, we have the following equalities:

$$\begin{aligned} E_{yx}^{S11}(\vec{r}_o, \vec{r}_d) &= E_{xy}^{S11}(\vec{r}_o, \vec{r}_d) & ; & & E_{yx}^{S21}(\vec{r}_o, \vec{r}_d) &= E_{xy}^{S12}(\vec{r}_o, \vec{r}_d) \\ E_{yx}^{S12}(\vec{r}_o, \vec{r}_d) &= E_{xy}^{S21}(\vec{r}_o, \vec{r}_d) & ; & & E_{yx}^{S22}(\vec{r}_o, \vec{r}_d) &= E_{xy}^{S22}(\vec{r}_o, \vec{r}_d) \end{aligned} \quad (5.110)$$

We now turn our attention to vertical component of scattered electric field due to transversely oriented electric dipole over the scatterer structure. We assume a y

oriented dipole. If we observe equation (5.38), we can see that there are two S-Parameters contributing to $E_{zy}(\vec{r}_o, \vec{r}_d)$. Let's recall the contribution of S_{21} which is:

$$E_{zy}^{S_{21}}(\vec{r}_o, \vec{r}_d) = \frac{\omega\mu}{8\pi^2} \int_{-\infty}^{+\infty} \int_{-\infty}^{+\infty} \left\{ dk_x dk_y e^{-jk_x(x_o-x_d)} e^{-jk_y(y_o-y_d)} \frac{e^{-jk_z(z_o+z_d)}}{k_z} \right. \\ \left. \times \left[\frac{k_x}{k_s} S_{21}(k_\rho) \right] \right\} \quad (5.111)$$

Application of the coordinate change defined in (5.45) yields:

$$E_{zy}^{S_{21}}(\vec{r}_o, \vec{r}_d) = \frac{j\omega\mu}{8\pi} \int_0^{+\infty} k_\rho dk_\rho \frac{e^{-jk_z(z_o+z_d)} k_\rho}{jk_z k_s} S_{21}(k_\rho) \\ \times \frac{1}{\pi} \int_0^{2\pi} d\phi \cos(\phi) e^{-jk_\rho \rho \cos(\phi-\Psi)} \quad (5.112)$$

The $d\phi$ integration is decomposed as:

$$I = \frac{1}{\pi} \int_0^{2\pi} d\phi \cos(\phi) e^{-jk_\rho \rho \cos(\phi-\Psi)} = I_1 + I_2 \\ I_1 = \frac{1}{2\pi} \int_0^{2\pi} d\phi e^{j\phi} e^{-jk_\rho \rho \cos(\phi-\Psi)} \quad ; \quad I_2 = \frac{1}{2\pi} \int_0^{2\pi} d\phi e^{-j\phi} e^{-jk_\rho \rho \cos(\phi-\Psi)} \quad (5.113)$$

We make a change of variable as $\phi - \Psi = \psi$ to write I_1 and I_2 as follows:

$$I_1 = \frac{e^{j\Psi}}{2\pi} \int_0^{2\pi} d\psi e^{j\psi} e^{-jk_\rho \rho \cos(\psi)} \quad ; \quad I_2 = \frac{e^{-j\Psi}}{2\pi} \int_0^{2\pi} d\psi e^{-j\psi} e^{-jk_\rho \rho \cos(\psi)} \quad (5.114)$$

Bessel integral identity (A.6) and the identities in (A.8) are used to obtain the integration results in terms of Bessel function of order one as:

$$I_1 = -jJ_1(k_\rho \rho) e^{j\Psi} \quad ; \quad I_2 = -jJ_1(k_\rho \rho) e^{-j\Psi} \quad (5.115)$$

$$I = -j2 \cos(\Psi) J_1(k_\rho \rho) \quad (5.116)$$

Using (5.116) in equation (5.112) and organizing the terms inside the integrand yields the following integration which resembles the derivative of Sommerfeld Identity:

$$E_{zy}^{S_{21}}(\vec{r}_o, \vec{r}_d) = \frac{\omega\mu}{4\pi} \cos(\Psi) \int_0^{+\infty} \frac{e^{-jk_z(z_o+z_d)}}{jk_z} \frac{S_{21}(k_\rho)}{k_s} J_1(k_\rho \rho) k_\rho^2 dk_\rho \quad (5.117)$$

Following complex image approximation is made to be able to express the result of the integral in a closed form:

$$\frac{S_{21}(k_\rho)}{k_s} = \sum_{k=1}^{N_4} B_{4k} e^{-jk_z \gamma_{4k}} \quad (5.118)$$

Utilizing the derivative of Sommerfeld identity yields the following finite sum for $E_{zy}^{S_{21}}(\vec{r}_o, \vec{r}_d)$:

$$E_{zy}^{S_{21}}(\vec{r}_o, \vec{r}_d) = \frac{\omega\mu}{4\pi} \cos(\Psi) \rho \sum_{k=1}^{N_4} B_{4k} (1 + jk_s r_{4k}) \frac{e^{-jk_s r_{4k}}}{r_{4k}^3} \quad (5.119)$$

Since $\rho \cos(\Psi) = (x_o - x_d)$, we finally obtain:

$$E_{zy}^{S_{21}}(\vec{r}_o, \vec{r}_d) = \frac{\omega\mu}{4\pi} (x_o - x_d) \sum_{k=1}^{N_4} B_{4k} (1 + jk_s r_{4k}) \frac{e^{-jk_s r_{4k}}}{r_{4k}^3} \quad (5.120)$$

where r_{4k} is defined as:

$$r_{4k} = \sqrt{(x_o - x_d)^2 + (y_o - y_d)^2 + (z_o + z_d + \gamma_{4k})^2} \quad (5.121)$$

A similar derivation applies for the $E_{zy}^{S_{22}}(\vec{r}_o, \vec{r}_d)$ and it is found to be as:

$$E_{zy}^{S_{22}}(\vec{r}_o, \vec{r}_d) = \frac{\omega\mu}{4\pi} (y_o - y_d) \sum_{k=1}^{N_5} B_{5k} (1 + jk_s r_{5k}) \frac{e^{-jk_s r_{5k}}}{r_{5k}^3} \quad (5.122)$$

where the following complex image approximation is used:

$$\frac{S_{22}k_z}{k_s^2} = \sum_{k=1}^{N_5} B_{5k} e^{-jk_z \gamma_{5k}} \quad (5.123)$$

and r_{5k} is defined as:

$$r_{5k} = \sqrt{(x_o - x_d)^2 + (y_o - y_d)^2 + (z_o + z_d + \gamma_{5k})^2} \quad (5.124)$$

By using the similarities, expressions for $E_{zx}(\vec{r}_o, \vec{r}_d)$ can be found as follows:

$$E_{zx}^{S_{21}}(\vec{r}_o, \vec{r}_d) = -\frac{\omega\mu}{4\pi}(y_o - y_d) \sum_{k=1}^{N_4} B_{4k}(1 + jk_s r_{4k}) \frac{e^{-jk_s r_{4k}}}{r_{4k}^3} \quad (5.125)$$

$$E_{zx}^{S_{22}}(\vec{r}_o, \vec{r}_d) = \frac{\omega\mu}{4\pi}(x_o - x_d) \sum_{k=1}^{N_5} B_{5k}(1 + jk_s r_{5k}) \frac{e^{-jk_s r_{5k}}}{r_{5k}^3} \quad (5.126)$$

Now we take a look at the case of a vertical dipole over the scatterer. We deduce from the similarities of the corresponding expressions that:

$$\begin{aligned} E_{xz}(\vec{r}_o, \vec{r}_d) &= -E_{zx}(\vec{r}_o, \vec{r}_d) \\ E_{yz}(\vec{r}_o, \vec{r}_d) &= -E_{zy}(\vec{r}_o, \vec{r}_d) \end{aligned} \quad (5.127)$$

For the z component of the electric field, we recall that:

$$\begin{aligned} E_{zz}(\vec{r}_o, \vec{r}_d) &= \frac{\omega\mu}{8\pi^2} \iint_{-\infty}^{+\infty} \left\{ dk_x dk_y e^{-jk_x(x_o-x_d)} e^{-jk_y(y_o-y_d)} \frac{e^{-jk_z(z_o+z_d)}}{k_z} \right. \\ &\quad \left. \times \left[\frac{k_\rho^2}{k_s^2} S_{22}(k_\rho) \right] \right\} \end{aligned} \quad (5.128)$$

$$\begin{aligned} E_{zz}^{S_{22}}(\vec{r}_o, \vec{r}_d) &= \frac{j\omega\mu}{8\pi} \int_0^{+\infty} k_\rho dk_\rho \frac{e^{-jk_z(z_o+z_d)}}{jk_z} \frac{k_\rho^2}{k_s^2} S_{22}(k_\rho) \\ &\quad \times \frac{1}{\pi} \int_0^{2\pi} d\phi e^{-jk_\rho \rho \cos(\phi-\Psi)} \end{aligned} \quad (5.129)$$

$$E_{zz}^{S_{22}}(\vec{r}_o, \vec{r}_d) = \frac{j\omega\mu}{4\pi} \int_0^{+\infty} k_\rho dk_\rho \frac{e^{-jk_z(z_o+z_d)} k_\rho^2}{jk_z k_s^2} S_{22}(k_\rho) J_0(k_\rho \rho) \quad (5.130)$$

We make use of the following complex image approximation obtained by DCIM:

$$\frac{S_{22}(k_\rho) k_\rho^2}{k_s^2} = \sum_{k=1}^{N_6} B_{6k} e^{-jk_z \gamma_{6k}} \quad (5.131)$$

This opens the way for utilizing Sommerfeld Identity which yields the following closed-form expression for $E_{zz}(\vec{r}_o, \vec{r}_d)$:

$$E_{zz}(\vec{r}_o, \vec{r}_d) = E_{zz}^{S_{22}}(\vec{r}_o, \vec{r}_d) = \frac{j\omega\mu}{4\pi} \sum_{k=1}^{N_6} B_{6k} \frac{e^{-jk_s r_{6k}}}{r_{6k}} \quad (5.132)$$

with r_{6k} defined as:

$$r_{6k} = \sqrt{(x_o - x_d)^2 + (y_o - y_d)^2 + (z_o + z_d + \gamma_{6k})^2} \quad (5.133)$$

All components of the dyadic Green's functions for the scattered electric field due to a dipole source over the planar periodic structure are obtained in closed-form in this section and now it is time to present the results of the application of this formulation on some sample problems.

5.3 Numerical Results

Two cases are analysed with the proposed method and the results are compared to the results from a commercial 3-D EM software. Since HFSS [53] has the option of excitation with an Hertzian dipole, it is preferred here instead of CST which was used in reflection coefficient analysis. In the first case, the periodic structure is in free space while in the second one the periodic surface is printed on a dielectric slab as an example of a multilayered medium. The structure in consideration is infinitely periodic in x and y. HFSS results can be obtained for structures truncated at a finite number of cells. In order to see that HFSS results actually converge, the simulations

are performed multiple times increasing the number of cells at each run. $M \times M$ expression appearing in the legends of the plots states the number of unit cells at both directions used in the simulation to obtain the corresponding result.

5.3.1 Periodic Surface in Free Space

The sample problem is the same as in Fig. 3 of [52]. The scatterer is a square PEC patch array in free space. Geometry of the problem is shown in Fig. 5.3 and the values of the parameters of the problem is given in Table 5.1.

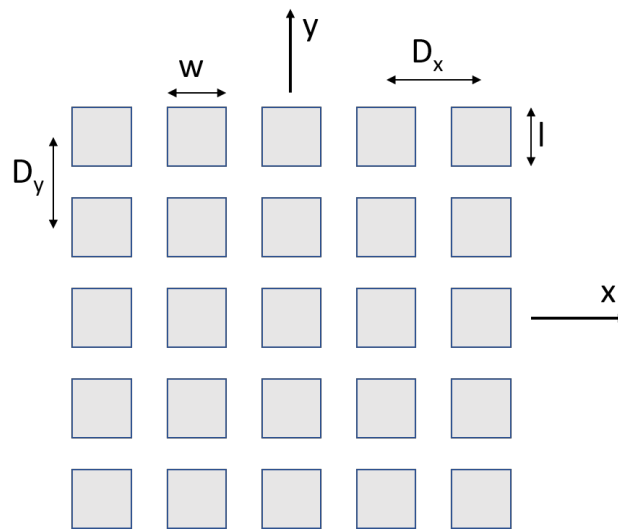


Figure 5.3: Periodic surface in free space

The selection of this geometry for analysis is based on the fact that the corresponding S-Parameters have negligible ϕ dependence which can be observed in Figure 5.4.

For dipole excitation, nine entities based on S-Parameters, whose closed forms are derived in section 5.2, are obtained in the form of complex exponential summation. To achieve this, sampling is performed along 200 points on the path shown in Fig. 5.2. After this 200 point sampling, complex exponential set for each of nine entities are obtained by using DCIM. The number of complex exponentials used in approximations varies between 6 and 12.

We first present the results for z oriented dipole. Figure 5.5 shows magnitude of E_{yz} with respect to y_o on a line at $x_o = 0$ and $z_o = 5$ mm while Figure 5.6 shows the plot

Table 5.1: Parameters of the problem for free space case

Parameter	Description	Value
f	frequency	15 GHz
D_x	periodicity in x direction	2 mm
D_y	periodicity in y direction	2 mm
w	width of the PEC scatterer	1.8 mm
l	length of the PEC scatterer	1.8 mm
x_d	x position of the dipole	0 mm
y_d	y position of the dipole	0 mm
z_d	z position of the dipole	3 mm

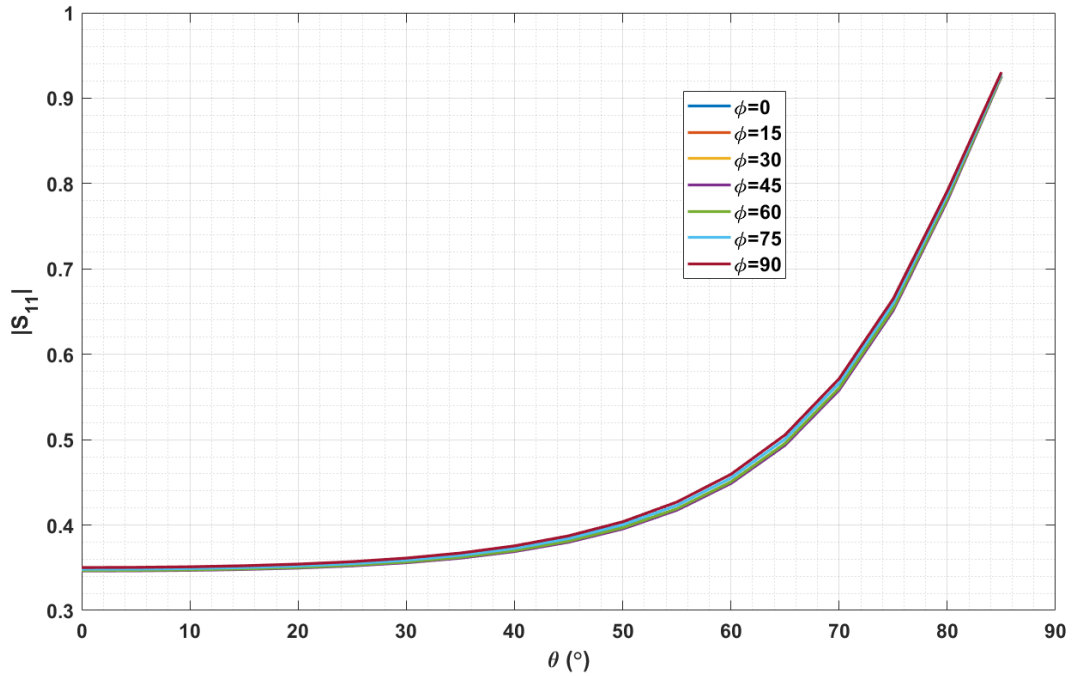


Figure 5.4: Magnitude of S_{11} for the structure described in Fig. 5.3 and Table 5.1

of same entity on $z_o = 2$ mm. Since the fields are complex quantities in general, phase plots are also presented to demonstrate the accuracy more completely. Argument of E_{yz} with respect to y_o on a line at $x_o = 0$ and $z_o = 2$ mm is plotted in Figure 5.7.

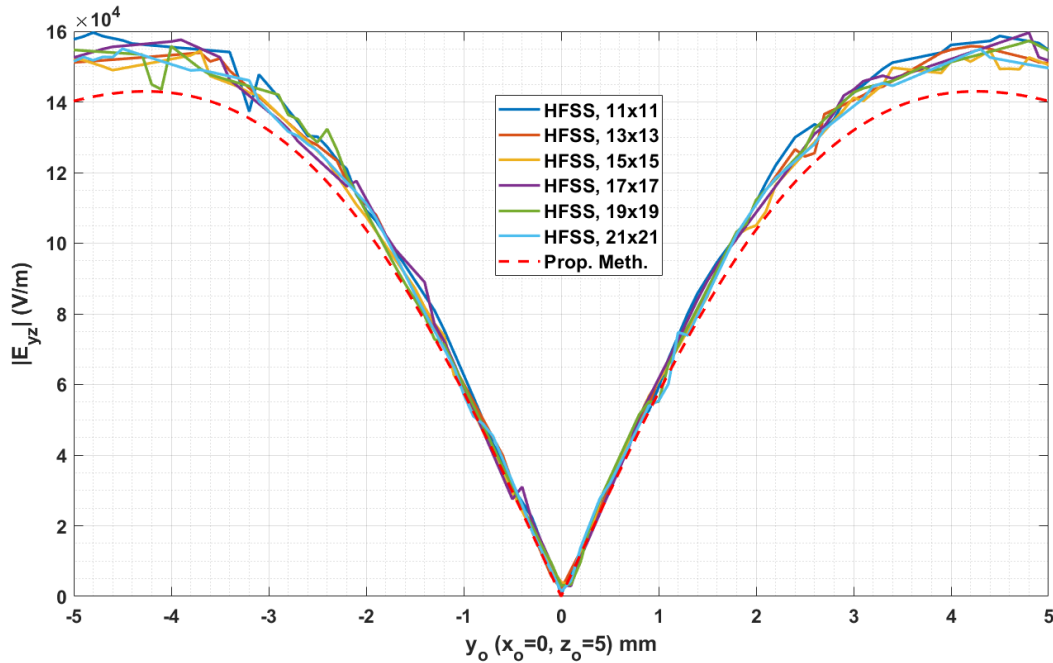


Figure 5.5: Magnitude of E_{yz} with respect to y_o ($x_o = 0$ and $z_o = 5$ mm), scattered from the 2-D periodic structure in free space

Magnitude and phase plots of vertical component of the scattered electric field from the structure due to a vertical Hertzian dipole above the surface are presented in Figures 5.8 and 5.9, respectively.

One can observe the good agreement of the results obtained by the proposed method with HFSS simulation results both in magnitude and phase. The results with transverse dipole excitation are presented next. The z and y components of scattered electric field are analyzed when the source above the periodic structure is y oriented.

Figure 5.10 shows magnitude of E_{zy} with respect to y_o on a line at $x_o = 0$ and $z_o = 5$ mm while Figure 5.11 shows the plot of same entity on $z_o = 2$ mm. Phase of E_{zy} with respect to y_o on a line at $x_o = 0$ and $z_o = 2$ mm is plotted in Figure 5.12.

The transverse components of the scattered electric field due to the y directed Hertzian dipole are analyzed, namely E_{yy} . This component of the scattered field is analyzed

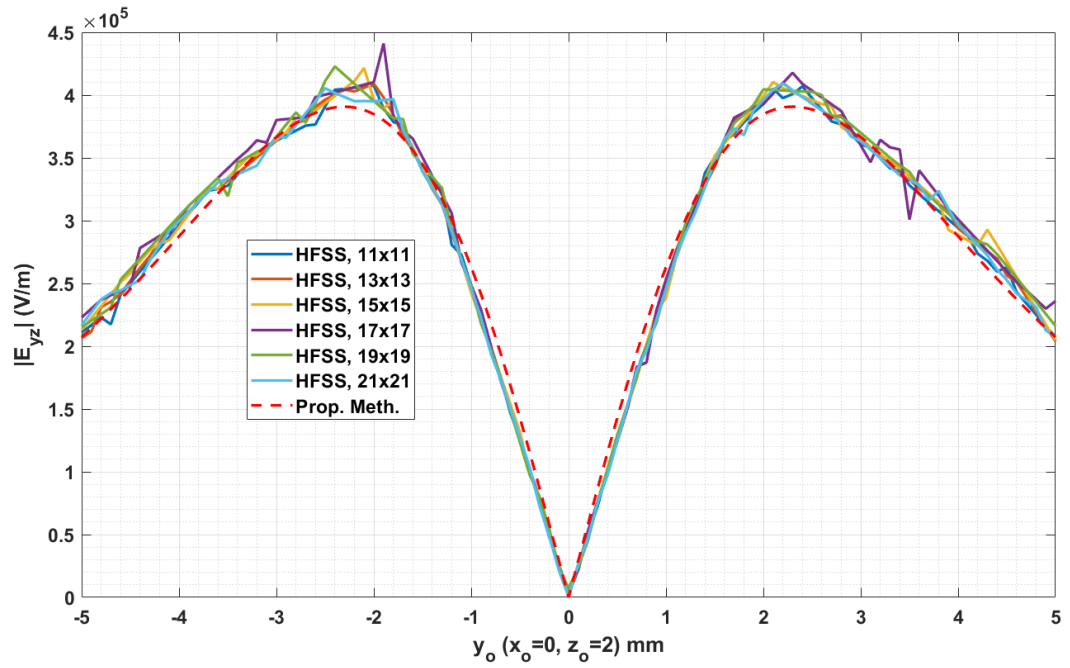


Figure 5.6: Magnitude of E_{yz} with respect to y_o ($x_o = 0$ and $z_o = 2$ mm), scattered from the 2-D periodic structure in free space

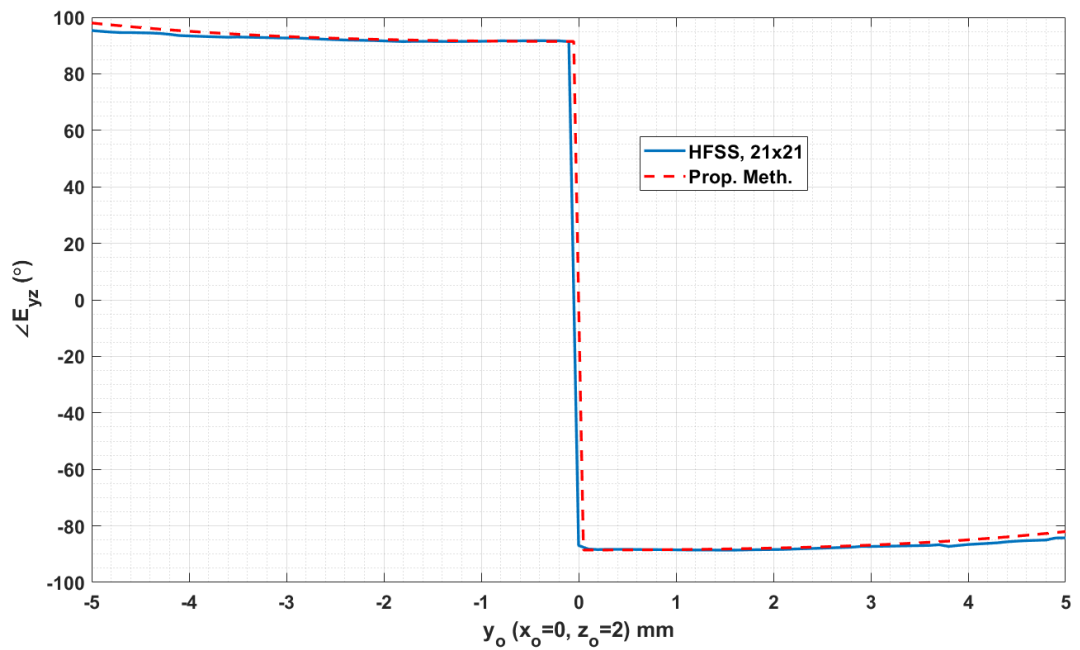


Figure 5.7: Phase of E_{yz} with respect to y_o ($x_o = 0$ and $z_o = 2$ mm), scattered from the 2-D periodic structure in free space

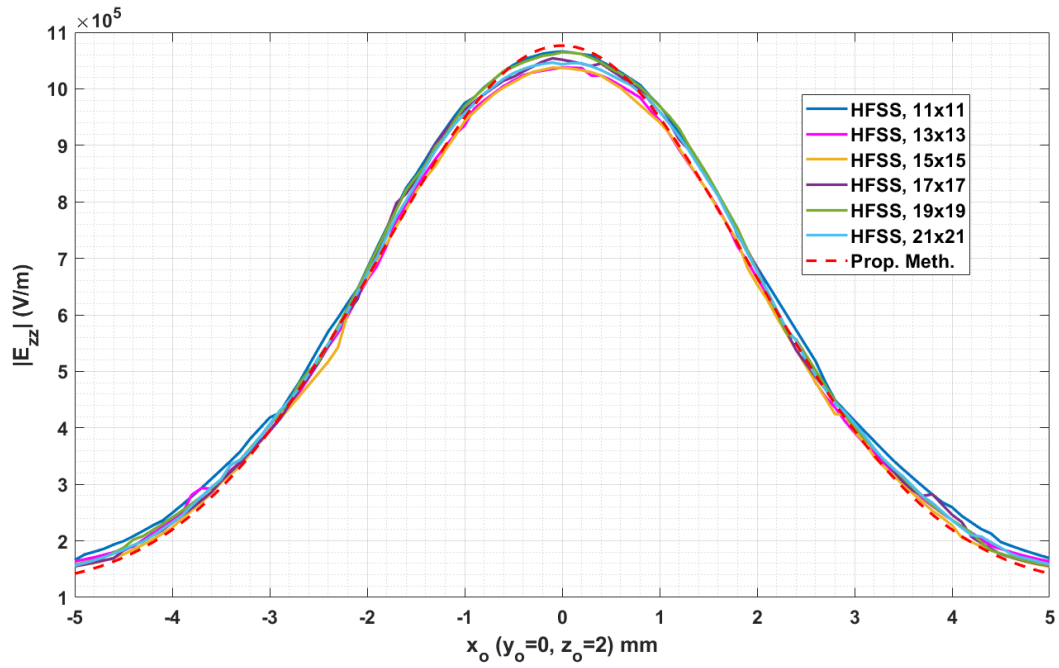


Figure 5.8: Magnitude of E_{zz} with respect to x_o ($y_o = 0$ and $z_o = 2$ mm), scattered from the 2-D periodic structure in free space

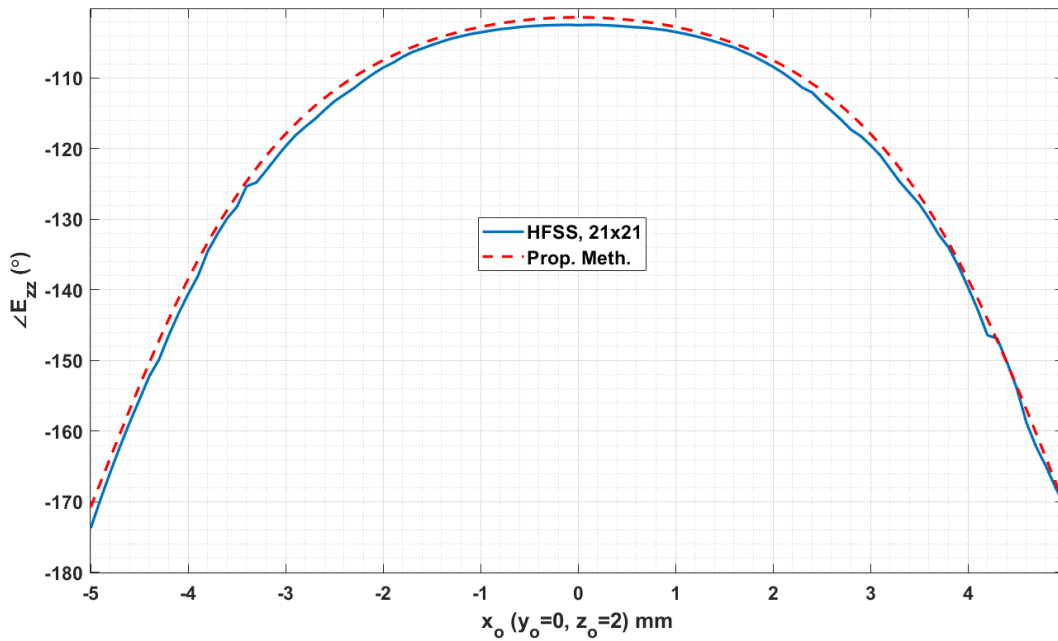


Figure 5.9: Phase of E_{zz} with respect to x_o ($y_o = 0$ and $z_o = 2$ mm), scattered from the 2-D periodic structure in free space

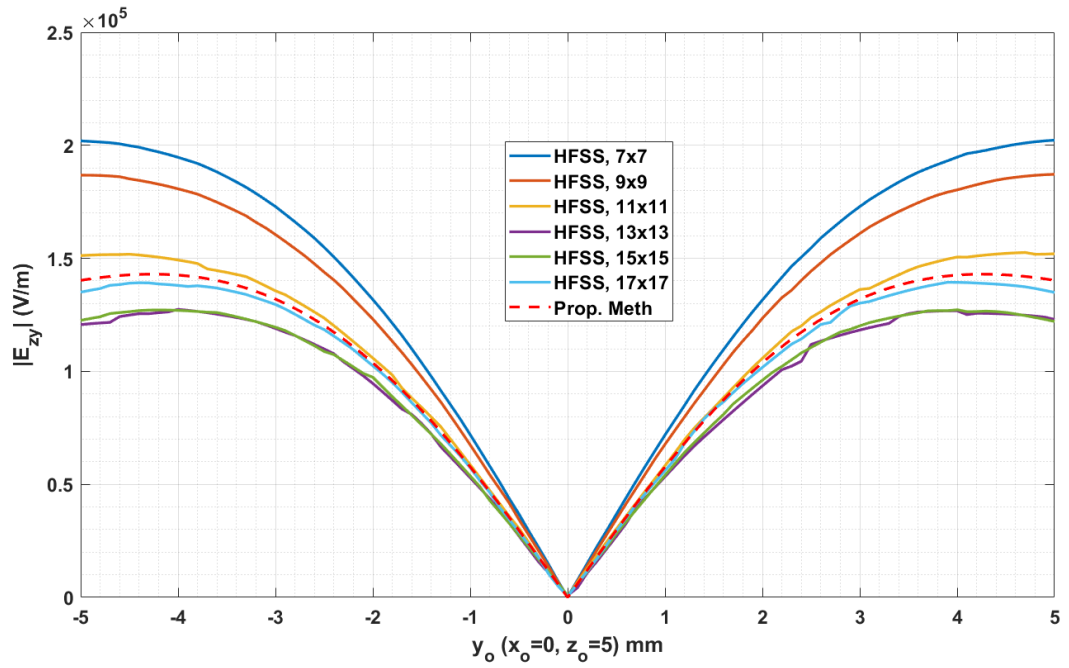


Figure 5.10: Magnitude of E_{zy} with respect to y_o ($x_o = 0$ and $z_o = 5$ mm), scattered from the 2-D periodic structure in free space

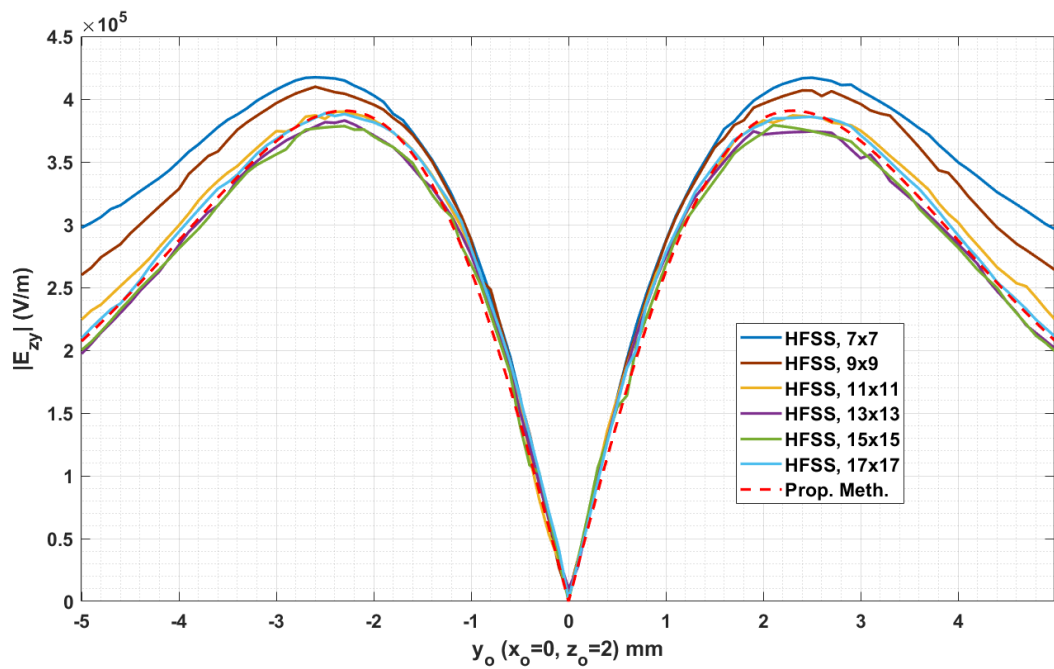


Figure 5.11: Magnitude of E_{zy} with respect to y_o ($x_o = 0$ and $z_o = 2$ mm), scattered from the 2-D periodic structure in free space

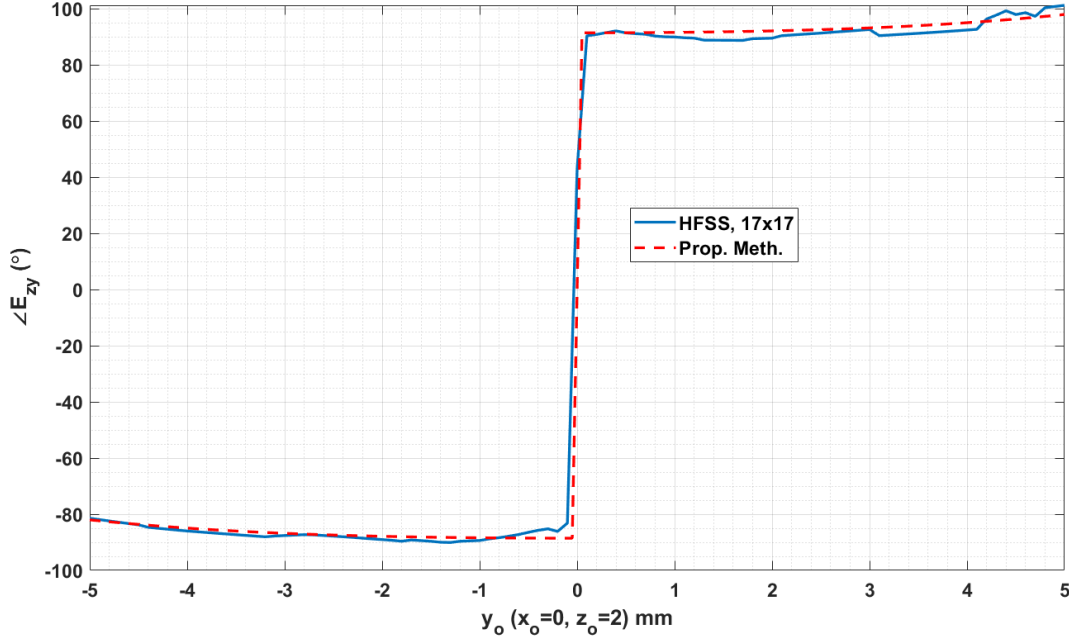


Figure 5.12: Phase of E_{zy} with respect to y_o ($x_o = 0$ and $z_o = 2$ mm), scattered from the 2-D periodic structure in free space

along the $x_o = 0$ line on the $z_o = 5$ mm plane first. The corresponding magnitude plot is in Figure 5.13. $|E_{yy}|$ is then plotted with respect to y_o along the $x_o = 0$ line but this time on the $z_o = 2$ mm plane, which is shown in Figure 5.14. Angle of E_{yy} on the same geometry is presented in Figure 5.15.

From Figures 5.13 and 5.14, one can deduce that for transverse fields due to horizontally oriented dipole, HFSS results need much more unit cells to converge. Actually, the variation of the HFSS results is still around 30% – 40% in these plots even though the number of unit cells used in each dimension is between 23 and 35.

It would be a more complete demonstration to test the proposed method along two orthogonal lines instead of one. Plots of E_{yy} with respect to x_o along $y_o = 0$ lines are presented in Figures 5.16 to 5.18. Magnitude of E_{yy} for $z_o = 5$ mm and $z_o = 2$ mm is shown in Figure 5.16 and 5.17, respectively. Phase response at $z_o = 2$ mm is presented in Figure 5.18.

We can again observe the very low convergence rate of the HFSS field values with respect to number of cells. This means an inefficiency in terms of computing resources.

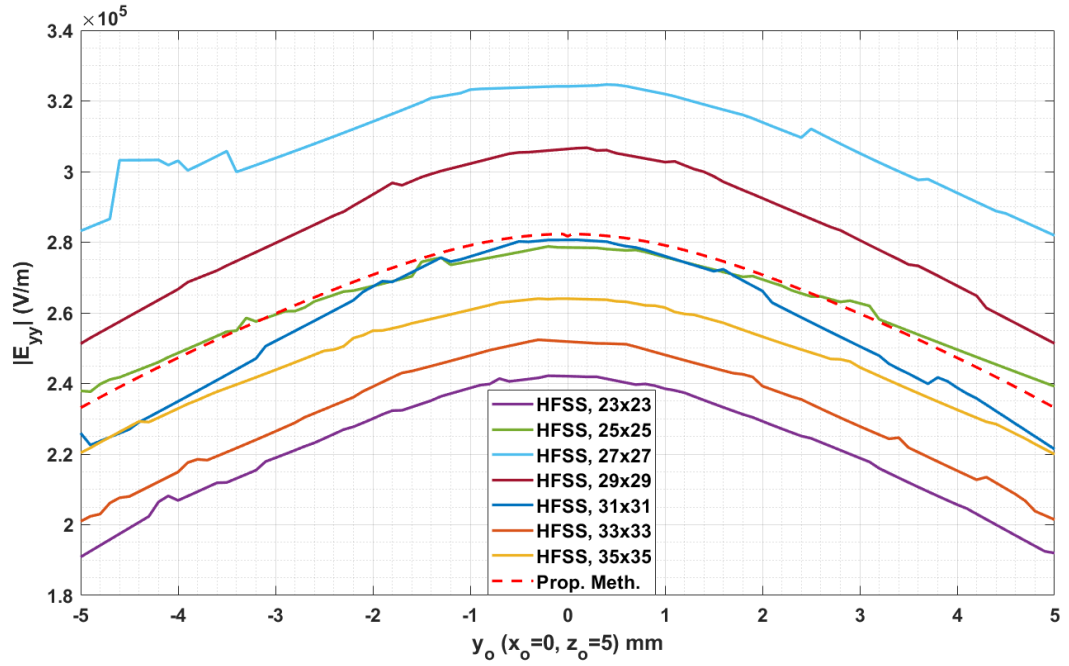


Figure 5.13: Magnitude of E_{yy} with respect to y_o ($x_o = 0$ and $z_o = 5$ mm), scattered from the 2-D periodic structure in free space

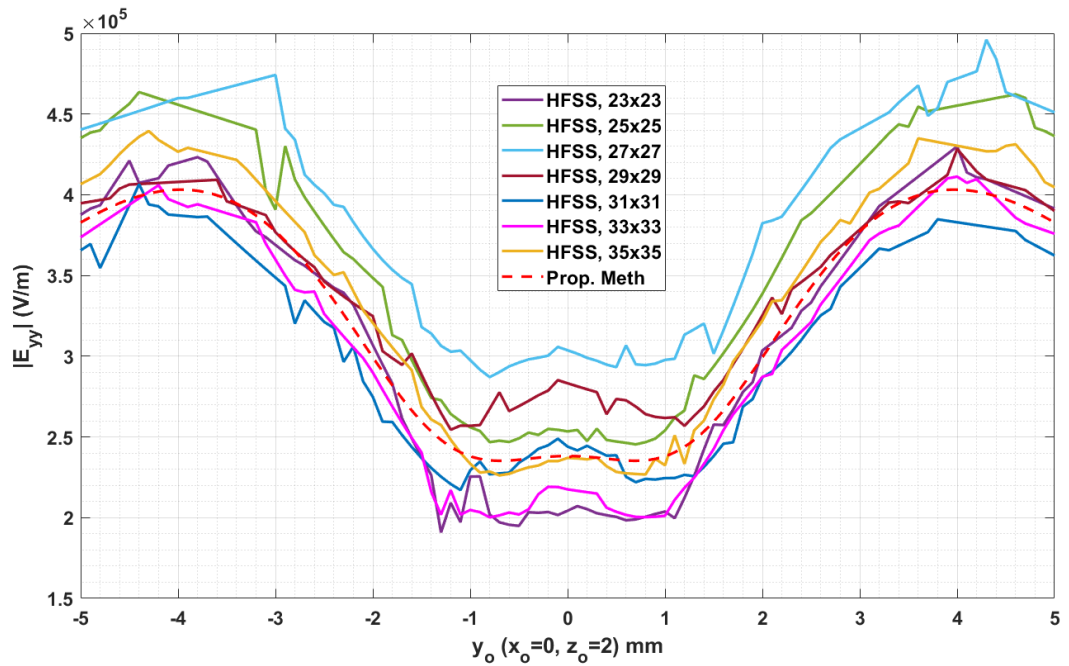


Figure 5.14: Magnitude of E_{yy} with respect to y_o ($x_o = 0$ and $z_o = 2$ mm), scattered from the 2-D periodic structure in free space

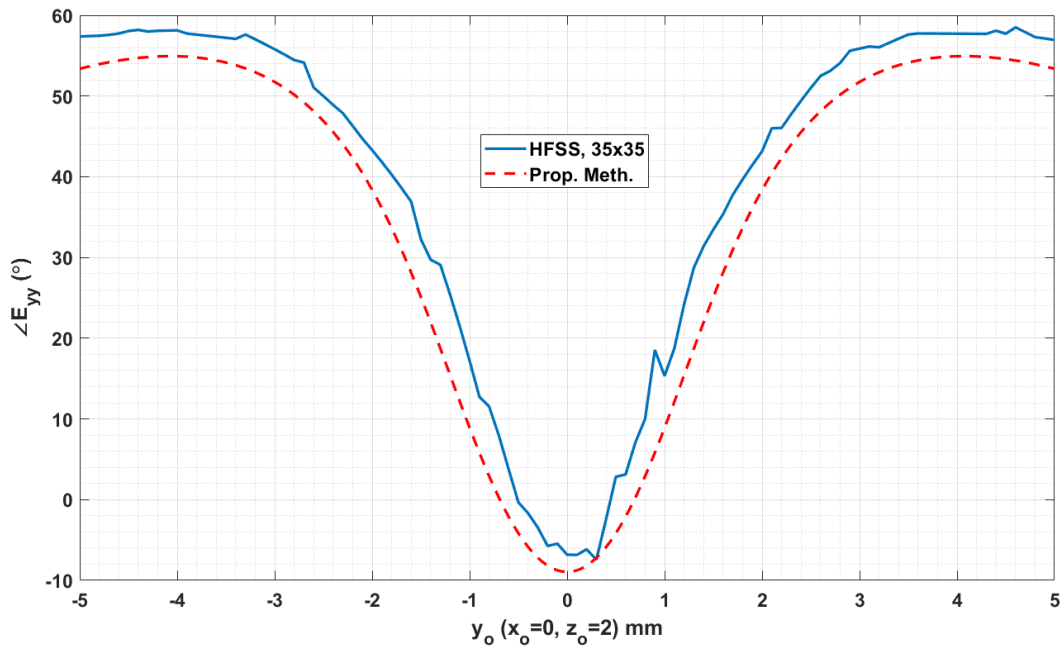


Figure 5.15: Phase of E_{yy} with respect to y_o ($x_o = 0$ and $z_o = 2$ mm), scattered from the 2-D periodic structure in free space

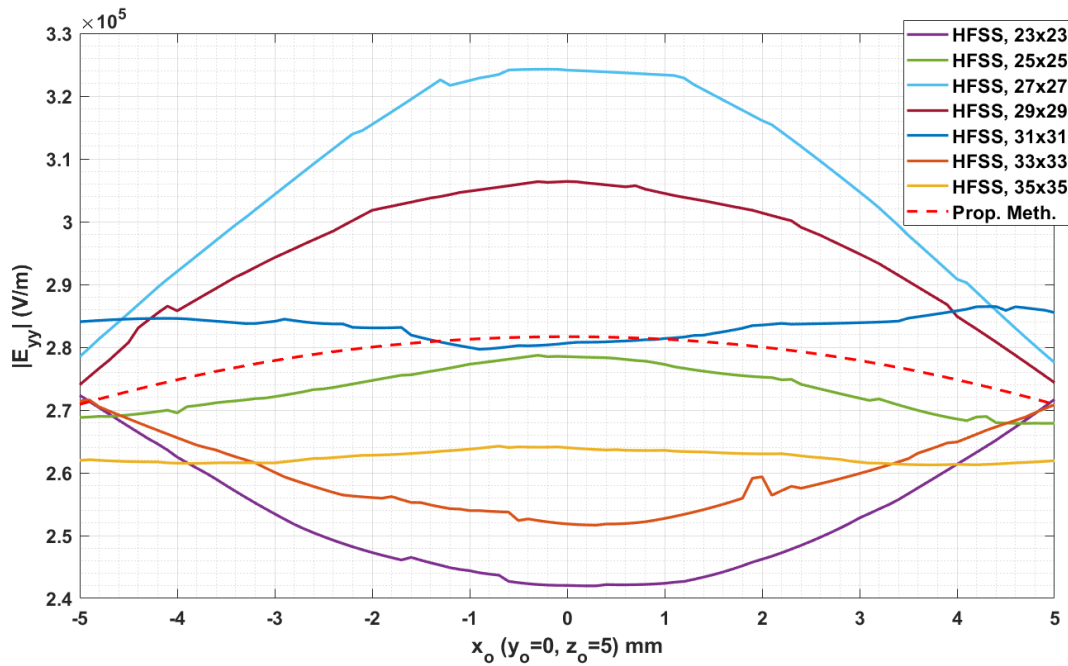


Figure 5.16: Magnitude of E_{yy} with respect to x_o ($y_o = 0$ and $z_o = 5$ mm), scattered from the 2-D periodic structure in free space

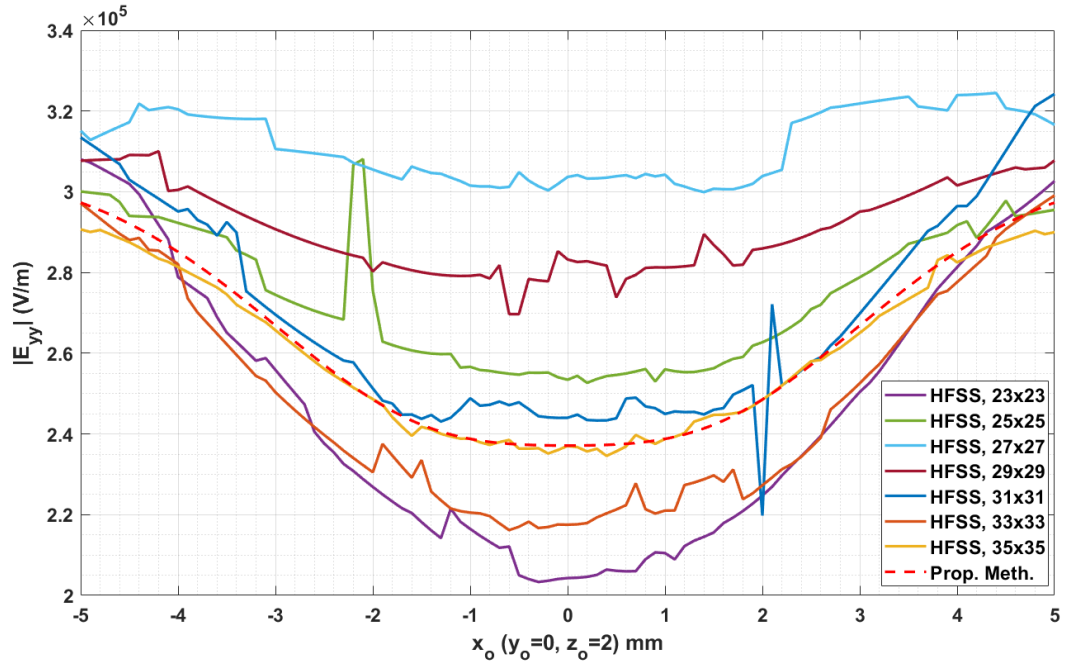


Figure 5.17: Magnitude of E_{yy} with respect to x_o ($y_o = 0$ and $z_o = 2$ mm), scattered from the 2-D periodic structure in free space

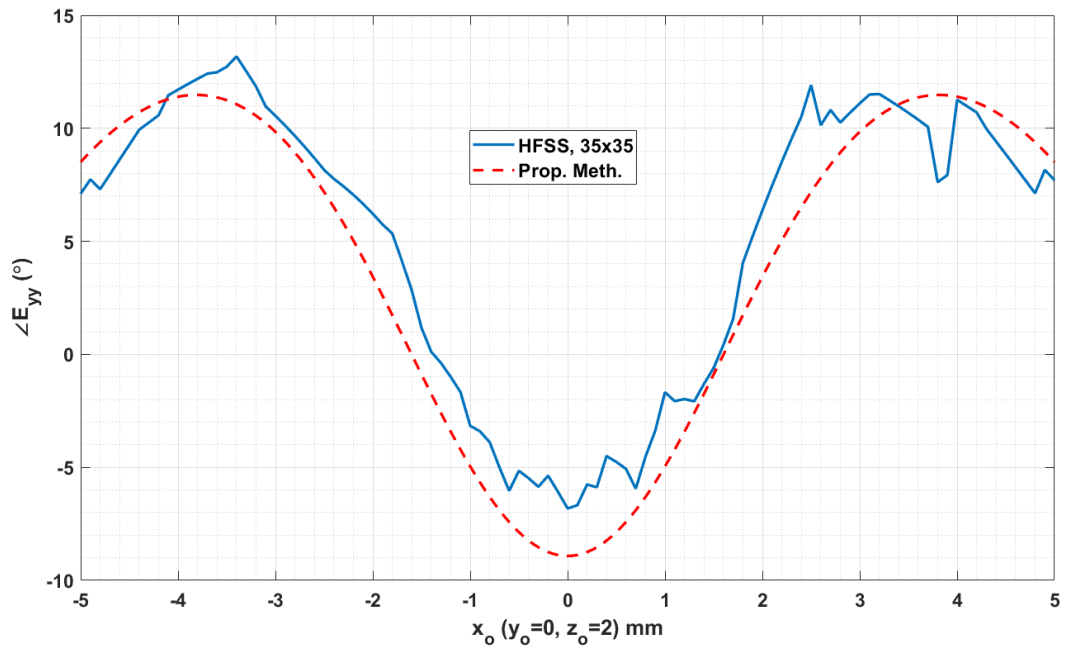


Figure 5.18: Phase of E_{yy} with respect to x_o ($y_o = 0$ and $z_o = 2$ mm), scattered from the 2-D periodic structure in free space

The formulation of the proposed method takes into account the infinite periodicity which means the concept of convergence with respect to cell number is not applicable. Once S-Parameters are calculated on the sampling path mentioned in section 5.1, all 9 scalar components of the dyadic Green's function becomes available by simple operations with negligible processing time and power.

5.3.2 Periodic Surface Printed on Dielectric Slab

The periodic array of the free space problem analyzed in section 5.3.1 is printed on a dielectric slab and this structure is analyzed as a sample problem of periodic surface on multilayered media. The geometry of the problem is shown in Fig. 5.19 and the values of the parameters of the problem are given in Table 5.2.

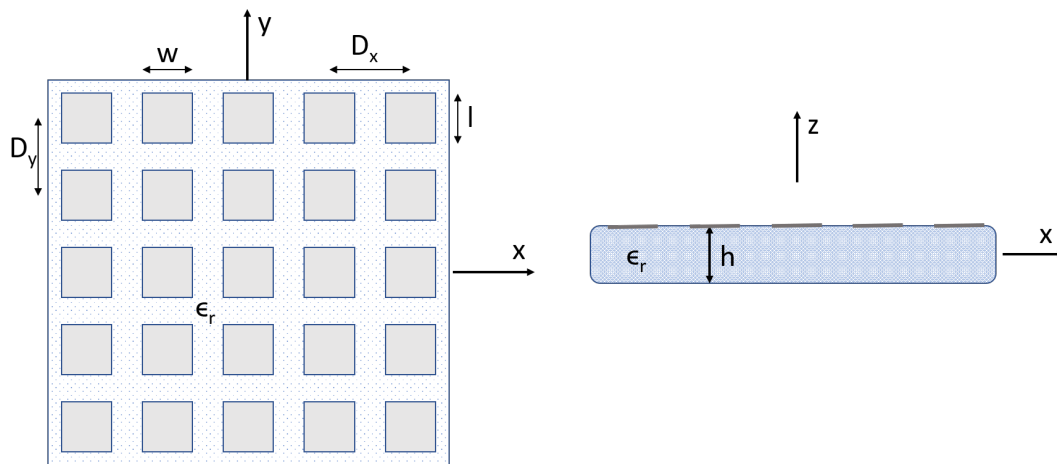


Figure 5.19: Periodic surface printed on dielectric slab

The sampling is performed along the path shown in Fig. 5.2 again by using 200 points. For the approximation of nine S-Parameter based entities, the number of complex exponentials used in DCIM varies between 8 and 15.

We start by presenting the results for a z oriented dipole. Figure 5.20 shows magnitude of E_{yz} with respect to y_o on a line at $x_o = 0$ and $z_o = 5$ mm while Figure 5.21 shows the plot of the same entity on $z_o = 2$ mm. The phase accuracy is demonstrated in Figure 5.22 where the argument of E_{yz} with respect to y_o on a line at $x_o = 0$ and $z_o = 2$ mm is plotted .

Table 5.2: Parameters of the problem for multilayered case

Parameter	Description	Value
f	frequency	15 GHz
D_x	periodicity in x direction	2 mm
D_y	periodicity in y direction	2 mm
w	width of the PEC scatterer	1.8 mm
l	length of the PEC scatterer	1.8 mm
x_d	x position of the dipole	0 mm
y_d	y position of the dipole	0 mm
z_d	z position of the dipole	3 mm
ϵ_r	relative permittivity of the dielectric	3.38
h	height of the dielectric slab	2 mm

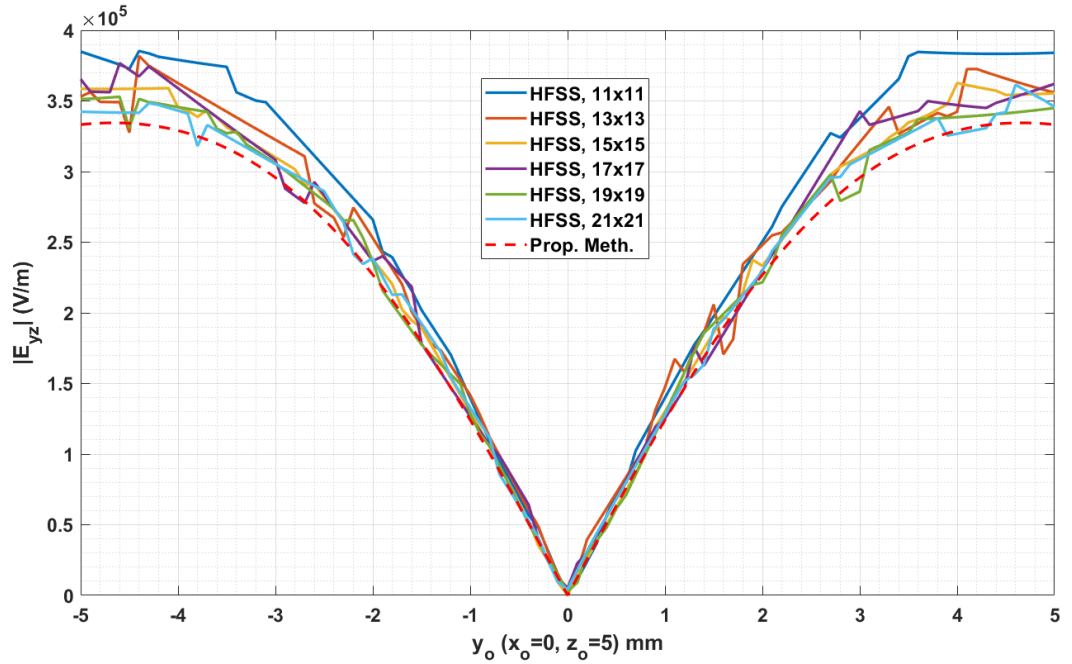


Figure 5.20: Magnitude of E_{yz} with respect to y_o ($x_o = 0$ and $z_o = 5$ mm), scattered from the 2-D periodic structure printed on dielectric slab

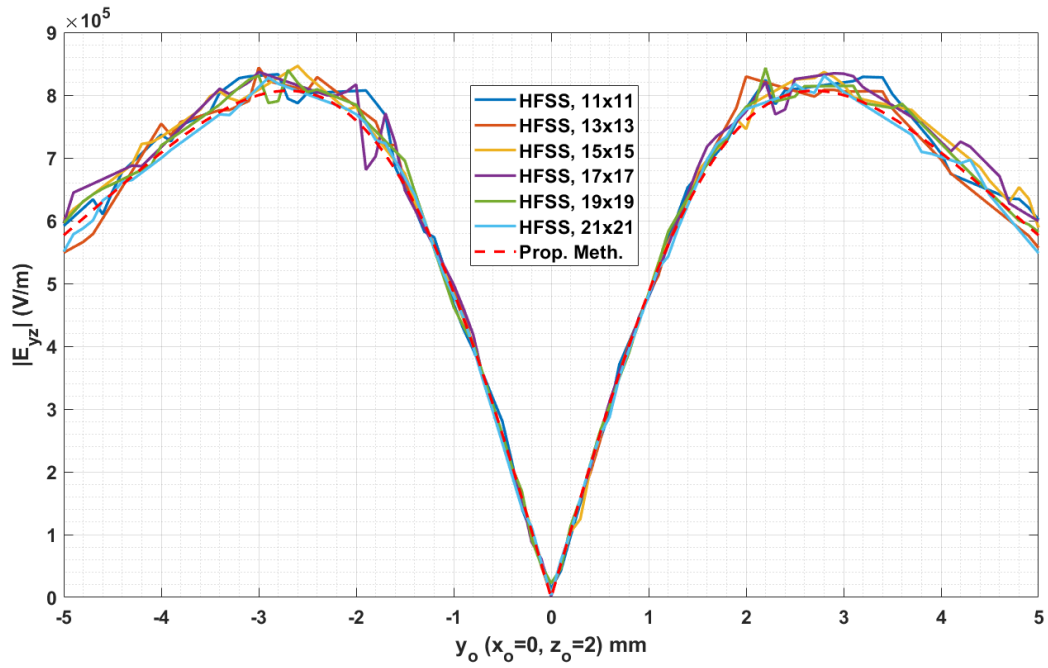


Figure 5.21: Magnitude of E_{yz} with respect to y_o ($x_o = 0$ and $z_o = 2$ mm), scattered from the 2-D periodic structure printed on dielectric slab

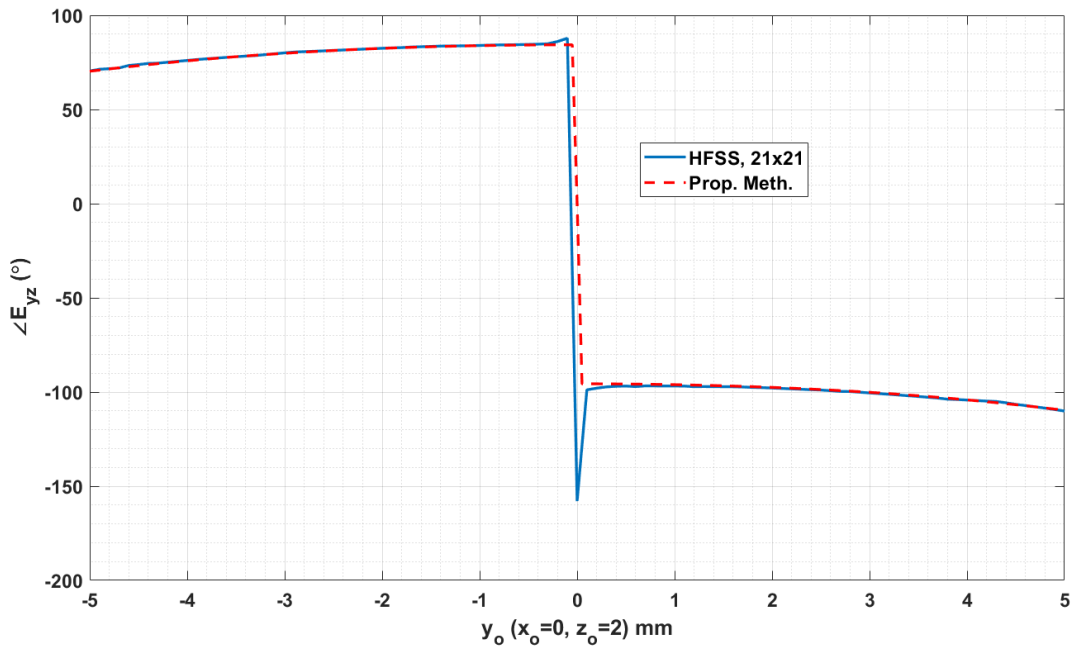


Figure 5.22: Phase of E_{yz} with respect to y_o ($x_o = 0$ and $z_o = 2$ mm), scattered from the 2-D periodic structure printed on dielectric slab

Vertical component of the scattered electric field from the structure due to a vertical Hertzian dipole above the surface is analyzed and the results are plotted in Figures 5.23 and 5.24, showing the magnitude and phase, respectively.

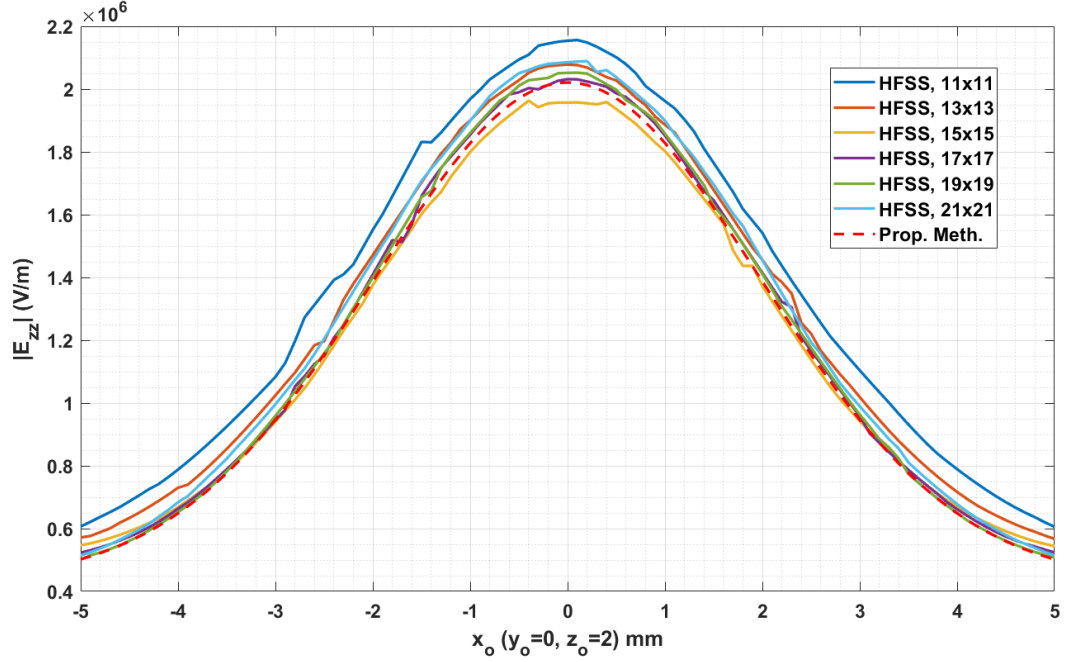


Figure 5.23: Magnitude of E_{zz} with respect to x_o ($y_o = 0$ and $z_o = 2$ mm), scattered from the 2-D periodic structure printed on dielectric slab

The agreement of the results obtained by the proposed method with results obtained by HFSS is very good for the case of z directed electric source. This agreement is observed in both magnitude and phase plots.

Next, we present the results with transverse dipole excitation. The z and y components of the scattered electric field are analyzed when the source above the periodic structure is y oriented. Figure 5.25 shows magnitude of E_{zy} with respect to y_o on a line at $x_o = 0$ and $z_o = 5$ mm while Figure 5.26 shows the plot of same entity on $z_o = 2$ mm. Phase of E_{zy} with respect to y_o on a line at $x_o = 0$ and $z_o = 2$ mm is plotted in Figure 5.27.

The analysis of the multilayered problem continues with the transverse components of the scattered electric field due to the y directed Hertzian dipole. This is the most difficult part for HFSS since the convergence of the results needs very large numbers

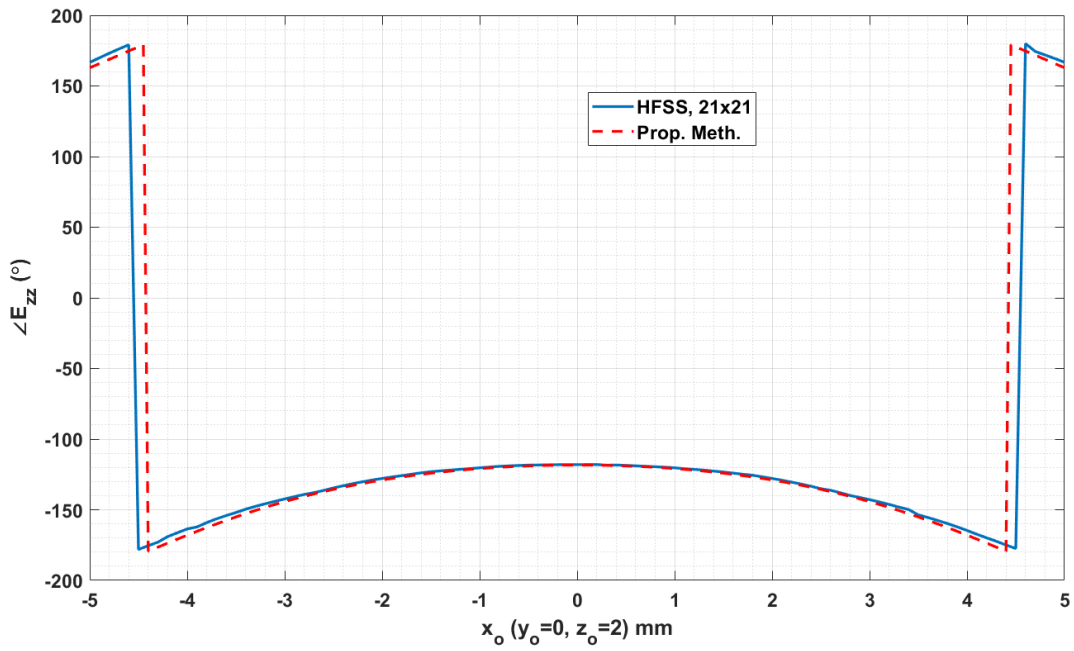


Figure 5.24: Phase of E_{zz} with respect to x_o ($y_o = 0$ and $z_o = 2$ mm), scattered from the 2-D periodic structure printed on dielectric slab

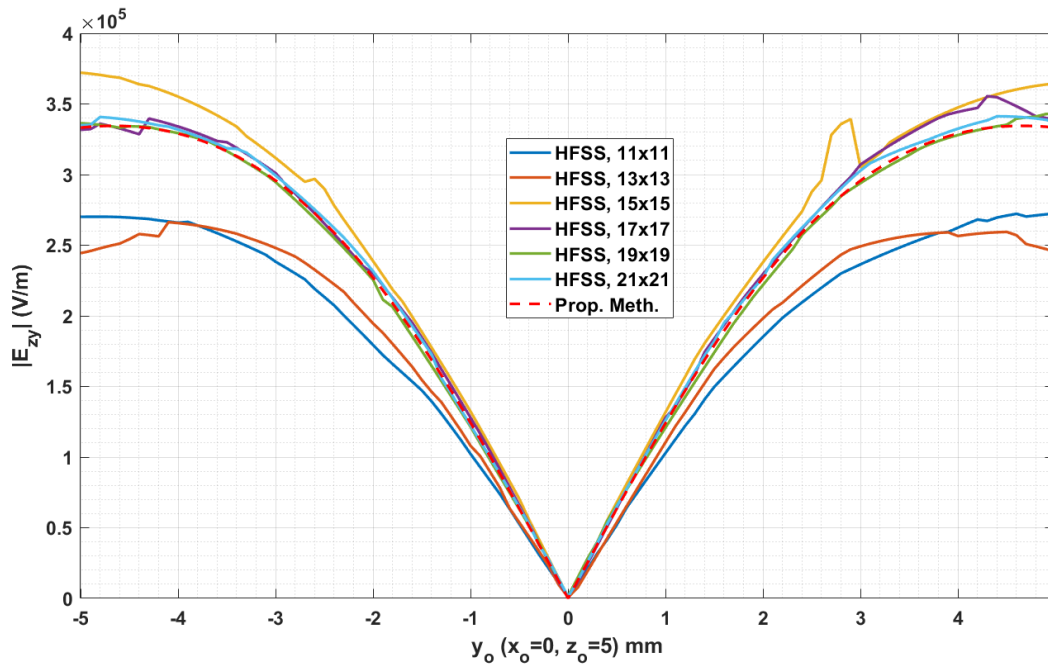


Figure 5.25: Magnitude of E_{zy} with respect to y_o ($x_o = 0$ and $z_o = 5$ mm), scattered from the 2-D periodic structure printed on dielectric slab

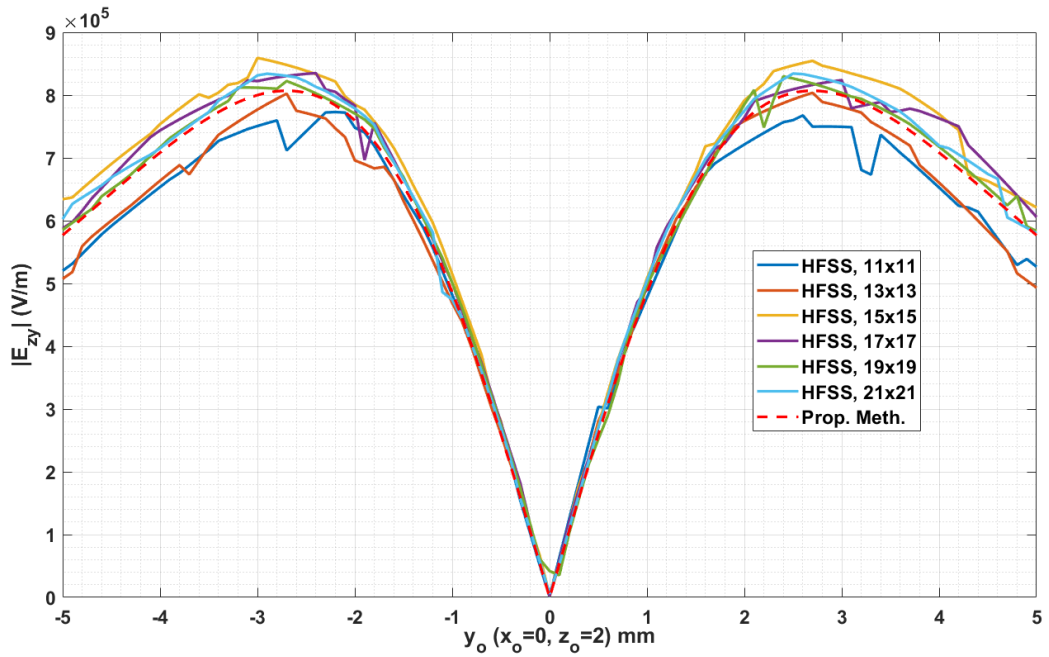


Figure 5.26: Magnitude of E_{zy} with respect to y_o ($x_o = 0$ and $z_o = 2$ mm), scattered from the 2-D periodic structure printed on dielectric slab

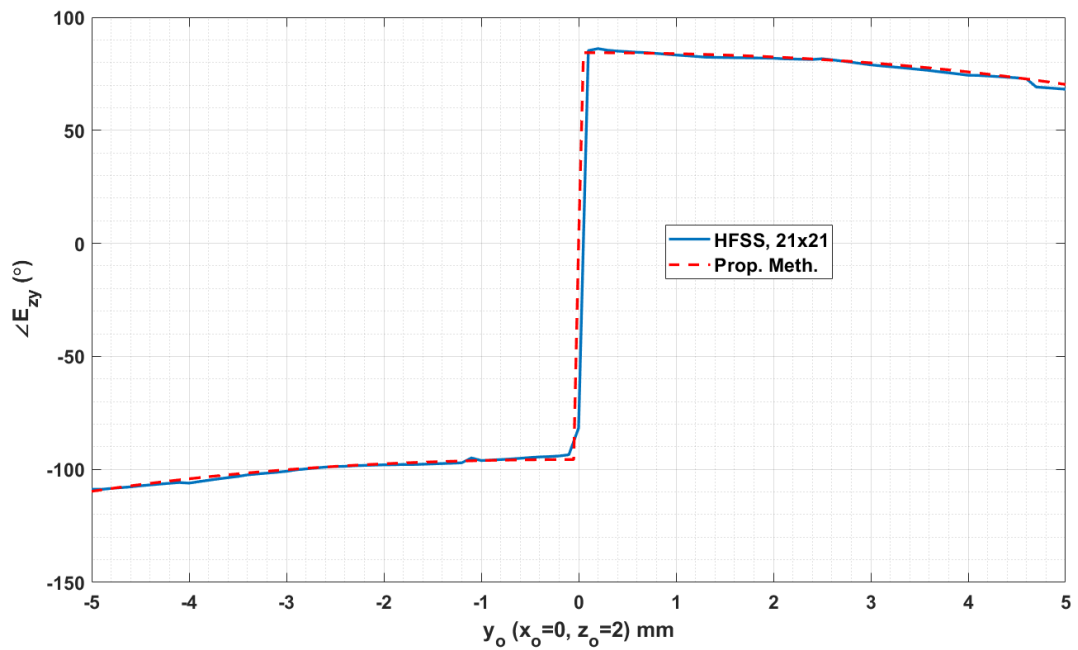


Figure 5.27: Phase of E_{zy} with respect to y_o ($x_o = 0$ and $z_o = 2$ mm), scattered from the 2-D periodic structure printed on dielectric slab

of cells which means a huge computation power and time.

Transverse (y) component of the scattered field is analyzed along the $x_o = 0$ line on the $z_o = 5$ mm plane first, as in the free space case. The corresponding magnitude plot is in Figure 5.28. $|E_{yy}|$ is then plotted again with respect to y_o along the $x_o = 0$ line but this time for $z_o = 2$ mm, which is shown in Figure 5.29. Phase of E_{yy} on the same geometry is presented in Figure 5.30.

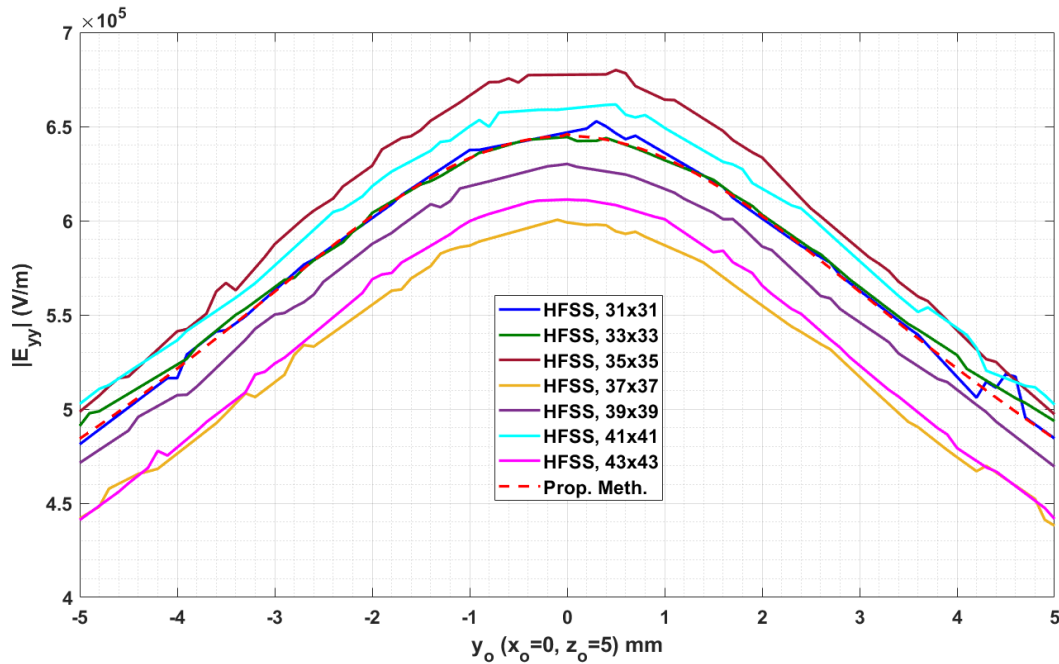


Figure 5.28: Magnitude of E_{yy} with respect to y_o ($x_o = 0$ and $z_o = 5$ mm), scattered from the 2-D periodic structure printed on dielectric slab

Because of the importance of the analysis of transverse components due to horizontal sources, the proposed method is tested along two orthogonal lines instead of one. Plots of E_{yy} with respect to x_o along $y_o = 0$ lines are presented in Figures 5.31 to 5.33. Magnitude of E_{yy} for $z_o = 5$ mm and $z_o = 2$ mm is shown in Figure 5.31 and 5.32, respectively. Phase response at $z_o = 2$ mm is presented in Figure 5.33.

The results in this section demonstrates that the proposed method yields the correct field values in an efficient way compared to the commercial full wave solver, HFSS. Especially when analyzing the transverse component of the scattered field due to the dipole sources placed horizontally above the surface, HFSS could not yield a fully

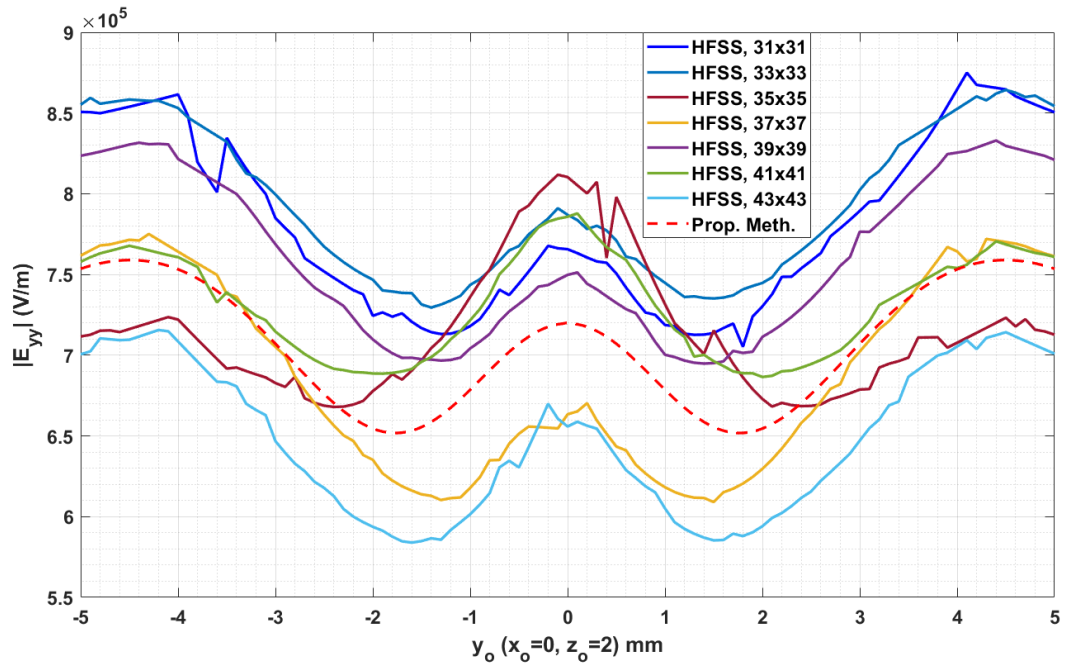


Figure 5.29: Magnitude of E_{yy} with respect to y_o ($x_o = 0$ and $z_o = 2$ mm), scattered from the 2-D periodic structure printed on dielectric slab

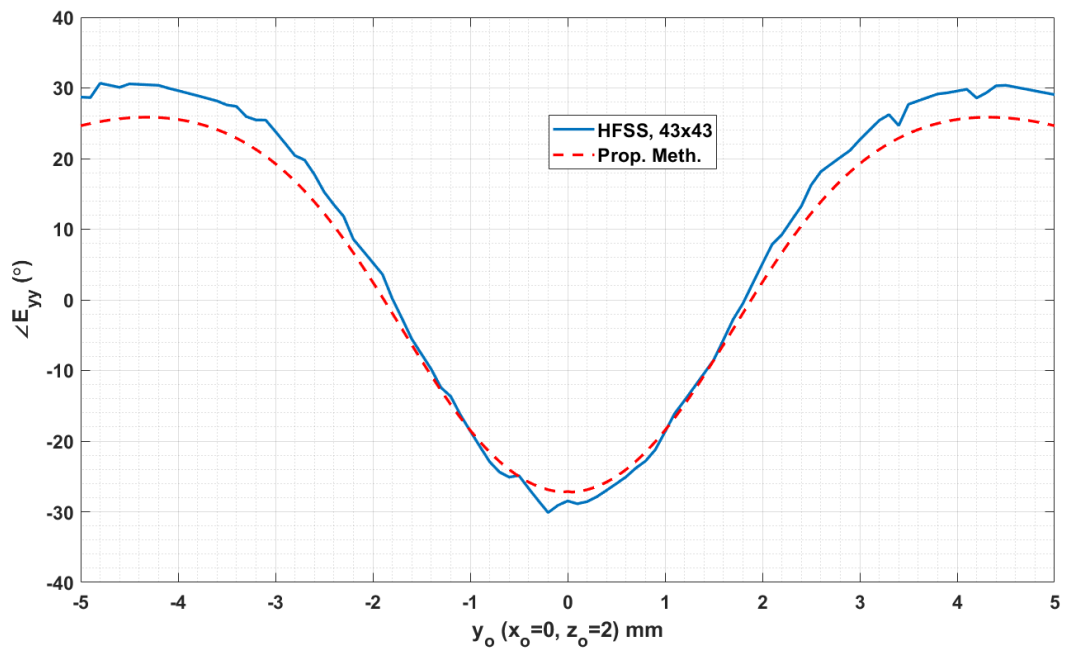


Figure 5.30: Phase of E_{yy} with respect to y_o ($x_o = 0$ and $z_o = 2$ mm), scattered from the 2-D periodic structure printed on dielectric slab

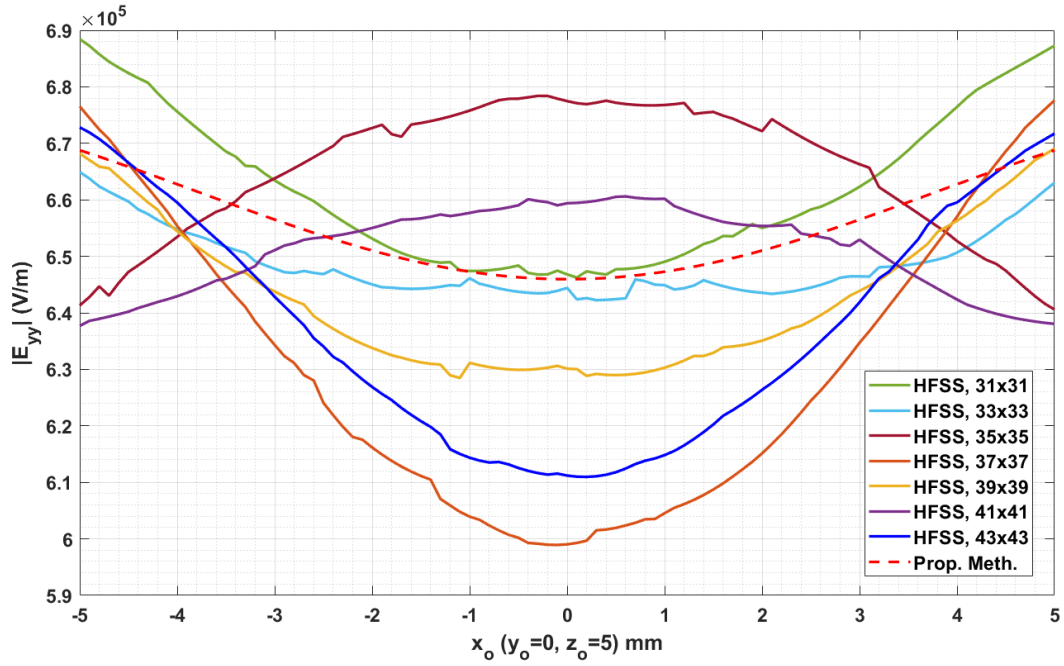


Figure 5.31: Magnitude of E_{yy} with respect to x_o ($y_o = 0$ and $z_o = 5$ mm), scattered from the 2-D periodic structure printed on dielectric slab

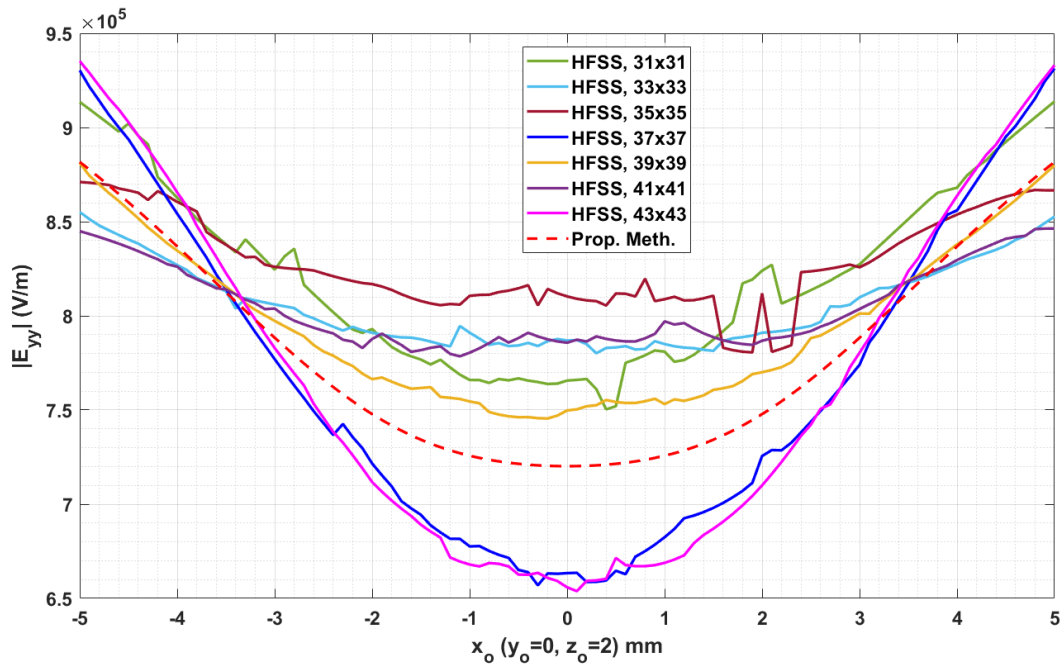


Figure 5.32: Magnitude of E_{yy} with respect to x_o ($y_o = 0$ and $z_o = 2$ mm), scattered from the 2-D periodic structure printed on dielectric slab

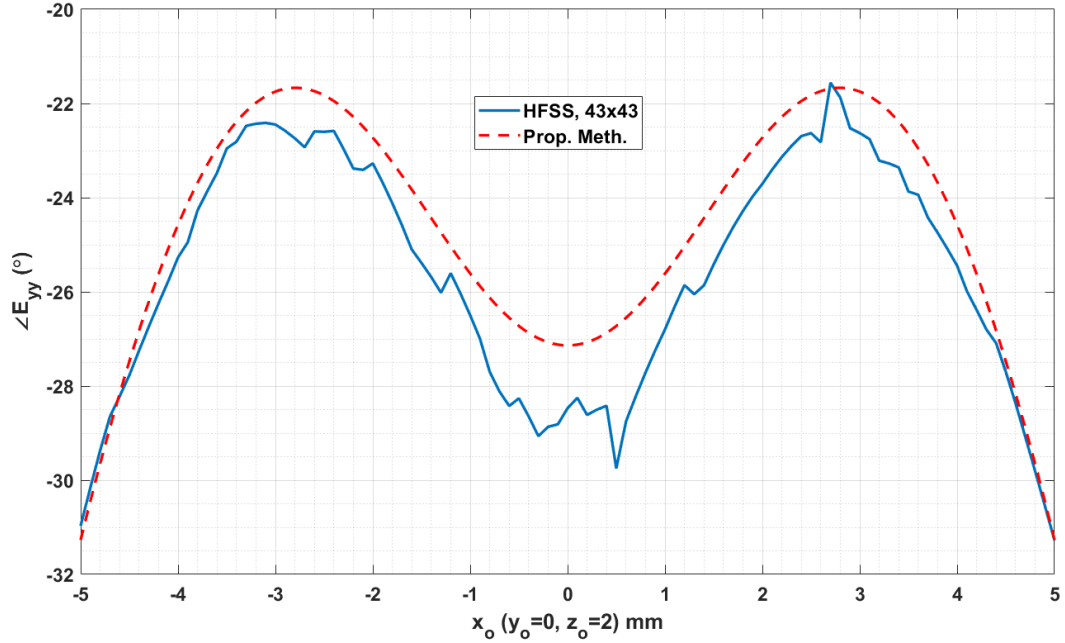


Figure 5.33: Phase of E_{yy} with respect to x_o ($y_o = 0$ and $z_o = 2$ mm), scattered from the 2-D periodic structure printed on dielectric slab

converged plot. Still, by observing the variations of the field plots obtained by HFSS, one can reasonably predict that the simulation results of the commercial solver will get even closer to the results of the proposed method as the number of cells involved in the simulation is increased.

An analysis is made to observe the effect of the scatterer on the field. The scattered electric field plots obtained in free space case and multilayered case are compared. Electric field plots obtained with the infinite dielectric slab alone are also included. Figure 5.34 shows the magnitude plots of E_{zz} along the line $y_o = 0$ with $z_o = 2$ mm. Figure 5.35 shows $|E_{zy}|$ along the line $x_o = 0$ at $z_o = 2$ mm plane. Figure 5.36 shows $|E_{yy}|$ along the line $y_o = 0$ and $z_o = 2$ mm. Finally, Figure 5.37 shows $|E_{yy}|$ with respect to y_o along the line $x_o = 0$ at $z_o = 2$ mm.

Once the S-Parameters are obtained along the aforementioned sampling path for different scattering structures, it is a very straightforward task to analyze the field values at any point as a result of the fact that the Green's functions of the structures are obtained as closed-form expressions.

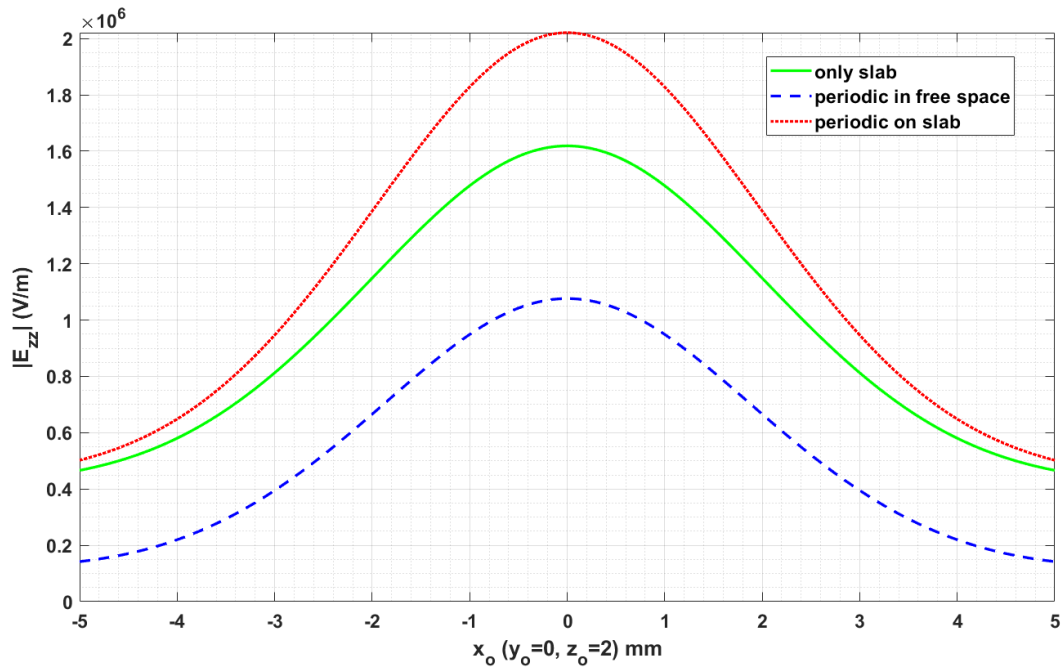


Figure 5.34: Comparison of magnitudes of E_{zz} with respect to x_o ($y_o = 0$ and $z_o = 2$ mm), obtained with various scatterers

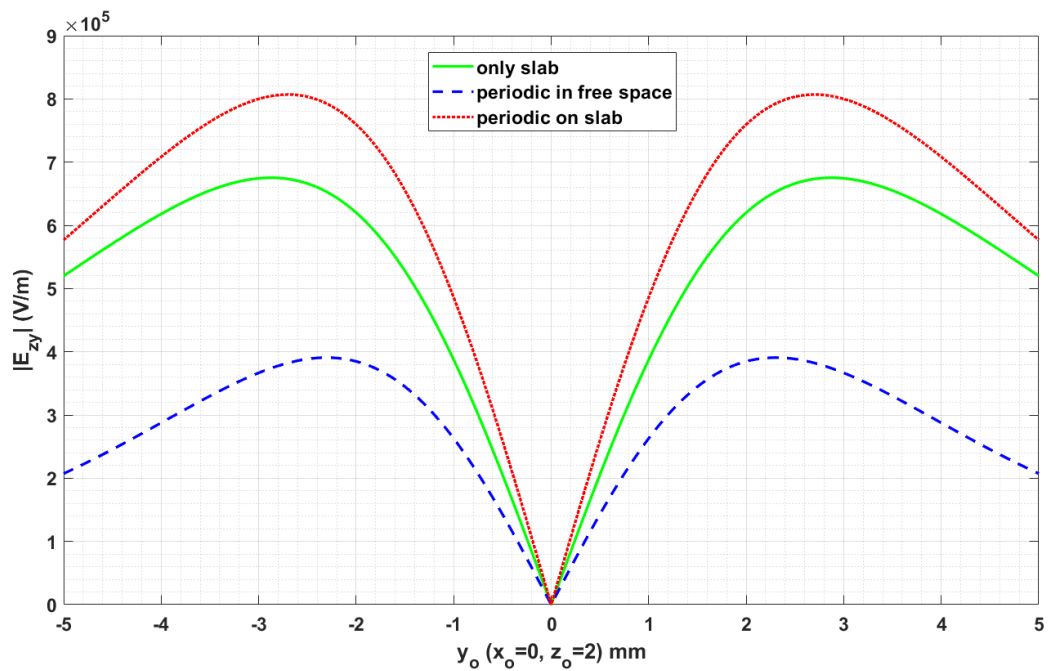


Figure 5.35: Comparison of magnitudes of E_{zy} with respect to y_o ($x_o = 0$ and $z_o = 2$ mm), obtained with various scatterers

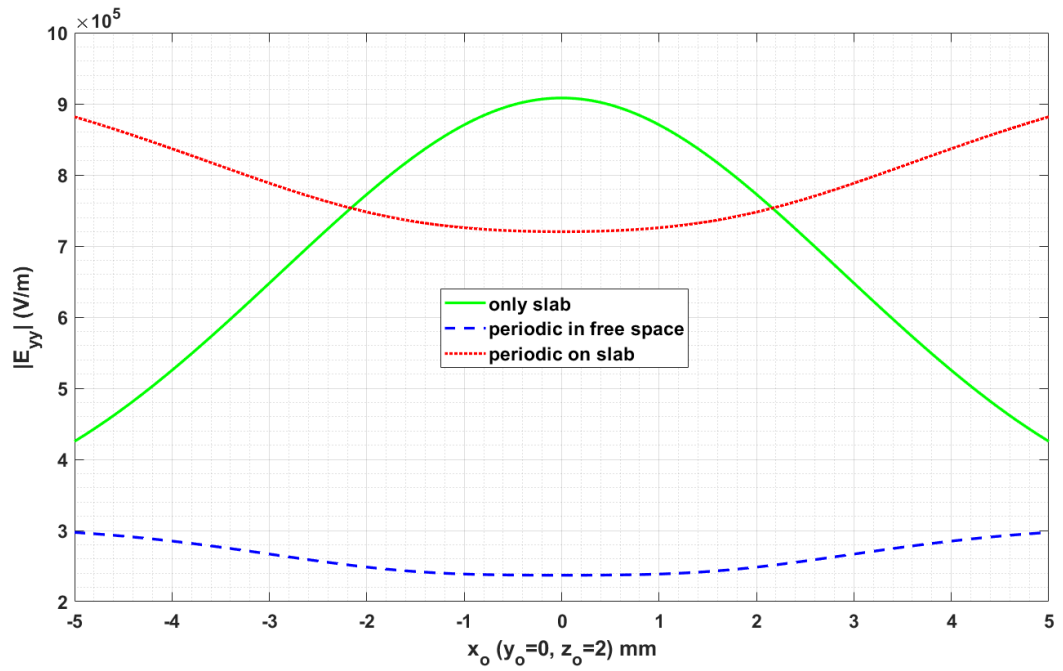


Figure 5.36: Comparison of magnitudes of E_{yy} with respect to x_o ($y_o = 0$ and $z_o = 2$ mm), obtained with various scatterers

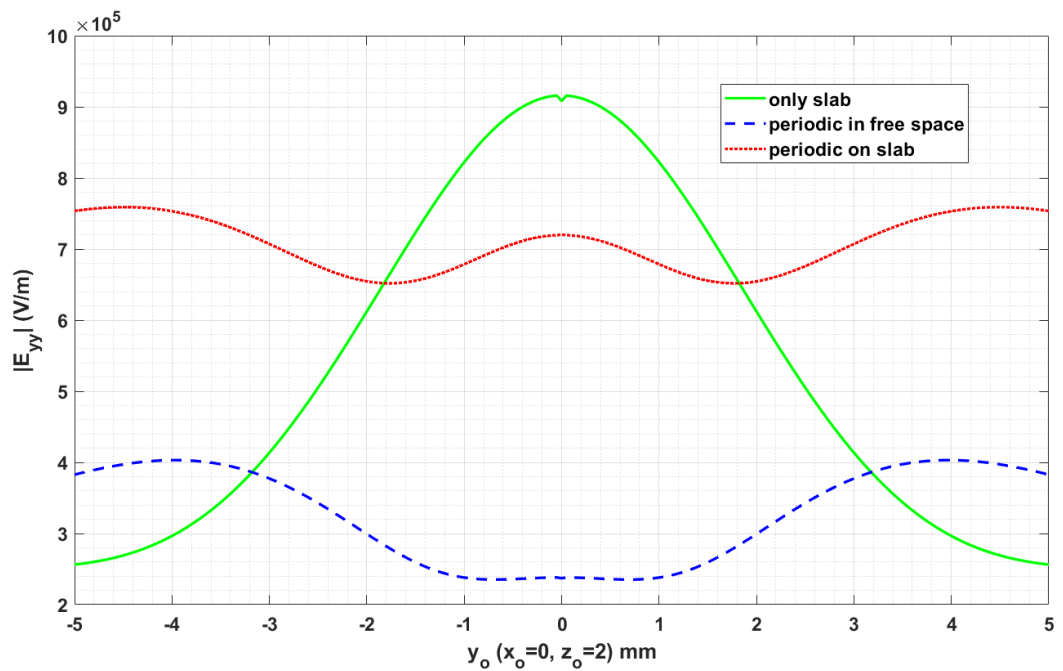


Figure 5.37: Comparison of magnitudes of E_{yy} with respect to y_o ($x_o = 0$ and $z_o = 2$ mm), obtained with various scatterers

As mentioned previously, number of sampling points used to calculate the S-Parameters is 200. For free space case, first sampling point requires 1.7 seconds and each of the other sampling points takes 1.2 seconds resulting a total of 4 minutes time for the calculation of all entries of the dyadic Green's function. For multilayered case, calculations at the initial sampling point takes 42 seconds while the time required for each of the remaining sampling points is 3.5 seconds. This makes a total of 12.3 minute calculation time for all the dyadic Green's function components. HFSS, on the other hand, requires separate runs for each dipole orientation. For excitation with a transverse dipole, calculations require around 2.4 hours (for 35x35 unit cells) to get reasonably converged field curves. When excited by a z oriented dipole, HFSS can complete the field calculations in 0.1 hours. Since the studied structures are symmetric, it is not needed to run separate simulations for x and y oriented dipole excitations. This means that HFSS requires a total of 2.5 hours to complete the calculations for all dyadic Green's function components (simulation times in HFSS for free space and multilayered cases are very close). Proposed method offers an efficiency improvement by a factor of more than 12.

In all of the numerical examples studied in this thesis, a work station type of notebook is used with a 128 GB of RAM. The processor of the computer is Intel Core i7-9750H CPU with 2.60GHz clock speed.

In order to assess the accuracy of the proposed method for different problem parameters and to determine a limit of validity of the approach in terms of periodicity, additional numerical examples are studied by modifying the scatterer size and/or periodicity of the structure. These analyses are given in the following sections.

5.3.3 Reducing Patch Size

The size of the patches in the unit cell of the periodic multilayered structure shown in Figure 5.19 is reduced compared to the one in Section 5.3.2. The size of the unit cell (periodicity) is kept constant. The parameters of this new problem is summarized in Table 5.3.

The y component of the scattered electric field due to a y oriented dipole is plotted

Table 5.3: Parameters of the problem for multilayered case with reduced patch size

Parameter	Description	Value
f	frequency	15 GHz
D_x	periodicity in x direction	2 mm
D_y	periodicity in y direction	2 mm
w	width of the PEC scatterer	1.5 mm
l	length of the PEC scatterer	1.5 mm
x_d	x position of the dipole	0 mm
y_d	y position of the dipole	0 mm
z_d	z position of the dipole	3 mm
ϵ_r	relative permittivity of the dielectric	3.38
h	height of the dielectric slab	2 mm

with respect to y_o and x_o in Figures 5.38 and 5.39, respectively. A good agreement is observed between the results of HFSS and the results of the proposed method.

The sampling is performed along the path shown in Fig. 5.2 again by using 200 points. For the approximation of nine S-Parameter based entities, the number of complex exponentials used in DCIM varies between 8 and 14.

5.3.4 Increasing Periodicity

The size of the unit cell of the periodic multilayered structure shown in Figure 5.19 is increased compared to the one in Section 5.3.2. The size of the patches in the unit cell is kept constant. The parameters of this new problem is summarized in Table 5.4.

The y component of the scattered electric field due to a y oriented dipole is plotted with respect to y_o and x_o in Figures 5.40 and 5.41, respectively. A good agreement is observed between the results of HFSS and the results of the proposed method.

The sampling is performed along the path shown in Fig. 5.2 again by using 200 points. For the approximation of nine S-Parameter based entities, the number of complex exponentials used in DCIM varies between 8 and 15.

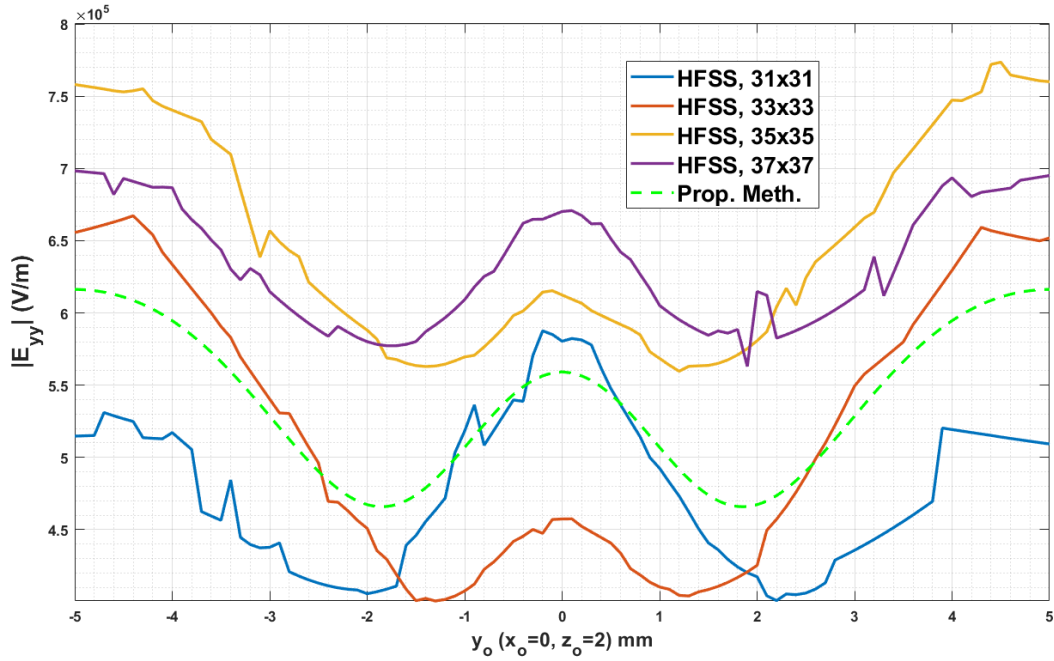


Figure 5.38: Magnitude of E_{yy} with respect to y_o ($x_o = 0$ and $z_o = 2$ mm), scattered from the 2-D periodic structure with parameters given in Table 5.3

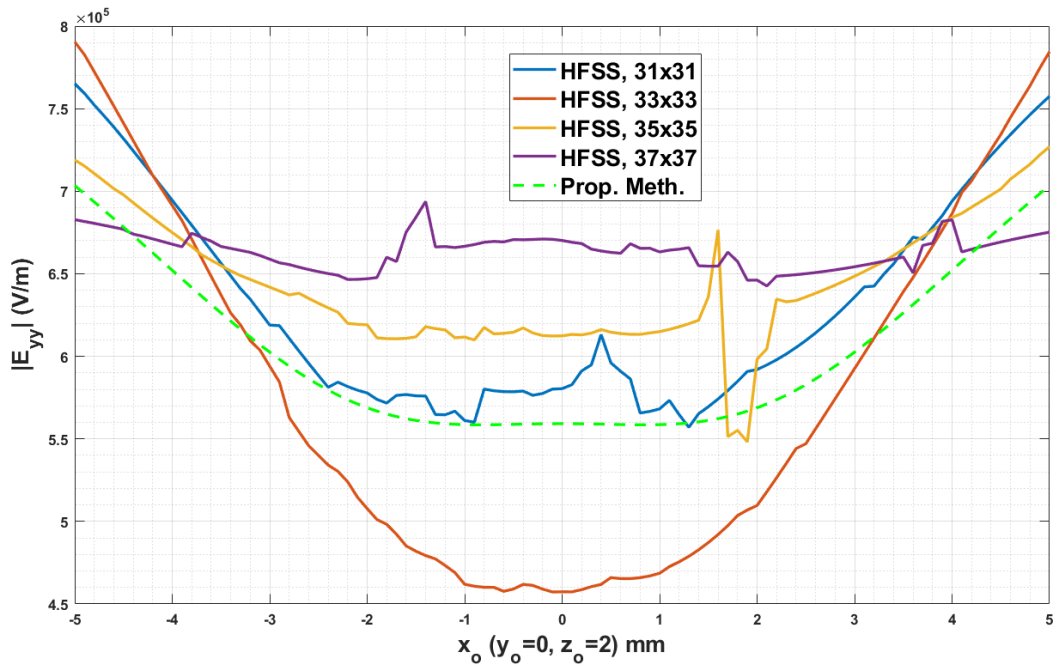


Figure 5.39: Magnitude of E_{yy} with respect to x_o ($y_o = 0$ and $z_o = 2$ mm), scattered from the 2-D periodic structure with parameters given in Table 5.3

Table 5.4: Parameters of the problem for multilayered case with increased periodicity

Parameter	Description	Value
f	frequency	15 GHz
D_x	periodicity in x direction	3 mm
D_y	periodicity in y direction	3 mm
w	width of the PEC scatterer	1.8 mm
l	length of the PEC scatterer	1.8 mm
x_d	x position of the dipole	0 mm
y_d	y position of the dipole	0 mm
z_d	z position of the dipole	3 mm
ϵ_r	relative permittivity of the dielectric	3.38
h	height of the dielectric slab	2 mm

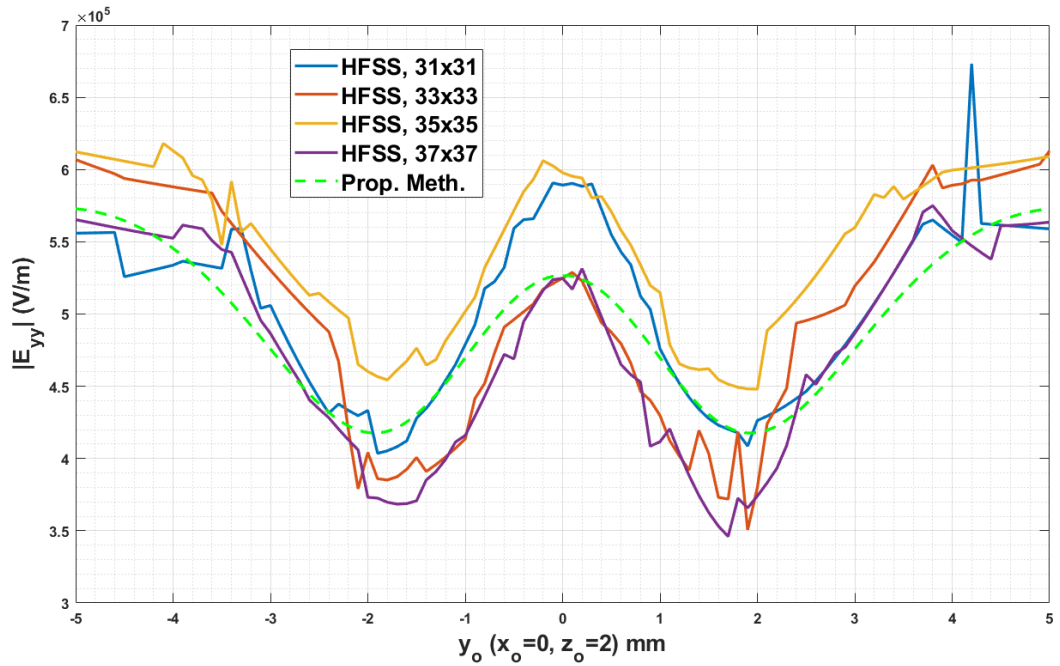


Figure 5.40: Magnitude of E_{yy} with respect to y_o ($x_o = 0$ and $z_o = 2$ mm), scattered from the 2-D periodic structure with parameters given in Table 5.4

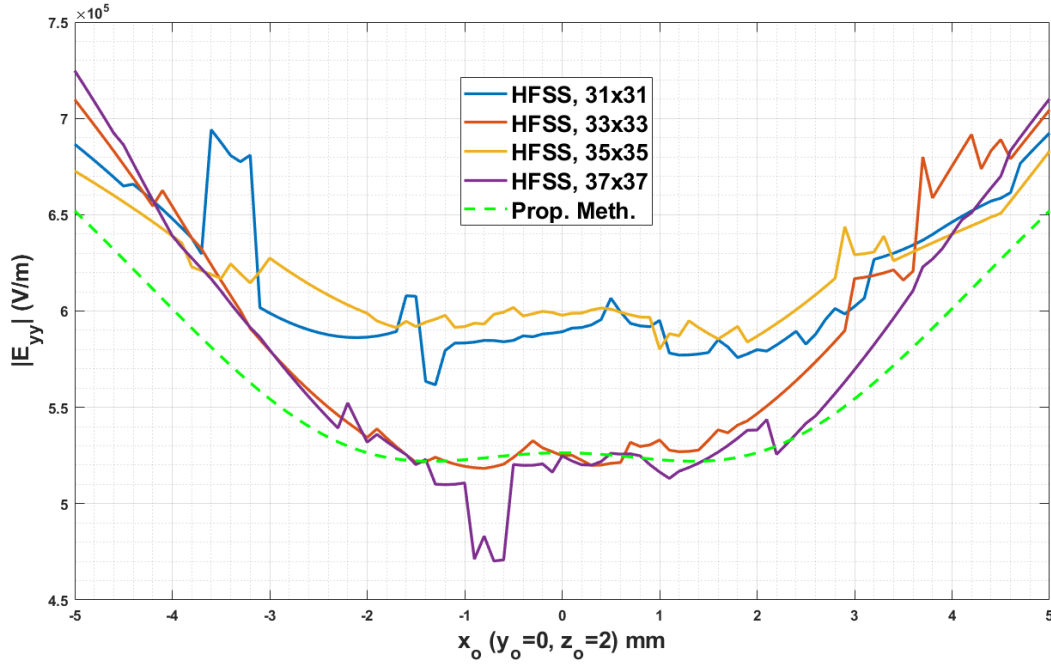


Figure 5.41: Magnitude of E_{yy} with respect to x_o ($y_o = 0$ and $z_o = 2$ mm), scattered from the 2-D periodic structure with parameters given in Table 5.4

5.3.5 Increasing Periodicity and Patch Size

The size of the unit cell of the periodic multilayered structure shown in Figure 5.19 is increased compared to the one in Section 5.3.3. The size of the patches in the unit cell is also increased by the same ratio. The parameters of this new problem is summarized in Table 5.5.

The y component of the scattered electric field due to a y oriented dipole is plotted with respect to y_o and x_o in Figures 5.42 and 5.43, respectively.

It is observed that the results of the proposed method are inconsistent with the results of HFSS. In order to investigate this issue further, accuracy of the complex image approximations in this problem (referred to as Prob-5 or Problem-5 in the following analyses and figures) is examined by plotting the sampled data together with the complex image approximation. The plots for the problem defined in Table 5.2 (referred to as Prob-2 or Problem-2 in the following analyses and figures) are also presented as a reference.

Table 5.5: Parameters of the problem for multilayered case with increased periodicity and patch size

Parameter	Description	Value
f	frequency	15 GHz
D_x	periodicity in x direction	4 mm
D_y	periodicity in y direction	4 mm
w	width of the PEC scatterer	3 mm
l	length of the PEC scatterer	3 mm
x_d	x position of the dipole	0 mm
y_d	y position of the dipole	0 mm
z_d	z position of the dipole	3 mm
ϵ_r	relative permittivity of the dielectric	3.38
h	height of the dielectric slab	2 mm

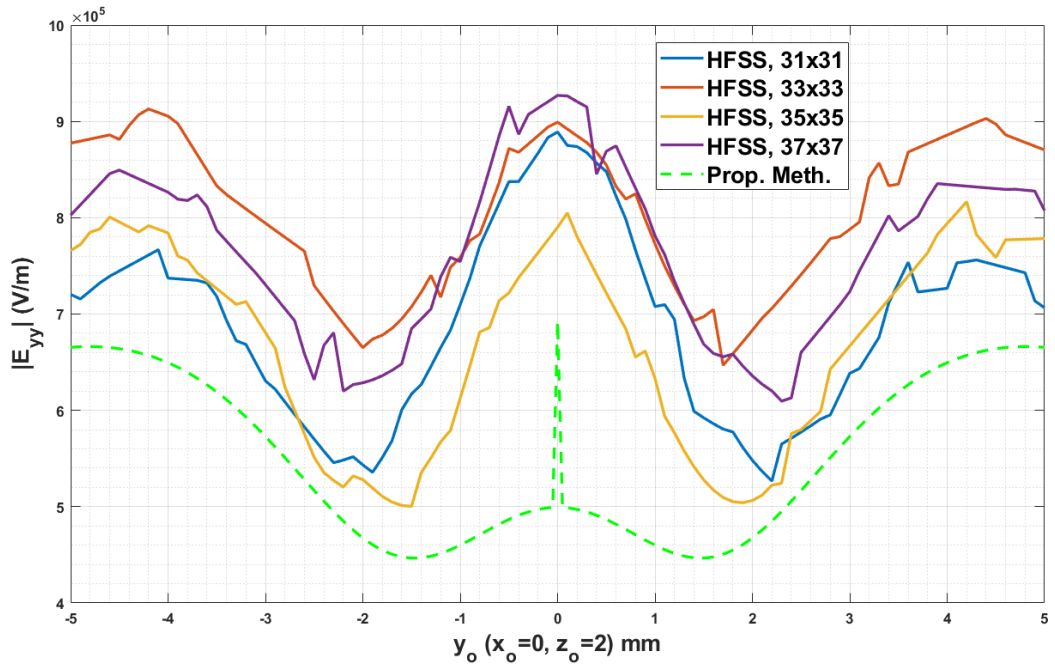


Figure 5.42: Magnitude of E_{yy} with respect to y_o ($x_o = 0$ and $z_o = 2$ mm), scattered from the 2-D periodic structure with parameters given in Table 5.5

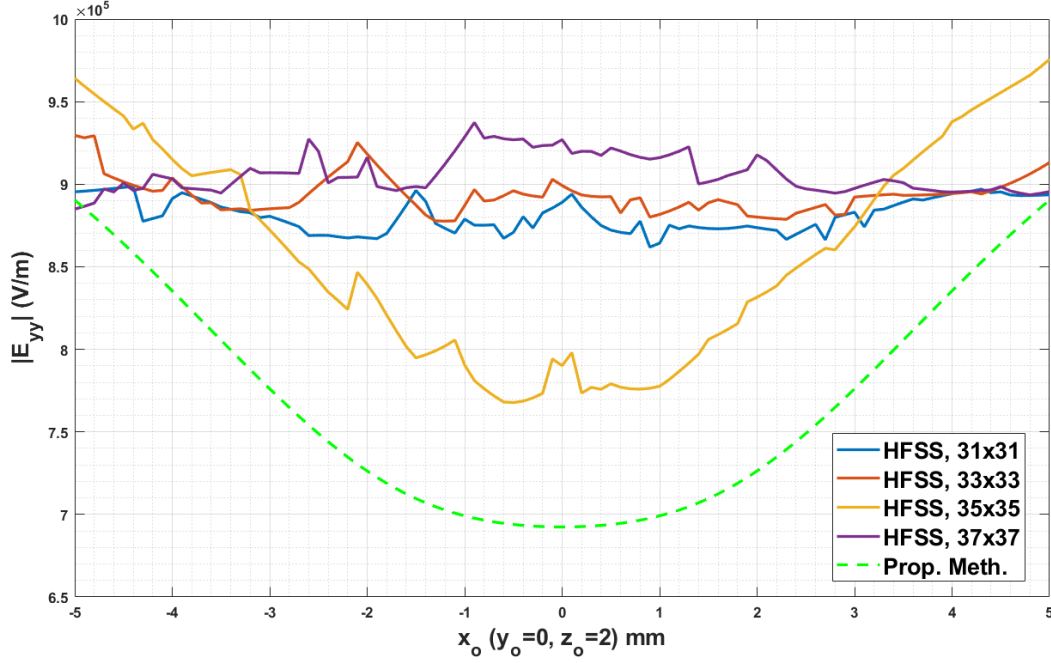


Figure 5.43: Magnitude of E_{yy} with respect to x_o ($y_o = 0$ and $z_o = 2$ mm), scattered from the 2-D periodic structure with parameters given in Table 5.5

Among the nine entities based on S-Parameters, whose closed forms are derived in section 5.2, SP1, SP3 and SP5 are chosen for analysis which are given as follows:

$$\begin{aligned}
 \text{SP1} &= S_{11}(k_\rho) = \sum_{k=1}^{N_1} B_{1k} e^{-jk_z \gamma_{1k}} \\
 \text{SP3} &= \frac{S_{22}(k_\rho) k_z^2}{k_s^2} = \sum_{k=1}^{N_3} B_{3k} e^{-jk_z \gamma_{3k}} \\
 \text{SP5} &= \frac{S_{22} k_z}{k_s^2} = \sum_{k=1}^{N_5} B_{5k} e^{-jk_z \gamma_{5k}}
 \end{aligned} \tag{5.134}$$

The sampling is performed along the path shown in Fig. 5.2 again by using 200 points. However, the distribution of the singular values are unusual for this problem, i.e. when sorted in decreasing order, the singular values does not decay in the expected rate. Applying the default threshold value (1×10^{-8}) for the truncation of singular values causes Matlab to encounter rank-deficient matrix issue which yields largely inaccurate complex exponentials. In order to avoid this deficiency, much

higher threshold values are applied which results in low accuracy approximation.

Complex image approximation of SP1 for Problem-2 is shown in Figure 5.44. The number of complex exponentials used in DCIM is 13. The relative error of the approximation is very low, 1.68×10^{-8} , as noted on the figure. On the other hand, complex image approximation of SP1 for Problem-5 has a larger relative error, 4.1×10^{-3} , as shown in Figure 5.45. There is a discontinuity in the curve of sampled data when $|k_\rho|/k_s$ is at around 4. This can be more easily observed on a zoomed-in view which is shown in the green box on the figure. The number of complex exponentials used in DCIM is 14 for this approximation.

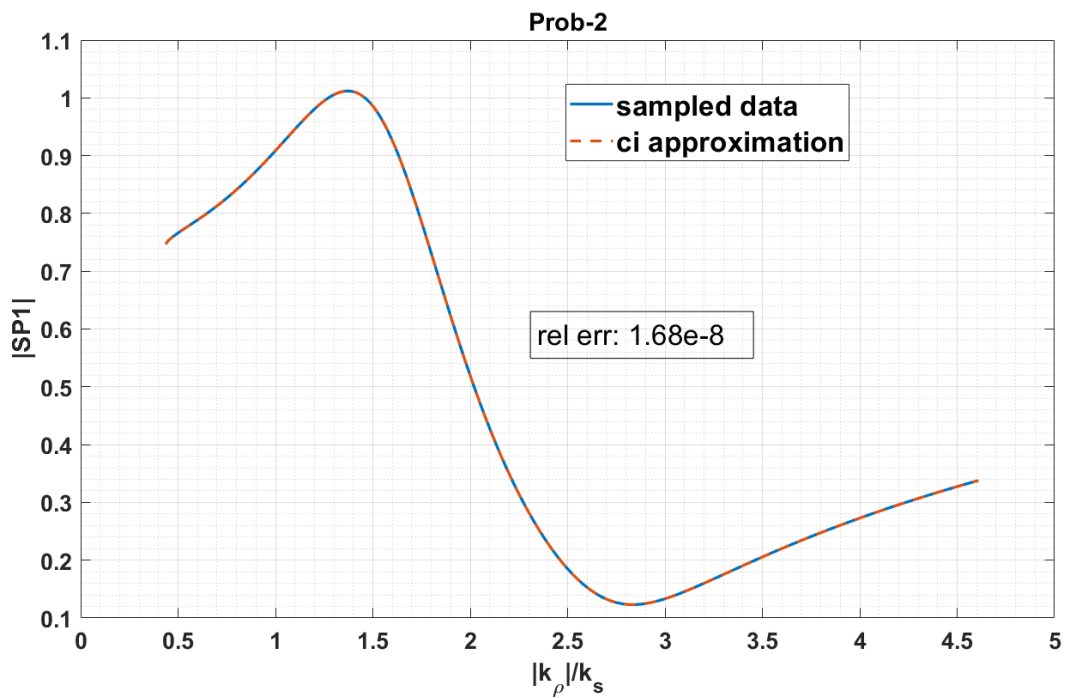


Figure 5.44: Sampled data (result of numerical calculation) and the complex image approximation (by DCIM) of SP1 for Problem-2

Complex image approximation of SP3 for Problem-2 is shown in Figure 5.46. The number of complex exponentials used in DCIM is 8. The relative error of the approximation is very low, 1.78×10^{-8} , as noted on the figure. On the other hand, complex image approximation of SP3 for Problem-5 has a larger relative error, 3.1×10^{-2} , as shown in Figure 5.47. There is again a discontinuity in the curve of sampled data when $|k_\rho|/k_s$ is at around 4, which is clearly seen on the zoomed-in view in the green

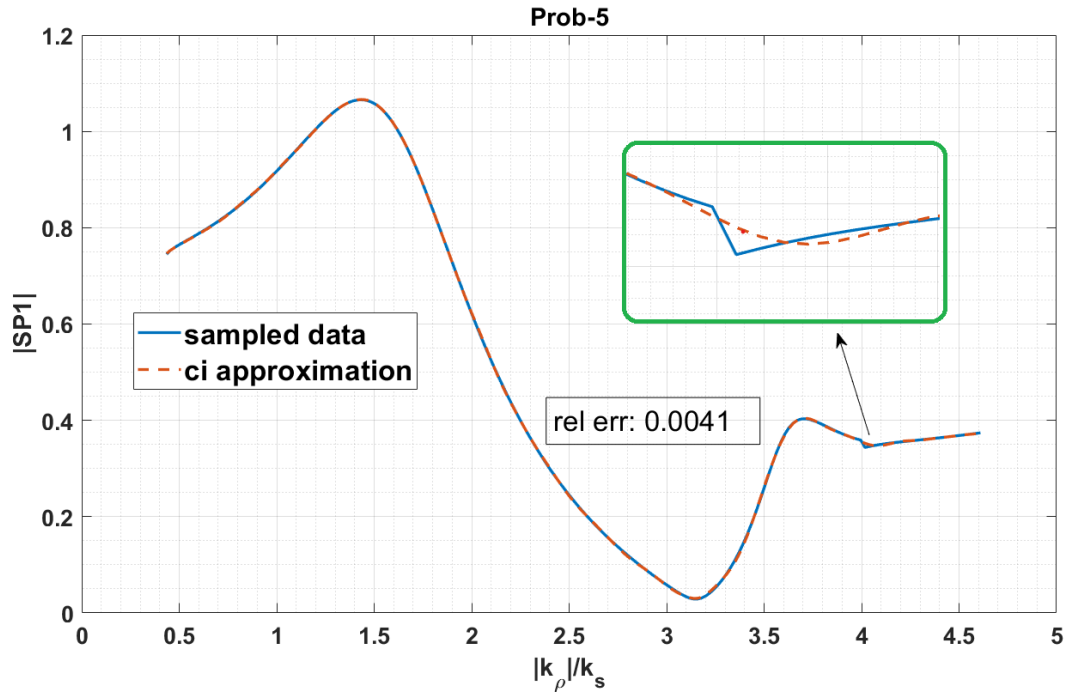


Figure 5.45: Sampled data (result of numerical calculation) and the complex image approximation (by DCIM) of SP1 for Problem-5

box. The number of complex exponentials used in DCIM is 5 for this approximation.

Complex image approximation of SP5 for Problem-2 is shown in Figure 5.48. The number of complex exponentials used in DCIM is 9. The relative error of the approximation is very low, 9.66×10^{-9} , as noted on the figure. On the other hand, complex image approximation of SP5 for Problem-5 has a larger relative error as shown in Figure 5.49. There is again a discontinuity in the curve of sampled data when $|k_\rho|/k_s$ is at around 4, which is seen on the zoomed-in view in the green box. Even though the approximation curve seems to fit the sampled data in the figure, the relative error is 7.02×10^{-4} which is much larger than the error in Problem-2. The number of complex exponentials used in DCIM is 31 for this approximation.

The discontinuity in the curves of sampled data of Problem-5 is the reason of the unusual distribution of the singular values which causes low accuracy in the approximations. This issue will further be analyzed to understand the underlying causes in order to be able to solve them. This is left as a future work.

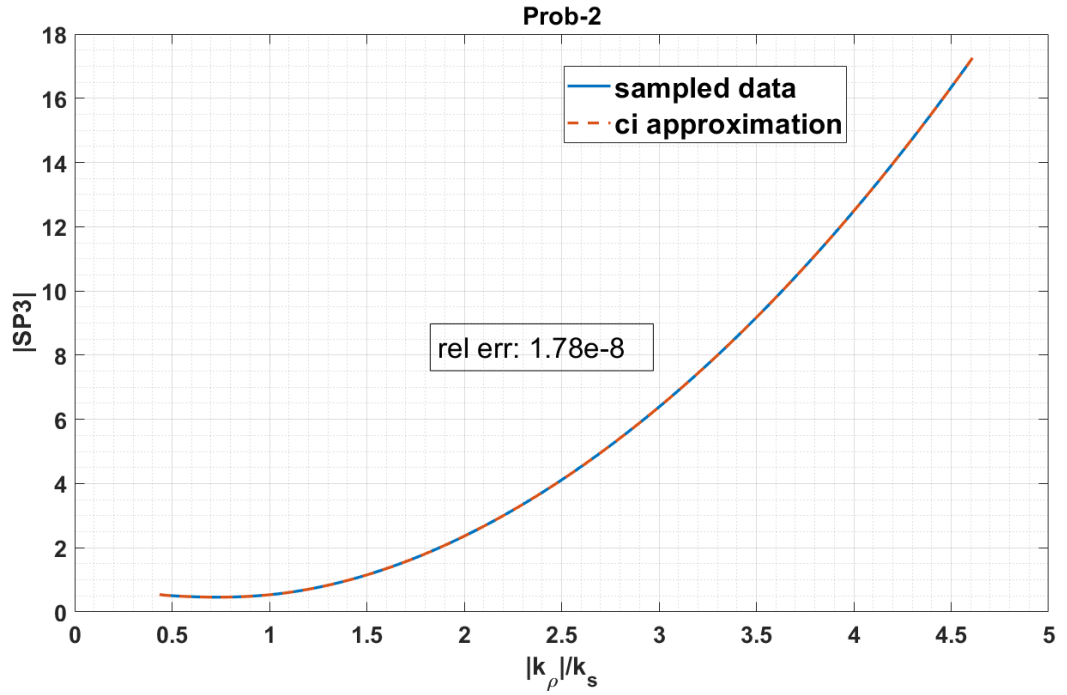


Figure 5.46: Sampled data (result of numerical calculation) and the complex image approximation (by DCIM) of SP3 for Problem-2

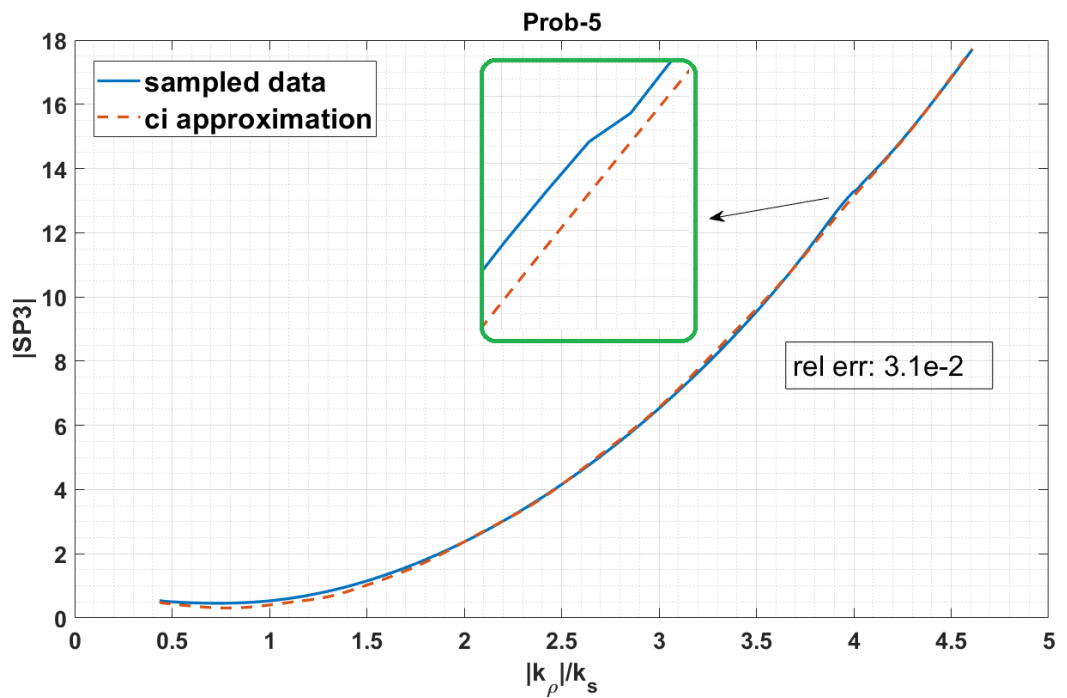


Figure 5.47: Sampled data (result of numerical calculation) and the complex image approximation (by DCIM) of SP3 for Problem-5

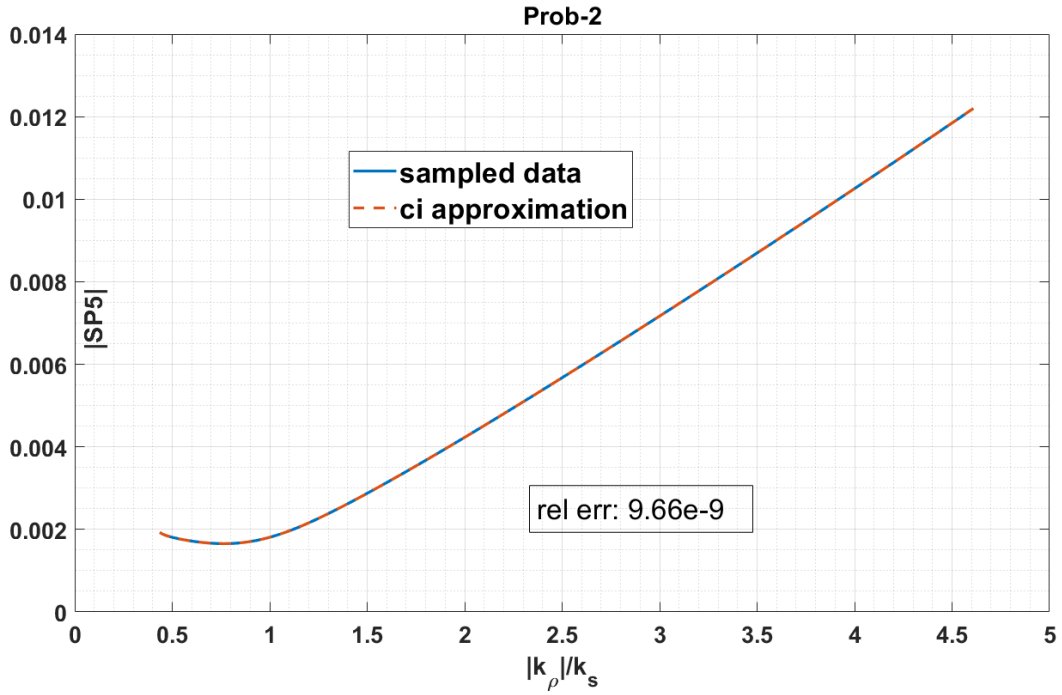


Figure 5.48: Sampled data (result of numerical calculation) and the complex image approximation (by DCIM) of SP5 for Problem-2

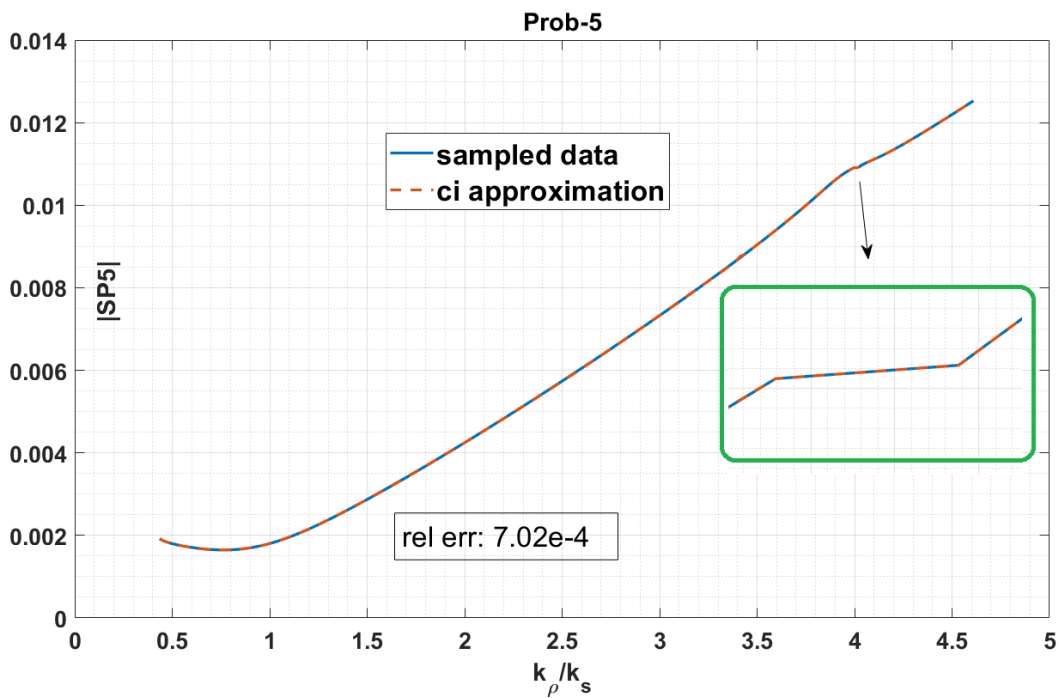


Figure 5.49: Sampled data (result of numerical calculation) and the complex image approximation (by DCIM) of SP5 for Problem-5

5.4 Proposals for Extending the Approach to Structures With ϕ Dependence

In this section, proposals for extending our approach to cover the asymmetric structures are presented.

We again consider the contribution of $S_{11}(\vec{k}_\rho)$ to $E_{yy}(\vec{r}_o, \vec{r}_d)$ for demonstration.

$$E_{yy}^{S_{11}}(\vec{r}_o, \vec{r}_d) = \frac{\omega\mu}{8\pi^2} \iint_{-\infty}^{+\infty} \left\{ dk_x dk_y e^{-jk_x(x_o-x_d)} e^{-jk_y(y_o-y_d)} \frac{e^{-jk_z(z_o+z_d)}}{k_z} \right. \\ \left. \times \left[-\frac{k_x^2}{k_\rho^2} S_{11}(\vec{k}_\rho) \right] \right\} \quad (5.135)$$

5.4.1 Fourier Series Approach

In this approach, Fourier series expansion is utilized to handle the ϕ -dependence in S-Parameters. The expression in equation (5.135) is transformed into cylindrical coordinates by the change of variables defined in (5.45).

$$E_{yy}^{S_{11}}(\vec{r}_o, \vec{r}_d) = -\frac{j\omega\mu}{8\pi} \int_0^{+\infty} k_\rho dk_\rho \frac{e^{-jk_z(z_o+z_d)}}{jk_z} \\ \times \frac{1}{\pi} \int_0^{2\pi} d\phi S_{11}(k_\rho, \phi) \cos^2(\phi) e^{-jk_\rho \rho \cos(\phi-\Psi)} \quad (5.136)$$

S-Parameter is now in the integrand of the integral with respect to ϕ . If we can separate the k_ρ and ϕ dependencies of the S-Parameter, we can handle this integral analytically provided that the ϕ -dependent function is suitable for this. Recalling the Bessel integral identity (A.6), the idea of Fourier series expansion arises. If we can expand $S_{11}(k_\rho, \phi)$ into a Fourier series as follows:

$$S_{11}(k_\rho, \phi) = \sum_{n=-\infty}^{+\infty} S_n^{11}(k_\rho) e^{jn\phi} \quad (5.137)$$

we can express the ϕ -dependent integral in terms of higher order Bessel functions.

Utilizing the recurrence relations of Bessel functions (A.7) together with the direct and derivative form of Sommerfeld Identities, one can reach closed form expressions for each component of electric field similar to the derivation presented in section 5.2.

The main challenge in this approach is about handling the high orders of Bessel functions arising as a result of the angle dependent integration. If we assume that truncating the Fourier series expansion at 2 is enough to handle the asymmetry accurately in a given problem, we can write the following:

$$S_{11}(k_\rho, \phi) \approx \sum_{n=-2}^{+2} S_n^{11}(k_\rho) e^{jn\phi} \quad (5.138)$$

Noting that we already have a $\cos^2 \phi$ term in the integrand, the total order of the exponential in the integral is 4, which means that a Bessel function of order 4, namely $J_4(k_\rho \rho)$, will arise as a result of this integral. In order to reach closed form expressions as a result of the k_ρ integration, we should be able to use the direct or derivative forms of Sommerfeld Identity which means that we should be able to express $J_4(k_\rho \rho)$ in terms of $J_0(k_\rho \rho)$ and $J_1(k_\rho \rho)$. This may be obtained by recurrence relations as follows:

$$\begin{aligned} J_4(k_\rho \rho) &= \frac{6}{k_\rho \rho} J_3(k_\rho \rho) - J_2(k_\rho \rho) \\ J_3(k_\rho \rho) &= \frac{4}{k_\rho \rho} J_2(k_\rho \rho) - J_1(k_\rho \rho) \\ J_2(k_\rho \rho) &= \frac{2}{k_\rho \rho} J_1(k_\rho \rho) - J_0(k_\rho \rho) \end{aligned} \quad (5.139)$$

Starting from the equation at the bottom and going to the top, we finally obtain the expression:

$$J_4(k_\rho \rho) = \frac{48}{k_\rho^3 \rho^3} J_1(k_\rho \rho) - \frac{8}{k_\rho \rho} J_1(k_\rho \rho) - \frac{24}{k_\rho^2 \rho^2} J_0(k_\rho \rho) + J_0(k_\rho \rho) \quad (5.140)$$

There are two main drawbacks associated with the expression in (5.140). The first one is the k_ρ^3 in the denominator of the first term. This will yield S-Parameters divided by k_ρ^4 that will be approximated by sum of complex images. Because of the fourth order pole at $k_\rho = 0$, one may encounter difficulties and possible inaccuracies in the complex image approximation.

Another drawback is related to the ρ^3 term dividing $J_1(k_\rho\rho)$ and ρ^2 term dividing $J_0(k_\rho\rho)$. These will yield $1/\rho^2$ factor in the final closed-form expressions and thus create second order poles numerically at $\rho = 0$ where no pole actually existed.

If the problem at hand does not allow to model its asymmetry by a Fourier series expansion truncated at 2, one will have to deal with Bessel functions of order larger than 4, which will make the closed-form expressions very tedious. Also, the drawbacks mentioned above will be more painful for these problems.

5.4.2 Averaging Approach

A simple approach to handle the angle dependency of S-Parameters is averaging the S-Parameter with respect to ϕ . This will not increase the order of Bessel functions in the solution as opposed to the Fourier series approach. Actually this technique may be seen as a special case of the Fourier series approach with the expansion truncated at $n = 0$. The main advantage of this approach is obviously its simplicity but it comes at the expense of losing some flexibility regarding the problem geometry as it may not yield results accurate enough for the geometries with high degree of asymmetry with respect to angle.

5.4.3 2-D Complex Image Approximation Approach

Assume that $S_{11}(\vec{k}_\rho)$ can be written in terms of complex exponentials as follows:

$$S_{11}(\vec{k}_\rho) = S_{11}(k_x, k_y) = \sum_{k=1}^M C_k e^{-jk_x a_k} e^{-jk_y b_k} \quad (5.141)$$

Putting this form of $S_{11}(\vec{k}_\rho)$ in equation (5.135) yields the following expression:

$$E_{yy}^{S_{11}}(\vec{r}_o, \vec{r}_d) = \frac{\omega\mu}{8\pi^2} \sum_{k=1}^M C_k \int_{-\infty}^{+\infty} \int_{-\infty}^{+\infty} \left\{ dk_x dk_y \frac{e^{-jk_z(z_o+z_d)}}{k_z} \right. \\ \left. \times \left[-\frac{k_x^2}{k_\rho^2} e^{-jk_x(x_o-x_d+a_k)-jk_y(y_o-y_d+b_k)} \right] \right\} \quad (5.142)$$

Now, this can be transformed into cylindrical coordinates by a suitable change of variables which is defined below:

$$\begin{aligned} k_x &= k_\rho \cos(\phi) \quad ; \quad k_y = k_\rho \sin(\phi) \\ x_o - x_d + a_k &= \rho_k \cos(\Psi_k) \quad ; \quad y_o - y_d + b_k = \rho_k \sin(\Psi_k) \\ dk_x dk_y &= k_\rho dk_\rho d\phi \end{aligned} \quad (5.143)$$

$$\begin{aligned} E_{yy}^{S_{11}}(\vec{r}_o, \vec{r}_d) &= -\frac{j\omega\mu}{8\pi} \sum_{k=1}^M C_k \left\{ \int_0^{+\infty} k_\rho dk_\rho \frac{e^{-jk_z(z_o+z_d)}}{jk_z} \right. \\ &\quad \left. \times \frac{1}{\pi} \int_0^{2\pi} d\phi \cos^2(\phi) e^{-jk_\rho \rho_k \cos(\phi-\Psi_k)} \right\} \end{aligned} \quad (5.144)$$

The integral with respect to ϕ (I) was studied in detail in section 5.2. $I = I_1 + I_{2a} + I_{2b}$ and these are given below as:

$$\begin{aligned} I_1 &= J_0(k_\rho \rho_k) \\ I_{2a} &= \cos(2\Psi_k) J_0(k_\rho \rho_k) \\ I_{2b} &= -\frac{2 \cos(2\Psi_k)}{\rho_k} \frac{1}{k_\rho} J_1(k_\rho \rho_k) \end{aligned} \quad (5.145)$$

$$E_{yy}^{S_{11}:I_1}(\vec{r}_o, \vec{r}_d) = -\frac{j\omega\mu}{8\pi} \sum_{k=1}^M C_k \int_0^{+\infty} k_\rho dk_\rho \frac{e^{-jk_z(z_o+z_d)}}{jk_z} J_0(k_\rho \rho_k) \quad (5.146)$$

$$E_{yy}^{S_{11}:I_1}(\vec{r}_o, \vec{r}_d) = -\frac{j\omega\mu}{8\pi} \sum_{k=1}^M C_k \frac{e^{-jk_s r_k}}{r_k} \quad (5.147)$$

where r_k is defined as:

$$r_k = \sqrt{(x_o - x_d + a_k)^2 + (y_o - y_d + b_k)^2 + (z_o + z_d)^2} \quad (5.148)$$

$$E_{yy}^{S_{11}:I_{2a}}(\vec{r}_o, \vec{r}_d) = -\frac{j\omega\mu}{8\pi} \sum_{k=1}^M C_k \cos(2\Psi_k) \frac{e^{-jk_s r_k}}{r_k} \quad (5.149)$$

For the contribution of I_{2b} , we have:

$$E_{yy}^{S_{11}:I_{2b}}(\vec{r}_o, \vec{r}_d) = \frac{j\omega\mu}{4\pi} \sum_{k=1}^M C_k \frac{\cos(2\Psi_k)}{\rho_k} \int_0^{+\infty} \frac{e^{-jk_z(z_o+z_d)}}{jk_z} \frac{1}{k_\rho^2} J_1(k_\rho \rho_k) k_\rho^2 dk_\rho \quad (5.150)$$

Comparing (5.150) to the derivative of Sommerfeld Identity, we have an extra $1/k_\rho^2$ term in the integrand which can be modeled by DCIM as a finite sum of complex exponentials in terms of k_z as follows:

$$\frac{1}{k_\rho^2} = \sum_{n=1}^N A_n e^{-jk_z c_n} \quad (5.151)$$

This modeling converts (5.150) to the one below:

$$E_{yy}^{S_{11}:I_{2b}}(\vec{r}_o, \vec{r}_d) = \frac{j\omega\mu}{4\pi} \sum_{k=1}^M C_k \frac{\cos(2\Psi_k)}{\rho_k} \sum_{n=1}^N A_n \int_0^{+\infty} \frac{e^{-jk_z(z_o+z_d+c_n)}}{jk_z} J_1(k_\rho \rho_k) k_\rho^2 dk_\rho \quad (5.152)$$

$$E_{yy}^{S_{11}:I_{2b}}(\vec{r}_o, \vec{r}_d) = \frac{j\omega\mu}{4\pi} \sum_{k=1}^M C_k \cos(2\Psi_k) \sum_{n=1}^N A_n (1 + jk_s r_{kn}) \frac{e^{-jk_s r_{kn}}}{r_{kn}^3} \quad (5.153)$$

where r_{kn} is defined as follows:

$$r_{kn} = \sqrt{(x_o - x_d + a_k)^2 + (y_o - y_d + b_k)^2 + (z_o + z_d + c_n)^2} \quad (5.154)$$

In this approach, there is no increase in the order of Bessel functions and thus there is no increase in the order of pole at $k_\rho = 0$ which may complicate DCIM modeling. Also there will be no singularity created at $\rho = 0$ point in the final closed-form expressions as opposed to the Fourier series approach. 2-D complex image approximation has the potential to handle the high degrees of ϕ dependence which makes this approach more accurate compared to averaging technique.

The question about this approach is whether one can model the S-Parameters as in (5.141). 2-D ESPRIT technique [84], which is successfully applied to 3-D structures in multilayered media (no periodicity) in [85], can be utilized to accomplish this modeling. A brief summary of the technique is given in Appendix B.

2-D ESPRIT method is applicable for a complex function with two real variables along which the function is sampled equally.

$$\begin{aligned} k_x &= (k_{xf} - k_{xi})t_x + k_{xi} \quad , \quad 0 \leq t_x \leq 1 \\ k_y &= (k_{yf} - k_{yi})t_y + k_{yi} \quad , \quad 0 \leq t_y \leq 1 \end{aligned} \quad (5.155)$$

The challenge in this approach is that if k_x and k_y parameters are sampled purely on real values, k_ρ is also purely real over the sampling area and it goes over $k_\rho = k_s$ points which form a circle in the $k_x - k_y$ plane. These are the branch points and the singularity they create causes the complex image approximation fail. The solution to this issue proposed here is to sample k_x and k_y on straight lines which are at a non-zero angle with the real axis of complex k_x and k_y planes respectively. For example if we choose $k_{xf} = k_{yf} = 5k_s(1 + j0.1)$ and $k_{xi} = k_{yi} = -5k_s(1 + j0.1)$ in (5.155), then:

$$\begin{aligned} k_x &= 5k_s(1 + j0.1)(2t_x - 1) \quad , \quad 0 \leq t_x \leq 1 \\ k_y &= 5k_s(1 + j0.1)(2t_y - 1) \quad , \quad 0 \leq t_y \leq 1 \\ k_\rho &= 5k_s(1 + j0.1)\sqrt{(2t_x - 1)^2 + (2t_y - 1)^2} \quad , \quad 0 \leq t_x, t_y \leq 1 \end{aligned} \quad (5.156)$$

This way, k_ρ will never pass over the $k_\rho = k_s$ ($k_z = 0$) circle, since there will always be a non-zero imaginary part of it. The sign of this imaginary part is positive which is consistent with the negative sign of the imaginary part of k_z satisfying the radiation condition.

CHAPTER 6

CONCLUSION

A novel approach has been developed in this thesis work to analyze the fields due to electric dipole sources in the vicinity of planar periodic structures.

The approach is based on reflection coefficient analysis of these structures by a MoM technique. Because of the importance of this analysis in the developed approach, the accuracy and efficiency of the implemented MoM solution for S-Parameter calculation has been demonstrated in detail in this thesis.

The closed-form Green's functions for the electric dipole over planar periodic structures have been derived in detail for all components of the electric field due to all orientations of the dipole source. The accuracy of the proposed method is demonstrated with various plots including both magnitude and phase of scattered electric fields. The very high computing cost of the commercial 3-D EM solvers compared to our approach can easily be seen in the figures of Chapter 5 presenting the tangential component of the scattered electric field due to horizontally oriented dipole, since in this case the required number of cells that should be included in the simulation by commercial solver is very high.

It is believed that the proposed method in this thesis work will fill an important gap in the literature by obtaining closed-form Green's function expressions for the dipole excitation of periodic planar structures. It will eliminate the need for calculating the inverse Fourier or Sommerfeld integrals at every different source-observation point pairs thanks to its output being in closed-form. It will achieve this efficiency while keeping the accuracy at high levels even for field variations at small scales thanks to the full wave MoM solution it is based on.

In addition to its current success, the proposed method has the potential to be extended to cover more general problems. For the structures with rotational asymmetry, three approaches have been proposed at the end of Chapter 5. By this future work, anisotropic metasurfaces could also be analyzed efficiently and accurately.

Another possible future work can be on the extension of the technique for higher order scattered field modes. Such an extension would make the efficient analysis of structures with larger periodicities possible. Covering the higher order Floquet modes could also make the analysis at closer observation points more accurate.

REFERENCES

- [1] C. L. Holloway, E. F. Kuester, J. A. Gordon, J. O'Hara, J. Booth, and D. R. Smith, "An overview of the theory and applications of metasurfaces: the two-dimensional equivalents of metamaterials," *IEEE Antennas and Propagation Magazine*, vol. 54, no. 2, pp. 10–35, Apr. 2012, doi: 10.1109/MAP.2012.6230714.
- [2] P. S. Neelakanta, *Handbook of electromagnetic materials: monolithic and composite versions and their applications*. Boca Raton: CRC Press, 1995.
- [3] A. H. Sihvola, *Electromagnetic mixing formulas and applications*, 1st ed./Reprint with new cover. London: Institution of Engineering and Technology, 1999.
- [4] S. Zouhdi, A. H. Sihvola, and M. Arsalane, *Advances in Electromagnetics of Complex Media and Metamaterials*. 2002. Accessed: Jul. 12, 2022. [Online]. Available: <https://doi.org/10.1007/978-94-007-1067-2>
- [5] L. Brillouin, *Wave propagation in periodic structures: Electric filters and crystal lattices*, 2nd edition. Dover Publications, 1953.
- [6] A. Ishimaru, *Electromagnetic Wave Propagation, Radiation, and Scattering*, 1 edition. Englewood Cliffs, N.J: Prentice Hall, 1990.
- [7] C. M. Soukoulis, Ed., *Photonic Band Gap Materials*, 1996th edition. Dordrecht ; Boston: Springer, 1996.
- [8] B. A. Munk, *Frequency Selective Surfaces: Theory and Design*. Hoboken, NJ, USA: John Wiley & Sons, Inc., 2000. doi: 10.1002/0471723770.
- [9] N. Engheta, R. W. Ziolkowski, and Institute of Electrical and Electronics Engineers, Eds., *Metamaterials: physics and engineering explorations*. Hoboken, N.J: Wiley-Interscience, 2006.
- [10] I. Brener, *Dielectric Metamaterials: Fundamentals, Designs and Applications*. 2020.

- [11] R. W. Ziolkowski and N. Engheta, “Metamaterials: two decades past and into their electromagnetics future and beyond,” *IEEE Transactions on Antennas and Propagation*, vol. 68, no. 3, pp. 1232–1237, Mar. 2020, doi: 10.1109/TAP.2019.2938674.
- [12] F. Yang and Y. Rahmat-Samii, Eds., *Surface electromagnetics: with applications in antenna, microwave, and optical engineering*. Cambridge, United Kingdom ; New York, NY: Cambridge University Press, 2019.
- [13] E. Martini and S. Maci, “Modulated Metasurfaces for Microwave Field Manipulation: Models, Applications, and Design Procedures,” *IEEE Journal of Microwaves*, vol. 2, no. 1, pp. 44–56, Jan. 2022, doi: 10.1109/JMW.2021.3126199.
- [14] D. Sievenpiper, Lijun Zhang, R. F. J. Broas, N. G. Alexopolous, and E. Yablonovitch, “High-impedance electromagnetic surfaces with a forbidden frequency band,” *IEEE Trans. Microwave Theory Techn.*, vol. 47, no. 11, pp. 2059–2074, Nov. 1999, doi: 10.1109/22.798001.
- [15] Fan Yang and Y. Rahmat-Samii, “Reflection phase characterizations of the EBG ground plane for low profile wire antenna applications,” *IEEE Trans. Antennas Propagat.*, vol. 51, no. 10, pp. 2691–2703, Oct. 2003, doi: 10.1109/TAP.2003.817559.
- [16] A. P. Feresidis, G. Goussetis, Shenhong Wang, and J. C. Vardaxoglou, “Artificial magnetic conductor surfaces and their application to low-profile high-gain planar antennas,” *IEEE Trans. Antennas Propagat.*, vol. 53, no. 1, pp. 209–215, Jan. 2005, doi: 10.1109/TAP.2004.840528.
- [17] Ying Zhang, J. von Hagen, M. Younis, C. Fischer, and W. Wiesbeck, “Planar artificial magnetic conductors and patch antennas,” *IEEE Trans. Antennas Propagat.*, vol. 51, no. 10, pp. 2704–2712, Oct. 2003, doi: 10.1109/TAP.2003.817550.
- [18] H. Mosallaei and K. Sarabandi, “Antenna miniaturization and bandwidth enhancement using a reactive impedance substrate,” *IEEE Trans. Antennas Propagat.*, vol. 52, no. 9, pp. 2403–2414, Sep. 2004, doi: 10.1109/TAP.2004.834135.
- [19] R. F. J. Broas, D. F. Sievenpiper, and E. Yablonovitch, “An application of high-impedance ground planes to phased array antennas,” *IEEE Transactions*

- on Antennas and Propagation*, vol. 53, no. 4, pp. 1377–1381, Apr. 2005, doi: 10.1109/TAP.2005.844408.
- [20] M. Li, S.-Q. Xiao, and B.-Z. Wang, “Investigation of Using High Impedance Surfaces for Wide-Angle Scanning Arrays,” *IEEE Transactions on Antennas and Propagation*, vol. 63, no. 7, pp. 2895–2901, Jul. 2015, doi: 10.1109/TAP.2015.2421936.
- [21] M. Li, S.-Q. Xiao, J. Xiong, and B.-Z. Wang, “Horizontal Dipole Located Close to Ground Plane With Bidirectional Endfire Radiation,” *IEEE Antennas and Wireless Propagation Letters*, vol. 13, pp. 1144–1147, 2014, doi: 10.1109/LAWP.2014.2331104.
- [22] M. Li, S.-Q. Xiao, Z. Wang, and B.-Z. Wang, “Compact Surface-Wave Assisted Beam-Steerable Antenna Based on HIS,” *IEEE Transactions on Antennas and Propagation*, vol. 62, no. 7, pp. 3511–3519, Jul. 2014, doi: 10.1109/TAP.2014.2321161.
- [23] Z. L. Ma and C. H. Chan, “A Novel Surface-Wave-Based High-Impedance Surface Multibeam Antenna With Full Azimuth Coverage,” *IEEE Transactions on Antennas and Propagation*, vol. 65, no. 4, pp. 1579–1588, Apr. 2017, doi: 10.1109/TAP.2017.2670320.
- [24] J. Tamura, H. Arai, and T. Itoh, “High-Impedance Surface-Based Null-Steering Antenna for Angle-of-Arrival Estimation,” *IEEE Transactions on Antennas and Propagation*, vol. 70, no. 5, pp. 3269–3276, May 2022, doi: 10.1109/TAP.2021.3137469.
- [25] A. M. Nicolson and G. F. Ross, “Measurement of the intrinsic properties of materials by time-domain techniques,” *IEEE Transactions on Instrumentation and Measurement*, vol. 19, no. 4, pp. 377–382, Nov. 1970, doi: 10.1109/TIM.1970.4313932.
- [26] W. B. Weir, “Automatic measurement of complex dielectric constant and permeability at microwave frequencies,” *Proceedings of the IEEE*, vol. 62, no. 1, pp. 33–36, Jan. 1974, doi: 10.1109/PROC.1974.9382.

- [27] D. R. Smith, S. Schultz, P. Markoš, and C. M. Soukoulis, “Determination of effective permittivity and permeability of metamaterials from reflection and transmission coefficients,” *Phys. Rev. B*, vol. 65, no. 19, p. 195104, Apr. 2002, doi: 10.1103/PhysRevB.65.195104.
- [28] C. L. Holloway, A. Dienstfrey, E. F. Kuester, J. F. O’Hara, A. K. Azad, and A. J. Taylor, “A discussion on the interpretation and characterization of metafilms/metamaterials: The two-dimensional equivalent of metamaterials,” *Metamaterials*, vol. 3, no. 2, pp. 100–112, Oct. 2009, doi: 10.1016/j.metmat.2009.08.001.
- [29] C. R. Simovski, M. S. Kondratjev, P. A. Belov, and S. A. Tretyakov, “Interaction effects in two-dimensional bianisotropic arrays,” *IEEE Transactions on Antennas and Propagation*, vol. 47, no. 9, pp. 1429–1439, Sep. 1999, doi: 10.1109/8.793323.
- [30] E. F. Kuester, M. A. Mohamed, M. Piket-May, and C. L. Holloway, “Averaged transition conditions for electromagnetic fields at a metafilm,” *IEEE Trans. Antennas and Propag.*, vol. 51, no. 10, pp. 2641–2651, Oct. 2003, doi: 10.1109/TAP.2003.817560.
- [31] S. Tretyakov, *Analytical Modeling in Applied Electromagnetics*. Boston: Artech House, 2003.
- [32] C. L. Holloway, M. A. Mohamed, E. F. Kuester, and A. Dienstfrey, “Reflection and transmission properties of a metafilm: with an application to a controllable surface composed of resonant particles,” *IEEE Transactions on Electromagnetic Compatibility*, vol. 47, no. 4, pp. 853–865, Nov. 2005, doi: 10.1109/TEMC.2005.853719.
- [33] C. L. Holloway and E. F. Kuester, “A homogenization technique for obtaining generalized sheet-transition conditions for a metafilm embedded in a magnetodielectric interface,” *IEEE Trans. Antennas Propag.*, vol. 64, no. 11, pp. 4671–4686, Nov. 2016, doi: 10.1109/TAP.2016.2600764.
- [34] C. L. Holloway and E. F. Kuester, “Generalized sheet transition conditions for a metascreen—a fishnet metasurface,” *IEEE Trans. Antennas Propag.*, vol. 66, no. 5, pp. 2414–2427, May 2018, doi: 10.1109/TAP.2018.2809620.

- [35] C. L. Holloway, E. F. Kuester, and A. H. Haddab, “Retrieval approach for determining surface susceptibilities and surface porosities of a symmetric metascreen from reflection and transmission coefficients,” *Progress in Electromagnetics Research*, vol. 166, pp. 1–22, 2019, doi: 10.2528/pier19022305.
- [36] C. L. Holloway, E. F. Kuester, and A. H. Haddab, “Using reflection and transmission coefficients to retrieve surface parameters for an anisotropic metascreen: With a discussion on conversion between TE and TM polarizations,” *Journal of Applied Physics*, vol. 125, no. 9, 2019, doi: 10.1063/1.5050987.
- [37] S. A. Tretyakov, A. J. Viitanen, S. I. Maslovski, and I. E. Saarela, “Impedance boundary conditions for regular dense arrays of dipole scatterers,” *IEEE Trans. Antennas Propag.*, vol. 51, no. 8, pp. 2073–2078, Aug. 2003, doi: 10.1109/TAP.2003.814737.
- [38] O. Luukkonen et al., “Simple and accurate analytical model of planar grids and high-impedance surfaces comprising metal strips or patches,” *IEEE Trans. Antennas Propag.*, vol. 56, no. 6, pp. 1624–1632, Jun. 2008, doi: 10.1109/TAP.2008.923327.
- [39] F. Capolino, D. R. Jackson, D. R. Wilton, and L. B. Felsen, “Comparison of methods for calculating the field excited by a dipole near a 2-D periodic material,” *IEEE Trans. Antennas Propag.*, vol. 55, no. 6, pp. 1644–1655, Jun. 2007, doi: 10.1109/TAP.2007.897348.
- [40] N. Kinayman and M. I. Aksun, *Modern Microwave Circuits*. Boston, Mass: Artech House, 2005.
- [41] R. Sigelmann and A. Ishimaru, “Radiation from periodic structures excited by an aperiodic source,” *IEEE Trans. Antennas Propagat.*, vol. 13, no. 3, pp. 354–364, May 1965, doi: 10.1109/TAP.1965.1138437.
- [42] V. Galindo and C. Wu, “Asymptotic behavior of the coupling coefficients for an infinite array of thin-walled rectangular waveguides,” *IEEE Transactions on Antennas and Propagation*, vol. 14, no. 2, pp. 248–249, Mar. 1966, doi: 10.1109/TAP.1966.1138647.

- [43] B. Munk and G. Burrell, “Plane-wave expansion for arrays of arbitrarily oriented piecewise linear elements and its application in determining the impedance of a single linear antenna in a lossy half-space,” *IEEE Trans. Antennas Propagat.*, vol. 27, no. 3, pp. 331–343, May 1979, doi: 10.1109/TAP.1979.1142089.
- [44] F. Capolino, D. R. Jackson, and D. R. Wilton, “Fundamental properties of the field at the interface between air and a periodic artificial material excited by a line source,” *IEEE Transactions on Antennas and Propagation*, vol. 53, no. 1, pp. 91–99, Jan. 2005, doi: 10.1109/TAP.2004.840518.
- [45] S. Paulotto, G. Lovat, P. Baccarelli, and P. Burghignoli, “Green’s function calculation for a line source exciting a 2-D periodic printed structure,” *IEEE Microw. Wireless Compon. Lett.*, vol. 20, no. 4, pp. 181–183, Apr. 2010, doi: 10.1109/LMWC.2010.2042542.
- [46] G. Lovat, R. Araneo, and S. Celozzi, “Dipole excitation of periodic metallic structures,” *IEEE Trans. Antennas Propagat.*, vol. 59, no. 6, pp. 2178–2187, Jun. 2011, doi: 10.1109/TAP.2011.2143660.
- [47] R. Araneo, G. Lovat, and S. Celozzi, “Shielding effectiveness of periodic screens against finite high-impedance near-field sources,” *IEEE Transactions on Electromagnetic Compatibility*, vol. 53, no. 3, pp. 706–716, Aug. 2011, doi: 10.1109/TEMPC.2010.2081367.
- [48] G. Lovat, R. Araneo, and S. Celozzi, “Electromagnetic shielding of resonant frequency-selective surfaces in presence of dipole sources,” *Applied Computational Electromagnetics Society Journal*, vol. 29, Jul. 2014.
- [49] A. Bakhtafrouz and A. Borji, “Application of the array scanning method in periodic structures with large periods,” *Electromagnetics*, vol. 35, no. 5, pp. 293–309, Jul. 2015, doi: 10.1080/02726343.2015.1047729.
- [50] G. Lovat, “Near-field shielding effectiveness of 1-D periodic planar screens with 2-D near-field sources,” *IEEE Trans. Electromagn. Compat.*, vol. 51, no. 3, pp. 708–719, Aug. 2009, doi: 10.1109/TEMPC.2009.2022273.
- [51] S. Paulotto, P. Baccarelli, P. Burghignoli, G. Lovat, G. W. Hanson, and A. B. Yakovlev, “Homogenized Green’s functions for an aperiodic line source

- over planar densely periodic artificial impedance surfaces,” *IEEE Trans. Microwave Theory Techn.*, vol. 58, no. 7, pp. 1807–1817, Jul. 2010, doi: 10.1109/TMTT.2010.2049917.
- [52] F. Liang et al., “Dyadic Green’s functions for dipole excitation of homogenized metasurfaces,” *IEEE Transactions on Antennas and Propagation*, vol. 64, no. 1, pp. 167–178, Jan. 2016, doi: 10.1109/TAP.2015.2501430.
- [53] HFSS, <https://www.ansys.com/products/electronics/ansys-hfss>, last accessed 08 Oct. 2022.
- [54] MATLAB, <https://www.mathworks.com/products/matlab.html>, last accessed 08 Oct. 2022
- [55] A. Azari, Z. H. Firouzeh, and A. Bakhtafrouz, “Calculation of potential Green’s functions for a planar metasurface excited by an electric dipole using homogenization method,” *Iran J Sci Technol Trans Electr Eng*, Jul. 2020, doi: 10.1007/s40998-020-00363-z.
- [56] A. Azari, Z. H. Firouzeh, and A. Bakhtafrouz, “Homogenized dyadic potential Green’s function for planar metasurface placed at two half spaces interface excited by vertical and horizontal ideal electric dipole,” *IEEE Trans. Antennas and Propag.*, vol. 68, no. 4, pp. 2965–2974, Apr. 2020, doi: 10.1109/TAP.2019.2963212.
- [57] A. Azari, Z. h. Firouzeh, and A. Bakhtafrouz, “Field calculation of electric dipole excitation of a metafilm printed on a finite-thickness dielectric slab using the susceptibility homogenization method,” *IET Microwaves, Antennas & Propagation*, vol. 15, no. 5, pp. 503–510, 2021, doi: 10.1049/mia2.12076.
- [58] A. K. Bhattacharyya, *Phased Array Antennas: Floquet Analysis, Synthesis, BFNs and Active Array Systems*, John Wiley and Sons Inc., NJ, 2006.
- [59] Chao-Chun Chen, “Scattering by a two-dimensional periodic array of conducting plates,” *IEEE Trans. Antennas Propag.*, vol. 18, no. 5, pp. 660–665, Sep. 1970, doi: 10.1109/TAP.1970.1139760.
- [60] D. M. Pozar, *Microwave Engineering*, 4th ed. Hoboken, NJ: Wiley, 2012.

- [61] S. Rao, D. Wilton, and A. Glisson, "Electromagnetic scattering by surfaces of arbitrary shape," *IEEE Trans. Antennas Propag.*, vol. 30, no. 3, pp. 409–418, May 1982, doi: 10.1109/TAP.1982.1142818.
- [62] D.A. Dunavant, "High degree efficient symmetrical gaussian quadrature rules for the triangle," *International Journal for Numerical Methods in Engineering*, vol.21, 1129-1148, 1985.
- [63] P. P. Ewald, "Die Berechnung optischer und elektrostatischer Gitterpotentiale," *Annalen der Physik*, vol. 369, no. 3, pp. 253–287, 1921, doi: 10.1002/andp.19213690304.
- [64] K. E. Jordan, G. R. Richter and P. Sheng, "An efficient numerical evaluation of the Green's function for the Helmholtz operator on periodic structures," *J. Comp. Phys.*, vol. 63, no. 1, pp. 222-235, Mar. 1986.
- [65] M. Abramowitz and I. A. Stegun, *Handbook of Mathematical Functions*. Washington DC: National Bureau of Standards, 1972.
- [66] CST, <https://www.3ds.com/products-services/simulia/products/cst-studio-suite/>, last accessed 08 Oct. 2022.
- [67] Y. L. Chow, J. J. Yang, D. G. Fang, and G. E. Howard, "A closed-form spatial Green's function for the thick microstrip substrate," *IEEE Trans. Microwave Theory Techn.*, vol. 39, no. 3, pp. 588–592, Mar. 1991, doi: 10.1109/22.75309.
- [68] A. Alparslan, M. I. Aksun, K. A. Michalski, "Closed-form Green's functions in planar layered media for all ranges and materials," *IEEE Trans. Microw. Theory Tech.*, vol. 58, pp. 602-613, Mar. 2010.
- [69] S. Adanir and L. Alatan, "Complete and accurate discrete complex image approximation of periodic Green's function in layered media," *IEEE Trans. Antennas Propag.*, vol. 62, no. 8, pp. 4115–4121, Aug. 2014, doi: 10.1109/TAP.2014.2323087.
- [70] Daoxiang Wang, Yung, Chen, Ding, and Tang, "On evaluation of the Green function for periodic structures in layered media," *Antennas Wirel. Propag. Lett.*, vol. 3, pp. 133–136, 2004, doi: 10.1109/LAWP.2004.831076.

- [71] Y. X. Yu and C. H. Chan, "On the extension of Ewald's method to periodic structures in layered media," *Microwave and Optical Technology Letters*, vol. 19, no. 2, pp. 125–131, 1998.
- [72] M. J. Park and B. Lee, "Efficient Calculation of the Green's Function for 2-D Periodic Line Sources Using Ewald Method," *IEEE Antennas Wireless Propag. Lett.*, vol. 8, pp. 565-567, 2009.
- [73] M. A. Khayat and D. R. Wilton, "Numerical evaluation of singular and near-singular potential integrals," *IEEE Trans. Antennas Propag.*, vol. 53, no. 10, pp. 3180–3190, Oct. 2005.
- [74] R. A. Kipp and C. H. Chan, "A numerically efficient technique for the method of moments solution for planar periodic structures in layered media," *IEEE Trans. Microw. Theory Tech.*, vol. 42, no. 4, pp. 635-643, Apr. 1994.
- [75] Y. Yu and C. H. Chan, "Efficient hybrid spatial and spectral techniques in analyzing planar periodic structures with nonuniform discretizations," *IEEE Trans. Microw. Theory Tech.*, vol. 48, pp. 1623–1627, Oct. 2000.
- [76] R. Florencio, R. R. Boix, and J. A. Encinar, "Fast and accurate MoM analysis of periodic arrays of multilayered stacked rectangular patches with application to the design of reflectarray antennas," *IEEE Trans. Antennas Propag.*, vol. 63, no. 6, pp. 2558–2571, Jun. 2015.
- [77] M. G. Duffy, "Quadrature over a pyramid or cube of integrands with a singularity at a vertex," *SIAM J. Numer. Anal.*, vol. 19, no. 6, pp. 1260–1262, 1982.
- [78] L. Rossi, P. J. Cullen, "On the fully numerical evaluation of the linear-shape function times the 3-D Green's function on a plane triangle," *IEEE Trans. Microw. Theory Tech.*, vol. 47, pp. 398-402, Apr. 1999.
- [79] M. A. Khayat, D. R. Wilton and P. W. Fink, "An improved transformation and optimized sampling scheme for the numerical evaluation of singular and near-singular potentials," *IEEE Antennas Wireless Propag. Lett.*, vol. 7, pp. 377-380, 2008.
- [80] S. Adanir and L. Alatan, "An application of singularity cancellation for periodic structures in free space," in *12th European Conference on Antennas and*

Propagation (EuCAP 2018), London, UK, 2018, p. 281 (3 pp.)-281 (3 pp.). doi: 10.1049/cp.2018.0640.

- [81] S. Adanır and L. Alatan, “Singularity cancellation for accurate MoM analysis of periodic planar structures in layered media,” *IEEE Antennas and Wireless Propagation Letters*, vol. 19, no. 8, pp. 1301–1305, Aug. 2020, doi: 10.1109/LAWP.2020.2997798.
- [82] Mathematica, <http://www.wolfram.com/mathematica/>, last accessed 08 Oct. 2022.
- [83] Y. Hua and T. K. Sarkar, “Generalized pencil-of-function method for extracting poles of an EM system from its transient response,” *IEEE Trans. Antennas Propagat.*, vol. 37, no. 2, pp. 229–234, Feb. 1989, doi: 10.1109/8.18710.
- [84] S. Rouquette and M. Najim, “Estimation of frequencies and damping factors by two-dimensional ESPRIT type methods,” *IEEE Transactions on Signal Processing*, vol. 49, no. 1, pp. 237–245, Jan. 2001, doi: 10.1109/78.890367.
- [85] Mengtao Yuan, Yu Zhang, A. De, Zhong Ji, and T. K. Sarkar, “Two-dimensional discrete complex image method (DCIM) for closed-form Green’s function of arbitrary 3D structures in general multilayered media,” *IEEE Trans. Antennas Propag.*, vol. 56, no. 5, pp. 1350–1357, May 2008, doi: 10.1109/TAP.2008.922176.
- [86] A. D. Poularikas, Ed., *Transforms and applications handbook*. 3rd ed. Boca Raton, Fla: CRC Press, 2010.
- [87] F. W. J. Olver, D. W. Lozier, R. F. Boisvert, and C. W. Clark, Eds., *NIST handbook of mathematical functions*. Cambridge ; New York: Cambridge University Press : NIST, 2010.

APPENDIX A

HANKEL TRANSFORM AND BESSEL IDENTITIES

The content is from [86] and [87].

The v^{th} order Hankel transform is defined as follows:

$$\tilde{F}_v(k_\rho) = \mathcal{H}_v\{f(\rho)\} = \int_0^\infty f(\rho) J_v(k_\rho \rho) \rho d\rho \quad (\text{A.1})$$

and the inversion formula is:

$$f(\rho) = \mathcal{H}_v^{-1}\{\tilde{F}_v(k_\rho)\} = \int_0^\infty \tilde{F}_v(k_\rho) J_v(k_\rho \rho) k_\rho dk_\rho \quad (\text{A.2})$$

where $J_v(z)$ is the Bessel function of the first kind of order v . The inversion formula is also known as Sommerfeld integral and for $v = 0$ we have the Sommerfeld identity given as:

$$\frac{e^{-jk_s r}}{r} = \int_0^\infty \frac{e^{-jk_z z}}{jk_z} J_0(k_\rho \rho) k_\rho dk_\rho \quad (\text{A.3})$$

Sometimes, it is needed to deal with first order inverse Hankel transforms. The derivative of the Sommerfeld Identity is useful in such situations. We take the derivative of both sides in Sommerfeld identity with respect to ρ to get:

$$\rho(1 + jk_s r) \frac{e^{-jk_s r}}{r^3} = \int_0^\infty \frac{e^{-jk_z z}}{jk_z} J_1(k_\rho \rho) k_\rho^2 dk_\rho \quad (\text{A.4})$$

In order to reach (A.4) from (A.3), we have used a derivative identity of Bessel function which is given as:

$$\frac{d}{dz}[z^{-v} J_v(z)] = -z^{-v} J_{v+1}(z) \quad (\text{A.5})$$

A useful integral representation of Bessel function of the first kind of integer order n is given as:

$$J_n(z) = \frac{j^{-n}}{2\pi} \int_0^{2\pi} e^{jz \cos \phi} e^{jn\phi} d\phi \quad (\text{A.6})$$

The recurrence relations are used to relate Bessel functions of different orders. A very useful one of them is given as follows:

$$J_{v-1}(z) + J_{v+1}(z) = \frac{2v}{z} J_v(z) \quad (\text{A.7})$$

Identities for negative argument and negative integer order are also worth mentioning as these are among the mostly used Bessel identities.

$$\begin{aligned} J_{-n}(z) &= (-1)^n J_n(z) \\ J_n(-z) &= (-1)^n J_n(z) \end{aligned} \quad (\text{A.8})$$

APPENDIX B

2-D ESPRIT METHOD

The procedure applied in 2-D ESPRIT method is summarized here. Details can be found in [84] and [85].

We assume that the function F of variables k_x and k_y can be expressed as summations of complex exponentials as in (B.1). The complex data is obtained numerically by sampling the function along two real variables.

$$F(k_x, k_y) \approx \sum_{k=1}^M C_k e^{-j(k_x a_k + k_y b_k)} \quad (\text{B.1})$$

The range of the transverse wavenumbers for this sampling is given in (B.2). The approximation takes the form in (B.3) in terms of t_x and t_y .

$$\begin{aligned} k_x &= (k_{xf} - k_{xi})t_x + k_{xi} \quad , \quad 0 \leq t_x \leq 1 \\ k_y &= (k_{yf} - k_{yi})t_y + k_{yi} \quad , \quad 0 \leq t_y \leq 1 \end{aligned} \quad (\text{B.2})$$

$$F(t_x, t_y) \approx \sum_{k=1}^M \tilde{C}_k e^{t_x X'_k + t_y Y'_k} \quad (\text{B.3})$$

We obtain a set of discrete data by sampling this expression as shown in (B.4) and (B.5). After utilizing the technique and find \tilde{C}_k , \tilde{X}_k and \tilde{Y}_k , we reach the original coefficients of the approximation through (B.6) and (B.7).

$$\begin{aligned} s(m, n) &= F((m-1)dt_x, (n-1)dt_y) \\ m &= 1, 2, \dots, M \quad ; \quad n = 1, 2, \dots, N \end{aligned} \quad (\text{B.4})$$

$$s(m, n) \approx \sum_{k=1}^M \tilde{C}_k \tilde{X}_k^m \tilde{Y}_k^n \quad (\text{B.5})$$

$$\begin{aligned} X'_k &= \log(\tilde{X}_k)/dt_x \\ Y'_k &= \log(\tilde{Y}_k)/dt_y \end{aligned} \quad (\text{B.6})$$

$$\begin{aligned} a_k &= \frac{X'_k}{-j(k_{xf} - k_{xi})} \\ b_k &= \frac{Y'_k}{-j(k_{yf} - k_{yi})} \\ C_k &= \tilde{C}_k e^{ja_k k_{xi}} e^{jb_k k_{yi}} \end{aligned} \quad (\text{B.7})$$

The technique starts with constructing an enhanced matrix \mathbf{F}_e from the samples $s(m, n)$. Here, K is the pencil parameter for t_x and L is the pencil parameter for t_y as described in the references.

$$\mathbf{F}_e = \begin{bmatrix} \mathbf{F}_1 & \mathbf{F}_2 & \dots & \mathbf{F}_{M-K+1} \\ \mathbf{F}_2 & \mathbf{F}_3 & \dots & \mathbf{F}_{M-K+2} \\ \vdots & \vdots & \vdots & \vdots \\ \mathbf{F}_K & \mathbf{F}_{K+1} & \dots & \mathbf{F}_M \end{bmatrix}$$

$$\mathbf{F}_m = \begin{bmatrix} s(m, 1) & s(m, 2) & \dots & s(m, N - L + 1) \\ s(m, 2) & s(m, 3) & \dots & s(m, N - L + 2) \\ \vdots & \vdots & \vdots & \vdots \\ s(m, L) & s(m, L + 1) & \dots & s(m, N) \end{bmatrix}$$

A singular value decomposition (SVD) is applied on \mathbf{F}_e to obtain the \mathbf{U}_1 matrix. From this matrix, we construct a new matrix \mathbf{G}_1 whose eigenvalues are the poles along t_x . $\underline{\mathbf{U}}_1$ is the matrix \mathbf{U}_1 with the last L rows deleted and $\overline{\mathbf{U}}_1$ is \mathbf{U}_1 with the first L rows deleted. The superscript $+$ means the pseudo-inverse of the matrix.

$$\mathbf{F}_e = \mathbf{U}_1 \mathbf{\Sigma}_1 \mathbf{V}_1^H \quad (\text{B.8})$$

$$\mathbf{G}_1 = \underline{\mathbf{U}}_1^+ \overline{\mathbf{U}}_1 \quad (\text{B.9})$$

From \mathbf{U}_1 , we obtain the matrix \mathbf{U}_2 by matrix product with the permutation matrix \mathbf{P} , which is defined in [84] by \mathbf{E}_1 .

$$\mathbf{U}_2 = \mathbf{P}\mathbf{U}_1 \quad (\text{B.10})$$

By a similar process to th one for \mathbf{U}_1 , we get a new matrix \mathbf{G}_2 whose eigenvalues are the poles along t_y .

$$\mathbf{G}_2 = \underline{\mathbf{U}}_2^+ \overline{\mathbf{U}}_2 \quad (\text{B.11})$$

We introduce a scalar parameter β and superpose \mathbf{G}_1 and \mathbf{G}_2 to obtain \mathbf{G} . From this \mathbf{G} , we find a common transformation matrix \mathbf{T} to diagonalize both \mathbf{G}_1 and \mathbf{G}_2 . The purpose of introducing β is explained in [84] as to avoid eigenvalues of multiplicity greater than 1.

$$\mathbf{G} = \beta\mathbf{G}_1 + (1 - \beta)\mathbf{G}_2 \quad (\text{B.12})$$

$$\mathbf{G} = \mathbf{T}\mathbf{D}\mathbf{T}^{-1} \quad (\text{B.13})$$

By diagonalizing \mathbf{G}_1 and \mathbf{G}_2 , we obtain the poles \tilde{X}_k and \tilde{Y}_k .

$$\begin{aligned} \Phi_1 &= \text{diag}_{1 \leq k \leq M} \{\tilde{X}_k\} = \mathbf{T}^{-1}\mathbf{G}_1\mathbf{T} \\ \Phi_2 &= \text{diag}_{1 \leq k \leq M} \{\tilde{Y}_k\} = \mathbf{T}^{-1}\mathbf{G}_2\mathbf{T} \end{aligned} \quad (\text{B.14})$$

To find the residues \tilde{C}_k , we build a matrix equation by using the complex data and equation (B.5).

Finally, we obtain the original coefficients of the approximation by using equations (B.6) and (B.7).

CURRICULUM VITAE

PERSONAL INFORMATION

Surname, Name: Adanır, Süleyman

Nationality: Turkish (TC)

Date and Place of Birth: 25 September 1986, Antalya

email: suleymanadanir@gmail.com

EDUCATION

Degree	Institution	Year of Graduation
M.S.	METU Electrical and Electronics Engineering	2011
B.S.	METU Electrical and Electronics Engineering	2008
High School	Özel Antalya Fen Lisesi	2004

PROFESSIONAL EXPERIENCE

Year	Place	Enrollment
2022-Present	Forefront RF	RF Engineer
2008-2022	ASELSAN, CIT	RF Engineer

FOREIGN LANGUAGES

Advanced English, Basic German

PUBLICATIONS

Journal Publications

[1] S. Adanir and L. Alatan, "Singularity cancellation for accurate MoM analysis of periodic planar structures in layered media," *IEEE Antennas and Wireless Propagation Letters*, vol. 19, no. 8, pp. 1301–1305, Aug. 2020, doi: 10.1109/LAWP.2020.2997798.

[2] S. Adanir and L. Alatan, "Complete and accurate discrete complex image approximation of periodic Green's function in layered media," *IEEE Transactions on Antennas and Propagation*, vol. 62, no. 8, pp. 4115–4121, Aug. 2014, doi: 10.1109/TAP.2014.2323087.

International Conference Publications

[1] S. Adanir and L. Alatan, "An application of singularity cancellation for periodic structures in free space," in *12th European Conference on Antennas and Propagation (EuCAP 2018)*, London, UK, 2018, p. 281 (3 pp.)-281 (3 pp.). doi: 10.1049/cp.2018.0640.

[2] S. Adanir and L. Alatan, "Discrete complex image approximation of periodic Green's functions in multilayer media," in *5th European Conference on Antennas and Propagation (EUCAP 2011)*, Apr. 2011, pp. 2459–2462.